

**MECHANICAL PERFORMANCE OF LAYERED
METALLIC COMPOSITES PROCESSED BY
ACCUMULATIVE ROLL BONDING**

A Dissertation

by

Dhyai Hassan Jawad Aljashaami

Submitted to the

Graduate School of Sciences and Engineering
In Partial Fulfillment of the Requirements for
the Degree of

Doctor of Philosophy

in the

Department of Mechanical Engineering

Özyeğin University

August 2019

Copyright © 2019 by Dhyai Hassan Jawad Aljashaami

Mechanical Performance of Layered Metallic Composites Processed by Accumulative Roll Bonding

Approved by:

Assoc. Prof. Dr. Güney Güven YAPICI,
Advisor,
Department of Mechanical Engineering
Head of Department
Özyeğin University


Assist. Prof. Dr. Altuğ BAŞOL,
Department of Mechanical Engineering
Özyeğin University

Assist. Prof. Dr. Zeynep BAŞARAN
BUNDUR,
Department of Civil Engineering
Özyeğin University

Assist. Prof. Dr. Alpay ORAL,
Department of Mechanical Engineering
Yıldız Technical University

Assist. Prof. Dr. Yasemin ŞENGÜL
TEZEL,
Faculty of Engineering and Natural
Sciences
Sabancı University

Date Approved: 20 August 2019



Dedicated to my family
(to my wife, for her unwavering support & the 2-Butterflies)

ABSTRACT

Mechanical Performance of Layered Metallic Composites Processed by Accumulative Roll Bonding

Multi-layered metal composites have received considerable attention due to their advanced mechanical and physical properties. The current work is an experimental study to fabricate the ultra-fine grained combination of similar and dissimilar composites utilizing accumulative roll bonding (ARB) process as a severe plastic deformation (SPD) technique. The experimental work was organized in two parts. The first part describes the combination of Al2024 and Al6061 in similar and dissimilar aluminum composites, while the second part has different Al/IF steel composites including Al6061, Al2024 and interstitial free (IF) steel in various stacking sequences.

Microhardness and uniaxial tensile tests were applied to analyse the surface and bulk mechanical properties of processed materials, respectively. This study not only investigates the monotonic mechanical behavior of multi-layered metal composites but also inspects the cyclic behavior of the prepared composites by employing the fatigue test. The high cycle fatigue (HCF) properties of layered metallic composites were investigated by cyclic testing under stress control with positive mean stress.

For the first part, the processed structure after four passes ARB contained the various layer combinations of Al2024 and Al6061. Remarkable enhancement was observed in the hardness level of the samples with increasing number of ARB passes. Accordingly, improvement levels, up to 1.5 and 2 times, were recorded for Al2024 and Al6061 layers, respectively. The tensile strength of the composite with an interchanging layer architecture reached over 320MPa after two cycles, coinciding with more than two-fold of the as-received

Al6061. The fatigue life was also improved, especially at the high stress amplitude. Microstructural observations revealed a significant grain refinement in further ARB processing along with the explanation of possible fracture mechanisms under tensile straining.

Additionally, the mechanical properties of processed materials were evaluated using shear punch testing (SPT). The correlation between the results of tension experiments and shear strengths was calculated. Experimental results demonstrated that the shear strength enhanced by increasing the number of ARB passes. However, the shear elongation exhibited a notable reduction when the number of ARB passes increased. Inspection of the tensile and SPT results revealed that they follow a similar trend for both strength and ductility. Therefore, it can be asserted that the shear punch test represents a useful and complementary tool in the mechanical analysis of the ARBed samples.

According to the SEM micrographs, in multi-passes ARB process, the interface of the previous pass bonds strongly during the next cycle, due to the improvement of the atomic diffusion and high pressure with further passes. The first ARB pass imposed a moderate strain and materials showed a ductile fracture with microvoids and dimples. With increasing cycles, the fracture mode remained as ductile with the existence of shear rupture and dimples. Nevertheless, these dimples were shallow and elongated, especially for the Al2024 layers as compared to those observed in Al6061.

For the second part, necking and fracture of IF steel layers were detected in the macrostructural observation after three passes of ARB process. Furthermore, after five ARB passes, a multi-layer IF steel/Al composite with homogeneously distributed IF steel lumps in aluminum matrix was attained for all stackings of IF/Al6061. However, the low difference between the hardness of the Al2024 and IF steel prevents the occurrence of the same

phenomena in Al2024/IF steel composites. Thus, the continuity of the layers after the third and fourth passes has remained for all stackings of IF/Al2024. Microstructure and mechanical characteristics of a fourth layer architecture were analyzed within a number of ARB passes.

The results revealed that the monotonic and cyclic behavior of all dissimilar composites were significantly increased compared to the base aluminum alloys, while the composites with the outer aluminum layers exhibited the highest fatigue life, due to crack branching at the interface region when it propagated from the softer to the harder layer. Fatigue fracture surfaces and crack propagation paths of the samples were observed by scanning electron microscopy (SEM). Also, fracture morphology analysis demonstrated that despite the surface cracks on the outer layers, indeed the fatigue cracks of interface layers were caused by the fracture of samples.

The ARB process was simulated utilizing finite element analysis. The effective stress and the distributions of equivalent strain along the thickness of ARBed sheets were determined. Results showed a significant agreement between the numerical simulations and the experimental findings. Finally, high cycle fatigue analysis was carried out and the results of the simulations were in decent agreement with the empirical data in terms of fatigue life. Also, as expected, the experimental fatigue life values for all conditions were lower than the simulations in relation with the existence of microcracks and scratches on the sample surface.

ÖZET

Birikmeli Hadde Yapıştırması ile İşlenmiş Katmanlı Metalik Kompozitlerin Mekanik Performansı

Çok katmanlı metal kompozitler üstün mekanik ve fiziksel özellikleri nedeniyle oldukça önem kazanmıştır. Bu tez çalışmasının amacı, benzer ve farklı kompozitlerin ultra-ince taneli kombinasyonunun birikmeli hadde yapıştırması (BHY) işlemi kullanılarak aşırı plastik deformasyon (APD) tekniği ile üretilmesidir. Deneysel çalışma iki bölüm halinde düzenlenmiştir. İlk bölüm benzer ve farklı alüminyum kompozitlerde Al2024 ve Al6061 kombinasyonunu tarif ederken, ikinci bölüm farklı istifleme düzeni ile Al6061, Al2024 ve arayer atomu içermeyen (IF) çelikler de dahil olmak üzere farklı Al/IF çelik kompozitlerini konu almaktadır.

İşlenik malzemelerin yüzeysel ve bütünsel mekanik özelliklerini analiz etmek için sırasıyla mikro sertlik ve tek eksenli çekme testi uygulanmıştır. Bu çalışma sadece çok katmanlı metal kompozitlerin monotonik mekanik davranışlarını incelemekle kalmamakta, aynı zamanda yorulma testi vasıtası ile dinamik davranışlarını da incelemektedir. Katmanlı metalik kompozitlerin yüksek çevrimli yorulma özellikleri gerilme kontrollü pozitif ortalama gerilmeli testler ile incelenmiştir.

İlk bölümde, dört kez BHY ile işlemik hale gelen yapı Al2024 ve Al6061'in çeşitli katman kombinasyonlarını içermektedir. Artan BHY paso sayısı ile malzemelerin mikro sertlik değerlerinde kayda değer artış gözlemlenmiştir. Buna göre, sırasıyla Al2024 ve Al6061 katmanları için 1.5 ve 2 kata varan iyileşme seviyeleri kaydedilmiştir. Değişmeli katman mimarisine sahip kompozitin çekme dayanımı, iki geçişten sonra orijinal Al6061'in iki

katından fazlasına denk gelen 320MPa, seviyesi üzerine ulaştı. Özellikle yüksek gerilme genliğinde, malzemenin yorulma ömrü de iyileşmiştir. Mikroyapısal incelemeler, BHY işleminde ortaya çıkan tane incelmesinin yanısıra çekme gerilmesi altındaki muhtemel kırılma mekanizmaları nı sergilemiştir.

Ayrıca işlenik malzemelerin mekanik özellikleri kesme zımba testi vasıtası ile değerlendirilmiştir. Çekme ve kesme zımba deneyleri sonuçları arasındaki ilişki hesaplandı. Deneyler sonucu artan BHY paso sayısının kesme dayanımını arttırdığı fakat kesme uzamasını azalttığı gözlemlendi. Çekme ve kesme testi sonuçları dayanım ve süneklik açısından benzer eğilim ortaya çıkarmıştır. Bu nedenle, kesme zımba testinin BHY numunelerinin mekanik analizinde kullanışlı ve tamamlayıcı olduğu ileri sürülebilir.

SEM mikrograflarına göre, çok pasolu BHY işleminde, önceki pasoda oluşan arayüz atomik difüzyon ve yüksek basınç sayesinde sonraki döngüde daha güçlü bir şekilde bağlanmaktadır. İlk BHY pasosu numunelere orta seviyede gerinim uygulamış ve mikro boşluklar ve çukurlar nedeni ile sünek kırılma sergilenmiştir. Geçiş sayısının artırılmasıyla kırılma şekli kayma kopması ve çukurların varlığıyla sünek karakterde kalmıştır. Bununla birlikte, bu çukurların özellikle Al6061'de gözlenenlere kıyasla Al2024 katmanları için sığ ve uzamış olduğu gözlemlendi.

İkinci kısımda üç BHY pasosunun ardından yapılan makro yapısal gözlemlerde IF çelik katmanlarında boyun verme ve kırılma tespit edildi. Ayrıca, beş BHY pasosu sonrasında, tüm IF/Al6061 istiflemeleri için alüminyum matris içinde homojen olarak dağılmış IF çelik öbeklere sahip çok katmanlı IF çelik /Al kompozit elde edilmiştir. Ancak, Al2024 ve IF çeliği sertliklerinin birbirine yakın olması, Al2024/IF çelik kompozitlerinde de benzer yapı oluşumunu engelledi. Böylece, üçüncü ve dördüncü pasolardan sonra katmanların sürekliliği,

tüm IF/AI2024 istiflemeleri için kalmıştır. Dördüncü katman mimarisinin mikroyapı ve mekanik özellikleri, bir dizi ARB geçişi içinde analiz edildi..

Sonuçlar, farklı tüm kompozitlerin monotonik ve dinamik davranışlarının, ana alüminyum alaşımına kıyasla dikkate değer derecede arttığını ortaya çıkarttı. Ayrıca yüzeyinde alüminyum katmanlara sahip olan kompozitlerde, yorulma çatlaklarının yumuşaktan sert katmana doğru yayılırken ara bölgede dallanmasından dolayı en yüksek yorulma dayanımı gözlemlenmiştir.

Numunelerin yorulma sonrası kırılma yüzeyleri ve çatlak ilerleme yolları taramalı elektron mikroskobu ile incelendi. Ayrıca, kırılma morfolojisi analizi, numunelerin dış katmanlardaki yüzey çatlakları nedeni ile değil, aslen ara yüz katmanlarında meydana gelen yorulma çatlakları nedeni ile kırıldığını göstermiştir.

BHY işlemi sonlu elemanlar analizi kullanılarak simüle edildi. BHY katmanları boyunca gerilme ve eşdeğer gerinim dağılımları belirlenmiştir. Sonuçlar, sayısal benzetimler ile deneysel bulgular arasında dikkate değer bir örtüşme olduğunu göstermiştir. Son olarak, yüksek çevrimli yorulma analizleri yapılmış ve benzetim sonuçlarının, yorulma ömrü açısından ampirik verilerle iyi bir uyum içinde olduğu gösterilmiştir. Ayrıca, beklendiği gibi, tüm koşullar için deneysel yorulma ömrü, değerlerinin benzetimlere göre daha düşük olması numunelerdeki mikro çatlaklara ve yüzey çiziklerine bağlanmıştır.

ACKNOWLEDGMENTS

Any accomplishment requires the efforts of many people, and this work is no different. This work was carried out under the supervision Dr. **Güney Güven Yapıcı** at the Department of Mechanical Engineering. I would like to express my sincere gratitude to my supervisor Dr. Güney Güven Yapıcı for his constant encouragement, scientific and professional discussions and constructive guidance during the last three years. I also wish to express my gratitude to my Ph.D. committee members **Dr. Altuğ BAŞOL** and **Dr. Yasemin Şengül Tezel** for their timely help and support at critical times.

The technical personnel at the Department of Mechanical Engineering deserve a huge acknowledgment. **Mr. Ulaş Yıldırım** has always been of timely help with sample preparation. I wish to record my sincere gratitude to higher executive officers **Mrs. Aylin Muhaddisoglu** and **Mrs. Gizem Bakir** at the Department of Mechanical Engineering. I am grateful for my supportive office mates within the MEMFIS group, **Ali Hosseinzadeh, Salar Salahi, Onur Bilgin and Görkem M Şimşek**. I record my deep sense of gratitude to my collaborators, friends, and colleagues in my research group who have helped me a lot during different stages of this work, **Dr. Isam Jabbar**.

Finally, I would like to thank all members of my family, especially my mother, and my wife for their unqualified love and encouragement, and my sister, for caring and taking my responsibility of looking after my mother when I am away from them. Their love means the world to me.

This work has been financed by the **Research Council of Iraq** under the **Strategic** of the **Iraqi Ministry of Higher Education** and Scientific Research Program Project Improvement.

TABLE OF CONTENTS

ABSTRACT.....	iv
ÖZET.....	vii
ACKNOWLEDGMENTS.....	x
TABLE OF CONTENTS.....	xi
LIST OF TABLES.....	xvi
LIST OF FIGURES.....	xvii
1.1 Motivation.....	1
1.2 Work summary.....	3
2. LITERATURE REVIEW.....	4
2.1 Overview.....	4
2.2 Severe plastic deformation (SPD).....	4
2.3 The accumulative roll bonding (ARB).....	9
2.3.1 Conventional Sheet Metal Rolling.....	9
2.3.2 Roll-Bonding and Bonding Mechanism.....	13
2.3.3 Bonding Mechanism.....	18
2.3.4 The advantage of the ARB process.....	22
2.3.5 Process Parameters.....	22
2.3.5.1. Temperature.....	22
2.3.5.2. Reduction per rolling cycle.....	24
2.3.5.3. Roll Diameter.....	25
2.3.5.4. Friction.....	25
2.3.5.5. The number of Rolling cycles.....	26
2.4 Aluminum alloys.....	27
2.4.1 ARB of aluminum alloys.....	28
2.4.2 ARB of Al6061.....	30
2.4.3 ARB of Al2024.....	34
2.5 ARB of IF steel.....	37
2.6 ARB of dissimilar material combinations.....	40
2.7 Evaluation of the mechanical behavior using the SPT.....	48

2.8 Cyclic behavior and fatigue properties of ARB processed materials.	51
2.8.1 Fatigue of ARB Processed Materials.....	53
3. EXPERIMENTAL PROCEDURE.....	58
3.1 MATERIALS.....	58
3.2 ACCUMULATIVE ROLL BONDING.....	59
3.3 MECHANICAL CHARACTERIZATION.....	61
3.3.1 Micro-Hardness Measurements.....	61
3.3.2 Tensile testing.....	62
3.3.3 Shear punch testing.....	62
3.3.4 Cyclic stress control tests (High-Cycle Fatigue test).....	63
3.4 MICROSTRUCTURAL INVESTIGATION.....	65
3.4.1 Metallographic procedure	65
3.4.2 Microstructure Characterization with optical microscopy (OM).....	66
3.4.3 Microstructure Characterization with scanning electron microscopy (SEM) (Fracture morphology analysis)	66
4. RESULTS AND DISCUSSION – MICROSTRUCTURE AND MECHANICAL PROPERTIES OF ARB PROCESSED ALUMINUM ALLOYS	67
4.1 Overview.....	67
4.2 ARBed microstructure.....	67
4.2.1 Bonding conditions of ARBed aluminum.....	67
4.2.2 Microstructure of ARBed similar layered aluminum composites.....	70
4.2.3 Microstructure of ARBed dissimilar layered aluminum composites.....	73
4.3 Mechanical properties.....	76
4.3.1 Al6061 sheets after ARBed.....	76
4.3.2 Al2024 sheets after ARBed.....	80
4.3.3 Al2024/Al6061 composite aluminum sheets after ARBed.....	82
4.4 Shear punch testing (SPT).....	87
4.5 Cyclic response under stress control.....	93
4.5.1 Fatigue properties of Al6061, Al2024, and composite Al2024/Al6061 sheets after the second cycle of ARBed	94
4.5.2 Fracture morphology analysis of Al6061 and Al2024 sheets.....	97

4.5.3 Fracture morphology analysis of Al2024/Al6061 dissimilar composites	99
4.5.4 Fracture morphology analysis after the fatigue test.....	102
4.5.5 Fracture morphology analysis after SPT.....	106
5. RESULTS AND DISCUSSIONS – MICROSTRUCTURE AND MECHANICAL PROPERTIES OF ARB PROCESSED ALUMINUM AND STEEL COMPOSITES	108
5.1 Overview.....	108
5.2 Microstructure of ARBed composites.....	110
5.2.1 Microstructure of ARBed Al6061/IF steel and Al2024/IF steel composites	110
5.2.2 Microstructure of ARBed Al2024/Al6061 Composite Aluminum with IF steel.....	117
5.3 Mechanical properties of Al6061/IF and Al2024/IF.....	118
5.3.1 Microhardness.....	118
5.3.2 Tensile behavior.....	120
5.3.3 Al2024/Al6061/IF steel composite fabricated by ARB process.....	125
5.4 Cyclic response under stress control.....	125
5.5 Characterization of microstructure.....	129
5.5.1 Fracture morphology analysis of Al6061/IF and Al2024/IF steel composites after the tensile test.....	130
5.5.2 Fracture morphology analysis of Al6061/IF/Al2024/IF composite	135
5.5.3 Fracture morphology analysis of Al/IF steel composites after fatigue test	137
6. NUMERICAL ANALYSIS.....	141
6.1 Introduction.....	141
6.2 Modeling of ARB process.....	142
6.2.1 Assumptions.....	142
6.2.2 Initial condition.....	143
6.2.3 Boundary condition.....	143
6.3 Results and discussion.....	146
6.4 Estimate the shear strain distribution over the thickness of sheets.....	150

6.4.1 Total equivalent strain distribution.....	151
6.5 High cycle fatigue (HCF) models.	155
6.5.1 Creating the model geometry.....	155
6.5.2 Mesh Generation.....	156
6.5.3 Simulation parameters.....	157
6.6 Result and discussion.	158
6.7 conclusions.....	163
7. CONCLUSIONS	164
8. OUTLOOK.....	168
8.1 Further improvement of the ARB process.	168
9. BIBLIOGRAPHY	169
PUBLICATIONS BASED ON THE WORK OF THIS THESIS.....	187
VITA.....	188

LIST OF TABLES

Table 2.1 Summary of major SPD processes [9]	9
Table 2.2 Example of the geometry changes after each accumulative roll bonding cycle commercially pure aluminum [30].....	15
Table 2.3 the Grain size, microstructure, and ultimate tensile strength of some different types of materials (metals and alloys) ARB processed in Osaka University [30].....	17
Table 2.4 Classification of wrought aluminum alloys [73].....	28
Table 2.5 Summary of some ARB-processed Al alloys, according to them series with some references.	29
Table 3.1 The chemical composition of Al6016	58
Table 3.2 The chemical composition of Al2024	58
Table 3.3 The chemical composition of (0.5 mm) IF steel	59
Table 4.1 Ultimate tensile strength and ultimate shear strength of different layers of ARB product.	93
Table 4.2 the results of σ_y , σ_{UTS} and ϵ of Al/IF steel composite after ARB process.....	126
Table 6.1 Tensile yield strength and effective stress of Al2024/Al6061 composite after one, two, and three ARB cycles.....	150

LIST OF FIGURES

Figure 2.1: Microstructure of Commercial pure Aluminum shows the shape of grains [8]... 5	5
Figure 2.2: Classification of metals by the grain size [9] 6	6
Figure 2.3: Schematic representation bottom-up and top-down approaches [9] 7	7
Figure 2.4: Illustrate a) Sketch of the rolling process display the deformation zone; b) shows the direction of friction action before and after the neutral point, N [34]. 10	10
Figure 2.5: Schematic of forces throughout the conventional flat rolling [35] 12	12
Figure 2.6: Schematic diagrams of the ARB process [4]. 16	16
Figure 2.7: The flextion of the embedded pin in the Al1100 one cycle ARB processed at room temperature without oil. Detected on a longitudinal section [51]. 18	18
Figure 2.8: Shear strain distribution along the thickness of the Al1100 ARB processed by (a) one, (b) two, (c) four, and (d) eight cycles [51]. 18	18
Figure 2.9: Schematic of the various steps included in bond formation: at the interface a) break-up of cover layer b) extrusion onset c) weld formation [58]. 21	21
Figure 2.10: Shear strength of the interlamellar bond of the AA6111 as a function of entry temperature [64]. 23	23
Figure 2.11: Shear strength of interlamellar bonding of the AA6111 as a function of rolling speed and percentage reduction [64]. 24	24
Figure 2.12: Equivalent strain distribution throughout the thickness against roll diameter $d\phi$ and friction coefficient [68]. 25	25
Figure 2.13: Shear strength of interlamellar bonding of the AA6111 as a function of roll pressure [64]. 26	26
Figure 2.14: Mechanical properties of the 1100 Al alloy at room temperature after ARB applied at 473K [31] 30	30
Figure 2.15: Effect of wire brushing on hardness near the bonded interface [93]. 31	31

Figure 2.16: Mechanical properties of the AA6061 roll bonded at room temperature [93].	32
Figure 2.17: Stress-Strain graphs for Al6061 within various cycles of ARB [88].	33
Figure 2.18: Mechanical properties (a) UTS and (b) elongation as a function of cycle number with various heat treatment procedure [94].	34
Figure 2.19: Engineering stress vs. Engineering strain curves of the different condition of Al2024 for various cycles [97].	35
Figure 2.20: Tensile properties of Al2024 represented for a different number of ARB cycles [78].	37
Figure 2.21: Tensile properties of the IF steel tested at ambient temperature after various cycles of ARB [39].	38
Figure 2.22: a) The microhardness, b) tensile strength, c) yield stress point, and d) elongation of IF steel as a function of various cycles of ARB process [95].	39
Figure 2.23: Truck bumpers made of cladding metals [104].	41
Figure 2.24: a) TEM micrograph of commercial purity aluminum after four cycles showing lamellar structure. b) Schematic illustrating the lamellar boundaries (LBs) and interconnecting boundaries (ICBs), in the rolling RD and normal directions ND, respectively [49].	42
Figure 2.25: Variations of the hardness of Al5005 and Al6061 with a number of ARB cycles.	44
Figure 2.26: Stress vs. Strain curves for composites of Al6061/Al1050 after the ARB process, and following by AR process [123].	46
Figure 2.27: Stress vs. strain curves of the layered composite Al/Al after 4 cycles of ARBed and the Al/ steel composites after ARBed [44].	48
Figure 2.28: a) Schematic drawing of the Shear Punch Test, b) the typical LDC curve [132,133].	50

Figure 2.29: Low cycle fatigue curve [144].	53
Figure 2.30: High-cycle fatigue (HCF) [145].	53
Figure 2.31: Illustration of fatigue crack growth paths of the AA1050/AA2024 N2 composite failed after fatigue test at stress amplitudes a) and b) lower than threshold stress ($\Delta\sigma/2 = 110\text{MPa}$) and c) and d) higher than threshold stress ($\Delta\sigma/2 = 180\text{MPa}$) [154].	55
Figure 2.32 The LMCs of AA5754/DC05 with different position of the steel layer a) 1/4, b) 1/8, of the total thickness of the sheet and c) at the outer surface [3].	57
Figure 3.1: The flow chart of the experimental work.	59
Figure 3.2: The experimental work for the ARB process.	60
Figure 3.3: Shows the equipment used in the experimental work.	61
Figure 3.4: Shear punch device die, specimen holder, and punch.	63
Figure 3.5: ASTM E466 standard high cycle fatigue specimens [157].	65
Figure 3.6: Scanning electron microscope (SEM), used for microstructure characterizations.	66
Figure 4.1: Optical microstructure of the Al 6061/Al 6061 composites after (a) One, (b) two, (c) three, (d) four, and (e) five passes ARB.	68
Figure 4.2: Optical microstructure of the Al2024/Al2024 composites after a) One, (b) two, c), and three passes ARB.	69
Figure 4.3: Al2024/Al2024 after three cycles illustrated the propagation of edge crack.	70
Figure 4.4: Microstructure of Al6061 a) as received, b) after the one cycle, c) after two cycles.	71
Figure 4.5: Microstructure of Al2024 a) as received, b) after one cycle, c) after two cycles ARB.	72
Figure 4.6: Optical micrographs of a) as received Al6061, b) as received Al2024, c) Al6061 after four ARB cycles, d) Al2024 after four ARB cycles, and e) illustration of the lamellar	

boundaries (LBs) and interconnecting boundaries (ICBs), where RD and ND are the rolling and normal directions, respectively.	74
Figure 4.7: Optical microstructure of the Al 2024/Al 6061 composites after a) one pass, b) two passes, c) three passes, and d) four passes ARB process.....	75
Figure 4.8: Variation of microhardness, a) with a number of ARB cycles, b) over the thickness of the sample after five cycles.....	78
Figure 4.9: Stress-strain response of the fabricated composites of 4layers Al6061/Al6061.	80
Figure 4.10: Variation of microhardness a) with a number of ARB cycles, b) over the thickness of the sample after three cycles.....	81
Figure 4.11: Stress-strain response of the fabricated composites Al2024/Al2024 after one, two, and three cycles.	82
Figure 4.12: Variation of microhardness a) with a number of ARB cycles, b) over the thickness of the sample after three cycles.....	83
Figure 4.13: Stress-strain response of the a) fabricated composites of Al2024/Al6061 b) comparison between Al6061/A6061, Al2024/Al2024 composites,, and Al2024/Al6061 composite after the second cycle.	86
Figure 4.14: Variations in mechanical properties as a function of cycle number for composite Al2024/Al6061.....	87
Figure 4.15: SPT curves for layered metal composites of A) Al6061/Al6061 and b) Al2024/Al2024 for the different ARB process.....	90
Figure 4.16: SPT curves for layered metal composites of Al2024/Al6061 with the different ARB process.	91
Figure 4.17: The correlation curve of USS with UTS for layered metal composites of Al2024/Al2024, Al2024/Al6061, and Al6061/Al6061 with the different ARB process.	92

Figure 4.18: a) The stress amplitude and fatigue life (S–N curve) for composites Al2024/Al6061 four-layer composites and for base-material the Al2024 and Al6061 b) Variations of microhardness at the interface area.....	96
Figure 4.19: Fracture surface of the specimen after the tensile test under strain rate of $0.001s^{-1}$ at room temperature for Al6061 at different conditions of a) and b) as-received, c) after one cycle (2 layers), and d) after three cycles (8layers).....	98
Figure 4.20: Fracture surface of the specimens tested at room temperature under the strain rate of $0.001s^{-1}$ for Al 2024 at different conditions of a) and b) as-received with different magnification c) after one cycle (2 layers), d) after two cycles (4layers).....	99
Figure 4.21: SEM images of the fracture surface of the layer metal composite a) after the second cycle, b) after the third cycle of the ARB process.....	100
Figure 4.22: SEM images of the fracture surface from the 6061 alloys, a) as-received, b) after one cycle, c) after four cycles of ARB, and from the 2024 alloy, d) as-received, e) after one cycle, f) after four cycles of ARB.....	101
Figure 4.23: SEM observations of fatigue damage at the surface close to the crack zone for 4layers of a) Al6061/Al6061 composite, b) Al2024/Al2024 composite.....	104
Figure 4.24: SEM observations of fatigue damage at the surface close to the crack zone for 4layers of a) Al6061/Al202 /Al6061/Al2024 composite, b) Al6061/Al2024/Al2024/ Al6061 composite.....	105
Figure 4.25: Optical microscopy (OM) of crack growth paths of the four layers a) Al6061/Al6061 composite b) Al2024/Al2024, and c) Al6061/Al2024/Al2024/Al6061. ...	106
Figure 4.26: SEM micrographs of shear failure surfaces of 4layers for a) Al6061/A6061, b) Al2024/Al2024, and c) Al2024/Al6061.....	107
Figure 5.1: A schematic illustration of the fabricating sequence of IF steel/Al composites.....	109

Figure 5.2: Optical micrographs of a) IF steel as received, b) Al6061 as received, c) IF steel after one ARB cycles, and d) Al6061 after one ARB cycles.....	111
Figure 5.3: Optical micrographs of a) as received IF steel, b) as received Al2024, c) IF steel after one ARB cycle, d) Al2024 after one ARB cycle, and e) IF after two ARB cycles.....	112
Figure 5.4: The layer shapes of multilayer Al6061/IF steel composite after one, two, three, four, and five cycles ARB.....	114
Figure 5.5: The layer shapes of multilayer Al2024/IF steel composite after one, two, three, and four cycles ARB.....	116
Figure 5.6: Optical micrographs of composite in the a) IF steel/Al2024 side after one cycle, b) IF steel/Al6061 side, after one cycle, c) IF steel/Al2024 side after the second cycle, d) IF steel/Al6061 side after the second cycle.....	118
Figure 5.7: Variation of microhardness with the number of ARB cycles for (Al6061/IF/IF/Al6061), (IF/Al6061/Al6061/IF) and (IF/Al6061/IF/Al6061).	119
Figure 5.8: Variation of microhardness with the number of ARB cycle group A, Al2024/IF/IF/Al2024, group B IF/Al2024/Al2024/IF and group C Al2024/IF/Al2024/IF.	120
Figure 5.9: Stress-strain response of the fabricated composites of a) Al6061/IF/IF/Al6061	122
Figure 5.10: Stress-strain response of the fabricated composites of a) Al2024/IF/IF/Al2024	124
b) IF/Al2024/Al2024/IF c) Al2024/IF/Al2024/IF.	124
Figure 5.11: Stress-strain response of the fabricated composites of Al6061, Al2024 & IF125	
Figure 5.12: Variations between stress amplitude and fatigue life (S–N curve) for composites Al6061/IF/IF/Al6061, IF/Al6061/Al6061/IF, Al6061/IF/Al6061/IF, IF/Al2024/Al2024/IF, Al2024/IF/IF/Al2024, Al2024/IF/Al2024/IF and	

IF/Al2024/Al6061/IF four-layer composites and for single material type the Al6061 and Al2024.....	129
Figure 5.13: The fracture surface of the as-received IF steel tested under the strain rate of 0.001s^{-1} a) low magnification and b) in high magnification.....	130
Figure 5.14: The fracture surface of 2 layers IF/Al6061 composite after one cycle ARB tested under the strain rate of 0.001s^{-1} in a) low magnification and in high magnification, b) the Al6061, and c) IF steel.....	131
Figure 5.15: The fracture surface of 4 layers IF/Al6061 /IF/Al6061 composite after two cycles ARB tested under the strain rate of 0.001s^{-1} in a) low magnification and in high magnification, b) IF steel, and c) Al6061.	132
Figure 5.16: The fracture surface of 4 layers IF/Al2024 /Al2024/IF composite after two cycles ARB tested under the strain rate of 0.001s^{-1} in a) low magnification and in high magnification, b) IF steel, and c) Al2024.	133
Figure 5.17: The fracture surface of 4 layers IF/Al2024 /Al2024/IF composite after two cycles ARB tested under the strain rate of 0.001s^{-1} in a) low magnification and in high magnification, b) the interface of Al2024/IF steel.....	134
Figure 5.18: The fracture surface of 8 layers IF/Al2024 /Al2024/IF composite after three cycles ARB tested a) low magnification and in high magnification for b) the interface of Al2024/Al2024, and c) the interface of Al2024/IF steel.	135
Figure 5.19: The fracture surface of 4 layers IF/Al2024 /IF/Al6061 composite after two cycles ARB tested under the strain rate of 0.001s^{-1} in a) low magnification and in high magnification for, b) of IF steel, c) the interface between IF steel/ Al2024, d) Al2024, e) interface between Al6061/IF and c) Al6061.....	136

Figure 5.20: SEM observations of fatigue damage at the surface close to the fracture zone of a) Al6061/IF/IF/Al6061 layered composite. b) IF/Al6061/Al6061/IF layered composite and, observation of different fatigue fracture morphologies.	138
Figure 5.21: SEM observations of fatigue damage at the surface close to the fracture zone of a) Al2024/IF/IF/Al2024 layered composite. b) IF/Al2024 /Al2024/ IF layered composite and, observation of different fatigue fracture morphologies.	139
Figure 5.22: SEM of crack growth paths of the four layers a) Al6061/IF/IF/Al6061 composite b) IF/Al6061/Al6061/IF.	140
Figure 5.23: SEM of crack growth paths of the four layers a) Al2024/IF/IF/Al2024 composite b) IF/Al2024/Al2024/IF.	140
Figure 6.1: The model applied to the simulation of ARB of the dissimilar composite.	142
Figure 6.2: a) The effective Plastic strain b) the effective stress (v-m) (MPa) during the first cycle.	144
Figure 6.3: Illustrated the effective stress (v-m) of third cycles a) before rolling b) during the rolling process.	144
Figure 6.4: Distribution of the equivalent strain along the sheet thickness for Al6061/Al2024 composite after one, two, and three cycles.	147
Figure 6.5: Histories of equivalent strain, ϵ_{eq} , at (1) center, (2) near the center and (3) surface during rolling, for Al6061/A2024 composite after one cycle.	148
Figure 6.6: Von Mises stress for Al6061/Al2024 after one, two, and three passes.	149
Figure 6.7: Schematic diagram showing the shear strain calculated by the embedded-pin method [51]: a) sketch before rolling, b) after rolling.	152
Figure 6.8: Shape of the embedded pin in the Al sheet processed by a) one ARB cycle, and b) two ARB cycles.	154

Figure 6.9: Equivalent strain distributions through the thickness of the Al composite sheet processed by one and two ARB cycle.....	154
Figure 6.10: The geometrical model imported in the ANSYS Workbench software.....	156
Figure 6.11: The meshing geometrical model of high cycle fatigue (HCF).....	156
Figure 6.12: The simulation parameters of the high cycle fatigue.	158
Figure 6.13: The fatigue life of Al6061/Al6061 under a) 90%, b) 80%, and c) 60% of yield stress.....	159
Figure 6.14: The fatigue life of Al2024/Al2024 under a) 90%, b)80%, and c)60% of yield stress.....	160
Figure 6.15: The fatigue life of Al6061/Al2024 under a) 90%, b) 80%, and c) 60% of yield stress.....	161
Figure 6.16: Comparison between experimental and theoretical results of fatigue life. ...	162

CHAPTER I

1.1 Motivation

Energy efficiency is one of the most critical topics which the factories and different types of industries are working on it. Strength to weight ratio is the main factor of energy efficiency in the aerospace and automotive industries. Therefore, they began to use, lightweight materials such as aluminum (2700kg/m^3), rather than using heavier steel (7800kg/m^3), this leads to reducing emissions and less fuel consumption. The use of lightweight materials instead of steel requires new composite or alloys which have similar mechanical properties.

Replacing metals with a comparatively high density and low strength and hardness such as steel with materials of relatively high strength and hardness such as aluminum or magnesium is yet another effective strategy to reduce vehicle weight. For example, an aluminum alloy structure provides weight reductions to a car body of 200 to 300kg [1].

For many years, researchers have been making strenuous efforts to improve the strength of materials using different processing techniques. Some techniques are characterized by the application of high strain with the refinement of grain structure, such as severe plastic deformation (SPD). From the design point of view, toughness, strength, and ductility of the metals can be the most important properties to be considered. SPD was used to enhance the strength of the metal with minimum effects on ductility. The products should stand the application of external forces both in the monotonic and cyclic regimes.

In this study, accumulative roll bonding (ARB) was applied as an SPD method to produce multi-layered metal composites. It was observed that a significant improvement in the strength of layered metallic composites (LMC) was achieved via ARB processing because of the work hardening and the grain refinement.

The main aim of this work is to identify the processing schedule to obtain a composite

of the aforementioned aluminum alloys exhibiting favorable mechanical performance. One of the most important advantages of a layered composite having dissimilar constituent is providing the ability to exhibit the advantageous features of both. For the present case, this approach offers the opportunity to complement the inherent corrosion resistance of Al6061 by the superior strength properties of Al2024 [1,2].

On the other hand, the lack of data about the cyclic behavior of multi-layered metal composites fabricated by ARB process has limited the application of them in engineering structures. Therefore, the present work concentrated on the fatigue behavior of the processed samples to characterize the cyclic behavior of the composites. Inspection of the results achieved from the fatigue tests revealed that the enhancement of fatigue strength was observed for the composite structure. Additionally, the fracture morphology of the composites was analyzed to predict the fracture behavior after processing with different stacking sequences.

Moreover, the monotonic and cyclic behavior of the consisting of interstitial free (IF) steel and aluminum LMCs are investigated. This section aims to find a layer architecture, where the global mechanical properties and fatigue life are enhanced. For this purpose, different layer architectures of aluminum and IF steel were used. It can be confirmed that all previous studies about the cyclic mechanical properties of LMC produced by ARB has been conducted using the 3-point bending test [3–5]. Therefore, in this study, the fatigue curve was carried out under tension-tension condition. However, detailed insight into the effects of layer architecture on the fatigue properties is still lacking and needed to be investigated.

Finally, as far as numerical modelling of the ARB is regarded, again an exhaustive numerical model of the process is still missing. Consequently, the experimental analysis was carried out to obtain the material behavior and to validate the numerical results in comparison with the data measured during the experimental tests (such as the effective stress, the equivalent strain distribution after the ARB process, fatigue life and fatigue strength under HCF).

1.2 Work summary

In this thesis, Chapter two begins with a literature review of pertinent subjects covered in this work. The third chapter is concerned with the methodology used for this study. The first part of the experimental work conducted to characterize the mechanical properties of as-received materials than the primary manufacturing methods and preparation of different types of specimen for various testing methods employed in this project. The results of different mechanical testing and microstructure observation of ARB processed aluminum composites were presented in chapter four. The results for tensile and fatigue tests of the interstitial-free (IF) steel and aluminum composite fabricated by accumulative roll bonding are presented in chapter five. In chapter six, using the finite element method (FEM), values of strain amplitude of the ARB processed structures were calculated. The simulations and results of the numerical method were compared with the obtained experimental results. Chapter seven contains the general conclusions of the thesis and finally, some suggestions for the design of composite structures and directions for future work were written in chapter eight.

CHAPTER II

LITERATURE REVIEW

2.1 Overview

Recently, ultra-fine grained (UFG) materials have received great attention for achieving superior mechanical performance. Different methods can be used to fabricate UFG and nanostructured (NC) materials and all of them have several advantages and disadvantages. The most common approach to modify the coarse-grained (CG) metals to the UFG is using severe plastic deformation (SPD). One of the major benefits of SPD methods is the potential of fabricating bulk materials with sub-micron grain size in large quantities. The aforementioned feature of SPD processes has an important role in industrial purposes in which mass production is needed. The accumulative roll bonding (ARB) method is a technique with excellent potential for fabricating large bulk sheet metals [6]. In this chapter, previous studies in the literature concerning the processing parameters, mechanical and cyclic behavior of different materials produced by the ARB process will be reviewed and discussed in detail.

2.2 Severe Plastic Deformation (SPD)

It is well known that all metals consist of atoms. These atoms have an arrangement with one another, and on the basis of this arrangement, the solid metals can be divided into amorphous (non-crystalline) and crystalline metals. In crystalline metals, the atoms are ordered in a long, repetitive row of atoms, while in non-crystalline metals such a large atomic arrangement is missing. Crystal structures of the crystalline metals can be face-centered cubic, body-centered cubic and hexagonal closed pack, which are classified into two categories: polycrystalline and single crystal. Single crystalline metals are characterized by a similar

interlocked with the same orientation, while the polycrystalline metals are composed of a high amount of single crystals (grains) with various crystal orientations Fig. 2.1. Most of the polycrystalline metal's characteristics are dependent on the microstructural property, particularly the grain size [7]. Grain size has a direct effect on the mechanical, chemical and physical properties of metals and their effect on mechanical properties can be observed through the Hall-Petch equation (2.1) [8]

$$\sigma_y = \sigma_0 + Kd^{-1/2} \quad (2.1)$$

where σ_0 is the friction stress, d is the grain size, and K is a constant.

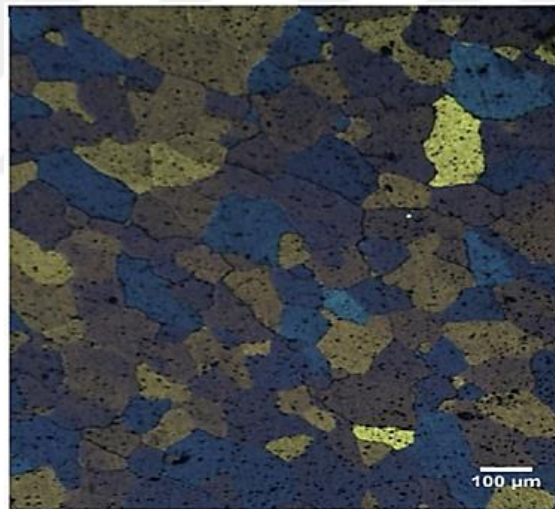


Figure 2.1: Microstructure of commercial pure aluminum shows the shape of grains [8].

Fig. 2.2 illustrates the classification of metals by the grain size to the: i) coarse-grained (CG) metals with a grain size of 10 μm, ii) Fine-grained metals with 1-10 μm grain size, iii) ultrafine-grained (UFG) materials with a grain size more than 100 nm and less than 1 μm, v) nanograined or nanostructured (NS) which have a grain size below 100 nm.

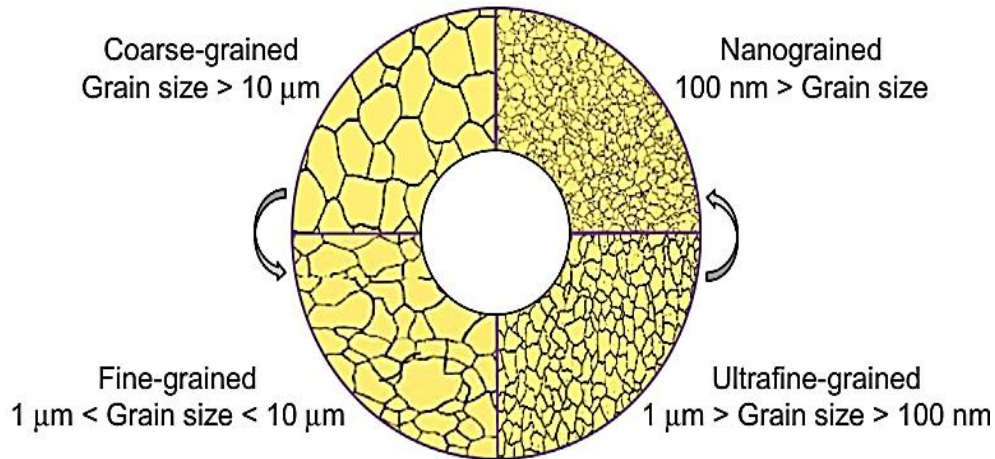


Figure 2.2: Classification of metals by the grain size [9].

The first type of material is generally produced by casting processes, while the fine-grained materials are manufactured by the industrial thermomechanical methods in which the metal-forming technique is carried out [10]. Two complementary approaches: bottom-up and top-down methods for producing UFG and NS materials, Fig. 2.3. The first method, which assembles materials atom by atom includes spray conversion processing [11], inert gas condensation [12], high-energy ball milling [13], sputtering [14], electrodeposited nanocrystals [15], and chemical vapour deposition [16]. This approach is economically inefficient due to small product size, contamination, porosity, and high cost [17]. Top-down is the second method; it depends on the refine initially coarse-grained materials to produce UFG and NS materials or a bulk metal with nanosized particles. The most useful treatments include severe plastic deformation (SPD), which are based on the second approach.

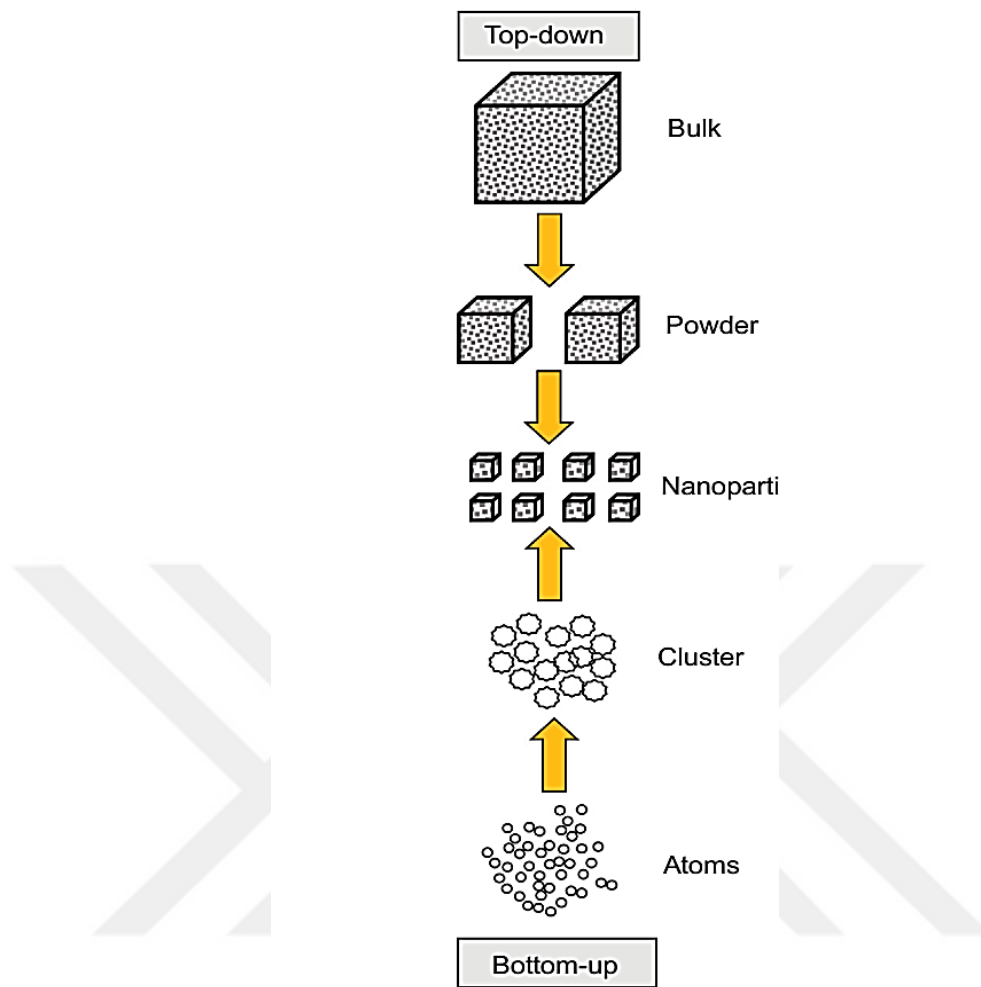



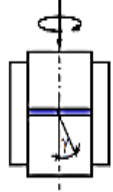
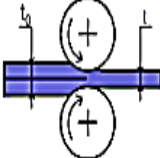
Figure 2.3: Schematic representation bottom-up and top-down approaches [9].

Processes with severe plastic deformation (SPD) can be named as metal forming methods in which an enormously large plastic strain is introduced into a bulk metal with the purpose of creating UFG materials. Above mentioned refinement happens through the shear and fracture of phases simultaneously with recrystallization processes (generally dynamic recrystallization). The critical part of the process is providing a balance between the work hardening rate and dynamic recovery, which determines the final microstructural outcome. It is known that the materials produced by these methods have extremely small average grain sizes of less than 1 μm . Another significant specification of these productions is high angle misorientation of grain boundaries. Increasing dislocation density is the fundamental mechanism

behind these techniques. In order to decrease the strain field blended with dislocation arrangement, they recover into cell wall structures and deformation shear bands. During room temperature recovery-recrystallization, microstructures can change into low-angle or high-angle grain boundaries. There are a number of non-traditional processes for severe plastic deformation such as High Pressure Torsion (HPT)[18], Equal-Channel Angular Extrusion (ECAE) [19], Cyclic Extrusion Compression (CEC) [20], Repetitive Corrugation And Straightening (RCS) [21], Severe Torsion Straining (STS) [22], Super Short Multi-Pass Rolling (SSMR) [23] Cyclic Closed-Die Forging (CCDF) [24], friction stir processing FSP [25], Torsion Extrusion [26] and Accumulative Roll Bonding (ARB) [27–31] which can be utilized to fulfill an UFG microstructure and consequently achieve an enhancement in mechanical properties including strength, hardness, cyclic deformation and /or ductility [32]. The most common SPD processes are summarized in Table 2.1 with schematic forms and the achievable plastic strain [9].

The most common SPD techniques require expensive equipment including expensive dies, large load capabilities, a limited sample size as well as low production efficiency. Hence, new trends in the production of nanomaterials and ultrafine-grained were introduced in 1998 using the ARB method, which is an economical process. ARB is the only promising process that has a potential for the continuous production of large bulk sheet materials for industrial applications [33].

Table 2.1 Summary of major SPD processes [9].

Process name	Schematic representation	Equivalent plastic strain
Equal channel angular extrusion (ECAE) (Segal, 1977)		$\epsilon = n \frac{2}{\sqrt{3}} \cot(\varphi)$
High-pressure torsion (HPT) (Valiev et al., 1989)		$\epsilon = \frac{\gamma(r)}{\sqrt{3}} \cdot \gamma(r) = n \frac{2\pi}{t}$
Accumulative roll-bonding (ARB) (Saito, Tsuji, Utsunomiya, Sakai, 1998)		$\epsilon = n \frac{2}{\sqrt{3}} \ln\left(\frac{h_0}{t}\right)$

2.3 The accumulative roll bonding (ARB)

2.3.1 Conventional Sheet Metal Rolling

Rolling is a metal forming process in which sheet metal is plastically deformed by passing among the rolls [34]. Throughout the rolling, sheet metal is exposed to high compressive stresses because of high surface shearing stresses arising from the friction force between the sheet and the rolls and squeezing action of the rolls. The purpose of the rolling process is not only decreasing the cross-section of the workpiece, from the original thickness to a predestined final thickness, but also gaining superior mechanical properties of the processed product. The most critical parameters of the rolling process are shown in Fig. 2.4 where h_0 and h_f are the initial and final thickness, V_0 and V_f are initial (entering) and final velocity of the sheet, R is the radius of rolls, ω and α are the rotational speed of the roll and angle of contact, respectively.

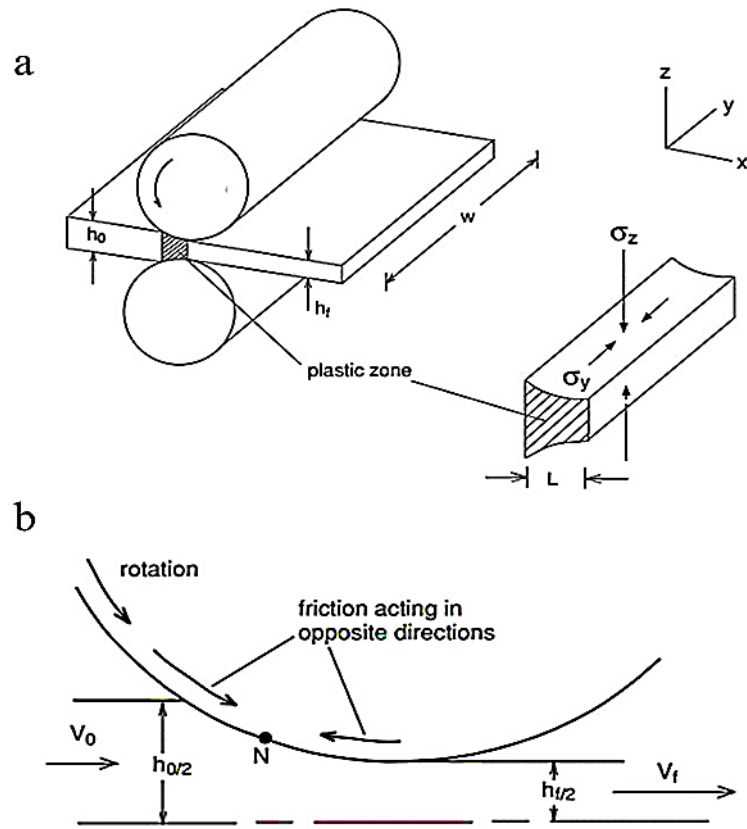


Figure 2.4: Illustrate a) Sketch of the rolling process display the deformation zone; b) shows the direction of friction action before and after the neutral point, N [34].

Also, w is sheet width and L is projected length of contact (deformation zone). The process of rolling in flat shape mode, generally assumed to be two-dimensional, because deformation of the material in width direction is very small compared to the thickness and length then it can be neglected. Also, the plane-strain plastic flow will be quite realistic with this assumption.

The reduction in thickness and the value of deformation, the strain can be calculated by equations (2.2) and (2.3) respectively.

$$\Delta h = h_0 - h_f \quad (2.2)$$

$$\varepsilon_h = \Delta h / h_0 \quad (2.3)$$

As previously explained, the increase in width can be neglected in the flat rolling process, then the velocity of the sheet can be obtained as.

$$v_0 \cdot h_0 \cdot w_0 = v_f \cdot h_f \cdot w_f \quad (2.4)$$

Since the material has a constant volume before and after rolling we have

$$w_0 = w_f \quad (2.5)$$

The velocity in rolling direction is

$$v_x = v_0 (h_0 / h_x) \quad (2.6)$$

The relationship to finding a deformation zone is:

$$L = [R(h_0 - h_f)]^{-1/2} \quad (2.7)$$

The mechanism of the rolling process can be summarized as follows; the slab is pulled through the rolls due to the frictional force between rolls and slab's surfaces. At the first point of contact, the speed of the slab is very slow and with passing through the roll speed of the slab is increasing up to the roll's rotational speed at deformation zone. The point which speed of the slab is reaching to the roll's speed is called the neutral point. On the departure side of the neutral point, the slab passes with a speed which is higher than the speed of the rolls and the direction of frictional force is reversed and will act as to oppose the material flow.

Before the rolling process, two necessary conditions should be satisfied. The slab must be taken and gripped by the rolls and then drawn through the rolls. The two relations can be derived from Fig. 2.5.

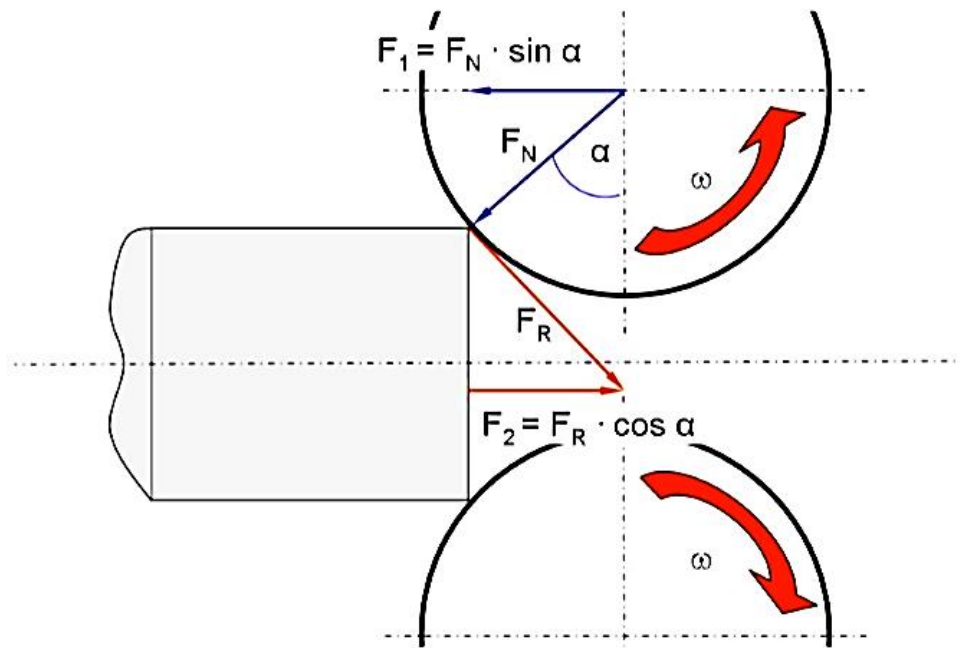


Figure 2.5: Schematic of forces throughout the conventional flat rolling [35].

Pull slab occurs if

$$F_2 \geq F_1 \quad (2.8)$$

From Fig. 2.5, F_1 , and F_2 can be found as follows.

$$F_1 = F_N \cdot \sin \alpha \quad (2.9)$$

$$F_2 = F_R \cdot \cos \alpha \quad (2.10)$$

Since $F_R = \mu \cdot F_N$ equation (2.10) can be rewritten as

$$F_2 = \mu \cdot F_N \cdot \cos \alpha \quad (2.11)$$

Hance,
$$\mu \cdot F_N \cdot \cos \alpha \geq F_N \cdot \sin \alpha \quad (2.12)$$

This gives
$$\mu \geq \tan \alpha \quad (1.13)$$

That means the first condition (grip condition) is

$$\mu \geq \alpha \quad (2.14)$$

Also for the draw sheet through the rolls, condition (pull condition) is

$$2 \cdot \mu \geq \alpha \quad (2.15)$$

Complex interactions between the rolls and the metal sheet in the rolling process may cause different kinds of defects inside the rolled product. These defects can be sheet bending in the rolling plate, waviness, non-uniform thickness in rolling direction or width, edge cracking, etc.

2.3.2 Roll-Bonding and Bonding Mechanism

Accumulative roll bonding (ARB) is a severe plastic deformation (SPD) process for fabricating sheet materials with improved mechanical behavior. The existence of an ultra-fine grained (UFG) microstructure is responsible for achieving desirable strength properties [36]. High strength, combined with the possibility of obtaining tailored microstructures, makes ARB processed composites, an excellent candidate for lightweight structural applications in various industries, including automotive, marine, and aerospace [37]. The ARB technique created by Saito et al. is an elegant rolling process that aims to provide a large plastic deformation and bond multiple layers [36]. Unlike other SPD methods, multi-layered materials can be obtained

by the utilization of ARB. It is possible to achieve functional grading by stacking dissimilar materials in a layered fashion [38].

ARB is one of the most widely used SPD methods and has been extensively utilized to produce NS/UFG in a scope of metallic alloys such as Al alloys, IF steel [39], Zr alloys [40], Ni alloys [41], LC steel and multilayer composites like Al/Cu [42], Zr/Cu [43], steel/Ti, Al/steel [44], Cu/Ti [45], Al/Ti [46], Al/ DC05 steel [3].

Many researchers were studying in this area, and they used different kinds of metals for this purpose [38]. ARB is an exceptional plastic straining procedure presenting ultra-high strains in the material. It includes roll bonding of two strips, cutting the rolled material into two equal parts, stacking them one on another and rolling once more. This working sequence of cutting, stacking and rolling described in Fig. 2.6 repeats at various times to carry out the required strain levels. Preheating of the specimens might be considered before rolling for some materials. Considering there is no limit for repeating the procedure which is mentioned above, imposing very large plastic strain on the sheet material is very easy and feasible in the ARB process. Table 2.2 summarizes the equivalent strain and total reduction in thickness for each number of layers and cycles in the ARB process, provided two parts of the sheets with 1 mm thickness, stacked and roll-bonded by 50% reduction per cycle. As it is described in Eq. (2.16) for n cycles, the total von Mises equivalent strain would be $0.8n$ due to 0.80 equivalent strains after each cycle of rolling with a 50% reduction in thickness. Generally, the ARB process is most applicable method compared with the other SPD techniques.

$$h = h_0/2^n \quad (2.16)$$

The total true effective strain of each processed material will be calculated using the following relation.

$$\varepsilon_T = (2/\sqrt{3})n \cdot \ln(1 - r) = 0.8n \quad (2.17)$$

where r is the reduction in thickness per rolling cycle ($r = \left(1 - \frac{h}{h_0}\right) = \left(1 - \frac{1}{2^n}\right)$) and n is the number of cycles.

Table 2.2 Example of the geometry changes after each accumulative roll bonding cycle commercial pure aluminum [30].

No. of cycles	1	2	3	4	5	6	7	8	9	10	n
No. of layers	2	4	8	16	32	64	128	256	512	1024	2^n
No of bonded boundaries	1	3	7	15	31	63	127	255	511	1023	$2^n - 1$
Layer interval (μm)	500	250	125	62.5	31.2	15.6	7.8	3.9	1.9	0.96	$1000/2^n$
Total reduction (%)	50	75	87.5	93.8	96.9	98.4	99.2	99.6	99.8	99.9	$(1 - 1/2^n) \times 100$
Equivalent strain	0.8	1.6	2.4	3.2	4.0	4.8	5.6	6.4	7.2	8.0	$\left(\frac{2}{\sqrt{3}} \ln 2\right) n = 0.8 n$

Also, there are some significant difficulties with the ARB process. Particularly, with regards to retaining structural and mechanical integrity of the material as the level of accumulated cold-working increases, the work hardening metals will become increasingly hard and brittle as the number of cycles increases, prompting extreme crack development along the rolling direction of the material through the rolling process. At the point when roll bonding different metals, the contrast in plastic flow will cause instabilities at the interfaces, prompting untimely crack initiation, after that the crack will propagate and make the fracture of the layers [47]. In specific types of the materials, such as Al-Mg alloy, the edge cracks considerably propagate into the center of the slabs. In this situation, continuing the process to the consequent cycles is not possible. Nevertheless, some techniques are used in order to fabricate sound bulk plates without such cracking by ARB in most of the metallic materials. Since the reduction is 50% per cycle, the new thickness can be calculated from the relation after n cycles [33].

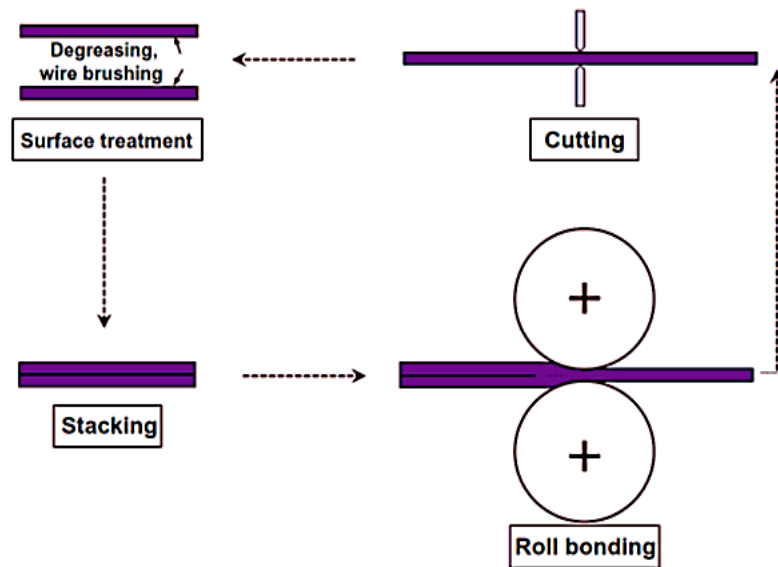


Figure 2.6: Schematic diagrams of the ARB process [4].

The materials produced by the ARB method have very high strength due to the elongated UFG structures. The strength and grain size of some UFG materials fabricated by ARB are listed in Table 2.3 [30].

The materials with low impurities usually tend to present a larger grain size. Conducting the ARB process at low temperatures produces the fine-grained structure of similar materials. On the other hand, the strength of the UFG metals is two or three times higher than the materials with conventional grain sizes. With the expense of limited losing ductility owing to the early plastic instability [48]. For example, low-temperature superplasticity of UFG 5083-Al alloy during the ARB process at 200°C was observed by Tsuji et al. [49,50]. As a result, the similar microstructure, including the lamellar boundaries of heavily deformed materials by conventional rolling, can be observed in the ARB processed materials with elongated UFG structures. [51].

It means that the UFG structures are produced not only by shear deformation like HPT or ECAP but also by another mode of plastic deformation in ARB [52]. According to the results reported by Huang et al. [53] the production of UFG structure in 99% ARB processed Al is

Table 2.3 the Grain size, microstructure, and ultimate tensile strength of some different types of materials (metals and alloys) ARB processed in Osaka University [30].

Materials [mass %]	ARB Process	Microstructure	Grain size [μm]	Tensile strength [MPa]
4N-Al	7 cycles at RT	pancake UFG	0.67	125
100-Al (99 % Al)	8 cycles at RT	pancake UFG	0.21	310
5052-Al (Al-2.4Mg)	4 cycles at RT	ultrafine lamellae	0.26	388
5083-Al (al-4.5Mg+0.57Mn)	7 cycles at 100°C	ultrafine lamellae	0.08	530
6061-Al (Al-1.1Mg-0.63Si)	8 cycles at RT	ultrafine lamellae	0.10	357
7075-Al (Al-5.6Zn-2.6Mg-1.7Cu)	5 cycles at 250°C	pancake UFG	0.30	376
OFHC-Cu	6 cycles at RT	ultrafine lamellae	0.26	520
Cu-0.27Co-0.09P	8 cycles at 200°C	ultrafine lamellae	0.15	470
Ni	5 cycles at RT	ultrafine lamellae	0.14	885
IF steel	7 cycles at 500°C	pancake UFG	0.21	870
0.041P-IF	5 cycles at 400°C	pancake UFG	0.18	820
SS400 steel (Fe-0.13C-0.37Mn)	5 cycles at RT	ultrafine lamellae	0.11	1030
Fe-36Ni	7 cycles at 500°C	ultrafine lamellae	0.087	780

much faster than that of the conventionally rolled 99% Al. It means that ARB is more beneficial for the refinement of microstructure than the conventional rolling. The redundant shear strain is the most probable reason for this difference. The roll-bonding in the ARB method has been regularly done without using a lubricant. Then a large amount of redundant shear strain is applied at the subsurface of the slabs in the rolling under the less-lubricated conditions. The calculation of redundant shear strain for the ARB of 1100-Al has been done by Lee et al. [54]. Fig. 2.7 demonstrates the flexion of the embedded pin after the first cycle [51]. Bending of the pin embedded to the slab before roll-bonding, especially surrounding the surface region, shows large redundant shear strain is imposed in relation with significant friction between the plate

and rolls. The distribution of shear strain (H) through the thickness of the specimen, determined from the flection in Fig. 2.7 is shown in Fig. 2.8.

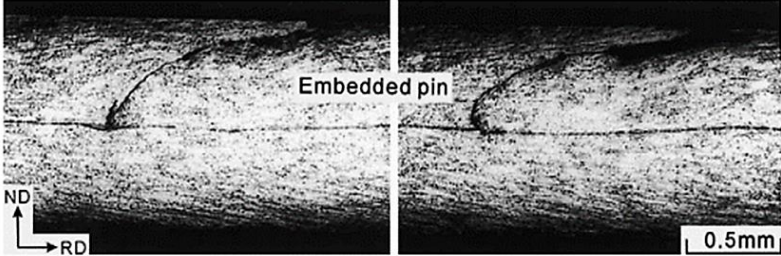


Figure 2.7: The flection of the embedded pin in the Al1100 one cycle ARB processed at room temperature without oil. Detected on a longitudinal section [51].

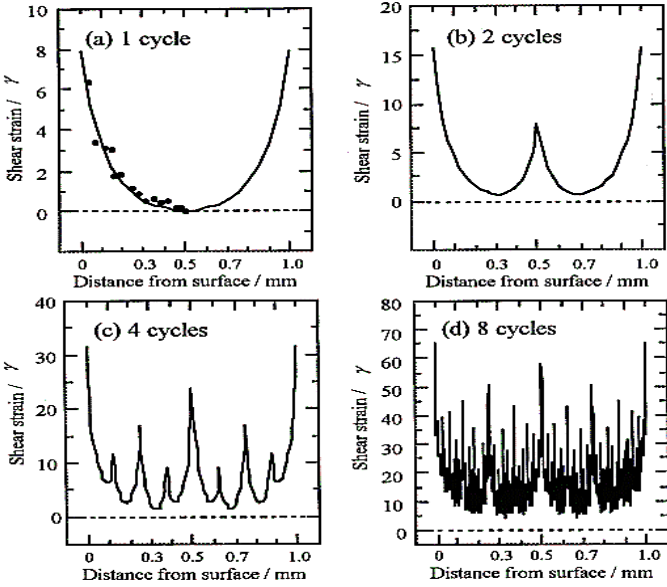


Figure 2.8: Shear strain distribution along the thickness of the Al1100 ARB processed by (a) one, (b) two, (c) four, and (d) eight cycles [51].

2.3.3 Bonding Mechanism

As mentioned previously, roll bonding is a solid-state process of bonding sheet metals together employing plastic deformation during the rolling. In metal bonding processes like cold

welding by forging, extrusion, rolling and friction welding, two basic coalescence or bonding mechanisms exist. Firstly, the brittle scratch-up layers are broken up by severe plastic deformation, then enhance the quality of contact and coalescing with the base second metal surface by high interfacial pressure. Therefore, plastic deformation and the degree of that deformation is a basic parameter of the bonding process [55].

Generally, the mechanism of roll bonding process of sheet metals is not well investigated, and the effect of process parameters is still unclear. However, several mechanisms of bonding were offered to describe the bonding of rolled metals. Nevertheless, the estimation of bonding properties with rigorous models is a scientific challenge, particularly in the case of dissimilar metal bonding. As stated before, the basic factor administering coalescence is the degree of deformation and it can be identified by surface exposure ‘Y’ or surface expansion ‘X’ of the bonding interface, which are mentioned as follows [56].

$$Y = \frac{A_1 - A_0}{A_0} \quad (2.18)$$

$$X = \frac{A_1 - A_0}{A_0} \quad (2.19)$$

where A_0 is the primary and A_1 the final cross-sectional area of the surface for the rolling process. The reduction ratio ‘R’ is expressed as surface exposure ‘Y’ and typically, bonding occurs only after the condition which the threshold deformation is reached [56]. Generally, in the process of rolling two similar sheet metals together end to end, the reduction is equal to the surface exposure ($Y = R$).

Also, Vaidyanath suggested another model based on the contaminant barriers besides the brittle scratch-up layers [56]. Then, the bond area ratio can be reformed as follows:

$$R = 1 - \left[\frac{1-R_f}{1-R_t} \right] \quad (2.20)$$

where R_t is the threshold thickness reduction for bonding and R_f is the final thickness reduction.

Based on the fact that there is a difference between the bond strength of the materials, it can be considered that the model of Vaidyanath is not comprehensive and it should be revised. Therefore, Wright proposed an empirical hardening factor H to the Vaidyanath's model and the model was extended:

$$\frac{\tau_B}{\tau_m} = H \left[1 - \left[\frac{1-R_f}{1-R_t} \right]^2 \right] \quad (2.21)$$

where τ_B is the bonding shear strength, τ_m is the metal shear strength in the composite.

Scratch brushing is the most effective part of surface preparation for cold welding due to the removing the surface contaminants which adhere and further act as an additional layer thus exposing a maximum area of virgin metal for potential bonding [57].

Bay et.al [56,58] have developed the basic mechanism of metallic bond of composites produced by cold welding that involves four main steps which are fracture of the contaminant surface or brittle cover layer, extrusion of base metal through the cracks, creation of contact with the base metal of the opposite surface, and finally coalescence with the base metal of the opposite surface. Schematic aforementioned steps are demonstrated in Fig. 2.9.

Temperature and pressure are also the factors which must be considered in the cold roll bonding of the metals. Yan and Lenard [59] investigated roll bonding of an aluminum alloy at the different condition of cold and warm. They found that increasing the temperature and interface pressure of the roll bonding process improves the shear strength of the bonds.

Additionally, they proposed that the required activation energy of the Q_B and the dependence of the bonding strength on entry temperature follows an Arrhenius type equation [59].

$$\frac{\tau_B}{\tau_m} = \exp\left(-\frac{Q_b}{RT}\right) \quad (2.22)$$

where R is the universal gas constant and T is the entry temperature in K.

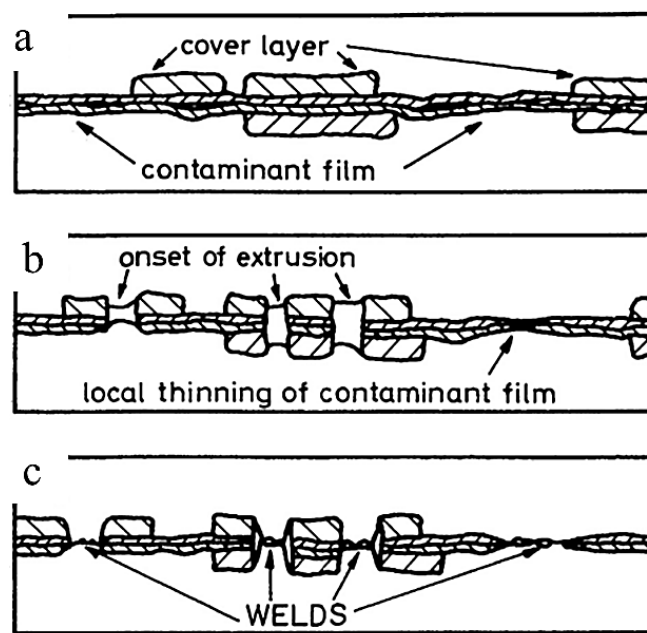


Figure 2.9: Schematic of the various steps included in bond formation: at the interface a) break-up of cover layer b) extrusion onset c) weld formation [58].

Through the experimental observations of the joining mechanism of two different metals, Haats et al. [60] reported that the combination of adhesion and diffusion theory is an accurate explication for the mechanism for cold pressure welding (bonding). According to Stachowiak and Batchelor [58], the strong adhesion between material in a high vacuum occurs due to the electron interaction between bonding surfaces. Nevertheless, the quality of bonding under normal atmosphere depends on the presence of brittle covering and passivation layers

and the percentage of the other contaminants such as water vapor and oil. Considering all parameters, the roll bonding mechanism for dissimilar metals is still not clearly defined.

2.3.4 The advantage of the ARB process

The cost of producing more reliable materials with ultrafine grains (UFG) or nanocrystalline structures requires either expensive die and /or advanced manufacturing techniques for all SPD methods. On the other hand, the ARB method is more economical in comparison with the other SPD methods and consequently preferred in industrial processes. The advantage of the ARB process is the simple requirement of equipment, the only equipment necessary is a rolling mill with high enough capacity to perform the thickness reduction needed for a sound bond. Another advantage of the ARB process, compared with the other SPD techniques such as ECAP is the potential of producing bulk workpieces with large dimensions, which is only limited by the capacity of the rolling mill [61].

2.3.5 Process Parameters

Several factors must be considered during the ARB process. The percentage of the reduction rate per cycle, working temperature, number of ARB cycles, speed and diameter of rolling machine, oxide layer thickness, and the friction between roll circumference and sheet metal are the most critical parameters that have a direct effect on the bonding process [35].

2.3.5.1. *Temperature*

The temperature of the process is one of the most critical parameters that affect the microstructure, thermal stability, and the quality of metallic strip bonding as well as mechanical properties. Typically, the optimal process temperature should be determined for each material. There is a clear correlation between thermal stability and strong bonding. However, for most of

the aluminum alloys, the temperatures above 200°C provides better bonding. The report of Slamova et al. reveals the importance of preheating between 200°C and 450°C on the thermal stability of the accumulative roll bonded of Al-Fe-Mn-Si [62,63]. Preheating and heat generated by the rolling process are two reasons for softening by dynamic recovery and/or partial re-crystallization process. Generally, high temperature or increase in the duration of preheating enhance grain growth, reduces the possibility of expected grain refinement. Furthermore, the temperature of the slabs influences the adhesion between the layers, consequently, which affects the bonding of the parent metal. In some metals, increase the temperature generating oxide layer that affects the quality of bonding between the strips. Yan et al. confirmed this Fig. 2.9 who investigated the effect of entry temperature (or process temperature) on the shear strength of the metal lamina bonding [64].

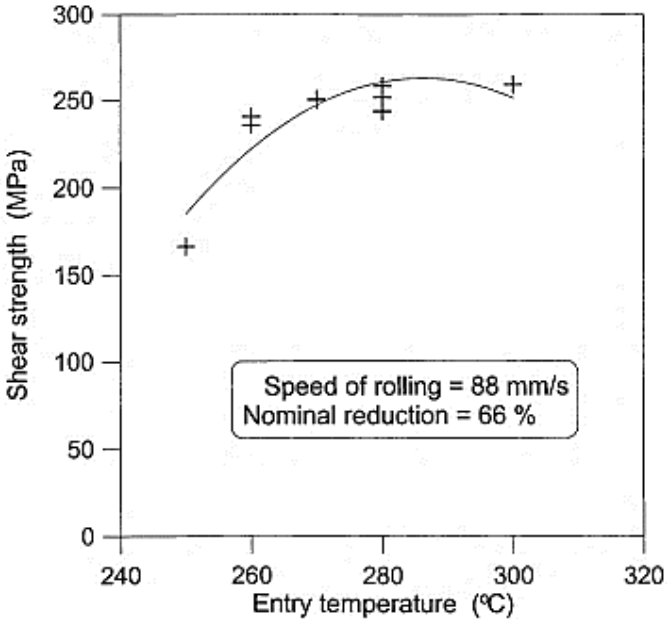


Figure 2.10: Shear strength of the interlamellar bond of the AA6111 as a function of entry temperature [64].

2.3.5.2. Reduction per rolling cycle

The major condition of the ARB process is thickness reduction of the rolled sheet to one-half of the thickness of the parent metal. This reduction rate is ideal for a good bond of many metals, including aluminum and its alloys, as well as interstitial free steel and titanium [53,65–67]. Kralliks et al. [44] reported that the bonding of the inner layers under 50% reduction in thickness leads to inequality and weak strength bonding between the slabs and that bonding above 50% results the edges cracking. Yan and Lennard [64] mentioned that the bond strength between interfacing layers increases with a higher rate of thickness reduction in aluminum alloy AA6111 (Fig. 2.10). Therefore, the critical parameter which must be considered in case of reduction rate is the acceptable quality of the bonds and the minimum crack propagation at the edges.

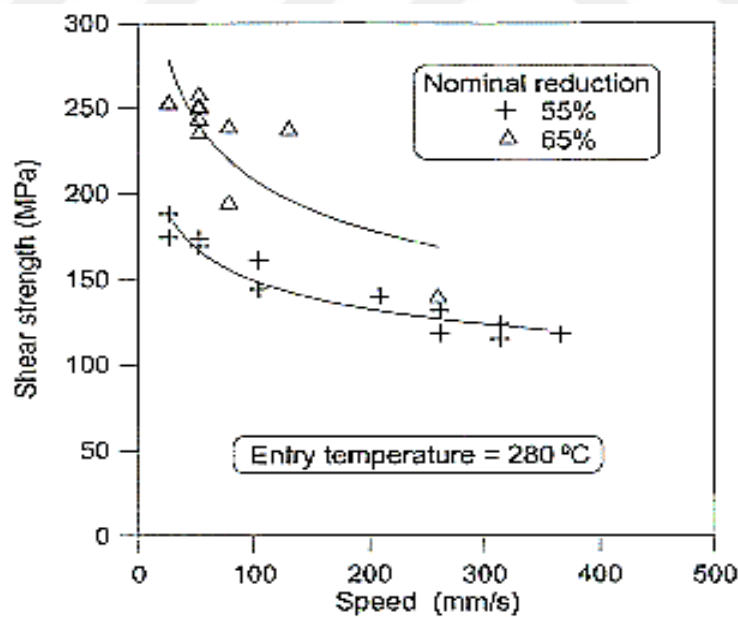


Figure 2.11: Shear strength of interlamellar bonding of the AA6111 as a function of rolling speed and percentage reduction [64].

2.3.5.3. Roll Diameter

The fine structure and hardness depend on the diameter of the roll, as well as the distribution of the equivalent strain along the thickness of the plates in the ARB process. This is because, the increase in roll diameter leads to a larger deformation area, Fig. 2.12 [68]. On the other hand, using small rolls decreases the deformation area, and therefore, the rolling pressures will be higher. Since higher rolling pressure improves the bonding between plates, the effect of that is exactly matching with the reduction rate parameter Fig. 2.13. The maximum bond strength has been obtained using the large roll diameter and lower roll speed in the experiment conducted in the AA6111 [35]. So the essential parameter in case of diameter and speed of the roll is having a slow peripheral speed.

2.3.5.4. Friction

The other important factor in ARB is the friction between the rolls and the sheet metal. The quality of the metal sheet bonding strongly depends on friction.

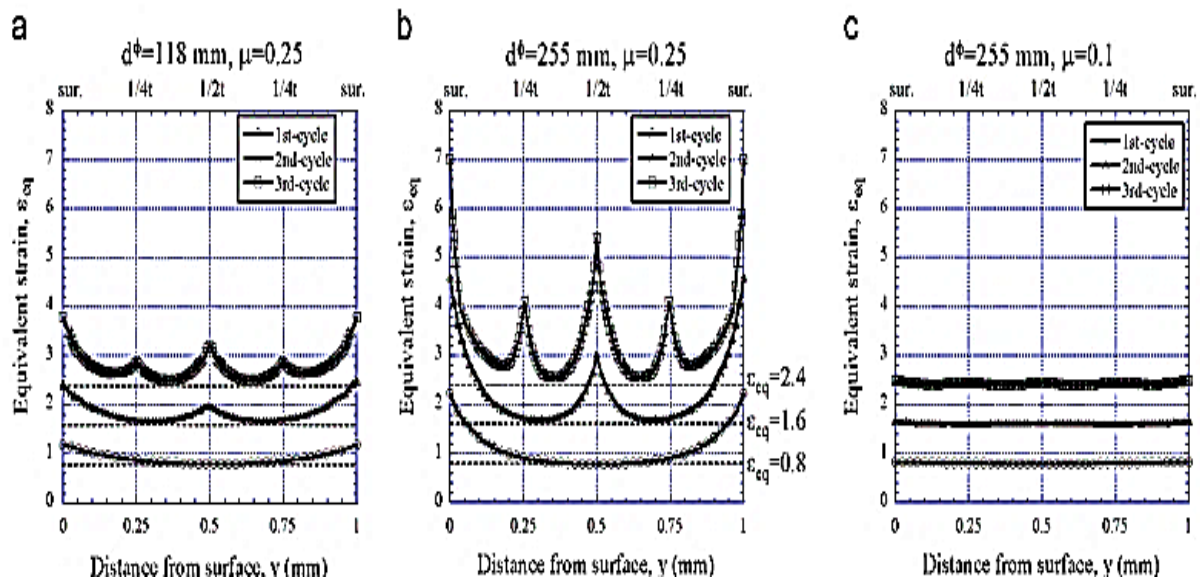


Figure 2.12: Equivalent strain distribution throughout the thickness against roll diameter $d\phi$ and friction coefficient [68].

Recently, researchers have studied the effect of friction between the rolls and the metal sheet on the equivalent strain along the thickness numerically. They found that the distribution of the equivalent strain greatly depends on the friction coefficient (μ) Fig. 2.12 [68]. On the other hand, the effect of friction in the ARB process has not been discussed experimentally in detail [32].

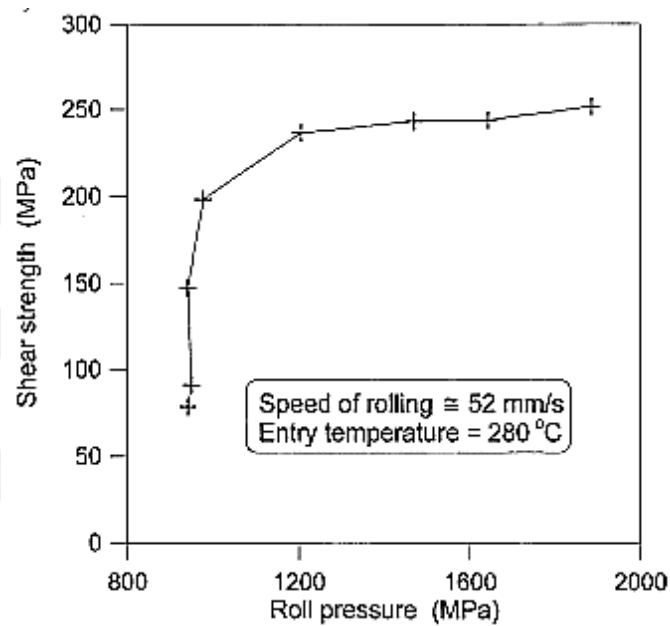


Figure 2.13: Shear strength of interlamellar bonding of the AA6111 as a function of roll pressure [64].

2.3.5.5. *The number of Rolling cycles*

Employing ARB approach, it is easy to produce ultra-fine grained materials with high yield, ultimate strength, and hardness. In the ARB process, the bonding with deformation are occurring simultaneously of the metallic sheet surfaces being rolled [69]. During the initial cycles of ARB, the work hardening is the main strengthening mechanism. Subsequently, due to the formation of UFG microstructure, the contributor of grain boundary strengthening becomes a major mechanism of strengthening. Tamimi and Amir roll bonded low Carbon steel, pure

copper and Al-1100 with 50% reduction in area at a temperature of 500°C for steel, 250°C for Al-1100 and 350°C for copper for a number cycles of ARB. They reported that both degrees of bonding and ultimate grain size, are depending on the reduction ratio and the number of rolling passes. As the number of cycles increased, the bonded layers also increased, and the delamination area reduced, suggesting that bond strength enhanced after several rolling [70].

2.4 Aluminum Alloys

In the last few decades, the application of aluminum and aluminum alloys as a structural part in the aerospace, automotive and marine industries have increased dramatically. Prompting increased demands for the development of manufacturing techniques, which can enhance the mechanical properties of Aluminum alloys [38]. Nowadays, reducing fuel consumption and consequently, CO₂ emissions is one of the most important challenges of engineering in both parts of the mechanical design and material selection in industries. Therefore, aluminum with the appropriate properties of lightweight, high strength, machinability, and formability is the best nominate of the material for structural parts and different components. However, the automotive industry is the first consumer of material in the world [71].

Aluminum alloys are generally classified into the two different series; wrought alloys and cast alloys. Cast alloys are typically expressed by four-digit number #xx.x and wrought alloys are indicated by an arrangement #xxx where # is the number meaning the principal elements added to the alloy while the other numbers express the quantity of alloying elements added. The aluminum series 2XXX and 6XXX are denoted as the wrought aluminum alloy with Cu and Mg as the main alloying element, respectively [72]. Table 2.4 depicts the classification of wrought aluminum alloys with a brief explanation of their properties and applications [73].

Table 2.4 Classification of wrought aluminum alloys [73].

Alloy Series	Principal Alloying Element	Definition and Properties
1xxx	99% minimum Aluminum	Controlled pure aluminum alloys, these series are generally used in the electrical and chemical industries.
2xxx	Copper	The 2xxx series aluminum alloys, which is the major alloying element of copper, is generally used in the aviation industry due to its high yield strength as high as 455 MPa.
3xxx	Manganese	Utilized as general-purpose alloys for building industry and other numerous products.
4xxx	Silicon	Silicon is the principal alloying element and 4xxx series are utilized as welding rods and brazing sheet. Silicon addition range from 0.6 to 6.2%.
5xxx	Magnesium	5xxx series are the aluminum/magnesium alloys, which are magnesium addition range is 0.2 to 6.2%. This series has high weldability, so they are used for different applications.
6xxx	Magnesium and Silicon	Aluminum/magnesium and silicon alloys have 1% magnesium and silicon additions. These additions produce magnesium-silicide, which ensures the ability to become solution heat treated for enhanced strength.
7xxx	Zinc	Zinc addition range is 0.8 to 12%. 7xxx series contain the highest strength aluminum alloys. These alloys are utilized in aircraft, aerospace, and sporting equipment applications.
8xxx	Other Elements	This series contains iron, lithium, or tin.

2.4.1 ARB of aluminum alloys

As it mentioned before, different methods have been developed to improve the mechanical properties of materials and due to the wide application of aluminum alloys in industries, modern techniques are applied to enhance the mechanical performance of the aluminum alloys [36,37]. Throughout the last decade, Severe plastic deformation methods,

especially ARB were one of the new techniques which has been successfully conducted on a wide range of aluminum alloys, and the results show that the mechanical properties of processed materials are considerably improved. Table 2.5 shows a brief summary of some investigation on ARB-processed Al alloys.

With applying ARB on the aluminum alloys in the various number of cycles and strain rates, the ultra-fine grained bulk sheets with the grain size of even several hundred nanometres were successfully achieved [91,92]. The UFG aluminum alloys fabricated by ARB process performed high strength at room temperature, which was up to 3.7 times larger than that of the base materials with the expense of decreasing ductility Fig. 2.14 [31].

Table 2.5 Summary of some ARB-processed Al alloys, according to them series with some references.

Alloy Designation	References and author	Year
AA1XXX	[36,48,53,74]Tuisji et.al,[54] lee et.al [75], Hiromoto et.al	1999, 2002, 2003, 2007, 2003, 2010
AA2XXX	[76] Schaarschuch et.al [77] Zheng et.al, [78] Alvand et. al	2015, 2016, 2017
AA3XXX	[79] Xing et. at,	2002
AA4XXX	No published attempts	
AA5XXX	[50,80] Tsuji et. al,	2009, 2003
AA6XXX	[81] park et. al, [64] Hongzhi et.al, [82] Lee et.al, [83] Hailiang et.al, [84] Lihong et. al, [85] Hollang et. al	2001, 2004, 2002, 2016, 2014, 2010
AA7XXX	[86] Alvandi et.al, [87] Hidalgo et.al	2015, 2014
AA8XXX	[88] Xing et. al, [89] Miroslav et. al, [90] Miroslav et. al	2002, 2009, 2014

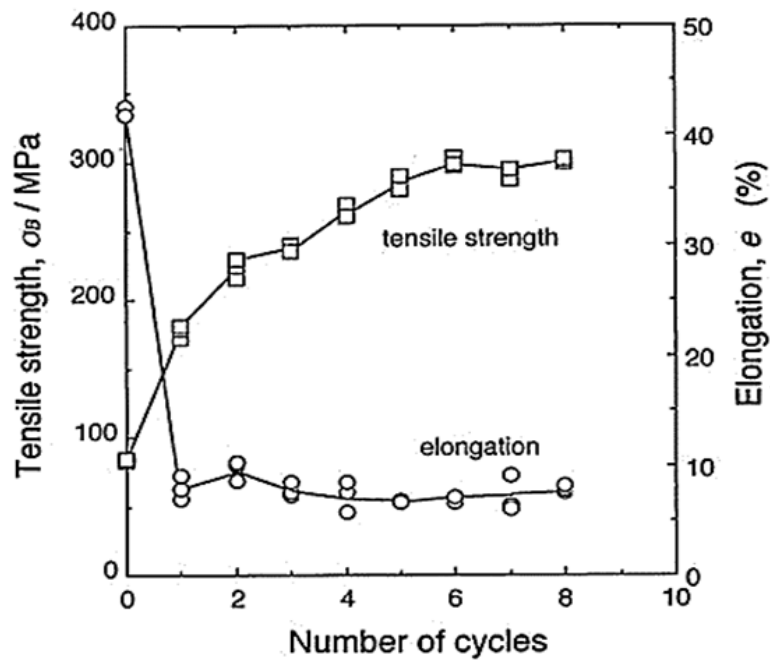


Figure 2.14: Mechanical properties of the 1100 Al alloy at room temperature after ARB applied at 473K [31].

2.4.2 ARB of Al6061

6XXX series of aluminum alloys are heat treatable alloys with a medium range of strength, and the main elements of this group are aluminum–magnesium–silicon (Al-Mg-Si). The unique properties of Al6061 alloy such as medium strength, formability, weldability, corrosion resistance, and low cost nominated it as a most commonly used metal in automotive and marine industries [82]. Still, it is necessary to enhance the formability and strength of them for further applications and ARB is one of the methods which is used for mentioning purpose.

Saito et al. [31] is the first one who introduced severe plastic deformation by using accumulative roll bonding (ARB). Recently, this technique has become remarkable in the

production of the ultra-fine grained (UFG) metals and alloys. The grain size range between 100 nm to 1000 nm can be obtained using the ARB process.

One of the most critical parameters in the formability of the metals is strain rate sensitivity at different temperatures. The materials which have good formability under high strain rates and low temperatures are the best selection of metal forming. The effect of the ARB process on the strain rate sensitivity of Al6061 was investigated by Search et al. [85] Who found that the strain rate sensitivity of Al6016 after eight cycles ARB, increases sharply at ambient temperature and moderately at very low temperatures.

Lee et al. [82] Used the accumulative roll-bonding (ARB) method to produce ultra-fine grained (UFG) alloy Al6061, and they explained that the boundaries of the ultra-fine grains started to appear at the third cycle and after eight cycles the average diameter of ultra-fine grains became 310 nm. Furthermore, they reported that the tensile strength of the processed Al6061 was about three times higher than that of the as-received material. Also, they investigated the effect of ARB process and surface brushing in ARB on the hardness of the processed material

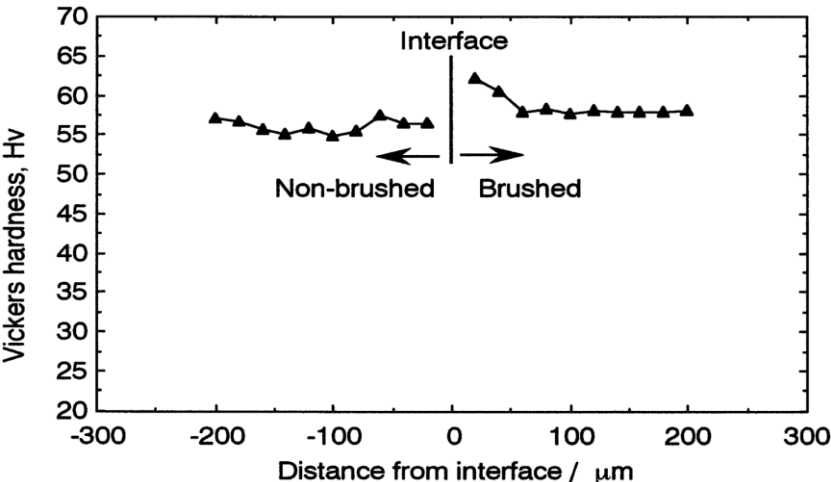


Figure 2.15: Effect of wire brushing on hardness near the bonded interface [82].

and they found that the trend of hardness distribution through the thickness is not homogeneous and there is a peak near to the surface and the center. They connected that behavior to the redundant shear strain near the surface and the wire-brushing before the roll-bonding Fig. 2.15.

Generally, the yield and ultimate tensile strength are raising while the ductility drops with increasing the number of cycles in the ARB process. Lee et al. [82] investigated the tensile behavior of the AA6061 after eight cycles ARB and results show that the tensile strength of the as-received materials increased up to three times after process and reached to a maximum value of 363MPa with the expense of decreasing ductility near to 5% Fig. 2.16.

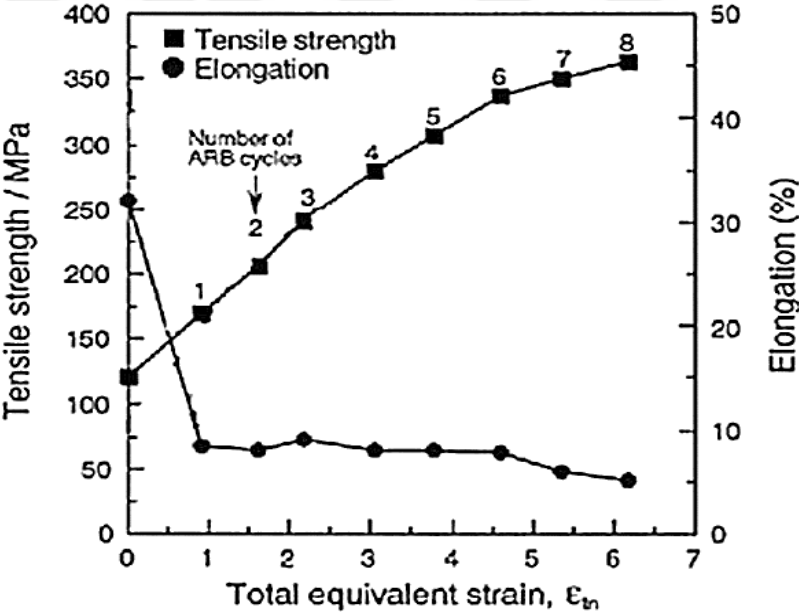


Figure 2.16: Mechanical properties of the AA6061 roll bonded at room temperature [82].

The ARB technique was employed on 6061 aluminum alloy up to 5 cycles at room temperature under dry condition with the conclusion that the tensile strength was significantly increased because of the high density of dislocations in the initial cycle of ARB due to the strain hardening, and in subsequent cycles to the grain refinement mechanism [81]. As shown

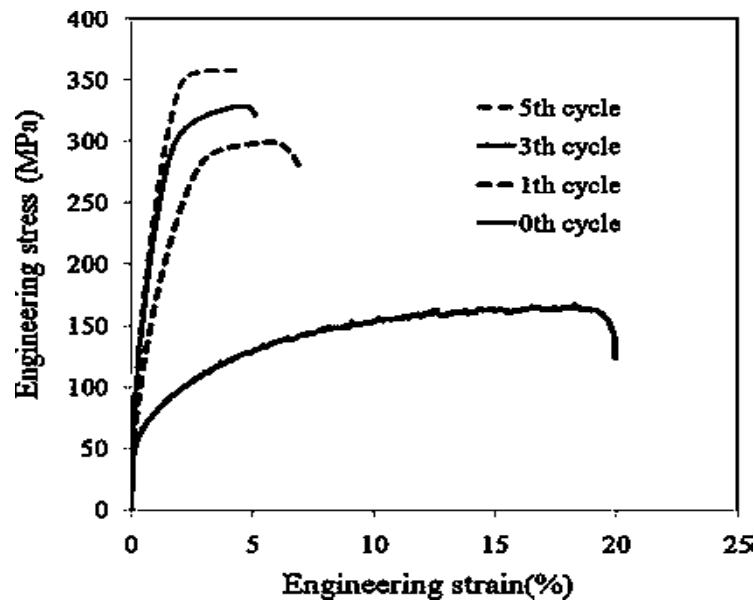


Figure 2.17: Stress-Strain graphs for Al6061 within various cycles of ARB [81].

in Fig. 2.17, significant enhancements in the strength was achieved after the first cycle and increased gradually for later cycles.

Rezaei et al. [93] utilized the ARB process following by ageing treatment and compared that with heat treatment without ARB to investigate the effect of different conditions on the strength and ductility of Al6061 alloy.

They observed that Peak-ageing conditions are achieved for the ageing duration of 5h at 433K and 48h at 373K for ARBed samples. Fig. 2.18 depicts that the strength and elongation enhanced after various ageing conditions in ARBed samples, simultaneously. Also, they reported that this behavior is due to the competition between precipitation and recovery, which lead to a drop of dislocation density through the ageing process.

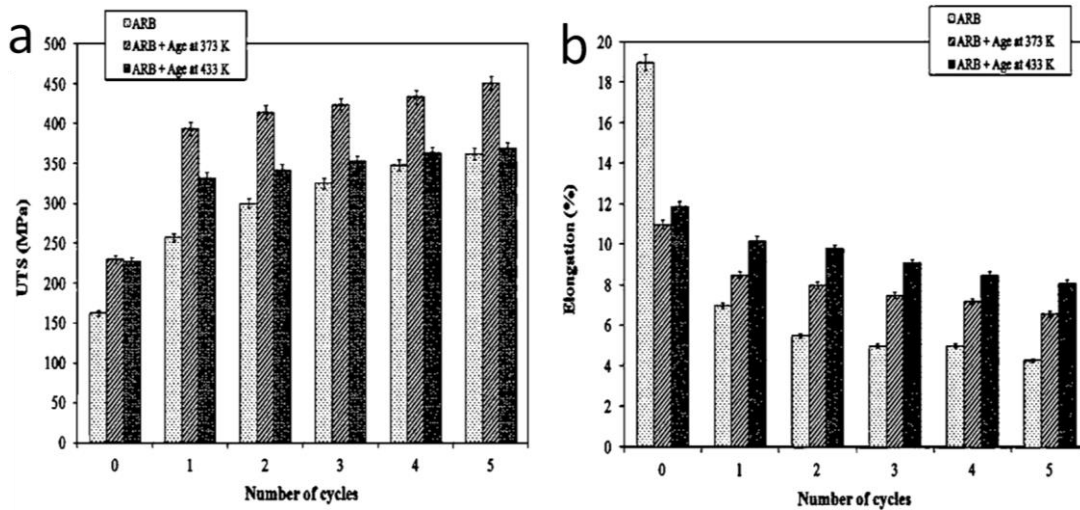


Figure 2.18: Mechanical properties (a) UTS and (b) elongation as a function of cycle number with various heat treatment procedure [93].

2.4.3 ARB of Al2024

The Al2024 alloys usually contain 2 - 10% copper as a main alloying element with the addition of a small amount of the other alloying elements such as magnesium, manganese, zirconium, silicon, etc. The percentage of the copper element in aluminum alloys increases the strength and promotes the precipitation hardening capacity of alloy. Al2024 is commercially available in sheet form and provides an appropriate mechanical property for structural parts [94]. The unique properties of Al2024 alloy such as higher strength, good machinability, fatigue resistance, surface finish capabilities, suitable workability, and highly sensitive to temperatures, nominated it as a most commonly used material for production of structural parts like gears, shafts, rivets, clock parts, truck wheels, computer parts, aircraft structures, missile parts, crew machine products, veterinary and orthopaedic equipment [95]. The main purpose of the SPD process is to produce fine grain sizes and a more significant number of dislocations, which dramatically increases the strength of materials. UFG form of Al2024 fabricated by ARB process presented high strength and low elongation [95].

Naseri et al. [94] applied a further process to enhance elongation of Al2024 alloy with a relatively high strength through ARB technology. This strategy includes the following procedures: In the first cycle, two annealed Al2024 strips were rolled at room temperature with a reduction ratio of 50% to prepare the sheet of two layers Al2024 with the thickness of 0.8mm. For the later cycles, 0.8mm thick annealed Al2024 strip was located between two rolls- bonded sheet to fabricate a sheet with 1.2mm thickness and five layers, then they repeated the last step up to four cycles with a final thickness of 2mm. As it is shown in Fig. 2.19, they found that elongation was improved and reached to about 10%, simultaneously with increasing the strength of 365MPa.

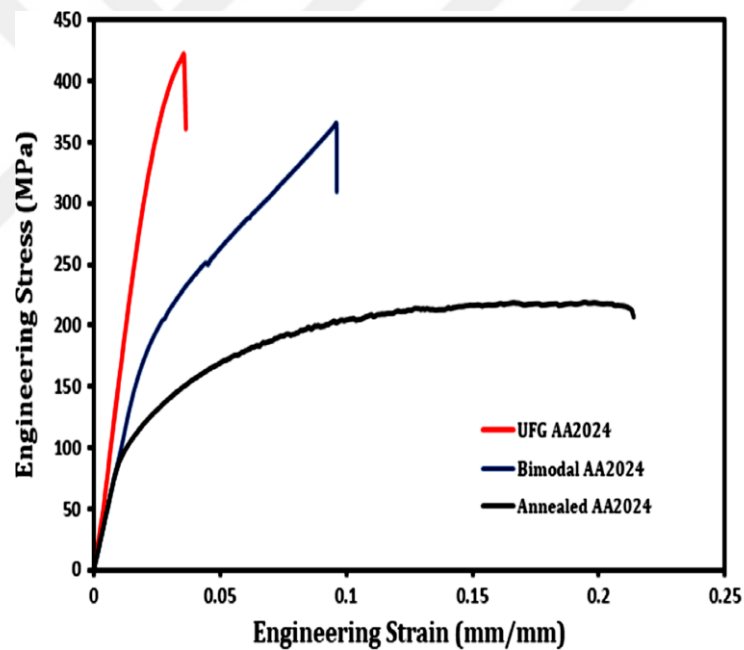


Figure 2.19: Engineering stress vs. Engineering strain curves of the different condition of Al2024 for various cycles [96].

Shahsavaria et al. [95] tried to improve the ductility of Al2024 aluminum alloy with high strength, using a Solid solution treating approach, rolling at cryogenic temperature and

aging. The optimal results of 653MPa tensile strength, 11% ductility, and 170Hv hardness were achieved after the mentioned procedure.

Bulk nanostructured Al2024 with suitable strength and ductility were successfully fabricated by Zheng et al. [77]. They reported that with the increasing number of ARB cycles and the cross-rolling process, the strength of processed material was improved gradually. The UTS of the samples after ARB followed by cross-rolling increased up to 600MPa, while the elongation at fracture dropped to 1.7%. They mentioned the limitation of strain hardening capacity after severe cold working as the main reason for the mentioned decrease of ductility. In order to enhance the ductility of samples, they conducted an aging treatment at 100°C for 20h, and results showed that the UTS and ductility of processed materials reached the 635MPa and 7% respectively. The mentioned enhancement was attributed to the precipitations which formed during the aging process. The nano-precipitations improved the strain hardening ability of material using orowan strengthening by trapping dislocations and making the dislocation loops around the precipitates.

Effect of (ARB) process on the microstructure and mechanical properties of Al2024 strip was investigated by Alvand et al. [78]. They reported that for later passes of ARB process, the mechanical properties of processed materials like hardness, yield and ultimate strength, were successfully increased and reached to the 141Hv, 345MPa, and 450MPa after 7 cycles, respectively Fig. 2.20.

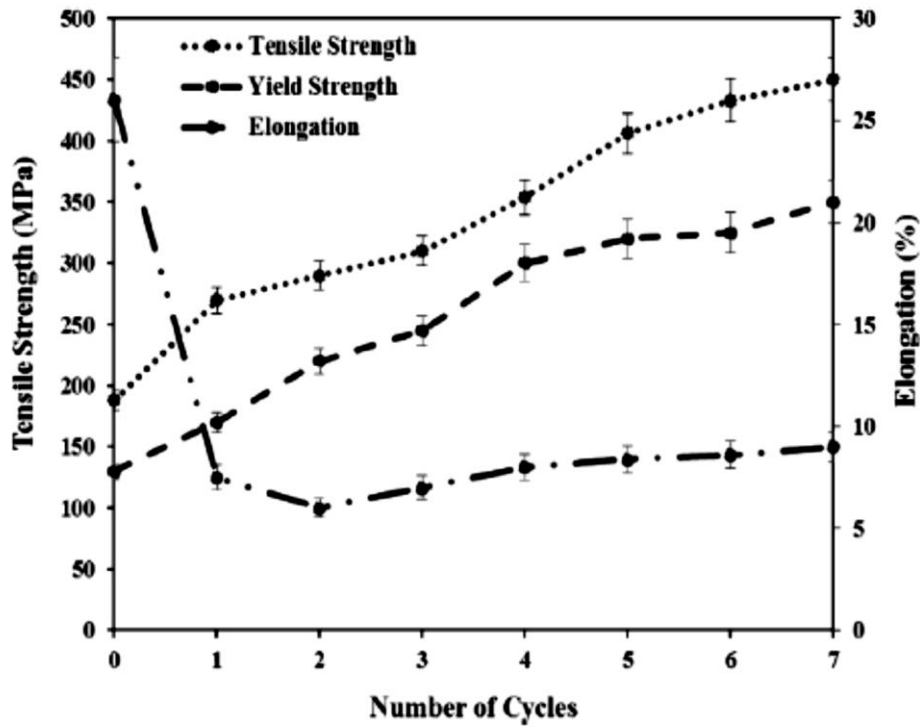


Figure 2.20: Tensile properties of Al2024 represented for a different number of ARB cycles [78].

2.5 ARB of IF steel

The interstitial free steel (IF) steel is a unique kind of steel with a low amount of alloying elements and impurities. The percentage of carbon in this alloy is less than 0.003%. During the preparation of IF steel, the nitrogen level is reduced and at the same time, the remaining amounts of carbon and nitrogen are tied by using Ti or Nb. The rolling temperature of steels is above 950°C. The major characteristic of IF is high formability (41–45% elongation) with low strength (138–165MPa yield strength) [24].

Tsuji et al. [39]. applied ARB method to produce the bulk steel strip with UFG. However, steel provides the advanced mechanical properties of structural metal parts, and therefore, UFG steels are one of the best nominations in many engineering applications. The

grain refinement of materials can improve the strength without the addition of alloying elements and the advantage of this strengthening is providing a good condition for recycling the parts. Fig. 2.21 demonstrates the improvement of tensile properties during the ARB process. It can be observed that the strength and elongation are totally similar when compared to the previously mentioned aluminum alloys.

The ARB technique created by Saito et al. is an elegant rolling process that aims to provide a large plastic deformation and bond multiple layers [31]. They used aluminum (1100), Al-Mg alloy (5083) and Ti-added interstitial free steel. They concluded that after several ARB processes, the materials show high strength with sub-micron grain structures. Finally, the grain size of IF steel was 420nm.

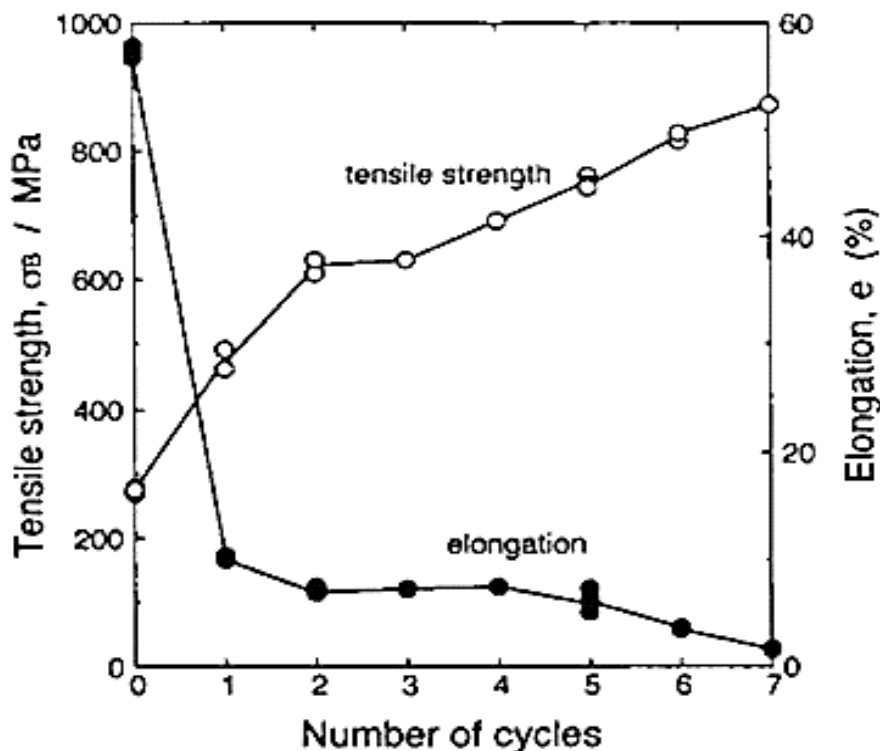


Figure 2.21: Tensile properties of the IF steel tested at ambient temperature after various cycles of ARB [39].

Tamimi et al. [95] used the ARB process up to ten cycles at 500°C to produce multi-layered UFG materials. They employed IF steel sheets and verified that with increasing ARB cycles, the microhardness and strength of processed materials are improving. The processed layered metal after eight cycles reached to the highest hardness of 247Hv, around 250% higher than the annealed condition (before rolling). Furthermore, the yield and ultimate tensile strength were enhanced three times higher than that of the initial condition. Fig. 2.22 displays the variation of microhardness, strength, yield and elongation as a function of cycle number of IF steel. As it is shown in Fig. 2.22, the elongation significantly reduced after the first pass of ARB, and then the reduction rate is minimal for the later passes.

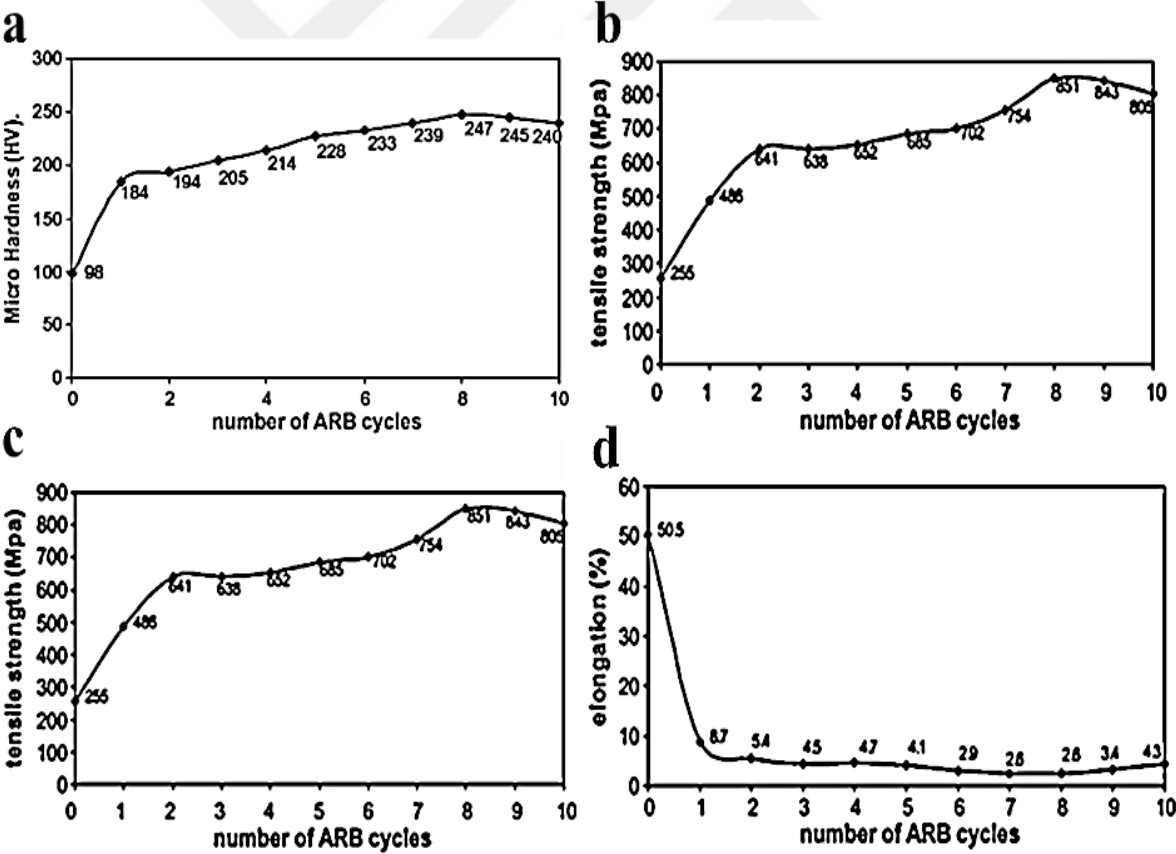


Figure 2.22: a) The microhardness, b) tensile strength, c) yields stress point, and d) elongation of IF steel as a function of various cycles of ARB process [95].

Also, by continuing the process (after the eighth cycle) the hardness, UTS, and yield stress decreased while ductility increased a little due to the saturation, static, and dynamic recrystallizations.

Tsuji et al. [97] applied the ARB process for interstitial free steel to study the elongation of ultrafine grains by electron back-scattered diffraction (EBSD). They reported that for the strain of 4% at 773K the ultrafine grains for IF steel are grains surrounded by high-angle grain boundaries rather than sub-grains. Also, they found that the UFG in the processed samples has the structure of both recrystallized grains and deformed microstructure.

2.6 ARB of Dissimilar Material combinations

The bulk multi-layer composites are fabricated by covering methods like ion coating and thin films created by evaporation of different materials [98]. The main downside hindering the universal use of LMCs has been the high fabricating price up to now. Recently, multi-layered composite materials have been manufactured and expanded by deformation procedures such as the "repeating cycle of rolling [99]. The ARB process has been attracted tangible benefits for the manufacturing of the LMCs due to low cost and the excellent result of mechanical properties as well as mass production capacity [100,101]. ARB is used to produce similar and dissimilar compounds and it is widely used in industry such as aircraft, marine, and defense applications [37].

Nowadays, composites instead of pure materials and alloys, are widely used in many industrial applications due to their advantages like high strength to weight ratio, good balance of quality and cost, and multi-functionality. Also, the other purpose of using composites can be listed as thermo-mechanical control, electrical, corrosion-resistant, and joining applications [102]. For instance, as it is shown in Fig. 2.23, a combination of steel and aluminum is used as

bumpers in the car to provide an appropriate requirement of strength and corrosion resistance [103]. To maximize the advantages and prevent disadvantages of elements inside the layered composites, various experiments have been applied in both academia and industry.

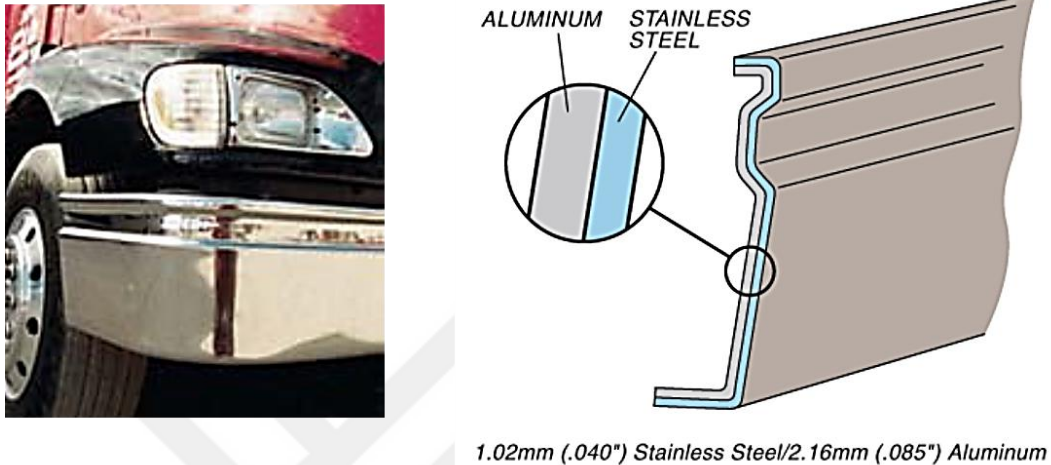


Figure 2.23: Truck bumpers made of cladding metals [103].

The usage of light metals like aluminum and magnesium instead of steel in the automotive industry is sharply increased in the last two decades. The multi-layered materials fabricated by the ARB process are relatively different from materials manufactured by other SPD techniques. For example, equal channel angular pressing (ECAP) or high-pressure torsion (HPT), the materials after ARB is more like a layered composite. Additionally, the use of dissimilar metals presents the opportunity to implement new characteristics, different from the properties of base metals.

The most common approach of making composites of the sheet metals is rolling, which is preferred for the purpose of bonding dissimilar metals with a large area. The accumulative roll bonding of dissimilar metals provides several advantages such as large-area welding on the plate plane achieved cost-effectively, and high production rate, fabrication of multi-layer

structures [55]. With considering the aforementioned advantages, the ARB process has been active research areas in the community of advanced materials manufacturing and processing.

Most of the research so far has tended to focus on similar alloys rather than dissimilar materials [86]. ARB process for similar alloys causes an ultra-fine grained (UFG) microstructure by forming two types of grain boundaries: lamellar boundaries (LB) along the rolling direction (RD) and interconnecting boundaries (ICB), linking one LB to another and finally leads to grain refinement and balanced grain structure Fig. 2.24 [33,53,104].

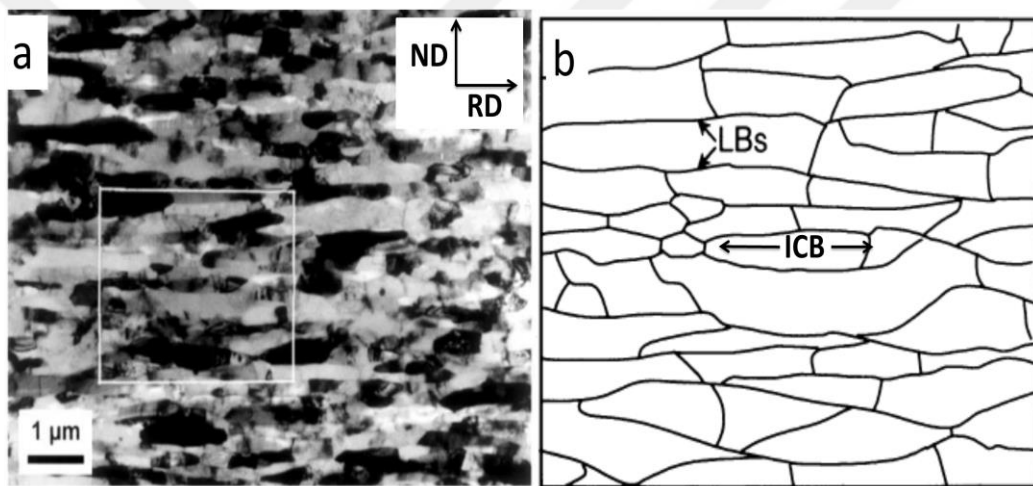


Figure 2.24: a) TEM micrograph of commercial purity aluminum after four cycles showing lamellar structure. b) Schematic illustrating the lamellar boundaries (LBs) and interconnecting boundaries (ICBs), in the rolling RD and normal directions ND, respectively [49].

Often, during the severe plastic deformation by ARB of non-identical metal systems, plastic instability occurs in one layer earlier due to the differences in mechanical properties and as the strain increases, the harder layer faces an early necking and fragmentation [100,105].

In general, the multi-layer metal compounds processed by ARB have two kinds of microscopic morphological structure. The necks of the hard layer are broken into several parts because of the difference in the mechanical properties of the material. After several stages of

the ARB, the hard phase is uniformly distributed in the soft layers to produce matrix as a reinforcement phase [106,107]. On the other hand, the continuity of the layers is conserved for several ARB cycles, although the interface is irregular and thickness reductions occur between the layers [76,108]. However, after the ARB process, the compound can be metal laminate sheets or a metal-based composite, based on the hard layer situation [109].

Numerous studies have been conducted using similar and dissimilar materials [43,47,116,117,76,92,110–115]. To highlight a few on dissimilar aluminum alloys, Su et al. fabricated a combination of Al5005 and Al6061 alloys by ARB, with the conclusion that the tensile strength can be improved to more than twice the base material after four passes [38].

As expressed by Hausöl et al. [118] dissimilar aluminum alloys have diverse properties and composition of various series of aluminum alloys by ARB could lead to a material with the combination of special properties of the base materials. UFG Al6014/Al5754 composite with changing the layers was produced and they reported that UTS of processed materials was about 100MPa higher than the initial Al6014. They found that the optimum condition with high strength and good ductility can be achieved after 4 passes ARB. The same group investigated the Al1050/AA5754 and Al6014/AA5754 composite as well; they manufactured sandwiches from AA1050 and AA6014 as external materials (clad) and AA5074 as intermediate (core) materials so that the bonding interfaces of each cycle are the same type of composite alloys. The researchers concluded that the well-bonded sandwich layer shows a combination of the positive properties of individual metal such as the high surface quality of the covered materials with high strength of the central materials [119].

Layered composite materials of Al5005 and Al6061 was made by Su et al. [38]. Two dissimilar alloys were fabricated by ARB up to 4 cycles with 200°C for 10 min preheating. They reported that the hardness and strength enhanced by increasing the number of ARB passes

to more than two times the initial values, whereas the ductility of composites was decreased significantly after the first pass, and with further ARB cycle the ductility stays approximately unchanged. In addition, they observed that the hardness of the Al5005 layer was relatively less than that of the Al6061 layer Fig. 2.25.

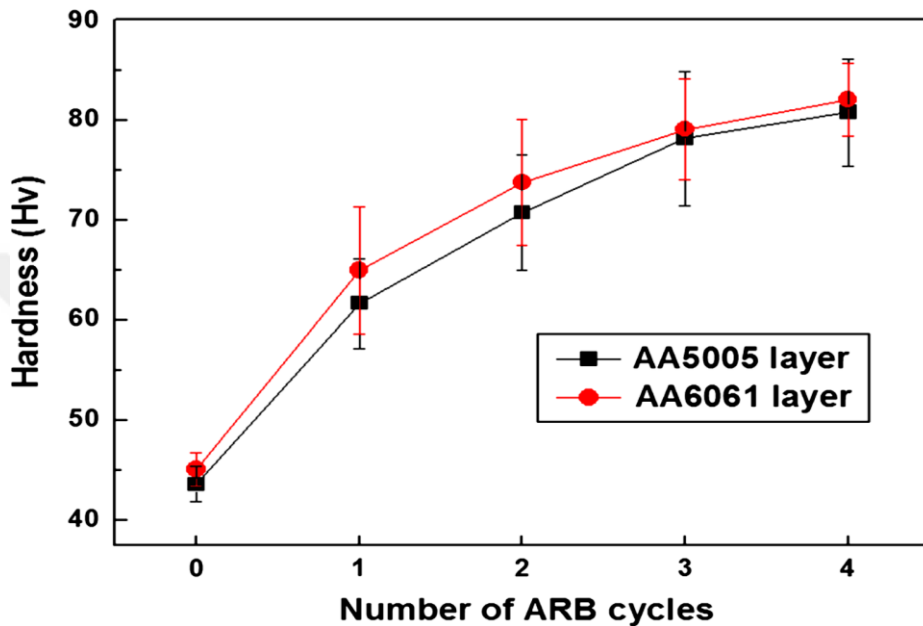


Figure 2.25: Variations of the hardness of Al5005 and Al6061 with a number of ARB cycles [38].

Slámová et al. used the ARB method to produce lamellar composites by cladding AlMg3 layers with high purity Al99.99, have achieved reduced cracking in the layered composite as compared to single material type AlMg3 with less intensive grain refinement [120]. ARB was also used to create strong bonding between the neighbouring layers of Al2219 and Al5086 accompanied by grain refinement [113,121]. ARB of two alloys, Al2219 and Al5086 was carried out up to 8 cycles. Throughout the ARB process, inhomogeneity of deformation for different layers with different mechanical properties results in interfacial instability, necking of the AA5086 layers, and fracture of necked regions after the 4th, 6th, and 7th pass respectively.

Al1005/Al7075 layered composite was prepared by the same process, finding that with an increased number of layers, the strength (yield strength and UTS) and ductility of Layered Metal Composites (LMCs) can be improved [114].

Al1050/Al5005 LMCs were processed with the ARB method up to 16 cycles. Investigator revealing that, with increasing number (N) of ARB cycle the layer thickness reduced and the best result of composite achieved with N10 which was provided 270MPa of UTS and 8% ductility [116].

Materialy et al. [19] used the ARB method to produce Al6063/Al2014 composites and they reported that the plastic deformation in the singular layers of the composite is identical with that in the single-phase alloys. Su et al. [21] used the ARB method to produce ultrafine-grained composite Al1050/Al6061 sheets, and they reported that severe shear bands combined during the cross-section of the 5-cycle ARB processed.

Hailiang et al. [122] utilized the ARB process followed by Asymmetric Rolling (AR) techniques to produced layered ultra-thin nanostructured bimetallic foils of Al1050/Al6061 composites. The two dissimilar alloys were rolled using ARB at 200°C, with a 50% reduction then the resulting bimetallic sheet was thinned to 0.04mm by four AR passes at room temperature. They concluded that the tensile strength of the bimetallic foil was increased with a reduction in thickness. On the other hand, the ductility of foil has dropped dramatically. Fig. 2.26 showed that the UTS strength of the metals after the ARB process is 200MPa, then after the first AR pass, it increased to 250MPa. With further AR cycles, the UTS strength of sheets growths gradually, near to 266MPa.

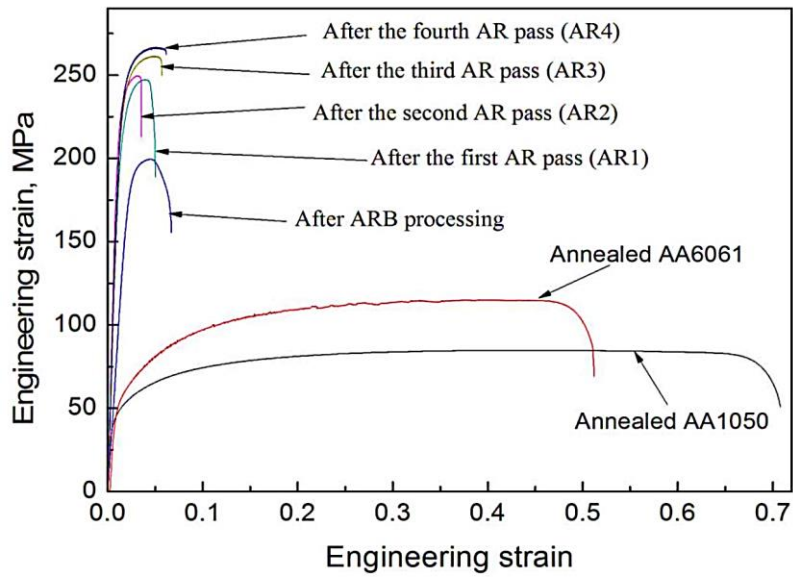


Figure 2.26: Stress vs. Strain curves for composites of Al6061/Al1050 after the ARB process, and following by AR process [122].

However, when two metals with contrast in flow properties subject co-deformation, plastic instabilities are happening, and the hard stage normally cracks and necks leaving behind a scattering of the hard phase in the matrix. This kind of composite might be appropriate for specific applications where layer continuity is not imperative like mechanical alloying, but rather different applications that require exact load redistribution between the constituent layers request layer continuity. Further, necking in the hard layer can act as a major band during the cross-section of the cycle ARB processed, the combined challenge of refining down to the nano-scale and the enhanced fatigue strength and stiffness of a multilayer roll bonded material can abuse just when the layers are continuous.

The aluminum density (2700kg/m^3) is less than that of the IF steel (7800kg/m^3), which means that the aluminum parts have the weight advantage. On the other hand, the main characteristic of IF steel compared with aluminum is high Young's modulus (IF steel = 205MPa , aluminum = 70MPa). So to compensate for this, the thickness of aluminum should be

more than the steel for the same structure. In addition, the cost of aluminum production is six times higher than that of steel. Therefore, the use of aluminum in transport vehicles to date is limited. Moreover, the use of aluminum in industrial applications requires special procedures like welding spot or welding process. Thus, the utilization of the ARB process reduces many of these difficulties as well as minimize costs.

The intermetallic compound formation, joint configuration results, and thermal brittleness can be eliminated using the ARB process. During the ARB process, two different crystalline structures can be deformed together, but with some difficulties compared to the same crystal structure [123].

From the few studies focusing on the ARB processing of IF steel with aluminum alloys, the work of Soltan and Haerian [124] attracts attention. Initial materials (aluminum Al1350 & IF steel) rolled with different pre-heat temperatures (200°C, 250°C, 300°C, and 400°C). They found that the bond strength of composites, at constant thickness reduction, increases with increasing the pre-heat temperature, which clarifies that as the preheat temperature increases, more atoms obtain the activation energy for bonding. In addition, they have shown that increasing the total thickness reduction during the ARB process promotes the strength of the Al / Steel composites bond.

Semiatin et al. [125] studied the formability of three-layers sandwich sheets of aluminum- stainless steel- aluminum and stainless steel- aluminum- stainless steel depends on defusing and the localized necking. They concluded that the arrangement of layers influences the final localization leading to fracture [125]. A combination of Al1100 and St-12 was fabricated by ARB process up to three cycles, and the results demonstrated that the tensile strength was significantly reduced, Fig. 2.27 and also, the steel layers, which are the hard part

of the composite, were necked and broken after the second cycle due to the significant difference in mechanical properties [44].

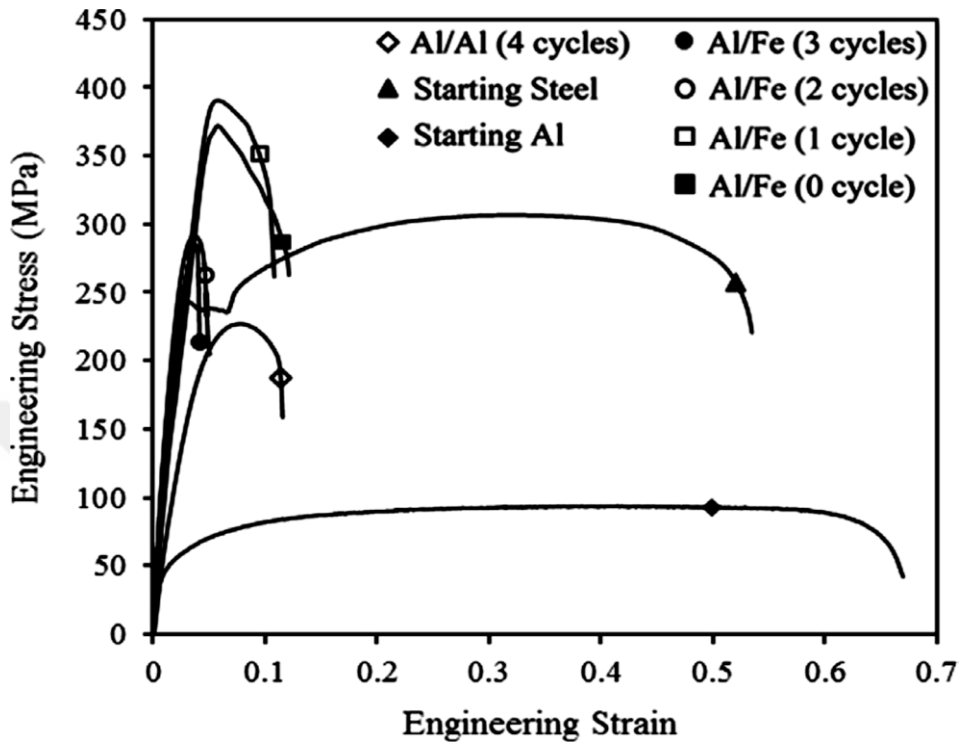


Figure 2.27: Stress vs. strain curves of the layered composite Al/Al after 4 cycles of ARBed and the Al/ steel composites after ARB [44].

2.7 Evaluation of the mechanical behavior using the SPT

The ability to form sheet metals created by ARB is very important for the successful use of these new products in the manufacturing process. The metal formability can be estimated by multiplying total elongation by the ultimate strength, which is known as formability index [126]:

$$\text{Formability Index (MPa\%)} = US \text{ (MPa)} \times El \text{ (\%)} \quad (2.23)$$

where the US is the ultimate strength (MPa), EI is an elongation percentage (%)

Also, shear punch test (SPT) is the typical tests used to estimate the sheet's formability [127,128]. SPT is important in order to characterize the sheet forming capability compared to other technological processes such as drawing, stretching, hydroforming, etc [129,130]. Furthermore, it can be used for evaluating the small test samples [131].

SPT is one of the most successful methods for evaluating mechanical properties such as the shear elongation percentage ($\%\epsilon_u$) shear yield strength (SYS), ultimate shear strength (USS) [132].

In this test, a flat cylindrical punch is pushed through the sample to be tested, which is installed between two dies. As a result, the punched area is deformed, and a circular disk is punched out from the sample. During punching, the load applied to the punch is recorded as a function of the punch displacement resulting in shear stress vs. displacement. This curve is named as load-displacement curve (LDC). Fig. 2.28 shows the setup used along with a schematic of the shear-punch test geometry. Maximum required force for constant displacement rate of punch in the shear, punch test has been recognized as an ultimate shear force that has been calculated by the following equation [133,134]:

$$\tau = p/2\pi rh \quad (2.24)$$

where p is force (N), r is the average radius (mm) of punch and die, h is sheet thickness (mm), τ is shear tension (MPa), which it can be estimated yield shear stress (YSS) (MPa), or ultimate shear strength (USS) (MPa).

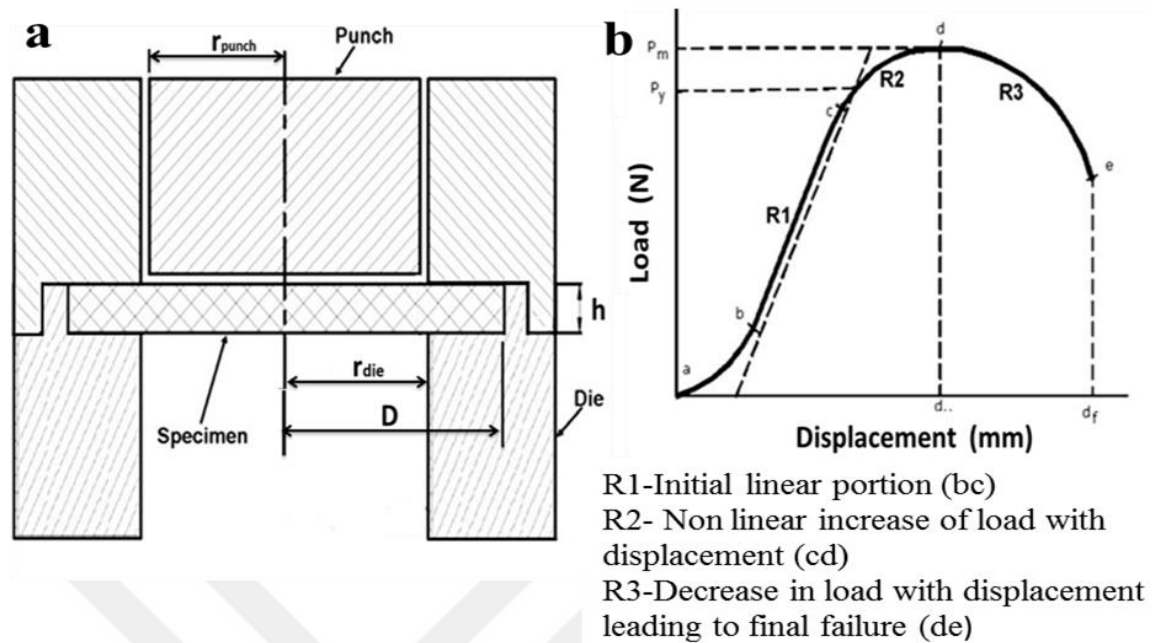


Figure 2.28: a) Schematic drawing of the Shear Punch Test, b) the typical LDC curve [131,132].

The linear relationship between the results of SPT (max shear strength (τ_{max})) and max strength values (UTS) obtained from the tensile test has been found to fulfill the linear correlation. Different values are used for A and B depending on the alloy classes [135–137].

$$UTS = A \tau_{max} + B \quad (2.25)$$

SPT methods can be more useful for characterizing and testing nuclear irradiated materials [137], biomaterials [131], heat-affected zone of weld process [133,138] and composites [128,134,139].

Bahrami et al. [134] used the aforementioned technique for determination of the shear strength of CP-Ti fabricated by the ARB process. They proved that the shear strength of samples improved with increasing the number of ARB passes and after four cycles the strength

decreased with afterward cycles due to specimen fracture and grain recovery they also showed, reduction of elongation after the first ARB cycle [134].

Lead sheets are another material, fabricated by ARB process for the purpose of applying as anodes in electrowinning metal production. Karbasi et al. [140] applied the SPT to determine the shear strength of the lead sheet product. The results of mechanical testing revealed that YS, UTS, and shear strength were enhanced 103%, 38%, and 35%, respectively, after ten passes of ARB process with the expense of 68% reduction in ductility.

2.8 Cyclic Behavior and Fatigue properties of ARB processed materials

Fatigue is a form of failure that occurs in the structures subjected to dynamic and fluctuating stresses (e.g., bridges, aircraft, and machine components). Under these circumstances, it is possible for failure to occur at a stress level considerably lower than the tensile or yield strength for a static load. The term “fatigue” is used because this type of failure normally occurs after a lengthy period of repeated stress or strain cycling [141]. Fatigue is important because it is the single largest reason of failure in the metals, estimated to comprise approximately 90% of all metallic failures; polymers and ceramics (except for the glasses) are also susceptible to this type of failure.

Furthermore, it is catastrophic and insidious, occurring very suddenly and without warning. Fatigue failure is brittle like in nature, even in normally ductile metals, in that there is very little, if any, gross plastic deformation associated with failure [142]. The process occurs by the initiation and propagation of cracks, and ordinarily, the fracture surface is perpendicular to the direction of applied tensile stress. The ASTM defines fatigue as the process of progressive localized permanent structural change occurring in a material subjected to conditions which

produce fluctuating stresses and strains at some point or points, and which may culminate in cracks or complete fracture after a sufficient number of fluctuations.

The fatigue process involves two basic fields of cyclic stress or strain. As it is known, in each case, the fatigue failure happens with different mechanisms [143].

1. Low-cycle fatigue (LCF) where critical plastic straining happens (Fig. 2.29). Low-cycle exhaustion includes great cycles with high amounts of plastic deformation and short life. The analytical system used to treat strain-controlled fatigue is usually alluded to as the Strain-Life, Crack-Initiation, or Critical Location approach [142–144].

2. High-cycle fatigue (HCF) where stresses and strains are generally limited to the elastic area (Fig. 2.30). High-cycle fatigue relates to the least load and long life. The Stress-Life (S-N) is typically utilized for high-cycle fatigue applications. Here, the stress applied to the sample is inside the limit below the yield strength of the material, and the quantity of cycles to failure is relatively high. While low-cycle fatigue is ordinarily correlating with fatigue life between 10 to 100,000 cycles, high-cycle fatigue is concerned with life more than 100,000 cycles.

Fatigue investigation can be one of the three approaches of local strain or strain life, ordinarily alluded to as the crack initiation method, which is concerned just with crack initiation (EN, or σ nominal) stress life, generally refers to total life (S-N, or nominal stress); and crack growth or damage possibility examination, which is concerned with the quantity of cycles until rupture [144]. The technique for calculating fatigue life is called Five Box Trick, it involves the parameters of the material, loading, geometry inputs, analysis and results [142,143].

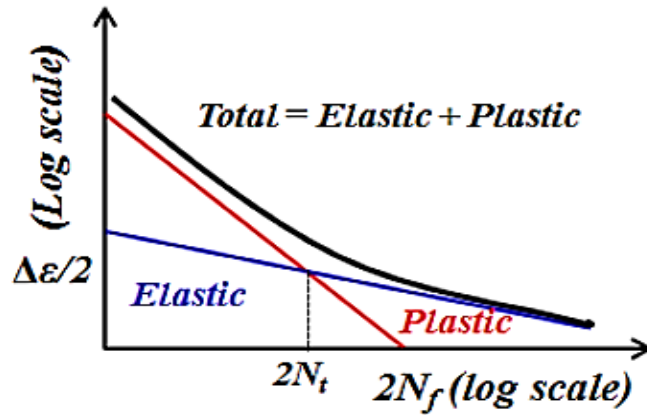


Figure 2.29: Low cycle fatigue curve [143].

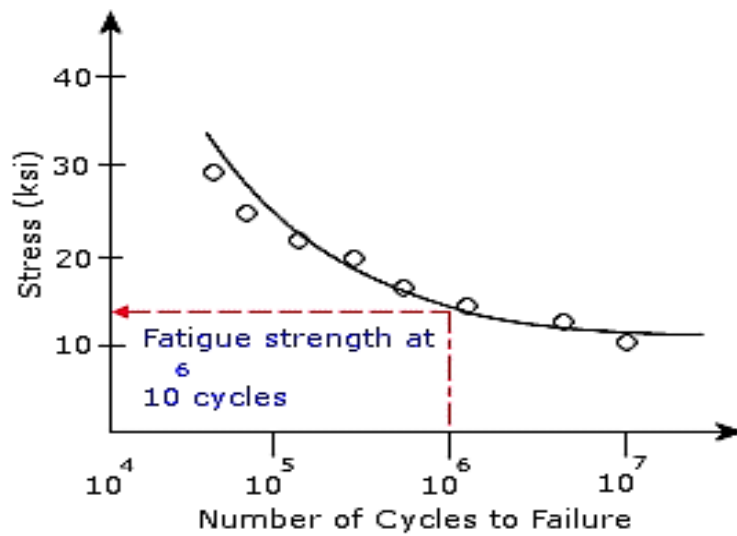


Figure 2.30: High-cycle fatigue (HCF) [144].

2.8.1 Fatigue of ARB Processed Materials

Grain size is a major structural factor affecting the mechanical response of metals and alloys. This certainly applies to fatigue behavior and fatigue life of the material for potential engineering applications of UFG materials, their fatigue properties under cyclic loading should be considered along with the strength and ductility. The application of ultra-fine-grained nanocrystalline metals in the present industry is associated with increasing understanding of

their damage resistance and the mechanical mechanisms required in the deformation, particularly under cyclic loading [145].

The production of nanostructures increases endurance and fatigue strength, but the experience of fatigue behavior of nanostructured metals is relatively weak and needs more research [146,147]. Höppel et al. [148] have studied the fatigue behavior in strain-controlled tests of an Al6061 alloy created by equal channel angular pressing (ECAP), and they reported that the UFG materials exhibited shorter fatigue lives in the low-cycle fatigue (LCF) regime.

Layered Cu/Cu and Cu/Al were produced by Zhang et al. [149] with different interfaces by a cold roll bonding technique, and they reported that compared with the cold-rolled Cu, the Cu/Cu composite with mechanical contrast appeared upgraded fatigue strength in high cycle fatigue regimes. Kitahara et al. [75] used the accumulative roll bonding (ARB) technique to produce ultrafine-grained (UFG) commercial pure Al (99.11% purity), and they reported that reducing the crack closure phenomena, would decrease the ΔK of Al after the 6-cycle of the ARB. Refinement ultrafine grain decreases the critical load for onset to propagate the fatigue crack and the fatigue crack growth rate.

Layered Al/Al₂O₃ composites were produced by Reihanian et al. [150] with two different particle sizes of 1 μ m and 0.3 μ m by accumulative roll bonding (ARB) technique and they reported that the fracture surface of the composites with 1 μ m and 0.3 μ m particle sizes shown ductile type fracture model manifested by relatively deep dimples. It was shown that the dimples in the composite with a particle size of 1 μ m were larger and deeper. Also, both composites show a much higher tensile strength compared with that of the annealed Al.

Layered Al/Mg composites were produced by Chun et.al. [151] used Al-1100 and Mg-AZ31 at 573K by accumulative roll bonding (ARB) technique and they reported that the tensile

strength of the first cycle ARB specimen was reduced by the cleavage and propagation of the crack deep into the Mg layer. In the four cycles ARBed specimen, defects induced a crack in the intermetallic layer, which led to a significant decrease in tensile strength.

Recently, the fatigue properties and crack growth path of LMCs has been investigated by several researchers. Studies on the fatigue crack growth path in LMCs were investigated by Sugimura et al. [152] and Pippan et al. [153]. They reported that the layered structures for the UFG metals enhanced fatigue properties. Furthermore, they described that if the stress amplitudes are higher than the yield stress of the outer softer layer, the fatigue cracks grow on the path from the lower strength to the higher strength layers, the crack propagation rate drops in the region of the connection simultaneously with crack branching (Fig. 2.31) [152,153].

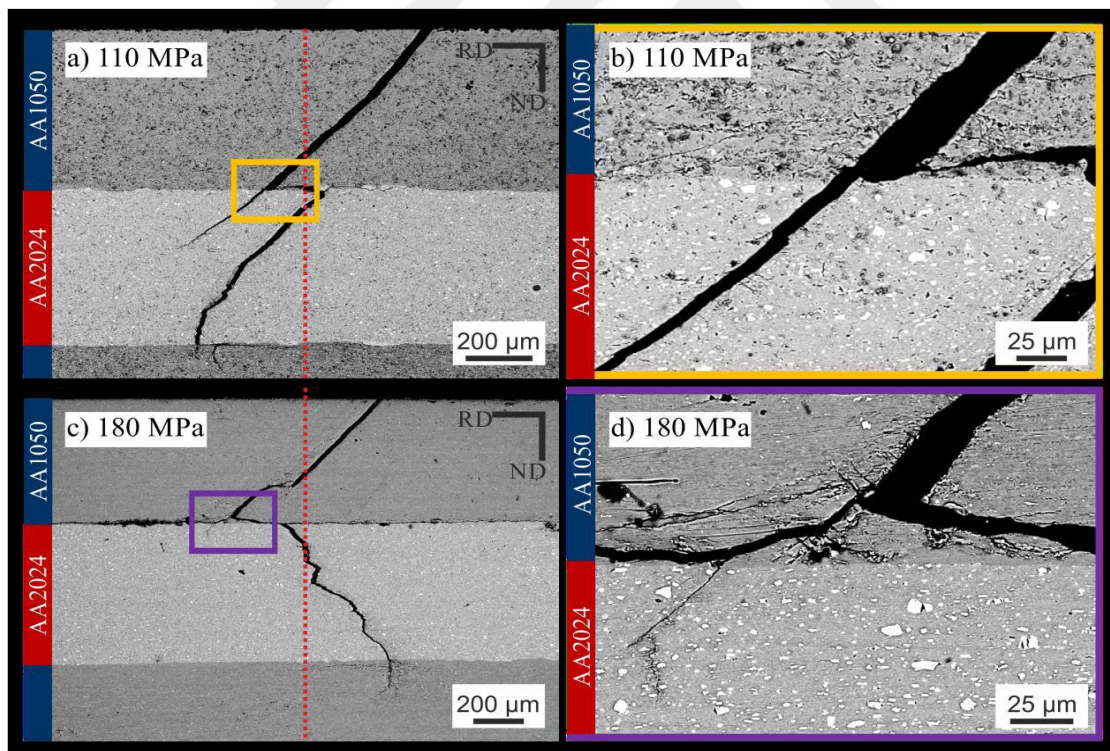


Figure 2.31: Illustration of fatigue crack growth paths of the Al1050/Al2024 N2 composite failed after fatigue test at stress amplitudes a) and b) lower than threshold stress ($\Delta\sigma/2 = 110\text{MPa}$) and c) and d) higher than threshold stress ($\Delta\sigma/2 = 180\text{MPa}$) [153].

The effect of changing the position of the steel layer from the surface was studied by Kümmel et al. [3]. in Al5754/DC05 steel composites (Fig. 2.32). They reported that the monotonic mechanical properties of the LMCs are significantly higher in the compounds with steel as outer surface layers when compared to the aluminum single material type reference specimens [3]. Moreover, they explain that the increase in fatigue life of the Al/steel composite is related to two different reasons: Due to the higher stiffness of the steel layers, a stress concentration into the inner steel layers takes place reducing the stress in the outer Al layers. Therefore, macro-crack initiation is strongly suppressed in these Al/steel composites enhancing the high cycle fatigue life. Furthermore, a pronounced crack deviation at the Al-steel interface occurs at higher stress amplitudes leading to a strongly enhanced low cycle fatigue life

The fatigue tests revealed that for UFG Al1050/Al5005 LMCs there is a remarkable improvement when compared to Coarse-Grained (CG) and UFG single material type due to crack branching when it passes from a soft layer to hard interface [5]. The fatigue life of Al1050/Al5005 and Al1050A/Al2024 layered metal composites can be significantly enhanced by increasing the hardness of interface material [4]. It is normal that the fatigue fracture behavior relies upon the SPD procedure since it is related to the microstructure of materials. For instance, the deformation process of the ARB and other SPD is completely dissimilar. However, the fatigue data of the UFG materials created by the other SPD method are still very limited [75]. Thus, further fatigue data are required to know the fatigue fracture behavior of the UFG materials. It is hoped that this study can add new information to understand the fatigue-fracturing behavior of LMCs materials resulting from ARB procedure.

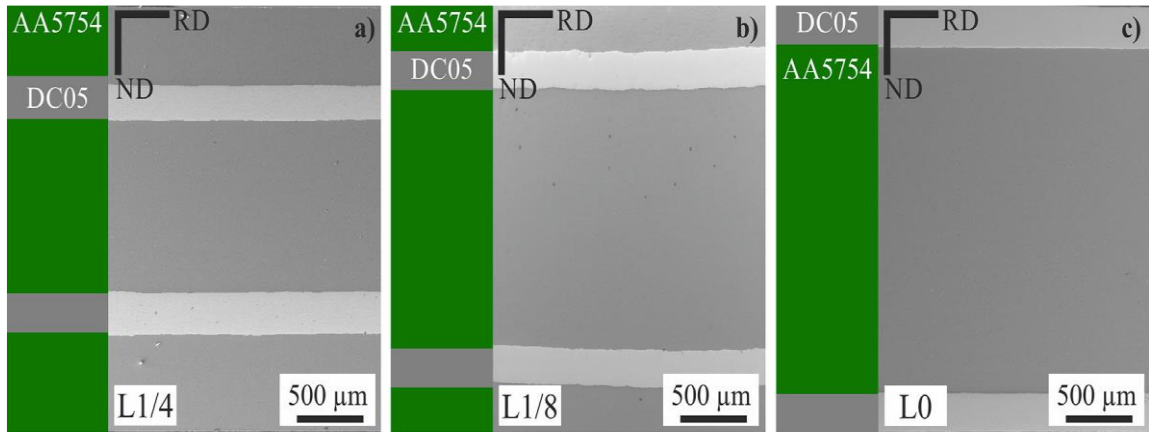


Figure 2.32 The LMCs of A15754/DC05 with different position of the steel layer a) 1/4, b) 1/8, of the total thickness of the sheet and c) at the outer surface [3].

CAPTER III

EXPERIMENTAL PROCEDURE

3.1 Materials

Al6061, Al2024 aluminum alloys, and interstitial free (IF) steel were utilized for the current study. The experimental work was divided into two different cases include similar combinations and dissimilar combinations. For the first case, two different groups of Al6061/Al6061 and Al2024/ Al2024 similar layered metal composites were investigated. In the case of dissimilar combinations, four groups of Al 6061/Al 2024, Al6061/IF steel, Al 2024/IF steel, and the combination of (Al 6061, Al2024) alloys with IF steel composites were examined. The as-received sheets were cut in the form of rectangular shapes with a width of 30mm and several lengths of 120mm and 300mm. Also, the thickness of sheets was 1mm for aluminum alloys and 0.5mm for IF steel. The IF steel was used as it acquired from the factory. The as-received aluminum alloys were in full annealed condition, known as the O temper. The chemical compositions of the delivered sheets of Al6061, Al2024, and IF steel are written in Table 3.1, Table 3.2, and Table 3.3, respectively.

Table 3.1 The chemical composition of Al6016.

component	Si	Cu	Fe	Mn	Mg	Cr	Zn	Ti	Al
wt%	0.75	0.23	0.43	0.13	0.87	0.18	0.05	0.15	Bal

Table 3.2 The chemical composition of Al2024.

component	Si	Cu	Fe	Mn	Mg	Cr	Zn	Ti	Al
wt%	0.08	4.48	0.12	0.53	1.49	0.01	0.04	0.036	Bal

Table 3.3 The chemical composition of (0.5 mm) IF steel.

component	Al	P	C	Cr	Mg	Mo	Ni	Ti	Cu	Ba
wt%	0.025	0.008	0.0015	0.025	0.1279	0.003	0.014	0.069	0.031	0.007

For the IF steel/Al multi-layer ARB processing, the initial (first time roll-bonded) sheet was IF steel/Al bimetal which was formed by roll-bonding. The IF steel strip with a thickness of 0.5 mm and Al strip with a thickness of 1 mm were used. The experimental work is summarized as follows Fig. 3.1.

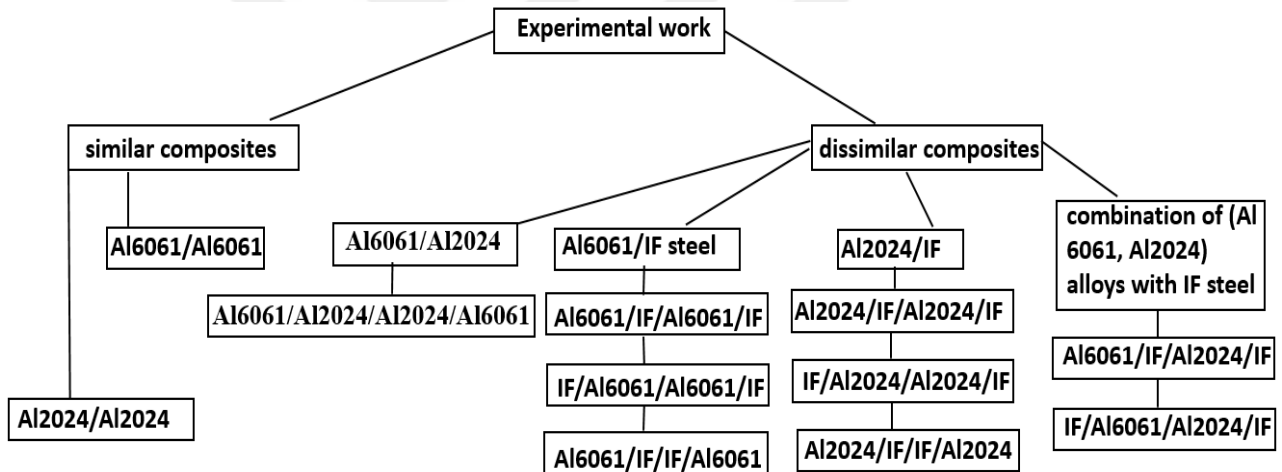


Figure 3.1: The flow chart of the experimental work.

3.2 Accumulative Roll Bonding

The experimental work for the ARB process is summarized as follows:

The process should follow the sequence described as following to carry out a successful bonding. The equipment used in this work is shown in Fig. 3.2. The first step of the

accumulative roll bonding process is surface preparation. Degreasing and wire brushing are the best methods for surface preparation technique [1]. The sheets for roll bonding were initially degreased with acetone until no noticeable soil or oil was detected on the surface.

The reason for the selection of acetone as the degreasing solution is due to its ability to resolve most oils and greases and its efficiency to dry up quickly from the surface. The next step was the installation of the sample on a flat surface and scratched by wire brushing. A rotary wire brush with a speed of about 3600rpm was utilized. Scratched surface sheets were cleaned again with acetone. After setting up the surfaces, the strips were riveted at two ends to prevent the slip during the roll bonding process. To carry out great bonding between the surfaces of the specimens, the stacked strips were fed into the rolls within 150 seconds after the surface preparation to avoid reformation of the oxide layer at the interface zone

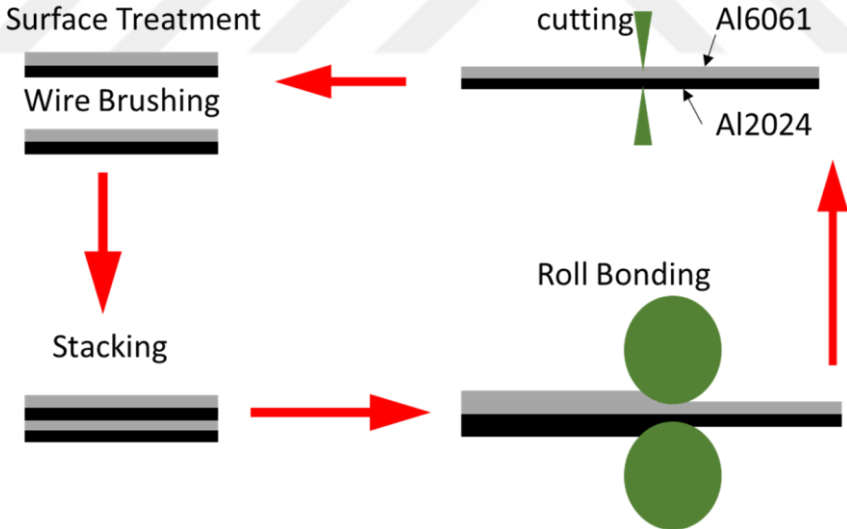


Figure 3.2: The experimental work for the ARB process.

To do accumulative roll bonding, the strips after the roll bonding were cut into two equal parts and restart the process from the beginning (Sample Preparation and then the other steps: wire brushing, stacking and rolling). This process was repeated for many times (Fig. 3.1). Preheating for the sheets before the ARB process is suggested by the other researches

[87,108,121]. Therefore, before each cycle, samples were preheated at 350⁰C/5min for Al/Al composites and 412⁰C/5min for Al/IF steel composites.



Figure 3.3: Shows the equipment used in the experimental work.

3.3 Mechanical Characterization

3.3.1 Micro-Hardness Measurements

The specimens were cut from the RD segment of the as-rolled material then ground with grit SiC water-cooled paper start from 1500 to 2500-with, 240rpm, until co-planar to prepare the sample for microhardness test. Then mechanically polished with 6- μ m Diamond on an Ultra-Pol (silk) cloth, with the rotational speed of 150rpm for 5 minutes and 1 μ m Diamond on a Trident cloth with the same rotational speed for 3 minutes [1]. The Vickers microhardness of the samples was measured using a load of 1000g and time of 15s on the surface of the cross-section of composites parallel to RD. Micro-hardness was measured randomly at five different points on the strips for each sample, and the mean hardness values were calculated. The standard deviation of values was determined to be lower than 5%. With the same procedure, the hardness of individual layers of the material was determined after each ARB cycle in the RD-ND plane.

3.3.2 Tensile testing

Uniaxial tensile testing prepares a precise valuation of mechanical properties of the material. Therefore, tensile properties were evaluated from stress-strain plots. The tensile test were performed according to the standard ASTM E646-98 using samples with 15mm gage length [154]. Mechanical test samples were prepared along the rolling direction (RD) by electro-discharge machining (EDM). The tensile tests were carried out under the strain rate of 10^{-3} s^{-1} at ambient temperature. An extensometer with $\pm 40\text{mm}$ gauge length has been used to capture the elongation depending on the requirement. The mechanical properties of composite sheets annealed for 5 min and the different value of temperatures were also evaluated using this test.

3.3.3 Shear punch testing

SPT was carried out to analyze the effect of the ARB process on mechanical properties of composite strips. The shear punch test for the miniature sample has been developed to evaluate the shear strength of metal composites fabricated by ARB method. The experimental setup of the device consists of a specimen holder, die, and flathead punches (cylindrical, shapes), as shown in Fig. 3.3. Small disc specimens of 6 mm diameter and 1 mm thickness were fabricated by electric discharge machining (EDM). The load-displacement curves (LDC) were obtained at a crosshead speed of 0.2mm/min at ambient temperature. All the tests were repeated for three times for each condition and the average values were used and the standard deviation of the results was lower than 5%.



Figure 3.4: Shear punch device die, specimen holder, and punch.

3.3.4 Cyclic stress control tests (High-Cycle Fatigue test)

It has been observed that samples are susceptible to buckling under a compressive load due to the small thickness of the sheet. Thus, tension-tension cyclic loading (high-cycle fatigue test (HCF)) was applied for fatigue tests in this study. The HCF data are typically presented as a plot of stress, with the number of cycles to failure, log scale is used for the number of cycles. The value of stress can be the minimum stress, the maximum stress, or the stress amplitude. The S-N relationship is usually calculated for a specified value of the mean stress, or one of the two ratios, stress ratio R or amplitude ratio A [154]. HCF was performed using the standard high cycle fatigue sample, as shown in Fig. 3.4, according to ASTM E466 [155] using a servo-hydraulic mechanical test frame. The values of R, for composites, vary widely from 0.1 to 0.5 [142]. Therefore, all fatigue tests were conducted under stress control at an R level of 0.1, utilizing a sinusoidal waveform with a frequency of $\omega=20\text{Hz}$ at room temperature. Generally, the necking of the hard layer leads to a significant decline in strength and ductility. Therefore, the fatigue performance of ARBed samples was limited, with four layers (N2) due to the necking of the steel layers after the second cycle for all Al/IF composites [3]. The single material type composites of Al6061, Al2024 with the same processing history was also loaded

under cyclic conditions to obtain a good comparison. Testing was performed for different stress amplitudes. Since there is a wide range of metals, available in this work and the different number of ARB passes and layer architecture, having the materials with different strength is inevitable. The compositions for fatigue tests were selected based on the results of mechanical testing. The following equations are applied to define the stress cycle [143]. The stress amplitude is half of the stress range given as.

$$\sigma_a = \frac{\sigma_{max} - \sigma_{min}}{2} = \frac{\Delta\sigma}{2} \quad (3.1)$$

The mean stress of the maximum and minimum stress.

$$\sigma_m = \frac{\sigma_{max} + \sigma_{min}}{2} \quad (3.2)$$

The stress ratio R

$$R = \frac{\sigma_{min}}{\sigma_{max}} \quad (3.3)$$

Moreover, the amplitude ratio A is calculated as.

$$A = \frac{\sigma_a}{\sigma_m} \quad (3.4)$$

Usually, high-cycle fatigue tests are performed for 10^7 cycles. The fatigue life is the number of cycles to failure at a specified stress level, while the fatigue strength (also referred to as the endurance limit) is the stress below which failure does not occur [154].

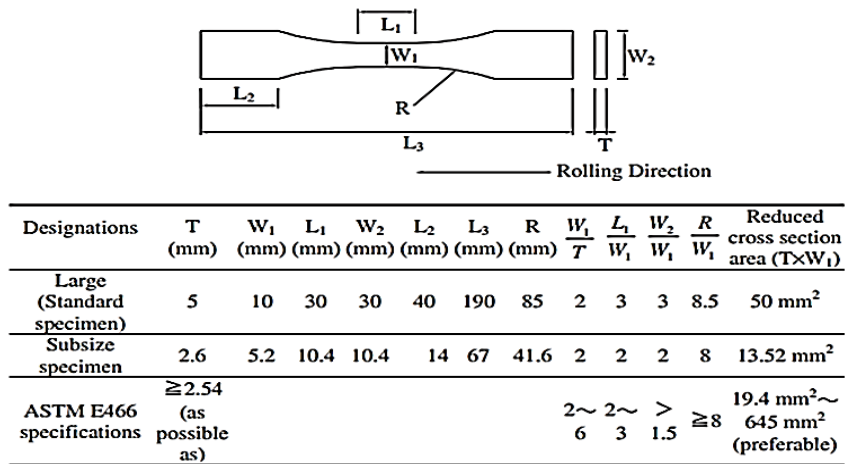


Figure 3.5: ASTM E466 standard high cycle fatigue specimens [155], all dimensions in mm.

3.4 Microstructural Investigation

The observation of material structure is one of the most important processes to understanding the behavior of metals. The structure includes atomic arrangements, chemical composition and microscopic structure on the grain scale. The following equipment was used to describe the structure of processed materials.

3.4.1 Metallographic procedure

The longitudinal-section of multilayer composites in the rolling direction (RD) (i.e. ND–RD plane) was prepared. The samples were cut in dimensions of 10 mm length in RD, 10 mm width in TD and 1mm thickness in ND. The samples were selected from the center of the RD–TD surface to minimize the influence of the edge cracks on the test results. The standard metallographic preparation approach was used, and samples mounted using epoxy and hardener to easily handle during the testing process. Composite samples after mounting are ground and then mechanically polished using 1- μ m Diamond after various roll- bonding cycles.

3.4.2 Microstructure Characterization with optical microscopy (OM)

Microscopic properties were carried out through optical microscopy and electronic scanning. To observe the microstructure under optical microscopy (OM), samples were initially cut, ground, mechanically polished and chemically etched by immersing the samples in Keller's reagent solution for aluminum alloy (Al6061&Al2024) and Marshall's reagent for IF steel [156,157]. The microstructure of the roll surface was observed using an optical light microscope.

3.4.3 Microstructure Characterization with scanning electron microscopy (SEM) (Fracture morphology analysis)

In order to detect the fracture morphology of various conditions for both Al/Al composites and Al/IF steel composites after the tensile test and fatigue test, scanning electron microscopy (SEM) was applied. Scanning electron microscopy (SEM) studies aimed at investigating the fracture mechanisms were conducted in a ZEISS SEM equipped with energy-dispersive X-ray spectroscopy (EDS) detector at an accelerating voltage of 15kV Fig. 3.5.



Figure 3.6: Scanning electron microscope (SEM), used for microstructural characterizations.

CHAPTER IV

RESULTS AND DISCUSSION – MICROSTRUCTURE AND MECHANICAL PROPERTIES OF ARB PROCESSED ALUMINUM ALLOYS

4.1 Overview

In the current chapter, mechanical properties of the aluminum composites fabricated via ARB process were investigated using a uniaxial tensile test and microhardness and optical microscopy observation. Furthermore, using the data achieved from the monotonic mechanical behavior of the composites, the appropriate cases and parameters were selected to study the cyclic mechanical behavior and related mechanisms.

4.2 ARBed Microstructure

Because the microstructure of metals considerably influences their response and mechanical behavior, it may also be wise to conduct a comprehensive analysis of the microstructure in order to understand some of the response and behavior of materials processed.

4.2.1 Bonding conditions of ARBed Aluminum

Fig. 4.1 and Fig. 4.2 demonstrate the Optical micrographs of Al6061 and Al2024 respectively in RD-ND planes after one, two, three, four and five cycles for Al6061 and one, two, and three cycles for Al2024 of ARB processing. Inspection of optical micrographs revealed that the layers are perfectly bonded; however, a few unbonded regions were detected in the interfaces between layers after the ARB process. With subsequent rolling, the bonding between the interfaces provided in the previous pass was improved. The ARB was successfully carried out up to three cycles for Al2024 and five cycles for Al6061 without any waving or necking in shape of the layers. This indicates that the interface has been effectively bounded by

reducing the thickness by 50%. After the third cycle, the edge cracks appeared, for Al2024 and started to propagate through the center of the samples Fig. 4.3. Thus, the initiation and propagation of cracks indicate that the subsequent ARB process would not be helpful. The reduction in the thickness of each individual layer was increased after each cycle and the thickness of each layer was about $31.25\mu\text{m}$ and $125\mu\text{m}$ after five passes for Al6061/Al6061 and three passes for Al2024/Al2024 which can be calculated from Eq. 2.16.

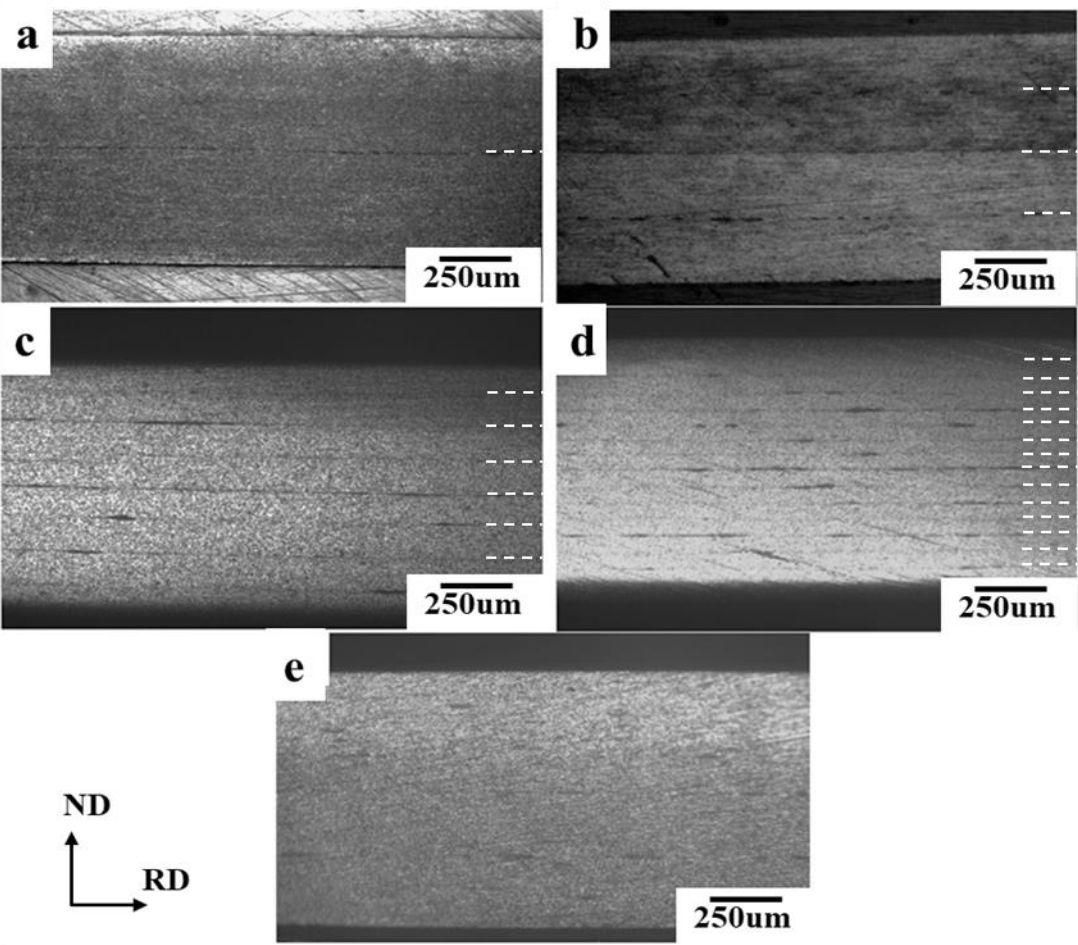


Figure 4.1: Optical microstructure of the Al 6061/Al 6061 composites after (a) One, (b) two, (c) three, (d) four, and (e) five passes ARB.

Also, the layers were still in a flat shape, and the wavy layers were not formed throughout the process for both Al6061/Al6061 and Al2024/Al2024. Although the ARB method is a very applicable and simple procedure, difficulties such as the roughness variation during the wire burnishing, contamination of the degreased and wire-brushed surfaces, the tendency of the layers to develop the cracks make it more challenging. Contaminants and residual oxides can also remain between the layers and brittle intermetallic can appear within reactive metal combinations in the ARB process, therefore it can influence the integrity of the samples.

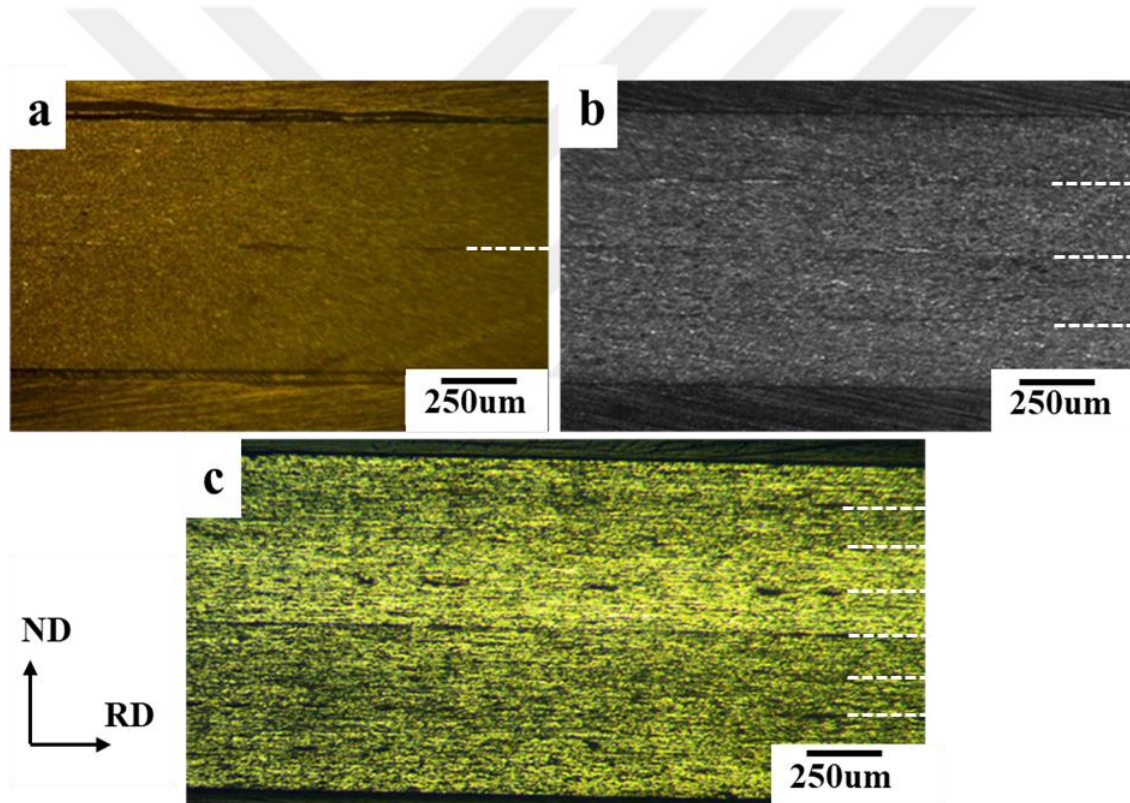


Figure 4.2: Optical microstructure of the Al2024/Al2024 composites after a) One, (b) two, c), and three passes ARB.

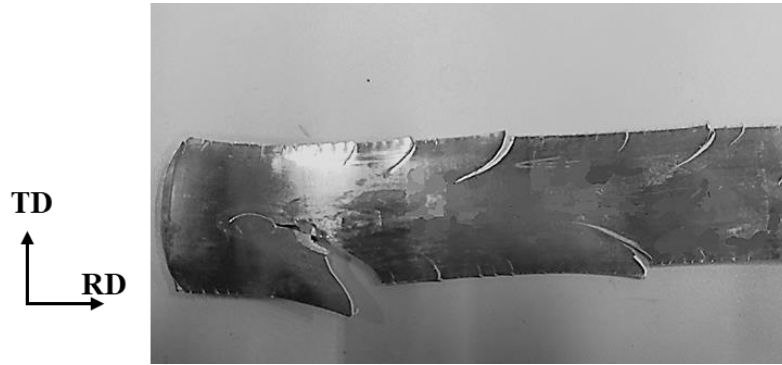


Figure 4.3: Al2024/Al2024 after three cycles illustrated the propagation of edge crack.

4.2.2 Microstructure of ARBed similar layered aluminum composites

OM of the Al6061/Al6061 and Al2024/Al2024 ARB-processed specimens at the rolling plane (RD-ND) is shown in Fig. 4.4 and Fig. 4.5, respectively. In both cases, the optical microstructures were observed in all condition of as received, after one, and two cycles. Generally, UFG structures after the ARB process is not three-dimensionally equiaxed, but there is a pancake-shaped structure, which is elongated in the RD and reduced in ND. This microscopic characteristic is similar for all classes of metals and alloys.

After one cycle of the ARB process, the microstructure of the specimen presented clear grain boundaries, elongated in the rolling direction and relatively large grains. For the later ARB cycles, the finer and complicated microstructure were detected. Therefore, increasing the ARB cycles, enhanced grain refinement. In this study, after three cycles of ARB, it is difficult to detect the shape of grains and boundaries via optical microscopy.

Normally, plastic deformation is inherently an inhomogeneous method, and as a result, the microstructure after one cycle is a mixture of deformed and slightly deformed or approximately undeformed grains Fig. 4.4b and Fig. 4.5b. Moreover, the redundant shear strain

gets scattered in a complex form into the thickness of the ARBed layers producing significant inhomogeneity in the microstructure.

Also, coarse grains were deformed (elongated) in the rolling direction and reduced in the normal direction with semi-convergent structures. Fig. 4.4c and Fig. 4.5c demonstrate noticeable improvement and grain refinement in the microstructure of composite layers after the second pass of ARB.

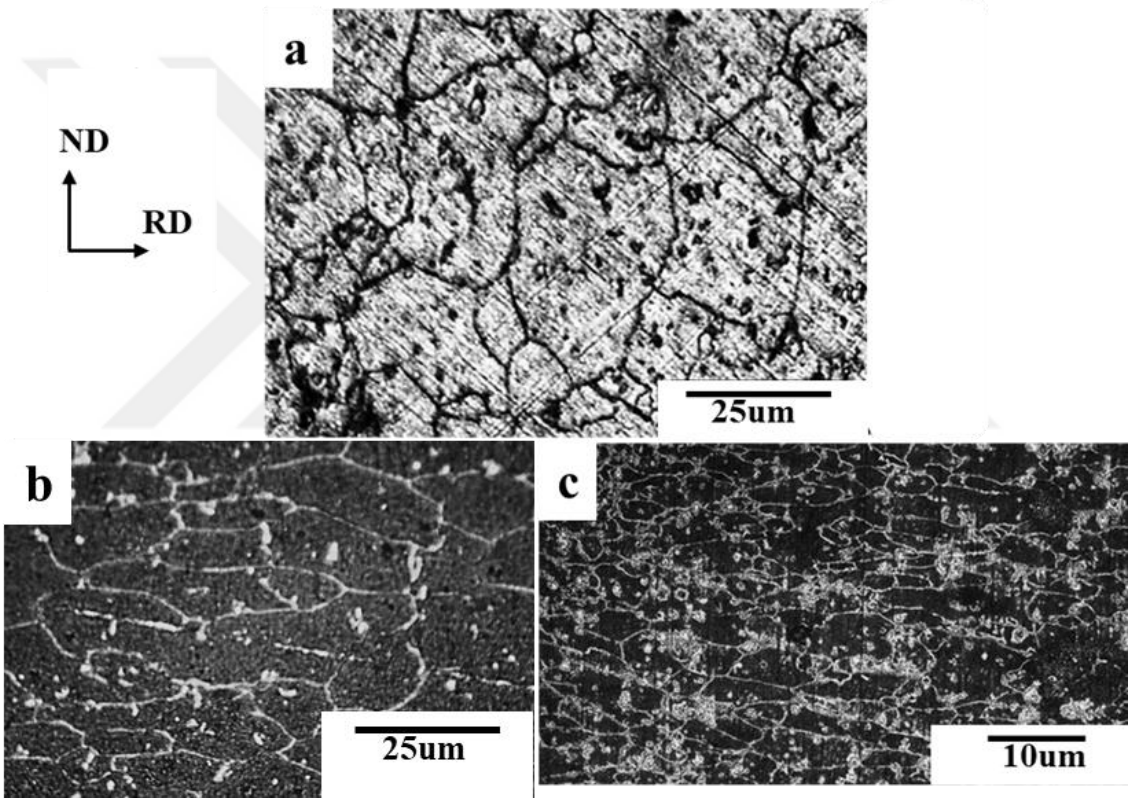


Figure 4.4: Microstructure of Al6061 a) as received, b) after the one cycle, c) after two cycles.

As shown in Fig. 4.4 and Fig. 4.5 the workpiece microstructure was notably different from the as-received sample due to the presence of fine grains like a lamellar (or irregularly bent lamellar) morphology, which were elongated in the roll direction, indicating that the plastic

strain process causes a significant grain refinement in the Al 6061 and Al 2024 structure after the second cycle.

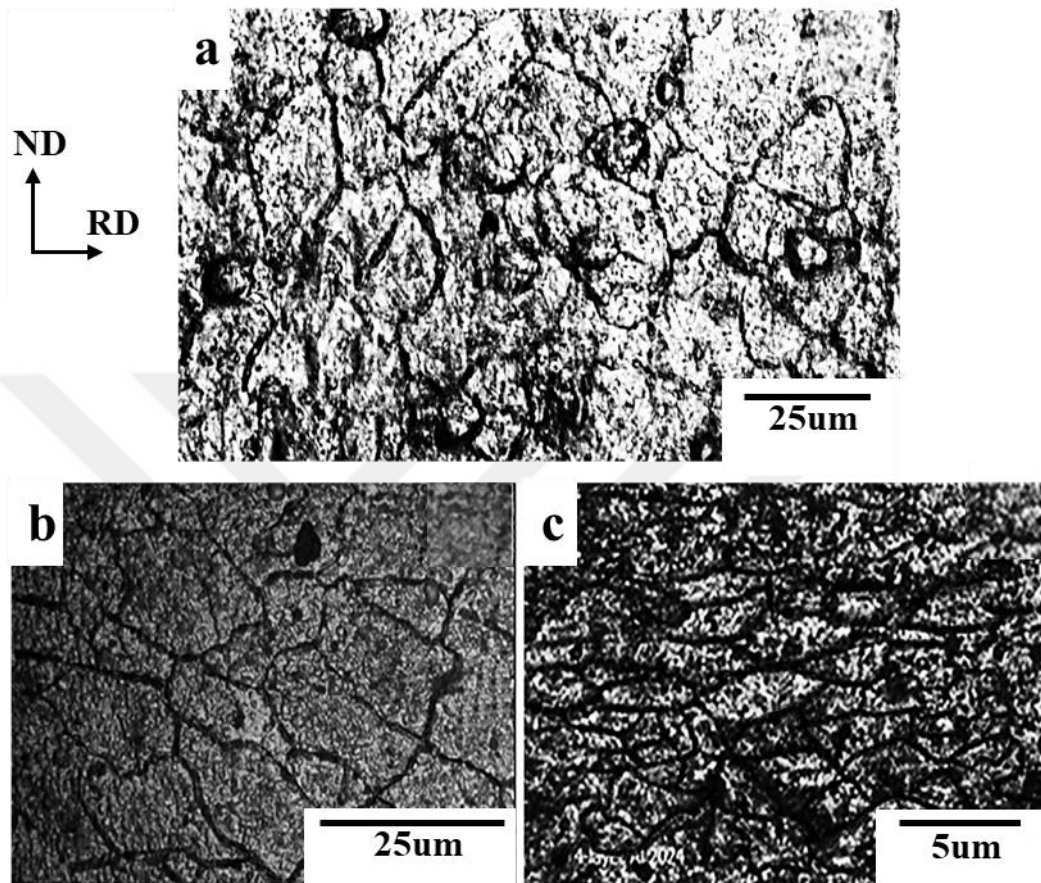


Figure 4.5: Microstructure of Al2024 a) as received, b) after one cycle, c) after two cycles ARB.

Comparing the results of the optical microscopy observation revealed that grain refinement of Al2024 throughout the ARB process was significantly higher than the Al6061 for both one and two passes (Fig. 4.4 and Fig. 4.5). This difference in grain refinement is related to the high impurity of Al2024 compared with the Al6061, which is affecting the grain sizes during the ARB process. Additionally, the grain size of the Al2024 in as-received condition was smaller than that of Al6061 in as-received condition. The aforementioned observation was well agreed with the literature [115,158].

4.2.3 Microstructure of ARBed dissimilar layered aluminum composites

Micrographs were recorded to observe the microstructural evolution and bonding characteristics of the layers after ARB. Figs. 4.6a-d show the as-received microstructures along with the effect of four ARB cycles. The average grain size for Al6061 and Al2024 are similar and measured as 38 μ m and 30 μ m, respectively. Accordingly, both alloys exhibited lamellar structures after the fourth ARB pass. The level of refinement is not comparable for the two constituents. Namely, while refinement down to the sub-micron regime was prevalent in Al2024, the formation of fine structures was not observed in Al6061 with an average grain size of 5 μ m. This could be attributed to the comparably higher amount of impurity content in the former. Thus, not only the dynamic recovery of dislocations is impeded, but also grain boundary mobility is restricted. Both reasons contribute to achieving finer grain size in Al2024 [115,158]. The microstructure demonstrates two types of grain boundaries: lamellar boundaries (LB) along the RD and interconnecting boundaries (ICB), linking one LB to another, as shown in Fig. 4.6e [53,159]. This was especially observed for Al6061 where LBs were found to orient along RD as seen in Figs. 4.6c and 4.6e.

Li et al. reported that the above-mentioned phenomenon occurs after six passes of ARB for aluminum and copper [160]. This type of lamellar formation is with the virtue of dislocations arranging themselves to stable configurations [97]. The same behavior comparing with the similar layered composites was found in the microstructure of the Al6061 and Al2024, and the grains were more refined in ND direction in Al2024 layers.

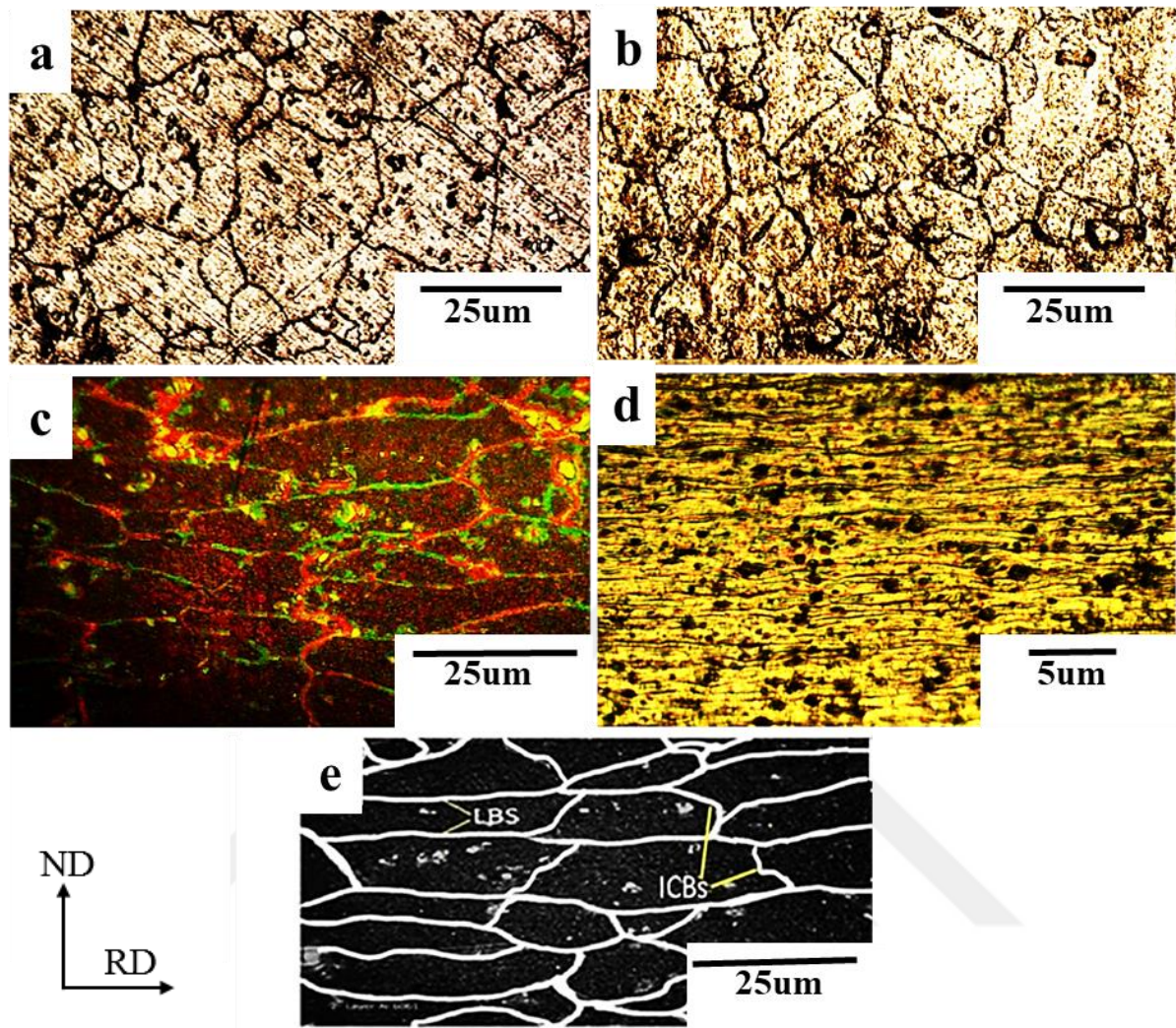


Figure 4.6: Optical micrographs of a) as received Al6061, b) as received Al2024, c) Al6061 after four ARB cycles, d) Al2024 after four ARB cycles, and e) illustration of the lamellar boundaries (LBs) and interconnecting boundaries (ICBs), where RD and ND are the rolling and normal directions, respectively.

A decrease in individual layer thickness observed with increasing number of ARB cycles. ARB presented the perfect interfacial bonding between dissimilar layers of Al2024 sheet and Al6061 for composites after the four passes without any wavy or necking in layers shape. The small hardness difference between Al2024 and Al6061 is the main reason for remaining composite in a flat shape without the formation of waves in layers. However, with increasing

number of passes, even this low hardness different can cause the wavy layers in the composites [44].

However, it was not possible to do more cycles because of the formation of edge cracks in later of the cycle. Since the reduction is 50% per cycle, the new thickness after n cycles can be calculated from Eq. 2.16. So, the thickness of the layer obtained is $62.5\mu\text{m}$. Moreover, the number of layers is related to the number of cycles as 2^n and the number of interface lines increased according to the relationship is 2^{n-1} [33].

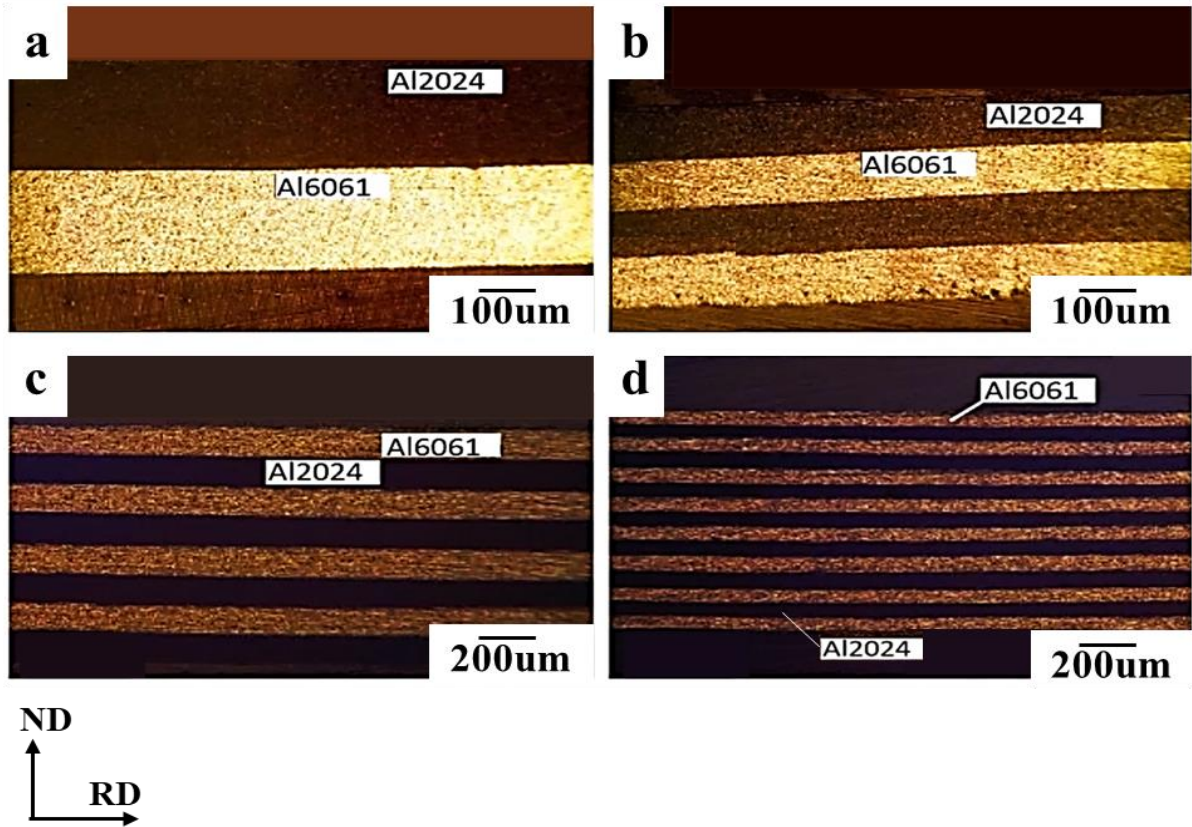


Figure 4.7: Optical microstructure of the Al2024/Al6061 composites after a) one pass, b) two passes, c) three passes, and d) four passes ARB process.

4.3 Mechanical properties

The mechanical response of the metal composites corresponds well with the modification in microstructure under the severely plastic deformations discussed in the previous section. The most important relationship between the microstructure and mechanical properties is represented by Hall-Patch Eq. 2.1, describing that the refinement of grains increases the hardness and also the strength of the material which was well agreed with the results of tensile and microhardness tests after the ARB process.

4.3.1 Al6061 sheets after ARB

The Vickers microhardness of the Al6061/Al6061 ARBed sheet is presented in Fig. 4.8 with respect to the number of cycles and through the thickness. Fig. 4.8a demonstrates a harsh enhancement in the hardness after the initial stage (first cycle) due to the strain hardening and an increase in dislocation density and interaction between them during the rolling process. Afterward the slope of hardness improvement decreased in relation with changing the hardening mechanism from the strain hardening to the grain refinement in the next cycles of ARB [161]. The saturation state was achieved at high strains, which was previously observed in the other UFG materials fabricated by SPD methods [79,162,163]. This phenomenon is related to the fact that after a few ARB cycles, the density of dislocations reaches a steady state. This hardness improvement is linked to the strain hardening due to high redundant shear strain induced by the friction between the metal sheets and roll surface in the ARB process.

The layers present a uniform microhardness across the thickness. Fig. 4.8b illustrates the variation of microhardness over the thickness of the samples for different cycles of the ARB process.

Inspection of the results for the first cycle throughout the thickness illustrates that hardness improvement was not homogeneous and enhancement of the hardness in the center was higher than the surfaces. It can be related to the wire brushing of the surfaces which can produce the extra strain hardening before the ARB process. The effect of wire brushing on the mechanical properties of layers is investigated by Lee et al. [82]. On the other hand, the average microhardness of the Al6061 was increased around two folds of the as-received condition after two cycles ARB. The mean hardness of as-received material rises from 39Hv up to around 93Hv after four cycles and saturates at this level. A significant jump in hardness at the interface was detected for both cycles implying that the two sheets are directly bonded and there is no transition region. Generally, the hardness of the Al6061 layers is somehow homogeneous, having higher values in the interface region and near the surface. The same observation was previously observed, and they reported that the reason for high microhardness in the interfaces is a redundant shear strain near the surfaces [91]. Moreover, high-density precipitates of Al6061 is the other important factor of increasing the hardness. Also, these precipitates may cause an inhomogeneous microstructure, which is represented by the fluctuation of the hardness profile (Fig. 4.8b).

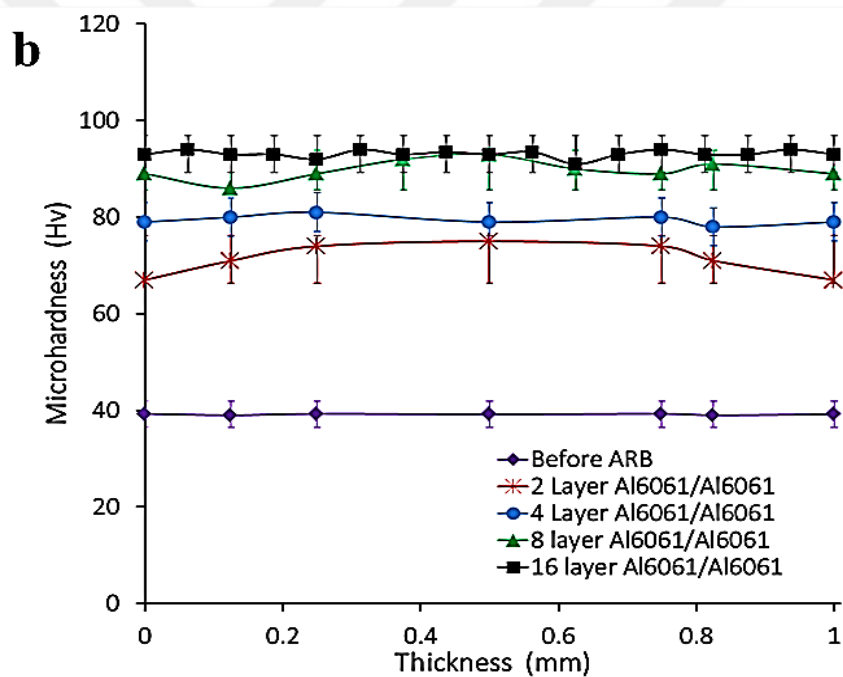
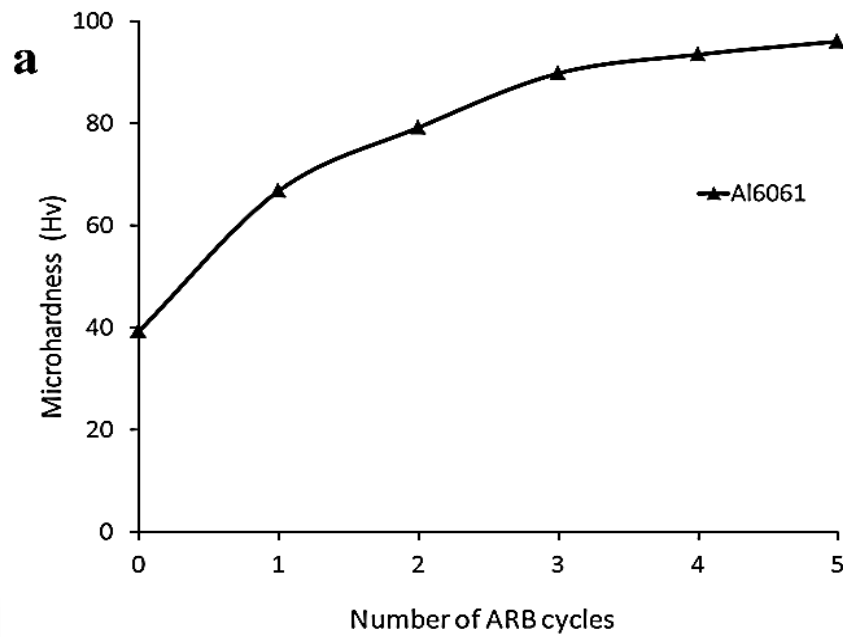


Figure 4.8: Variation of microhardness, a) with a number of ARB cycles, b) over the thickness of the sample after five cycles.

The monotonic mechanical properties of the Al composites were investigated using the uniaxial tensile test at the ambient temperature under the quasi-static strain rate of 10^{-3} s^{-1} . Fig. 4.9 illustrates the effect of ARB cycles on the tensile behavior of each group of processed materials. It was found that both yield and ultimate tensile strength (UTS) of the Al6061/Al6061

composites increased noticeably, with the expense of decreasing ductility for all groups. The enhancement of strength is attributed to the high density of dislocations after the first and second cycle of ARB due to the strain hardening, contributed to the grain refinement with the formation of micro subgrains during the later cycles. The resultant UTS values after five cycles were ~ 255MPa, which was greater than that of base metal (~ 124MPa). The reason for this improvement in strength is the work-hardening of the aluminum layer, which is associated with the ARBed. Also, the production of ultrafine-grained microstructure due to the accumulation of SPD is the main reason of this enhancement [110,162]. Furthermore, the presence of Mg in Al6061 solid solution, which is around 1.16wt% reduces the stacking fault energy and thus recrystallization and recovery characteristics of the alloy. The precipitates contain Mg may affect the microstructural features of aluminum in two different methods. The first method is pinning effect on dislocations and hindering their motions (solute–dislocation interaction), and the second way is preventing the annihilation of dislocations throughout the deformation which can increase the density of dislocations (dislocation–dislocation interaction) [164].

On the other hand, with increasing number of cycles for group Al6061/Al6061 composite, the ductility increased up to 6%, while the strength remained approximately constant due to the saturation of the dislocation after a few ARB cycles [165,166]. Also, similar behavior was previously detected [118] for the UFG aluminum alloys, explained by the steady-state density of dislocation and high misorientation of grain boundaries in aluminum after four passes ARB.

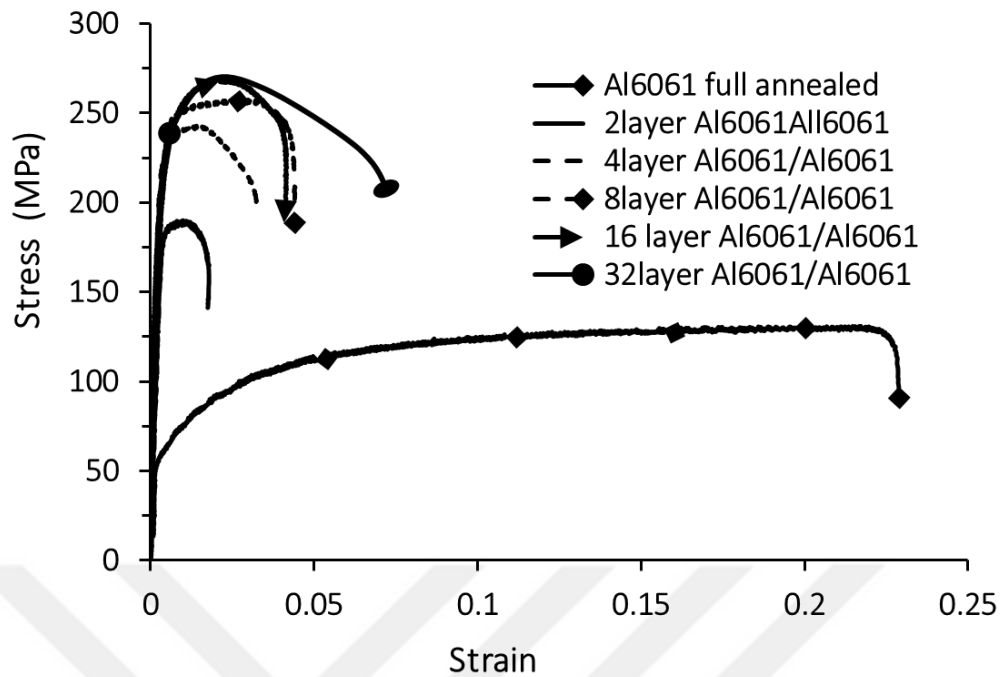


Figure 4.9: Stress-strain response of the fabricated composites of four layers Al6061/Al6061.

4.3.2 Al2024 sheets after ARBed

Fig. 4.10 depicts the microhardness evolution during the ARB process for Al2024. Microhardness enhanced rapidly by the first cycle and then the slope of improving hardness reduced by further rolling. A notable enhancement of microhardness, which was more than 150% of the as-received sheet was observed after three passes ARB. The similar trend was observed for the hardness of Al2024, which was highly enhanced at the first cycle, then decrease in the slop of hardness improvement for further ARB passes. Also, Fig. 4.10b reveals that the hardness of the Al2024 has the same profile as Al6061 throughout the thickness with some fluctuations.

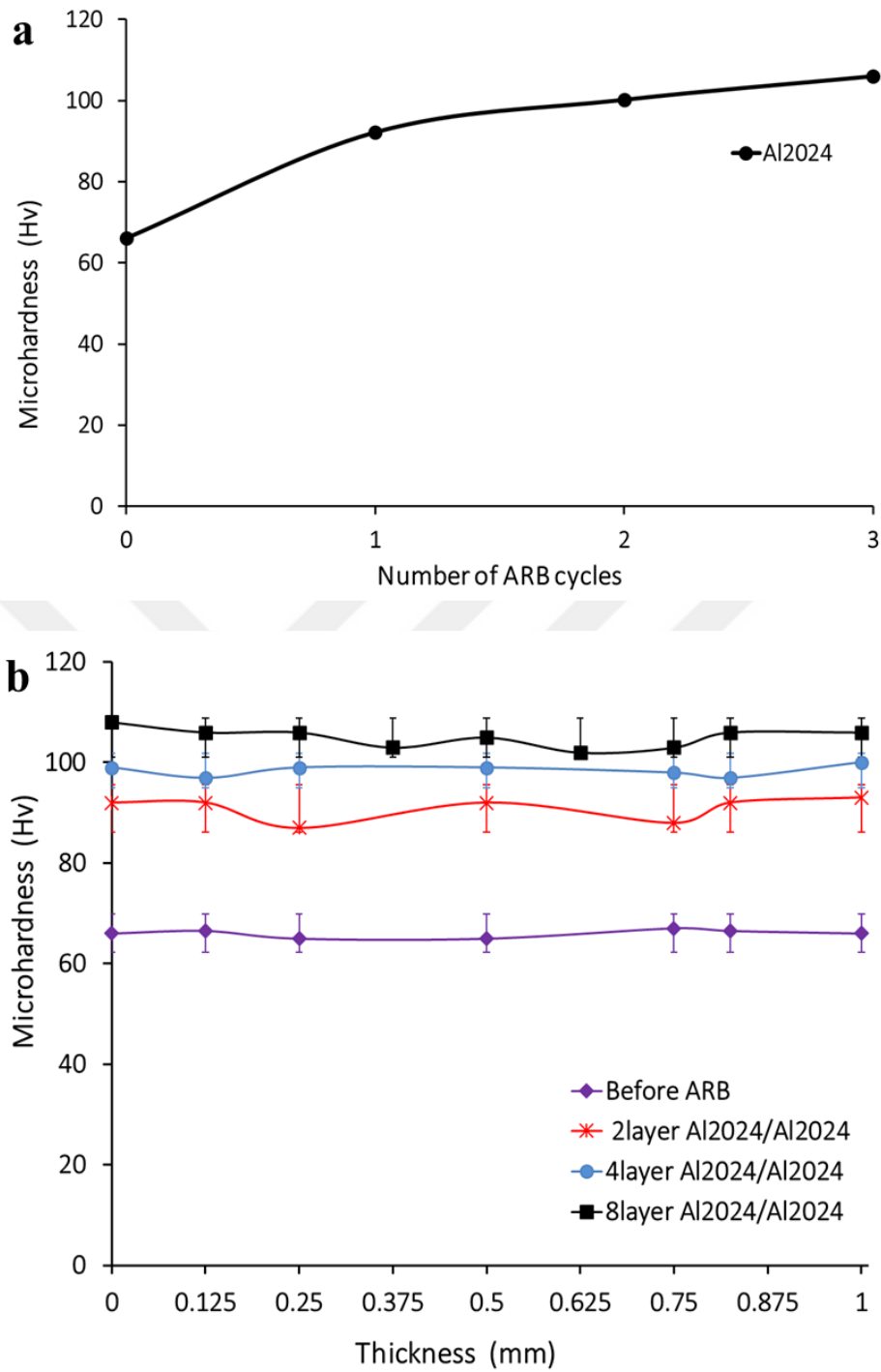


Figure 4.10: Variation of microhardness a) with a number of ARB cycles, b) over the thickness of the sample after three cycles.

As shown in Fig. 4.11, the tensile behavior of the ARBed Al2024 at first three cycles is very similar to the ARBed Al6061 with the same trend of increasing strength with a reduction

in ductility. Firstly, after one pass ARB, the UTS was increased from about 190MPa to 350MPa with the reduction of ductility to 3%. Then after the second pass, the strength, enhanced to 420MPa, The reason for this improvement in strength is the work-hardening of the aluminum layer, which is associated with the ARBed. Also, the production of ultrafine-grained microstructure due to the accumulation of SPD is the main reason of this enhancement [165,166].

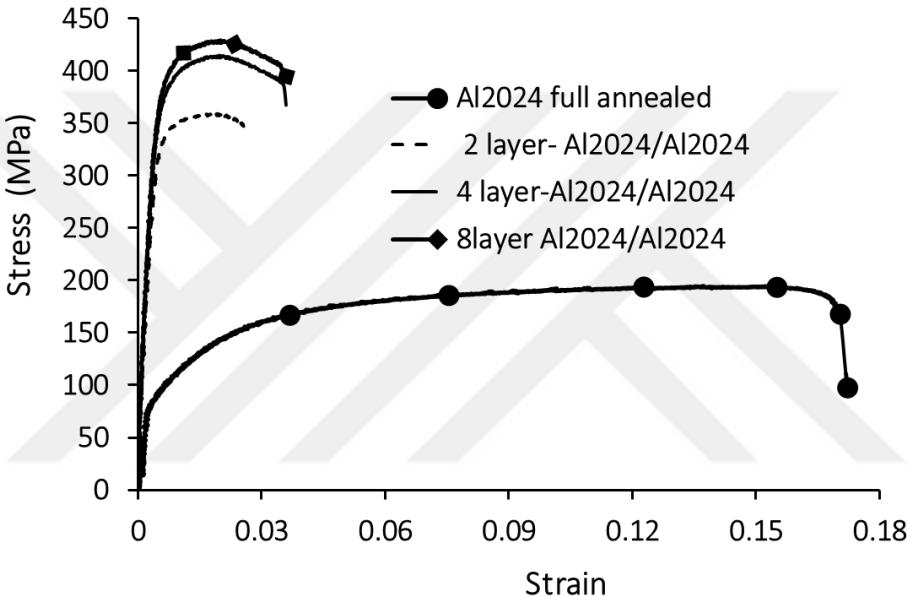


Figure 4.11: Stress-strain response of the fabricated composites Al2024/Al2024 after one, two, and three cycles.

4.3.3 Al2024/Al6061 composite aluminum sheets after ARBed

Fig. 6a. displays the hardness variation of each material with ARB cycle number. During the first and second cycles, hardness progressed quickly. This is especially true for Al2024, where the maximum hardness around 100Hv is reached after the second pass and the augmentation was less considerable for the ensuing cycles. As a result, the average hardness of Al2024 exceeded 150% of the initial value. A similar observation holds true for Al6061

displaying a more than twice improved, where the progress occurred at a decreasing rate up to four ARB cycles. Since the refined grain size of constituent layers is different, similar ultimate hardness levels indicate the dominant influence of accumulated strain.

In general, the hardness of the layered composite remarkably increased after the severe plastic deformation, which is also represented in Fig. 4.12. It can be seen that the higher hardness values are recorded on the surface of the samples due to the friction-induced, redundant shear strain [27-29].

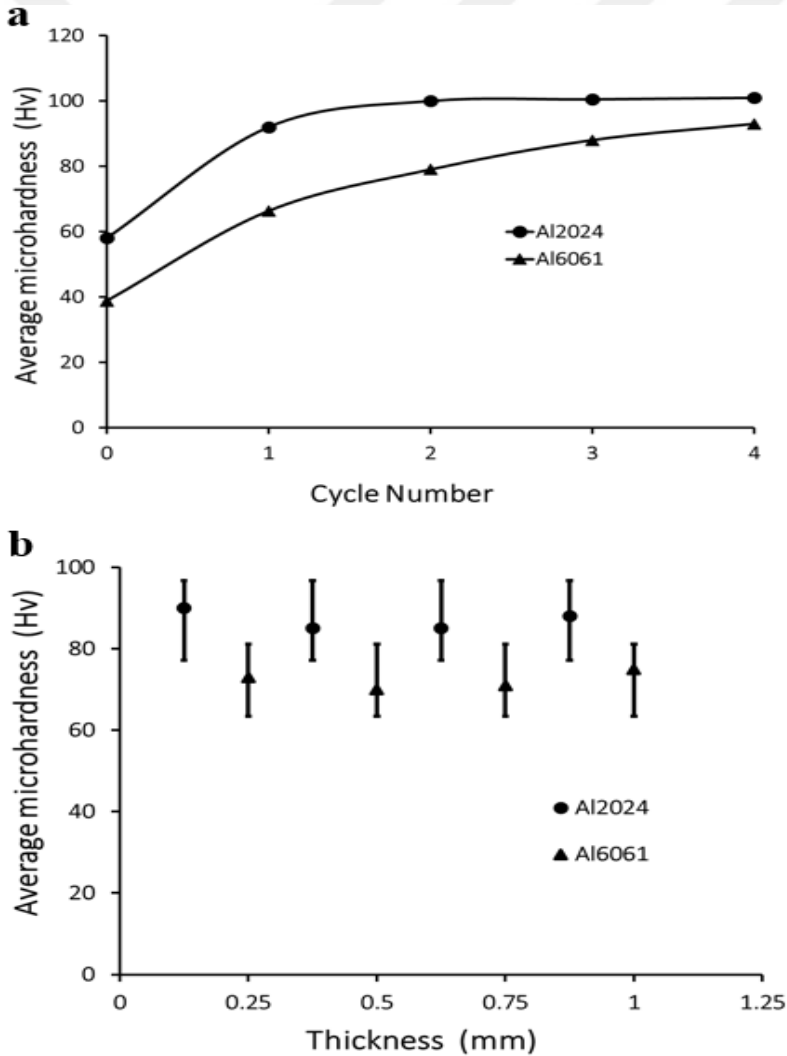


Figure 4.12: Variation of microhardness a) with a number of ARB cycles, b) over the thickness of the sample after three cycles

Still, uniform hardness levels were achieved among different layers of the same constituent alloy. Fig. 4.12b also indicates that with three cycles of processing, the number of interface lines rose according to the relationship 2^{n-1} , where n indicates the number of ARB passes [170]. Moreover, this has an effect on the value of hardness converging to be approximately constant along the thickness, especially with a high number of ARB cycles [170,171].

Tensile behavior obtained after various numbers of ARB cycles are shown in Fig. 4.13. The stress-strain curves indicate a significant increase in strength levels exceeding both base materials with a reduction in failure elongations (Fig. 4.13a). The highest strength was obtained in the four-layered composite; however, the ductility remained below 5% due to limited strain hardening ability after yielding in the cold-worked microstructure [77]. The ultimate tensile strength (UTS) of 324MPa for this sample is about 1.7 and 2.4 times of that for Al2024 and Al6061, respectively. Further processing did not improve the strength as was demonstrated by Xing et al. [88] in his study on 8011 aluminum alloy processed by ARB at 200°C. A similar finding was also reported by Lu et al. [172] on Al6060, and this phenomenon was explained in relation to the continuous recrystallization, dynamic recovery and static recovery during and/or after ARB. Thus, the mechanical behavior is dictated based on the competition between recovery mechanisms and structural refinement. Since recrystallisation decreases the dislocation density; the increase in strength is inhibited during the following cycles. While increased strength for the initial cycles is ascribed to the growth in dislocation density leading to work hardening, but that at the subsequent cycles can be linked to the decreased grain size [35,36].

To further improve the ductility, the four-layered composite samples were subjected to post-ARB heat treatment. A short annealing period at 250°C led to partial restoration of strain hardening to around 5% fracture elongation underlining a lower bound for exploitation in structural applications. Another outcome of the treatment was a slight decrease in strength down to 304MPa, still standing at a considerable improvement over the as-received conditions. Fig. 4.13a and b represent a comparative look on the mechanical response of Al6061/Al6061, Al2024/Al2024, and Al2024/Al6061 composites. It can be seen that increasing the number of cycles are beneficial for improving the strength regardless of the composite type. In addition, the Al2024/Al6061 composite shows behavior that can be approximated as the average of Al6061/Al6061 and Al2024/Al2024 single material type composites. Since the strength of producing composites directly depends on the contribution of different layers, the strength of layered material is a combination of both strength of Al2024 and Al6061 for Al2024/Al6061 composite, and the results proved that the yield and ultimate strength of this composite is approximately the average of Al2024/Al2024 and Al6061/Al6061 layered materials.

Fig. 4.14 illustrates the variation of yield strength (YS), UTS, and elongation concerning the number of ARB cycles of both materials investigated in this study. The YS and UTS increased up to two cycles, followed by a decrease in the third cycle and ending up with a rise at the last cycle. As such, the peak strength values obtained after two cycles exceeded 320MPa.

Nevertheless, the ductility decreased substantially down to below 5% after the first cycle and remained around this value during further processing, indicating a widely pronounced deprivation in formability [67].

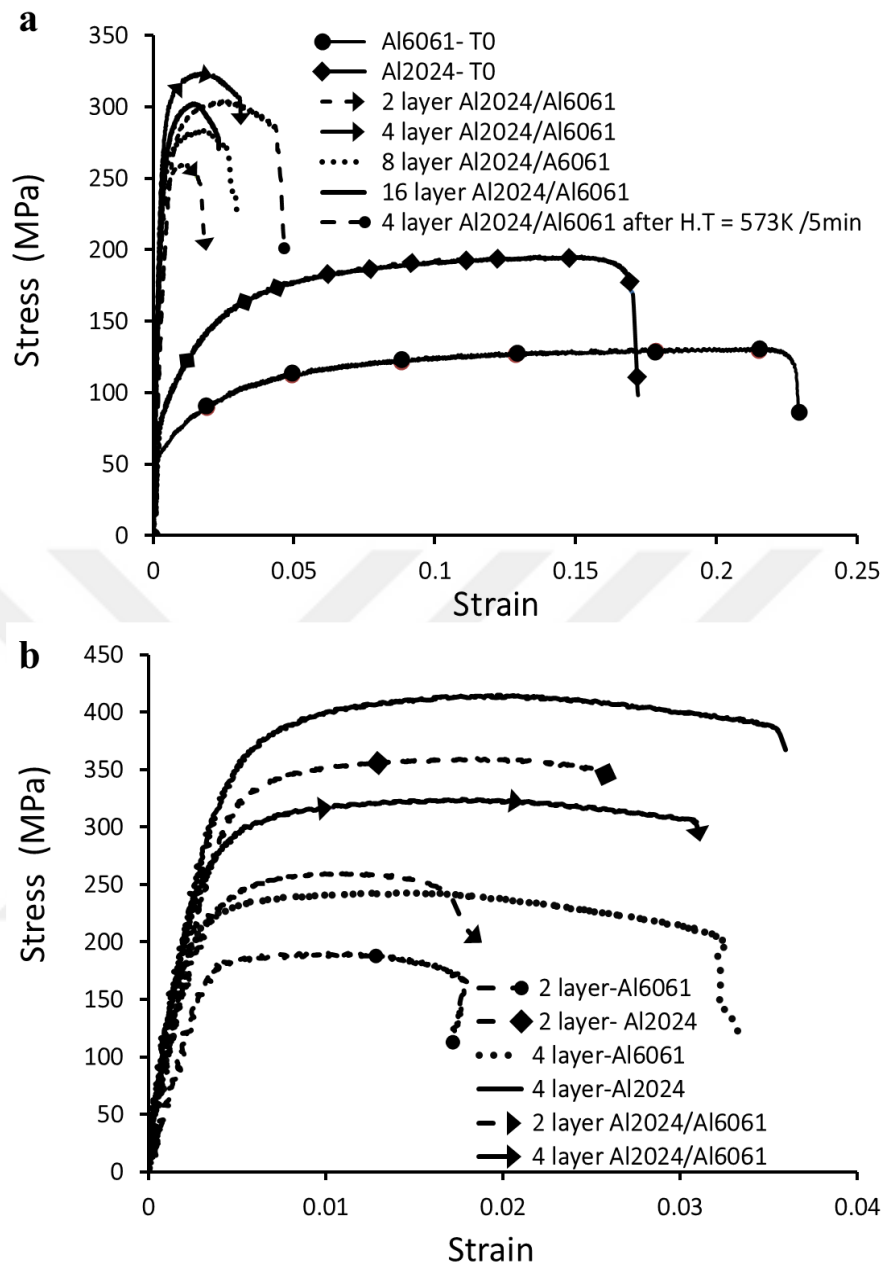


Figure 4.13: Stress-strain response of the a) fabricated composites of Al2024/Al6061 b) comparison between Al6061/Al6061, Al2024/Al2024 composites, and Al2024/Al6061 composite after the second cycle.

The strength of the Al2024/Al6061 composite can also be calculated by the rule of mixture implementing the following equation [175]:

$$\sigma_{cp} = f_{2024}\sigma_{2024} + f_{6061}\sigma_{6061} \quad (4.1)$$

, where f_{2024} and f_{6091} are the volume fractions and, σ_{2024} and σ_{6061} are the tensile strength values of the Al2024/Al2024 and Al6061/Al6061 composites, respectively.

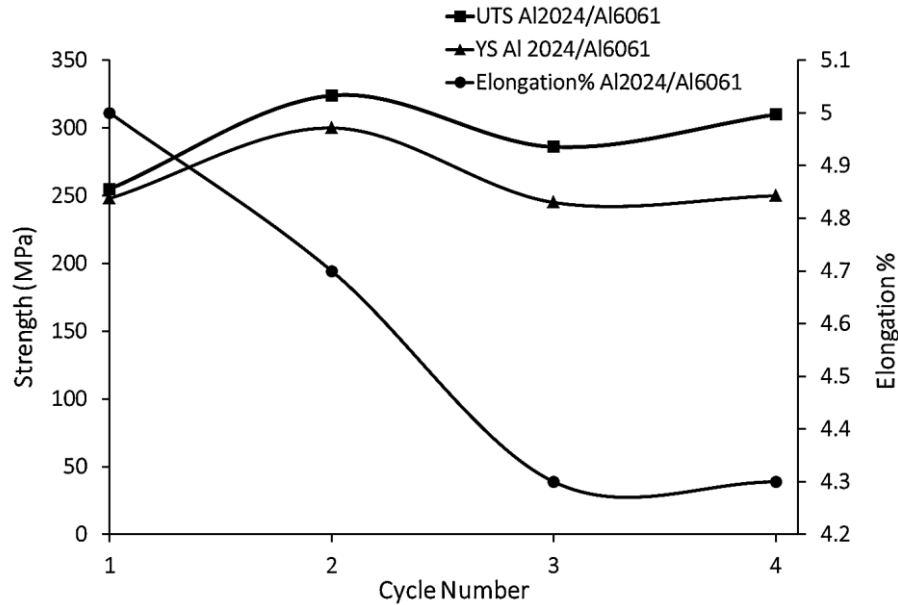


Figure 4.14: Variations in mechanical properties as a function of cycle number for composite Al2024/Al6061.

4.4 Shear punch testing (SPT)

Shear punch testing (SPT) is one of the most successful methods for estimating the mechanical properties such as the shear elongation percentage ($\% \epsilon_u$), shear yield strength (SYS), and ultimate shear strength (USS). The exciting advantage of SPT is the simplicity of sample manufacturing. Also, the quality of the SPT sample edges does not affect the test results, while the condition of the surfaces and sides of the tensile samples are directly affecting the results of the tests [176]. Therefore, the SPT was carried out to determine the mechanical characteristics of the composite after the ARB process.

The load-displacement curves for different similar layered composites with different ARB passes are represented in Figs. 4.15a, and b. The peak load of the as-received condition was low, which is associated with the presence of large grains in the microstructure of the sheet. Subsequently, the load increases with the increasing number of layers, which means that shear strength enhanced with further ARB passes. The load (shear force (SF)) varies with the number of ARB cycles in the three cycles (8layer) seems to be the highest one in all cases. For a better comparison of similar composites, the load-displacement curves for 2, 4, 8, 16, and 32 layers, for Al6061/Al6061 and 2, 4, 8 layers for Al2024/Al2024 as well as the initial material, are shown in Figure 4.15a and b. Moreover, the ultimate shear force (USF) obtained from the curves was listed in Table 4.1 with the number of layers. Besides, the ultimate shear force was converted to the ultimate shear stress using Eq. (2.24).

According to the Table 4.1, ARB process enhanced the strength of the sheets up to 131MPa and 210MPa after three cycles for Al6061/Al6061 and Al2024/Al2024 respectively, afterward, the reduction in strength was observed for the Al6061 compound. The reason for this improvement in strength is due to the work-hardening and grain refinement during the SPD for aluminum layer, which is associated with the ARBed [110,162].

On the other hand, the reduction of USF values with the increase in the number of cycles is due to the fact that, after a few ARB cycles, the density of dislocations reaches a steady-state (saturation state) at high strains [165,166]. This is in good agreement with previous results of other researchers which believe that the steady-state density of dislocation and high misorientation of grain boundaries in aluminum after four cycles ARB can reduce the strength [118].

According to Fig. 4.15a and b. in the first cycles, the displacement dropped from 1.05mm and 0.7mm to the 0.83mm and 5.5mm for a layered composite of Al6061/A6061 and

Al2024/Al2024 respectively, but after the second cycle, the elongation remained approximately constant due to limited strain hardening ability after yielding in the cold-worked microstructure [77]. It can be noted that in general, there is a similar behavior for conventional tensile stress-strain curves and those from the SPT.

Fig. 4.16 represent the load-displacement curves for the Al2024/Al6061 dissimilar layered composites fabricated by ARB process. As-received Al6061 and 16-layer Al2024/Al6061 layered composite have the minimum and maximum shear loads, respectively. According to Table 4.1 and Fig. 4.16, the ARB process improves the ultimate shear strength of the sample up to 167MPa after four cycles. On the other hand, by increasing the number of ARB cycles, the elongation to fracture decreased from 1.05mm for as-received Al6061 to around 0.6mm for the 16 layers composite. Elongation in shear depends on the softer constituent (Al6061) in the layered composite. The maximum elongation was observed in the samples after the first and second cycles. After the second cycle, the elongation gradually dropped with further ARB cycles. The rise in shear strength within the relatively low strains regime was consistent with the finding of various investigators [133,137]. Many researchers have reported that the sharp increase in power at relatively low pressure is mainly due to the stress stiffness resulting from increased decomposition intensity and the formation of sub-grains. By comparing shear strength curves with tensile strength curves, it can be realized that there is a linear relationship between the shear and tensile strength [177].

The ultimate shear force was converted to the ultimate shear stress using Eq. (2.24). To verify the SPT -tensile data correlation the ultimate shear strength of (SPT) and ultimate of the tensile strength (UTS) is plotted. The linear regression analysis shows a good relationship between these tests.

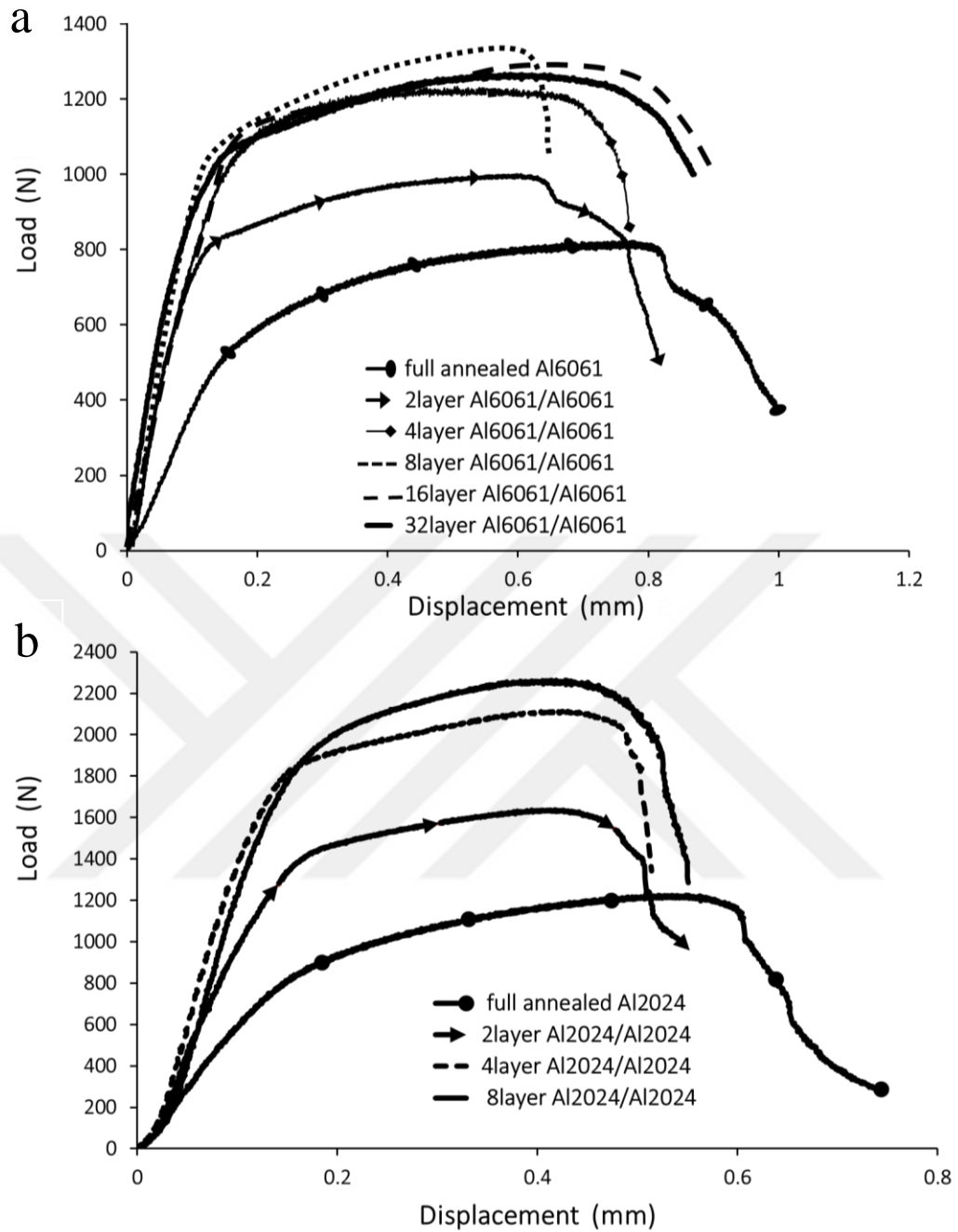


Figure 4.15: SPT curves for layered metal composites of A) Al6061/Al6061 and b) Al2024/Al2024 for the different ARB process.

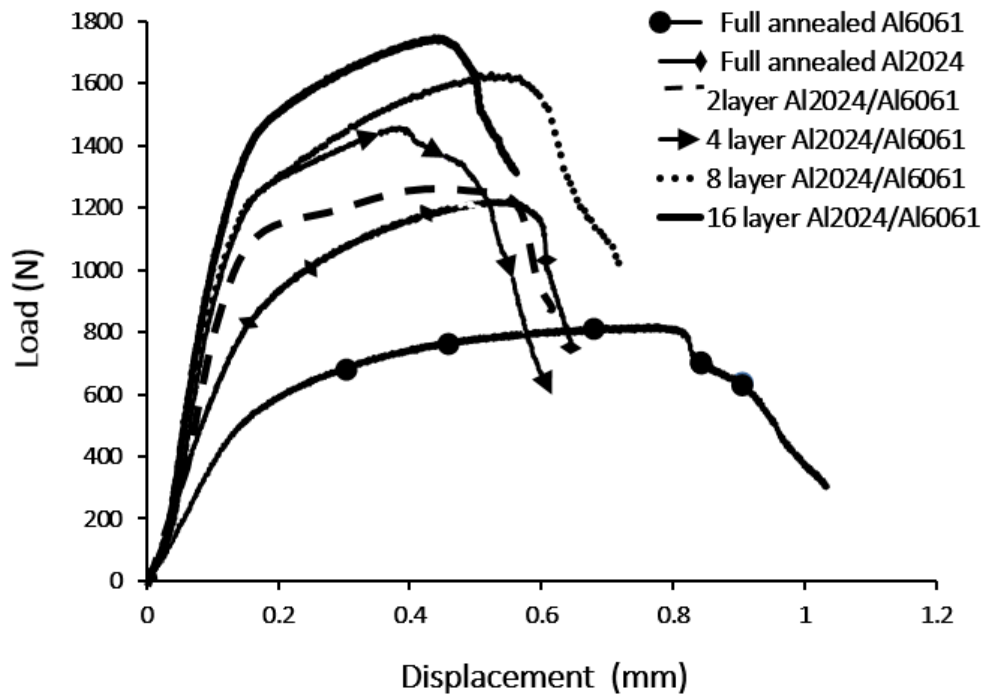


Figure 4.16: SPT curves for layered metal composites of Al2024/Al6061 with the different ARB process.

The correlation between the ultimate tensile and ultimate shear strength after ARB processes for composite Al2024/Al2024, Al6061/Al6061, and Al2024/Al6061 are shown in Fig. 4.17. Here the measurements from the four-layer samples of Al2024/Al6061 were not included as considered outliers. Accordingly, the correlation line satisfies the below relations.

$$UST_{Al2024} = 2.2431USS_{Al2024} - 35.22 \quad (4.2)$$

$$UST_{Al6061} = 2.423931USS_{Al6061} - 39.5 \quad (4.3)$$

$$UST_{Al2024/Al6061} = 1.1339USS_{Al2024/Al6061} - 114.8 \quad (4.4)$$

It can be observed that a linear relationship exists between the shear and ultimate tensile strengths with some deviations which were detected with a slope of (0.877, 0.777 and 0.99). The slopes of the fitted lines between the tensile data and shear data indicated the correlation coefficient (m). The m values were found about 2.2431, 2.4239, and 1.1339 for Al2024/Al2024,

Al6061/Al6061, and Al2024/Al6061, respectively. The magnitude of m value was reported within the range of 1.01-2.5 for several materials [128,129,179,181]. However, it should be noted that the correlation coefficient may depend on some factors, including the strain hardening capability of the material [129] and the variety of loads exerted during SPT [179]. The results of the ultimate shear force, ultimate shear strength, ultimate tensile strength and ultimate tensile strength calculated by the correlation equation of samples for similar layered metal composites of Al2024 and Al6061 as well as for dissimilar layered composites of Al2024/Al6061 are summarized in Table 4.1.

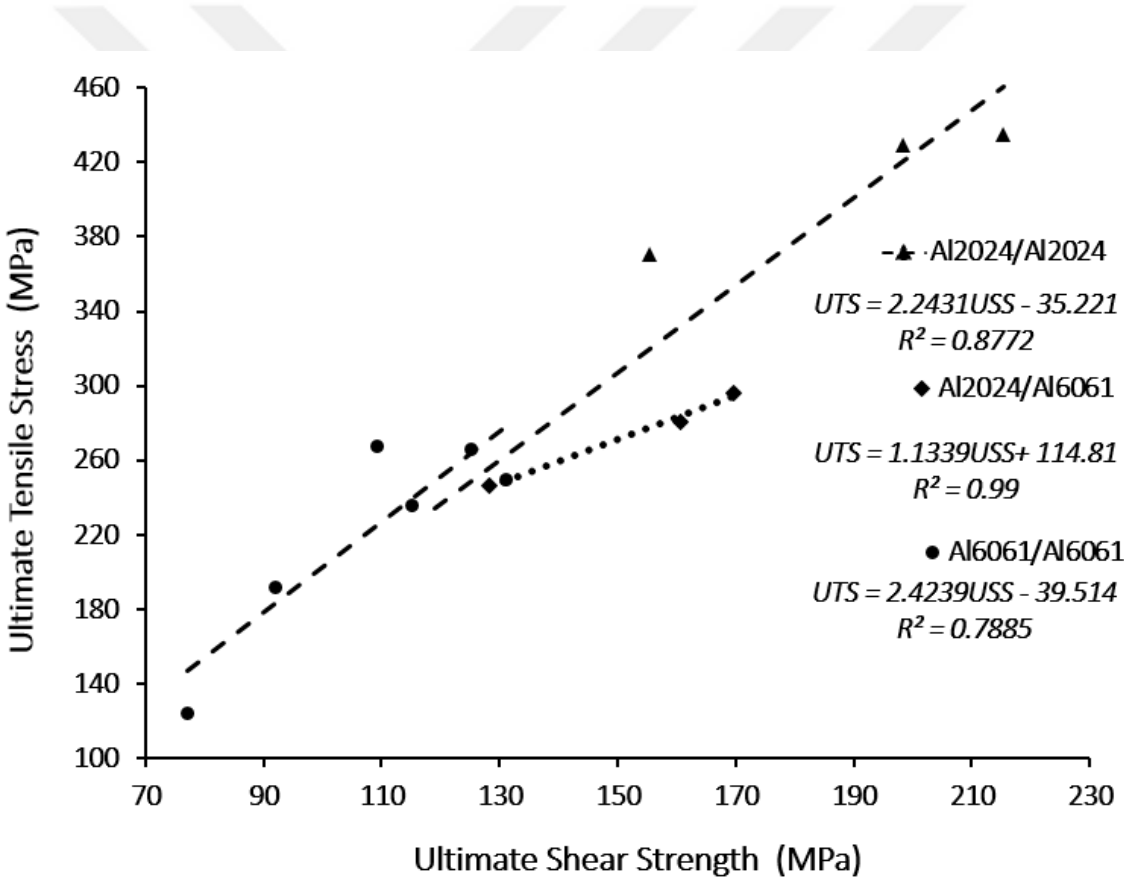


Figure 4.17: The correlation curve of USS with UTS for layered metal composites of Al2024/Al2024, Al2024/Al6061, and Al6061/Al6061 with the different ARB process.

Table 4.1 Ultimate tensile strength and ultimate shear strength of different layers of ARB product.

specimen	USF (N)	USS (MPa)	UTS (MPa)	UTS (calculated from correlation equations) (MPa)	Deviation %
As received Al6061	780	77	124	146	17.7
2 layers Al6061/Al6061	985	92.2	192	185	3.6
4 layers Al6061/Al6061	1227	115	236	253	7.2
8 layer Al6061/Al6061	1398	131	254	240	5.5
16 layer Al6061/Al6061	1334	125	266	240	9.3
32 layer Al6061/Al6061	1163	109	268	204	23.8
As received Al2024	1190	118	195	229	17.4
2 layer Al2024/Al2024	1750	160	359	325	9.4
4 layer Al2024/Al2024	2100	196	414	407	1.7
8 layer Al2024/Al2024	2250	210	430	436	1.4
2 layer Al2024/Al6061	1250	124	258	254	1.55
4 layer Al2024/Al6061	1440	143	324	276	14.8
8 layer Al2024/Al6061	1600	159	284	295	3.8
16 layer Al2024/Al6061	1680	167	302	303	0.38

4.5 Cyclic Response under Stress Control

One of the main reasons for investigating the monotonic deformation response of aluminum composites in the previous section was characterizing the parameters of cyclic mechanical testing of processed conditions. The necessity of studying the fatigue properties of layered material composite (LMC) is testing its performance under periodic loads has drawn our observation toward the “cyclic deformation response (CDR)” of these composites.

In many cases, parts of the machine are failed due to the fatigue, usually at the high-stress point (point of ‘stress concentration’) caused by cyclic stress. Failure happens abruptly as a result of the propagation of cracks without plastic deformation even when the stress level is much less than the elastic limit [144].

Until now, high cycle fatigue (HCF) behavior at room temperature has not been

considered for LCM processed by ARB technique. Therefore, the aim of this section is to examine the cyclic stability of the ARB processed aluminum alloy in different states. In this quest, CDR and microstructural evolution of four layers of similar and dissimilar composites at different stress amplitudes are presented.

4.5.1 Fatigue properties of Al6061, Al2024, and composite Al2024/Al6061 sheets after the second cycle of ARB

The fatigue life (S-N) curves of the tested samples are exhibited in Fig. 4.18a. It is obvious that fatigue life increases by reducing the applied stress amplitude for all cases. Comparison between the composite with its single material type counterparts indicates that in line with the monotonic behavior, the S-N curve of the former lies between the latter samples.

Among the tested samples, Al2024 composites display the highest fatigue strength at a given number of loading cycles, whereas Al6061 composites show the lowest. This can also be deduced from the stress-strain response depicted previously in Fig. 4.13b. The highest toughness demonstrated by Al2024 composites indicates the resistance to early necking and improved plasticity, both of which are favorable features for enhanced cyclic behavior [172]. In addition, the layer interface strength is an influential parameter dictating the fatigue strength. In this respect, the highest fatigue strength was observed in the Al2024 laminate having the highest interface strength, as indicated in Fig. 4.18b.

Regarding the Al2024/Al6061 composite, one would anticipate a different S-N response as compared to that of the single material type composites. According to the rule of mixtures Eq. (4.1), a curve exhibiting an average response is expected. However, the fatigue limit of the bi-metallic composite is slightly higher than the convenient prediction by the rule of mixtures. A similar observation was recorded for ARB processed aluminum-steel composite [175].

Especially at the low cycle regime, the composite displays noticeably higher fatigue strength pointing to a larger deviation from the rule of mixtures. In other words, at the higher stress levels, the composite demonstrates a higher number of cycles to failure. This can be explained by the strength mismatch between the layers. While the softer layers operate in the plastic regime, the harder layers deform elastically generating internal stresses between layers. Indeed, internal stresses acting against the applied stress, improve fatigue behavior [174,178]. As shown in the S-N curve, the fatigue life of composite Al6061/Al2024/Al2024/Al6061 is higher than that of composite Al2024/Al6061/Al2024/Al6061, for the same stress amplitude. The main reason of this difference is reducing the maximum stress in the outside aluminum layer attributed to the effective load transfer from the Al6061 softer layer to the Al2024 harder layer in the composite. This reduction of stress on the Al6061 surface can delay the crack initiation and improve the fatigue life of the composite with softer outside layers.

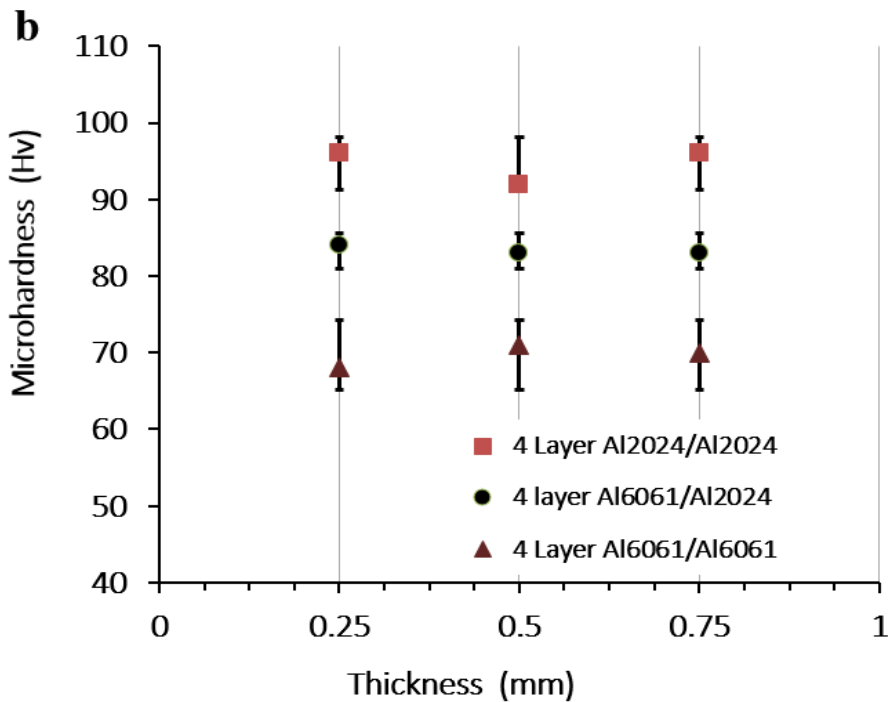
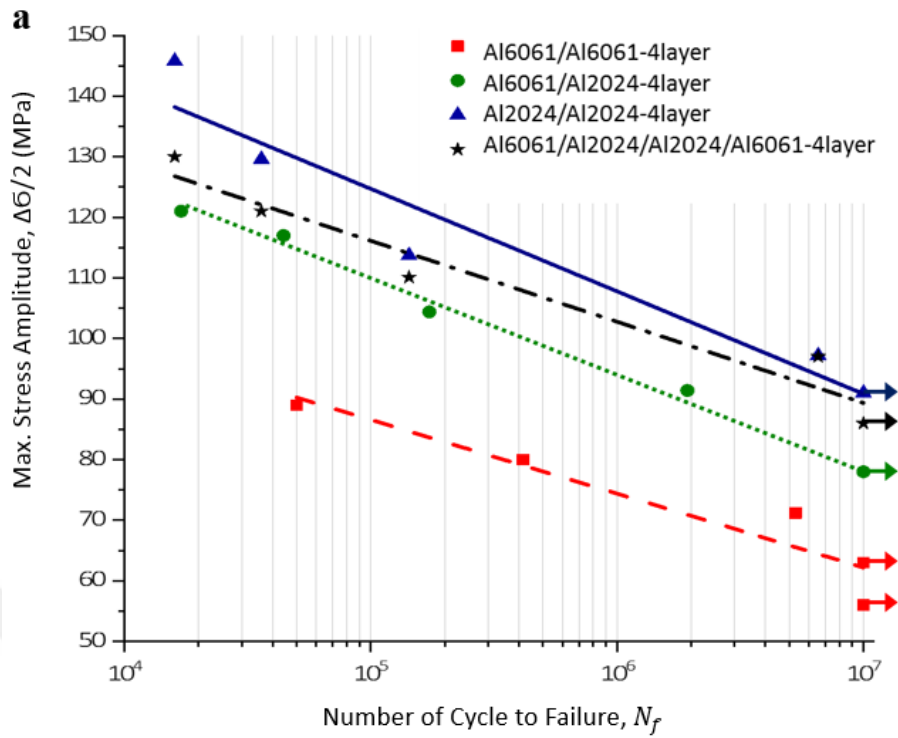


Figure 4.18: a) The stress amplitude and fatigue life (S–N curve) for composites Al2024/Al6061 four-layer composites and for base-material the Al2024 and Al6061 b) Variations of microhardness at the interface area.

4.5.2 Fracture morphology analysis of Al6061 and Al2024 sheets

Scanning electron microscopy observation was used for samples after tensile testing under strain rate of 0.01s^{-1} , for further investigation of bonding conditions and failure mechanisms in the ARB processed aluminum composites. Fig. 4.19 and Fig. 4.20 show the effects of plastic deformation on the fracture surfaces of the Al6061 and Al2024 composite after a various number of ARB cycles. The surface of all specimens presents a varying amount of dimples size and micro-voids, which confirms the occurrence of ductile fracture. Generally, ductile fractures in metals have a grey fibrous form with hemispheroidal or equiaxed dimples [180]. This type of rupture happens by the nucleation of microvoids and developed by coalescence to each other and then growth. Obviously, the shape of fracture surfaces for dimples strongly depends on the stress condition. Therefore, the dimples are elongated with the line of action for the shear stress [162,179]. The primary material appears to exhibit a common ductile fracture, where the deep dimples and the outer shear zones are determined (Fig. 4.19b and 4.20b). Al6061 before rolling offered deeper and larger dimples compared with the Al2024, indicated that Al6061 is softer and more ductile. After the first ARB process, the sample showed a ductile fracture, with dimples and shear zones, but the size of the dimples decreased, for both composite Al6061/Al6061 and Al2024/Al2024 Fig 4.19c and 4. 20c respectively. It can be observed that the size of the dimple relatively reduced with increasing the number of ARB cycles. Fig. 4. 19d and 4. 20d depict SEM micrographs of the fracture surface after three cycles include the shallows and small dimples which could be classified as shear dimples. This reduction in dimple size can be attributed to the enhancement of the grain refinement due to the work hardening [180].

Also, the difference between the size of the dimple in the composite fracture surfaces for Al606 / Al6061, and Al2024 / Al2024 is noticeable which Al6061/Al6061 had a larger dimple size in all conditions. As a result, the fracture mechanism was a shear ductile rupture represented by shallow and small elongated shear dimples.

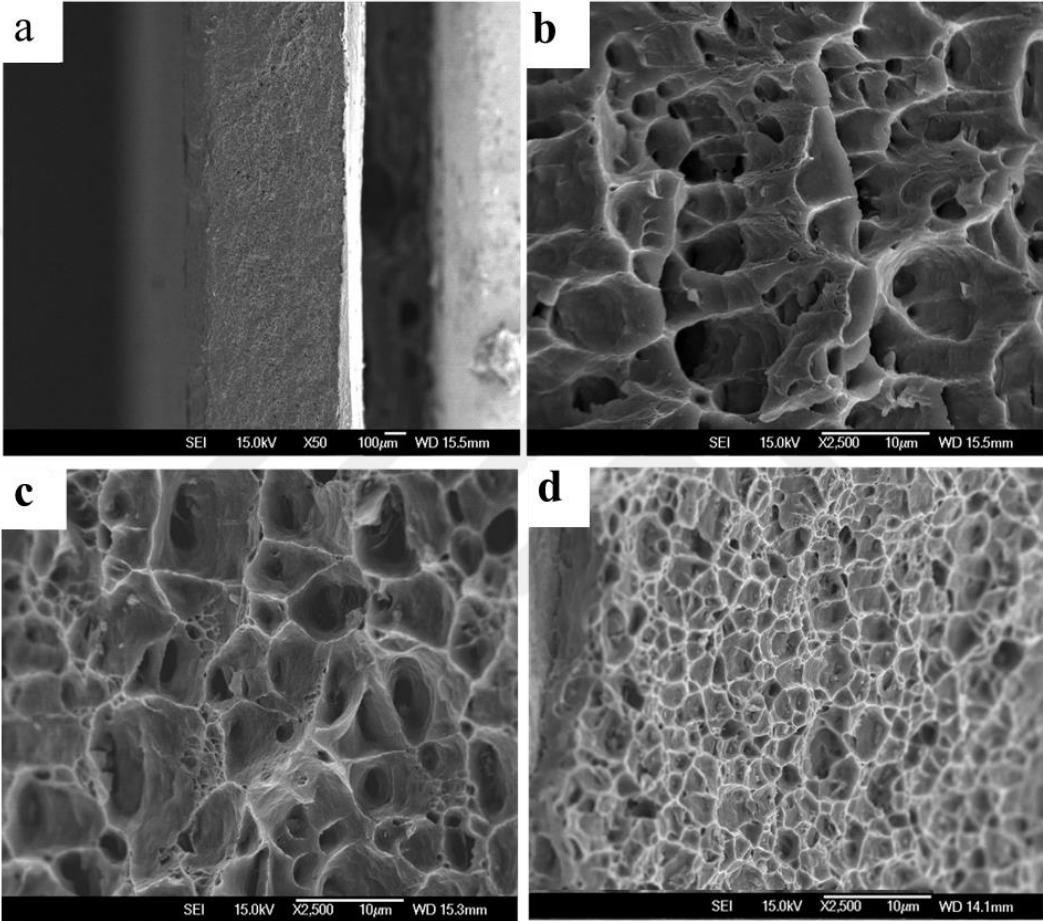


Figure 4.19: Fracture surface of the specimen after the tensile test under strain rate of $0.001s^{-1}$ at room temperature for Al6061 at different conditions of a) and b) as-received, c) after one cycle (2 layers), and d) after three cycles (8layers).

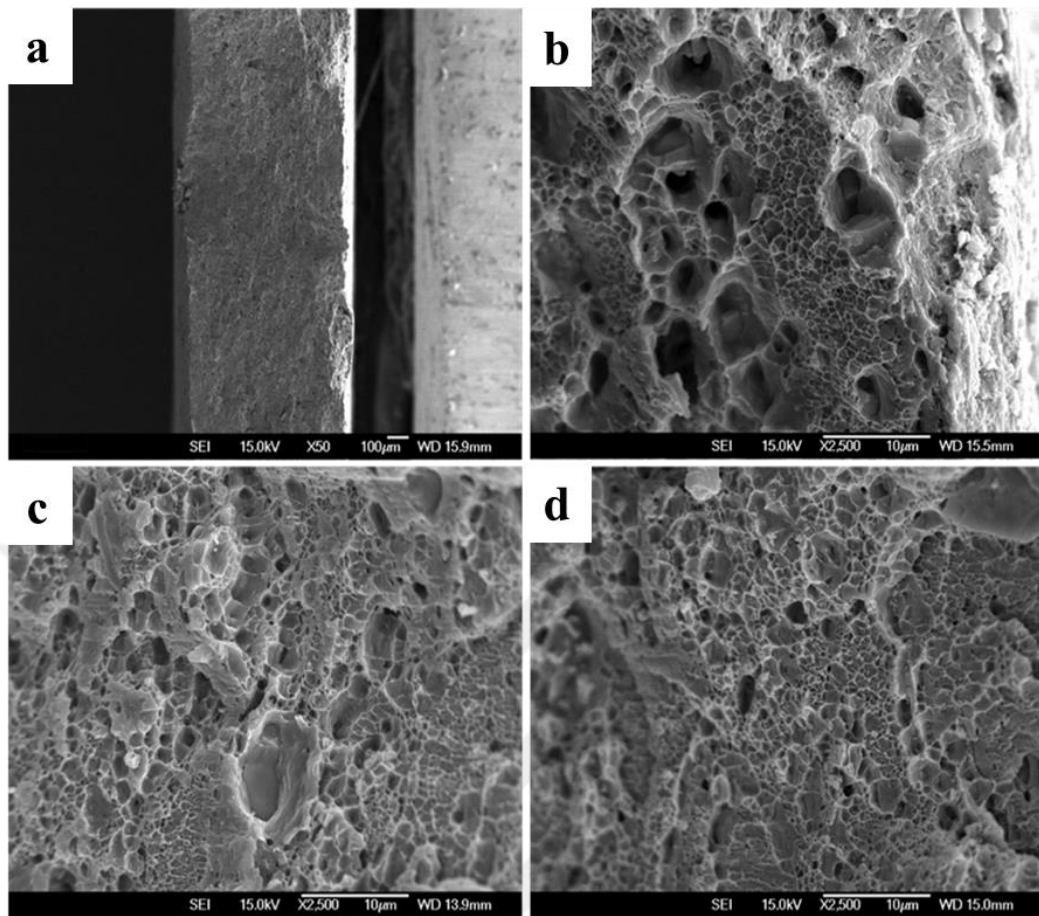


Figure 4.20: Fracture surface of the specimens tested at room temperature under the strain rate of 0.001s^{-1} for Al 2024 at different conditions of a) and b) as-received with different magnification c) after one cycle (2 layers), d) after two cycles (4layers).

4.5.3 Fracture morphology analysis of Al2024/Al6061 dissimilar composites

Fig. 4.21 shows the fracture appearance in the interlayer region after failure under tensile strain. Generally, in multiple passes ARB, the interface of the previous pass bonds strongly during the next cycle, due to increased atomic diffusion and high pressure with further processing. However, weak interface spots are suitable for crack initiation and propagation [67,78,97,181]. The fracture in the interface region of Al2024/Al6061 composite after the second ARB pass displayed deep and visible delamination at the interface area, as shown in Fig. 4.22a. The delamination, which appeared after the second and the third cycles, became

shallow and discontinuous, but still visible compared with that after the first ARB cycle. The interface between the initial layers began to disappear after the third ARB cycle, as shown in Fig. 4.22b. Other works also indicated that the interface area that was formed at the first pass became mostly obscure after several passes of ARB [78,182].

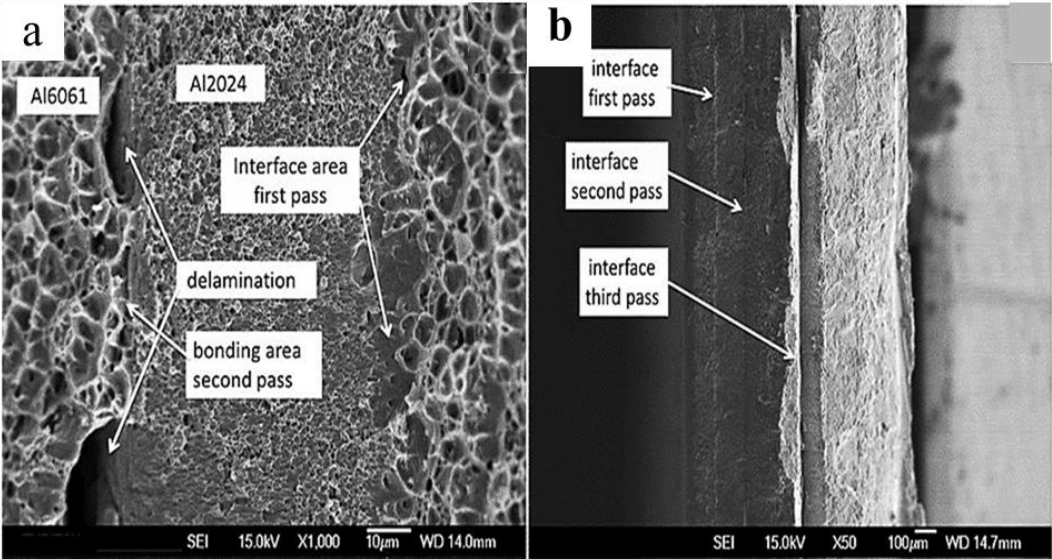


Figure 4.21: SEM images of the fracture surface of the layer metal composite a) after the second cycle, b) after the third cycle of the ARB process.

Fracture surface investigations also revealed information regarding failure characteristics. The as-received samples, as explained previously, showed a ductile fracture, as depicted by the deep dimples in Figs. 4.22a and 4.22d. The fracture surfaces exhibited microvoids, which had equiaxed or ellipsoid dimple shapes depending on the stress condition [162].

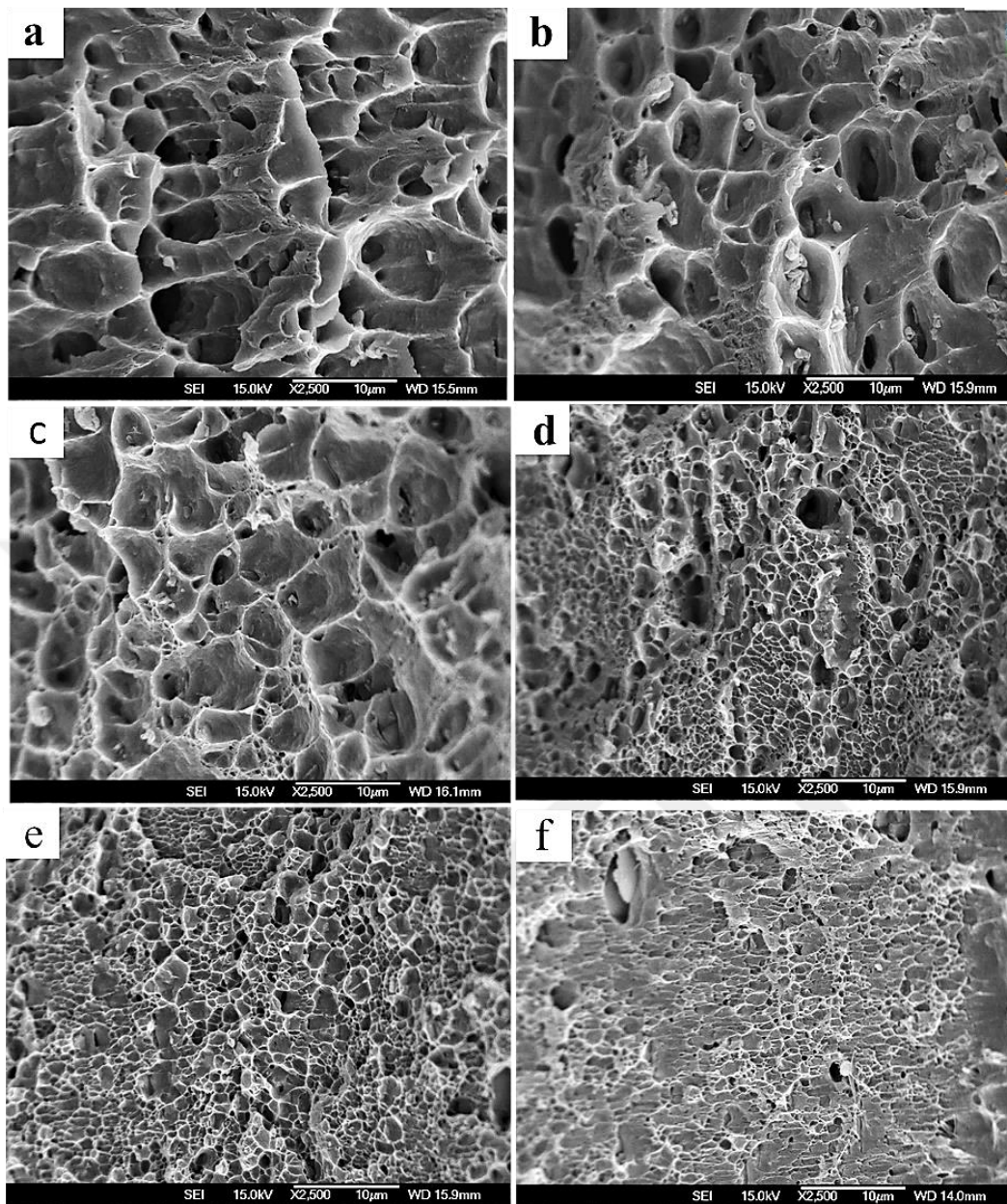


Figure 4.22: SEM images of the fracture surface from the Al6061 alloys, a) as-received, b) after one cycle, c) after four cycles of ARB, and from the Al2024 alloy, d) as-received, e) after one cycle, f) after four cycles of ARB.

Typically, fracture commences with the microvoid formation leading to subsequent growth and rupture. The first ARB pass imposes a moderate strain, and both materials showed a ductile fracture, with dimples and shear zones as shown in Figs. 4.22b and 4.22e. With increased cycle number, the fracture mode remained as ductile with the existence of shear

rupture and dimples. Nonetheless, these dimples were shallow and elongated, especially for the Al2024 layers as compared to those observed in Al6061.

4.5.4 Fracture morphology analysis after the fatigue test

SEM studies were performed to investigate the effect of ARB processing on the fracture behavior of the aluminum composite during cyclic loading. The SEM micrographs of ARBed aluminum composite, followed by HCF experiments at different layer architecture shown in Figs. 4.23a, b, 4.24a, and b. SEM micrographs were captured near the region of the crack initiation and along the propagation zone of the cracks for the fatigued samples. The surface of the fracture was observed, including the point of crack initiation at each of the layered composite. Generally, the crack initiation in the outer layers of composites due to the concentration of plastic deformation as a result of higher stresses, which is higher near to and at the surface [183].

Moreover, the microscopic stress concentrators like micro-grooves caused by surface step generated by dislocations, machining, and the second phase of the particles, which are active even under states of ideal uniaxial loading. Both of which create the highest stress on the surface and possibility to crack initiation in the outer layer. In addition, the surface grains have a fewer adjacent grain compared to internal grains, so the constraint is comfortable. In less restrictive surface grains, single slip accommodated faster than in strongly restrained bulk grains, where multiple slips may be more necessary [184].

Fig. 4.24a. a illustrates the crack initiation of Al6061/Al6061 sheet from the outer layer; the same behavior can be observed in other composite layers of Al202/Al2024 and Al2024/Al6061. The variation in the fatigue life of the layered composites for different layer

architecture in similar stress amplitudes is directly related to the cracking behavior (initiation and direction of crack propagation) in the layer of the samples.

The sequence of the layers in dissimilar layered composites is one of the most critical parameters which is affecting the fatigue failure. Inspection of fracture surfaces in Fig. 4.24a revealed that the difference between the hardness of the Al2024 and Al6061 caused to debonding between the layers, and this gap could be a potential region for crack initiation and propagation [154]. On the contrary, Fig. 4.24b shows a better bonding between the similar Al2024 layers in the centre of the composite.

The direction of crack propagation is a straight line with the angle of about 45 concerning the load direction. Furthermore, the cracks propagated in an uninterrupted route in relation to the lack of delamination and softer layers in the inner sections (Fig. 4.25a). But as shown in Fig. 4.25b, Al2024 layers were failed individually after the fatigue test. The cracks were initiated at both surfaces and debonding of the interface caused the propagation of the cracks separately [149].

On the other hand, Fig. 4.25c demonstrates that the direction of cracks started from the soft layer of Al6061 was changed after propagating to the hard layer of Al2024 while on the opposite side when it comes from the hard layer to the soft layer, the direction of crack propagation was not affected by the Al6061. The same method of crack propagation was found in Fig. 4.25d.

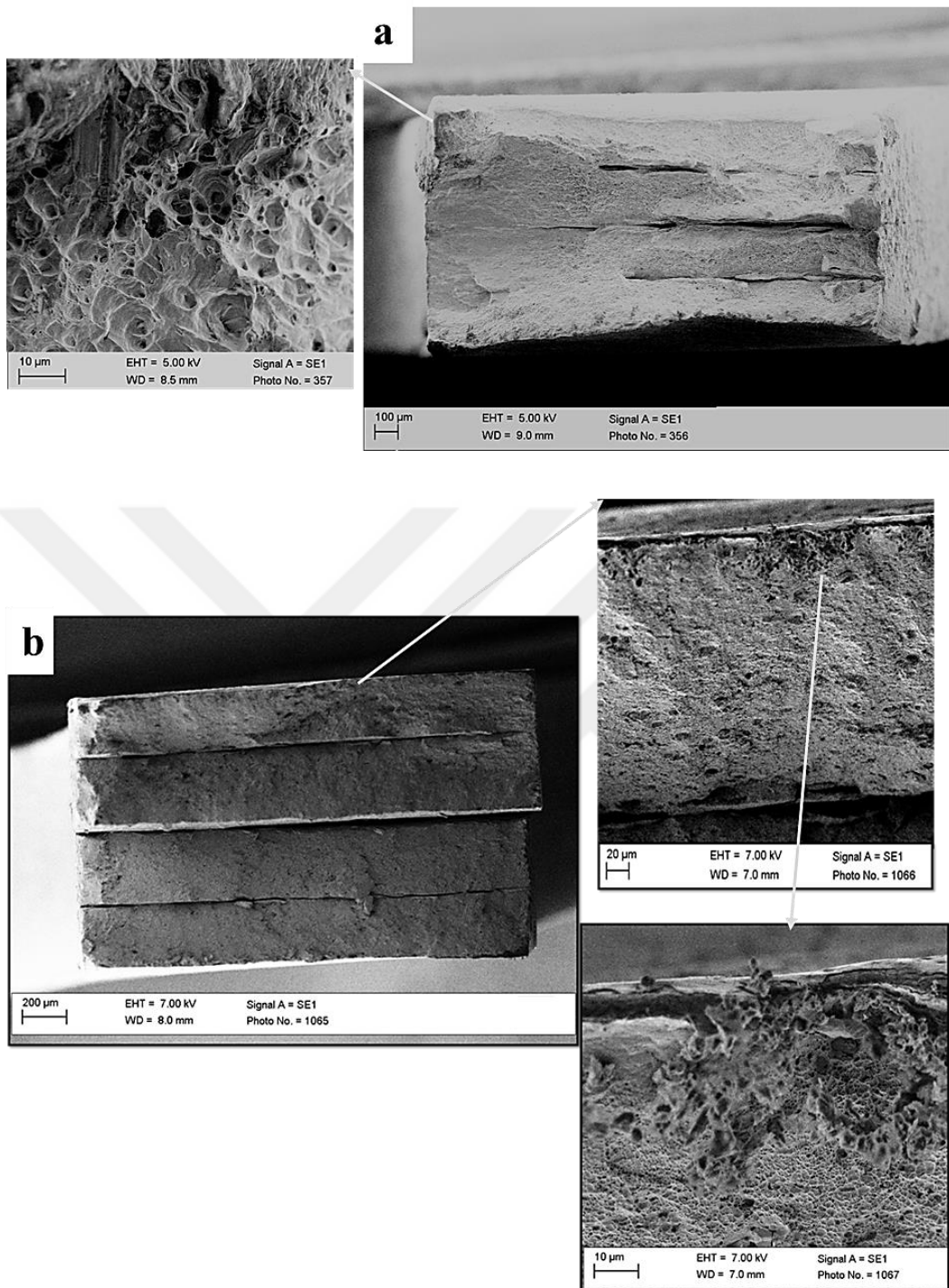


Figure 4.23: SEM observations of fatigue damage at the surface close to the crack zone for 4layers of a) Al6061/Al6061 layered composite, b) Al2024/Al2024 layered composite.

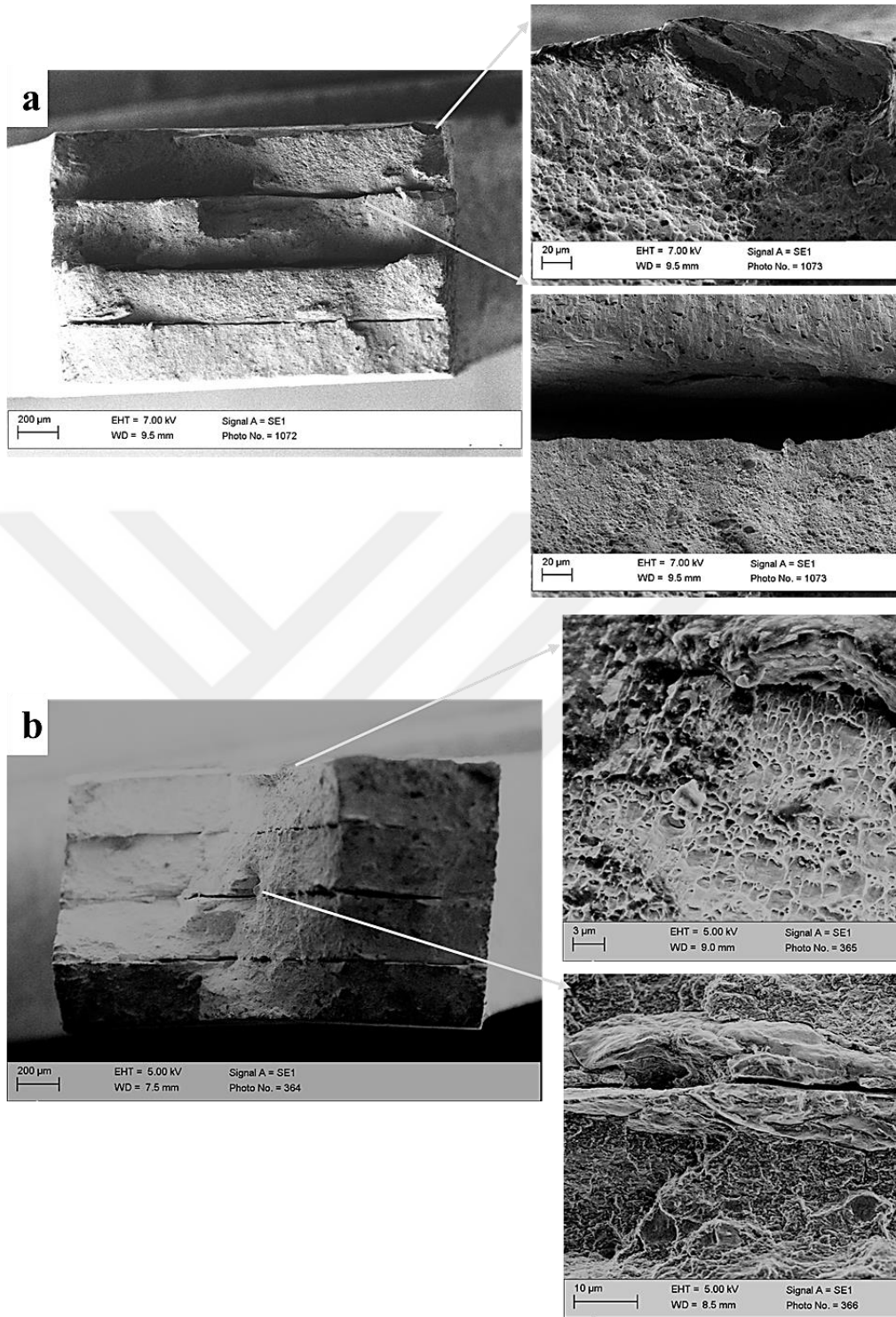


Figure 4.24: SEM observations of fatigue damage at the surface close to the crack zone for 4 layers of a) Al6061/Al202/Al6061/Al2024 composite, b) Al6061/Al2024/Al2024/Al6061 composite

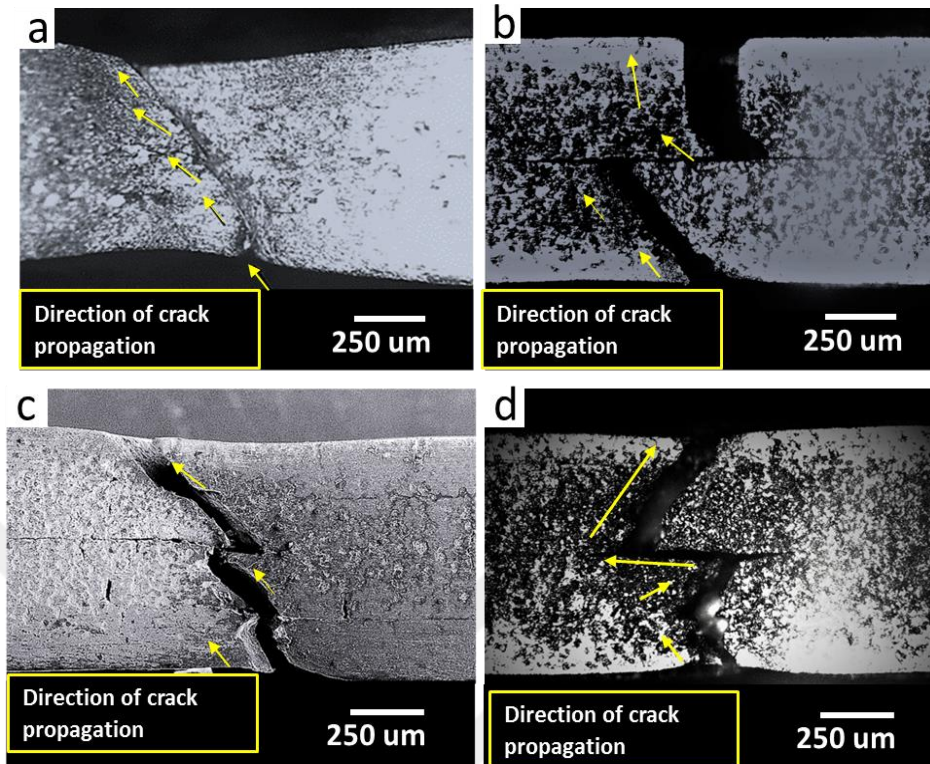


Figure 4.25: Optical microscopy (OM) of crack growth paths of the four layers a) Al6061/Al6061 composite b) Al2024/Al2024, c) Al6061/Al2024/Al6061/Al2024 and d) Al6061/Al2024/Al2024/Al6061.

4.5.5 Fracture morphology analysis after SPT

Scanning electron microscopy was employed to examine the features of the shear-failure surfaces of the punched-out SPT disks. Fig. 4.26 shows the sheared surfaces after the shear punch test for Al/6061/Al6061 and Al2024/Al2024 aluminum composite strips after two cycles ARB. The curved shape of the outer surface for Al6061 shows that the failure of this composite was more ductile compared with the Al2024 which has a flat surface (Fig. 4.26a and b). Visibly, the Al6061/Al6061 presented a rough morphology similar to a ductile fracture with dimple shear lines, and also the shear flattened surfaces. This type of SPT failure, generally, occurs as a result of microvoid formation. The orientation of the dimples reveals the direction of shear

extension. During the SPT process, the outer layers, (i.e., close to the die) under maximum tension strength, and the surface near the punch is under the compression stress, therefore, be broken before the inner layers Fig. 4.26c. Shear elongation is more dependent on the soft Al layer (Al6061) than on the harder Al layer (Al2024) in the composite.

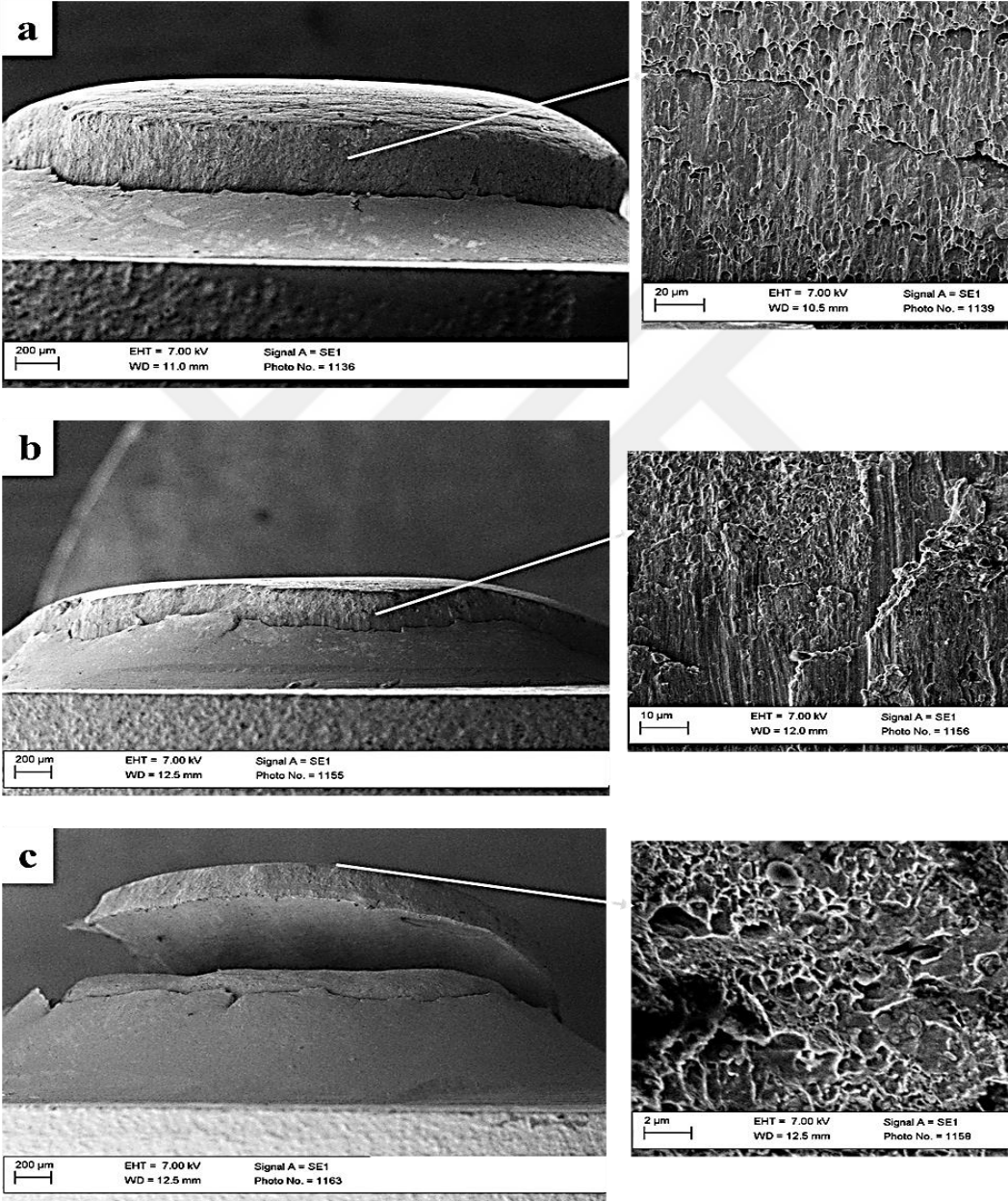


Figure 4.26: SEM micrographs of shear-failure surfaces of 4layers for a) Al6061/A6061, b) Al2024/Al2024, and c) Al2024/Al6061.

CHAPTER V

RESULTS AND DISCUSSIONS – MICROSTRUCTURE AND MECHANICAL PROPERTIES OF ARB PROCESSED ALUMINUM AND STEEL COMPOSITES

5.1 Overview

In the current chapter, mechanical properties of the aluminum/ IF steel composites fabricated via the ARB process were investigated using different layer architectures. The first cycle (N1) Al sheet was riveted with an IF steel sheet and then rolled to fabricate base compounds of Al/IF steel. In the second cycle, three different sets of layered metal compounds were produced. The stacking sequence and the final layer architecture of the composites are schematically shown in Fig. 5.1. The different arrangements of sheets were classified as group A, B, and C including dissimilar composites of Al2024, Al6061 and IF steel. The multilayer composites include two different alloys were located in various manners such as the conditions listed below:

1. The hard layers inside and soft layers outside of the composite.
2. The soft layers inside and hard layers outside of the composite.
3. Mixed stacking sequence of the soft and hard layers.

The tensile and microhardness test, as well as optical microscopy observation were used to investigate the mechanical properties for the Al/IF steel composite after the different number of ARB passes.

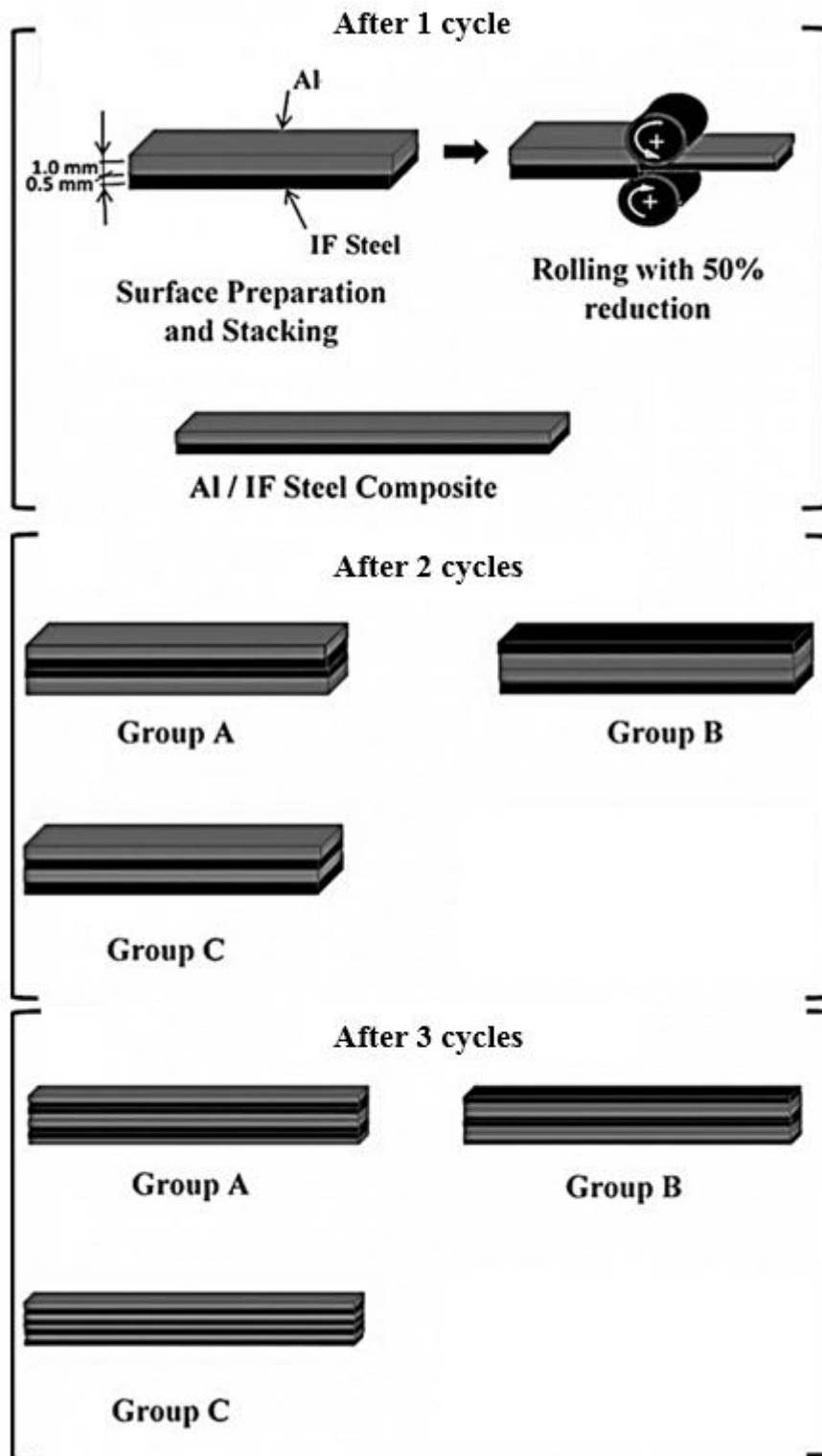


Figure 5.1: A schematic illustration of the fabricating sequence of IF steel/Al composites.

5.2 Microstructure of ARBed composites

According to the literature [106,152,153] when the hard and soft layers have an equal thickness, the continuity of the sheets maintain until several cycles of ARB, although some irregularities form at the interfaces and thickness variation occurs between the layers. Therefore, in the current work, the initial thickness of the steel (hard) layers is less than the thickness of the aluminum (soft) layers.

This section is divided into two different subsections, which explain the microstructure observation of composites produced from the Al6061 and Al2024 with IF steel separately and also composites fabricated from three different layers of Al2024, Al6061 and IF steel.

5.2.1 Microstructure of ARBed Al6061/IF steel and Al2024/IF steel composites

Fig. 5.2 and Fig. 5.3 show the grain structure of as-received and after one ARB-cycles observed by OM. The initial condition (0 cycles) represents a homogeneously distributed equiaxed grain for all materials of the composites (Al6061, Al2024 and IF steel). After one pass, the grains in both IF steel and Al layers are elongated along the RD such that the typical grain structure appears like a pancake. The lamellar grain structure detected in both materials, which develops considerably faster in the IF steel layers than in the Al ones, if it compared to the initial grain size. The reduction of thickness in some grains for IF steel layer after two cycles ARB is remarkable due to the fragmentation of the elongated grains in the rolling process. While even after two cycles there is a lot of coarse grains inside the structure of IF steel [185]. The new micro-grains have been introduced during the ARB process due to dynamic recrystallization and were formed at the boundaries of the original grains [186].

On the other hand, the grain structure of Al 6061 and Al 2024 has similar behavior as in the multilayer of similar and dissimilar layered material, which was discussed in the previous chapter. It is also observed that Although the grains are elongated remarkably after the first cycles for Al2024, still it is not as much as IF steel (Fig. 5.2d and Fig. 5.3d). The fine grain fraction increases with the ARB process due to the accumulated rolling stress level [185].

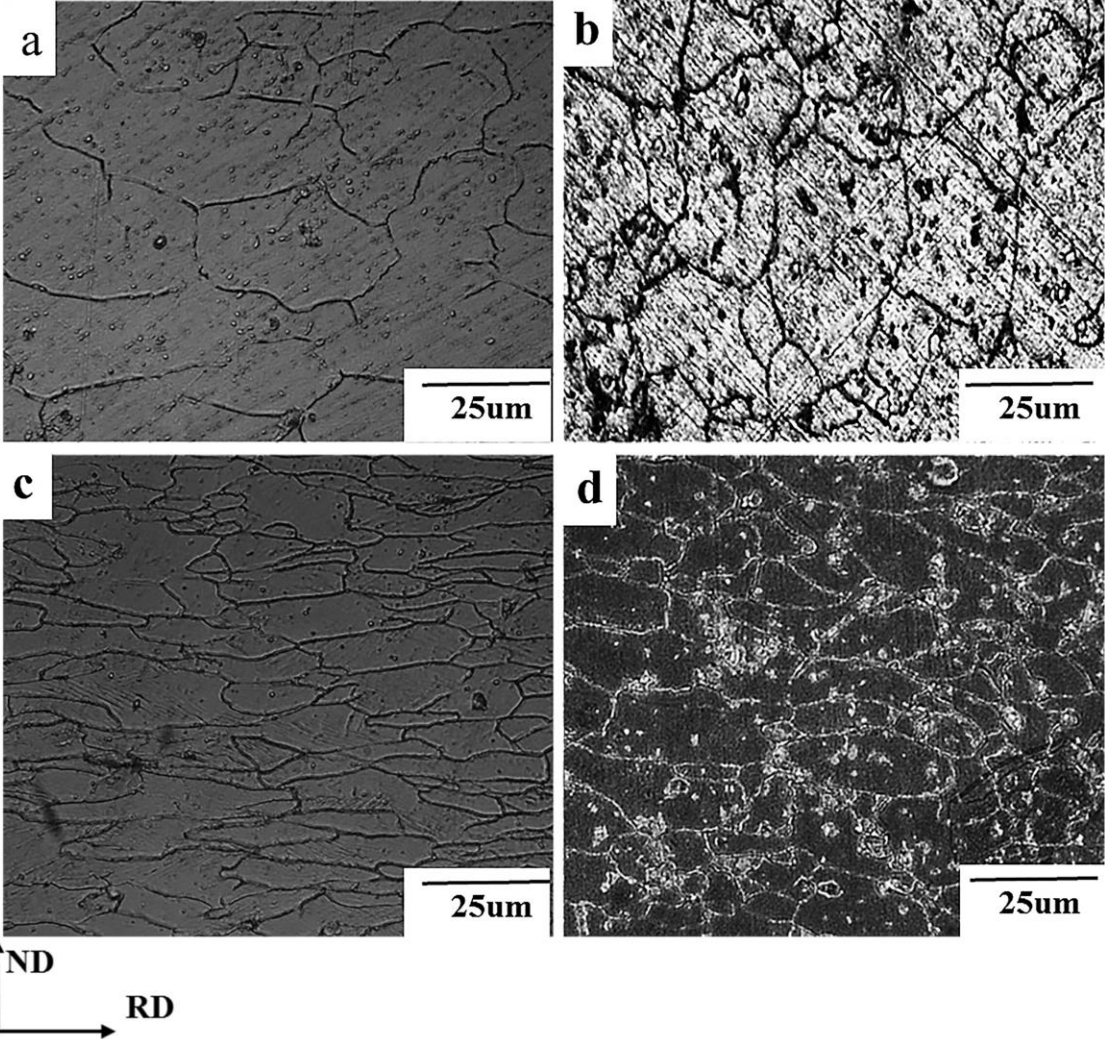


Figure 5.2: Optical micrographs of a) IF steel as received, b) Al6061 as received, c) IF steel after one ARB cycles, and d) Al6061 after one ARB cycles.

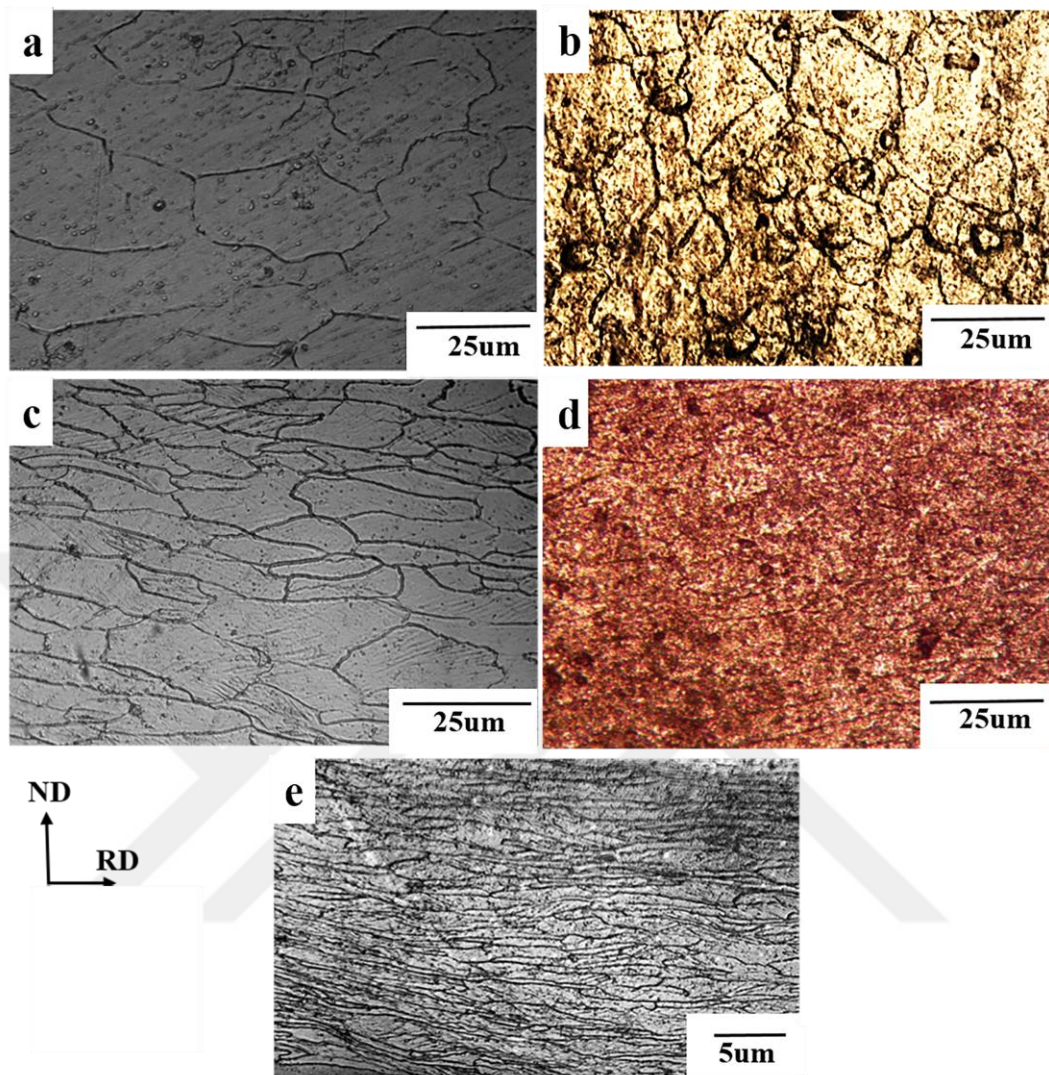


Figure 5.3: Optical micrographs of a) as received IF steel, b) as received Al2024, c) IF steel after one ARB cycle, d) Al2024 after one ARB cycle, and e) IF steel after two ARB cycles.

During the rolling process, high friction between the plates and the roll is expected to result in an inhomogeneous distribution of the grains throughout the thickness. This leads to a significant difference in microhardness between the one and two passes rolled aluminum and IF steel layers.

Fig. 5.4 demonstrates the progression of individual layer shapes and the interaction between the hard layer of IF steel and soft layers of Al6061 in the RD direction during the ARB

cycles. The perfect interfacial bonding between dissimilar layers of IF steel and Al6061 were introduced by ARB for both groups of composites after the second cycle (N2) without any necking. After the third cycle, the wavy shape layers were formed, and the hard layers necking commenced. Moreover, Fig. 5.4 shows the occurrence of necking and fragmentation of IF steel layers observed after N4 and N5. Fragmentation and diffusion of IF steel layers after the third cycle led to the remodeling of the combined structure from a layered metal composite to a particle-reinforced composite [106]. The aforementioned behavior may change the mechanical properties of the composites, and completely different tensile behavior can be observed after this stage of the ARB process [106]. Generally, the origin of necking and subsequent local fracture of the hard phase during the ARB process is different flow properties of the composite layers. Here, as it is shown in Fig 5.4. for group A, the Al6061 acted as an interface layer to transfer the load to the surface of IF steel layers and filled up the spaces between the fragmented part of these layers [187]. The transfer medium role of Al6061 formed a homogenized distribution of IF particles inside of the composite in group A, compared with the distribution of IF steel in group B.

On the other hand, the mixed sequence of Al6061 and IF steel in the layered composite of group C leads to an increase in the flow tendency of Al6061 into the IF steel layer. Therefore the necking and fracture of IF steel parts started and propagated a lot faster than group A and B. As shown in Fig. 5.4, after three cycles the IF steel layer initiated to the neck and fractured and consequently in fourth and fifth passes relatively homogenize the distribution of fragmented IF steel particles can be seen in the Al6061 matrix.

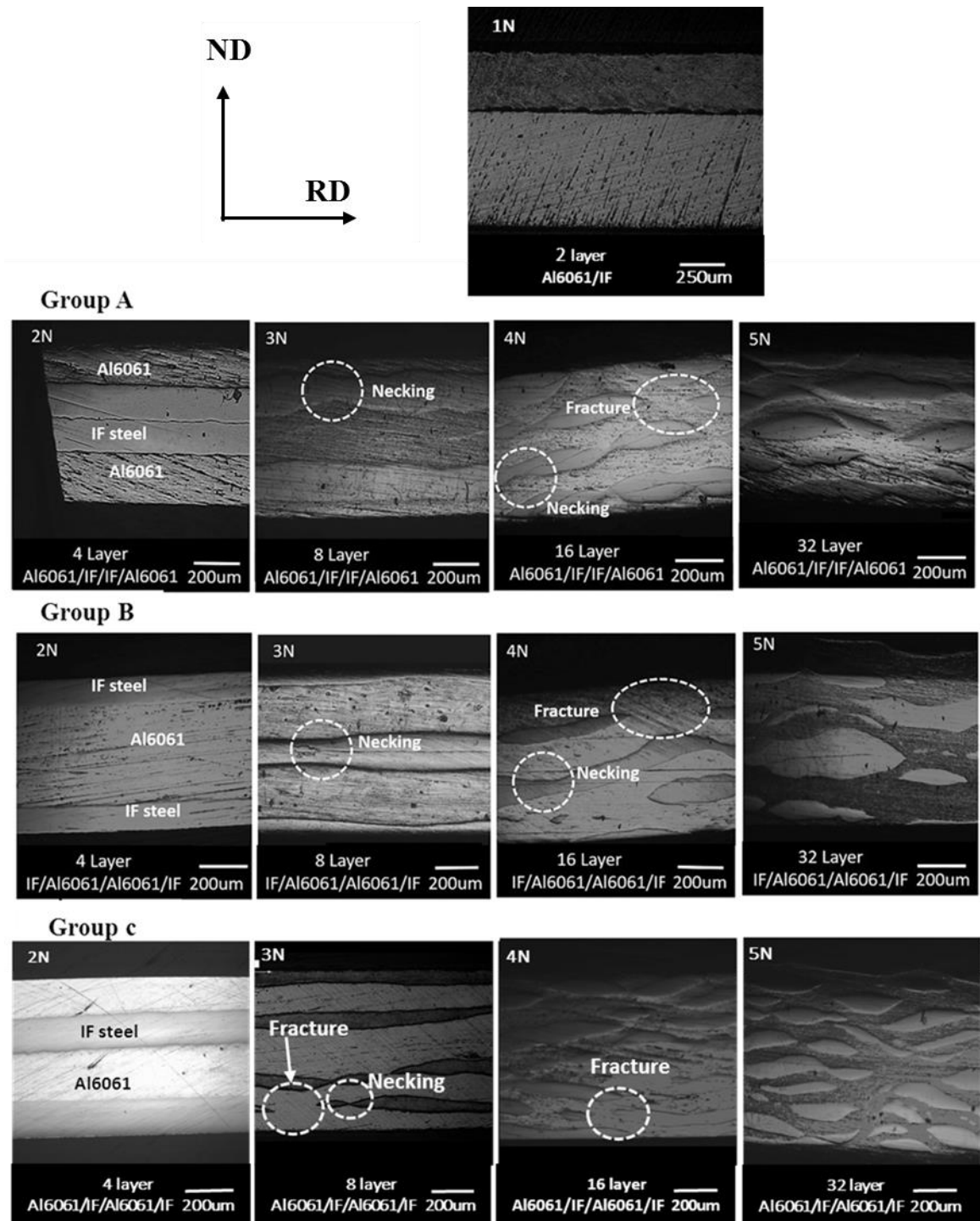


Figure 5.4: The layer shapes of multilayer Al6061/IF steel composite after one, two, three, four, and five cycles ARB.

In multilayer dissimilar metal composites, the primary strengths and the strain hardening properties of the two component metals are not identical [188]. This difference in properties appears in the form of reducing the thickness of two layers, especially in the initial stages of the ARB process. The hard layers have a lower reduction in thickness than the softer layers. Moreover, the deformation comes to be inhomogeneous for the hard layer. After several times of the ARB, the less hard alloy is deployed to fill the necking areas of the hardened alloy. As a result of this deformation, the interface area becomes unstable and resembles a wave shape.

As explained above, the difference in mechanical properties is the main reason of the necking and fragmentation in the composite. However, the difference between the hardness of the Al2024 and IF steel is a lot lower than the difference between the hardness of the soft Al6061 and IF steel, therefore deformation and fragmentation of the IF steel hard layer is more difficult. As shown in Fig. 5.5, the continuity of the layers after the third and fourth passes has still remained, and it is well agreed with the results of the other works [113].

The best condition of layer architecture for occurrence of necking and fragmentation of hard layer is a mixed stacking sequence, which is shown in group C. It can be observed that some parts in group C started to neck and fracture after four cycles ARB, while the major regions of the composite were still in a flat shape mode.

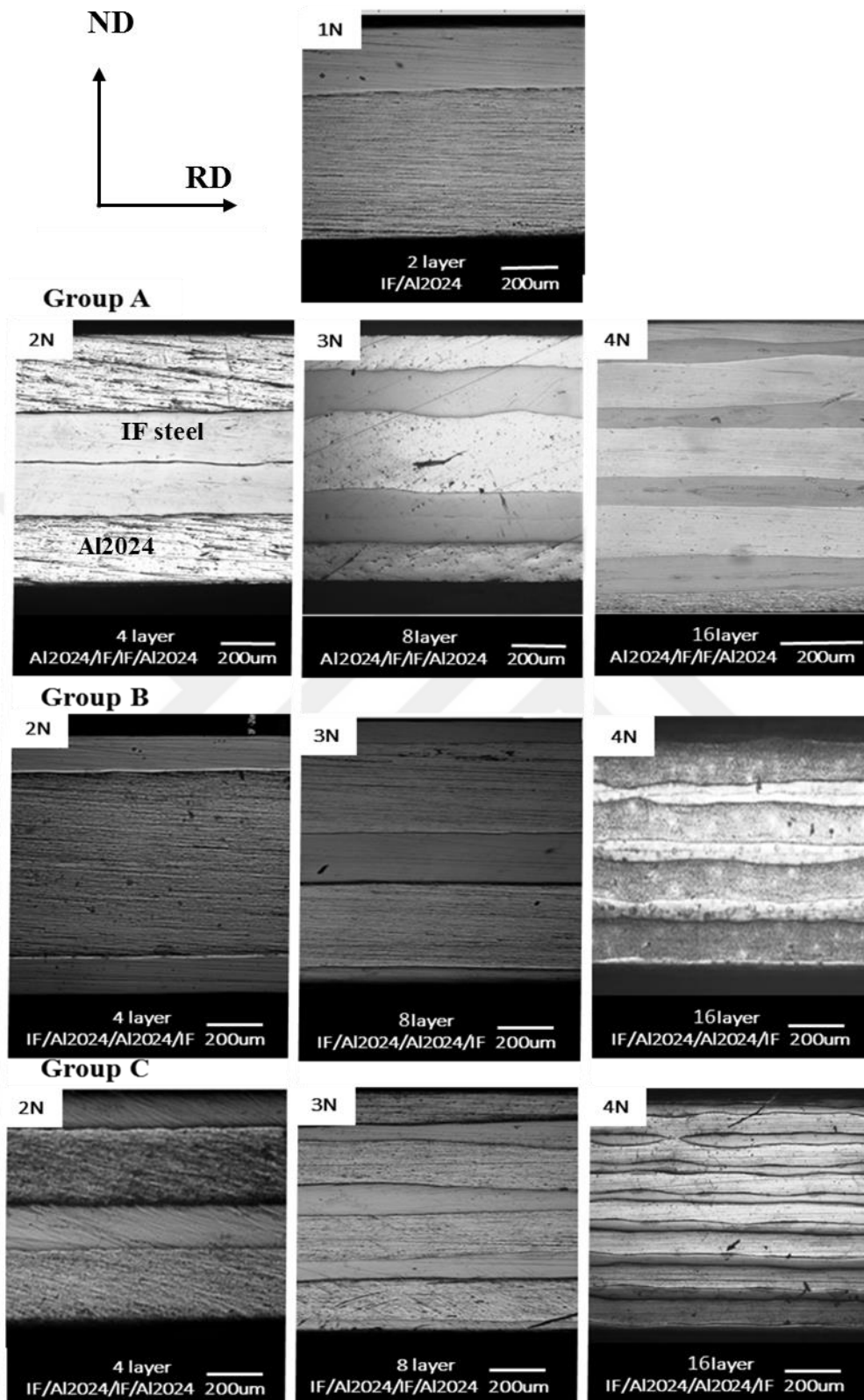


Figure 5.5: The layer shapes of multilayer Al2024/IF steel composite after one, two, three, and four cycles ARB.

5.2.2 Microstructure of ARBed dissimilar layered aluminum with IF steel composites

Fig. 5.6 demonstrates the optical microstructure of the IF steel/Al2024 and IF steel/Al6061 composite samples after one and two ARB cycles. All OM was captured in the RD-ND direction near the center of the interface.

By repeating the process of rolling over and over again, the process can be continued, but based on the results of preliminary works the mixed layer architecture, the crack initiation was started after the third pass and also the best mechanical properties were achieved after the second pass with four layers. Thus, in this section, just the composite with four layers was observed and analyzed. Similar to the previous cases, the elongated grains were observed in all parts of this composite after the second pass of the ARB process. Also, the perfect bonding between the Al6061, Al2024, and IF steel layer was achieved after the second pass. The grain refinement of the regions near the interface of the Al6061 and IF steel and also, Al2024 and IF steel was notably higher than the central parts due to the redundant shear strain which is introduced in the material [189–191].

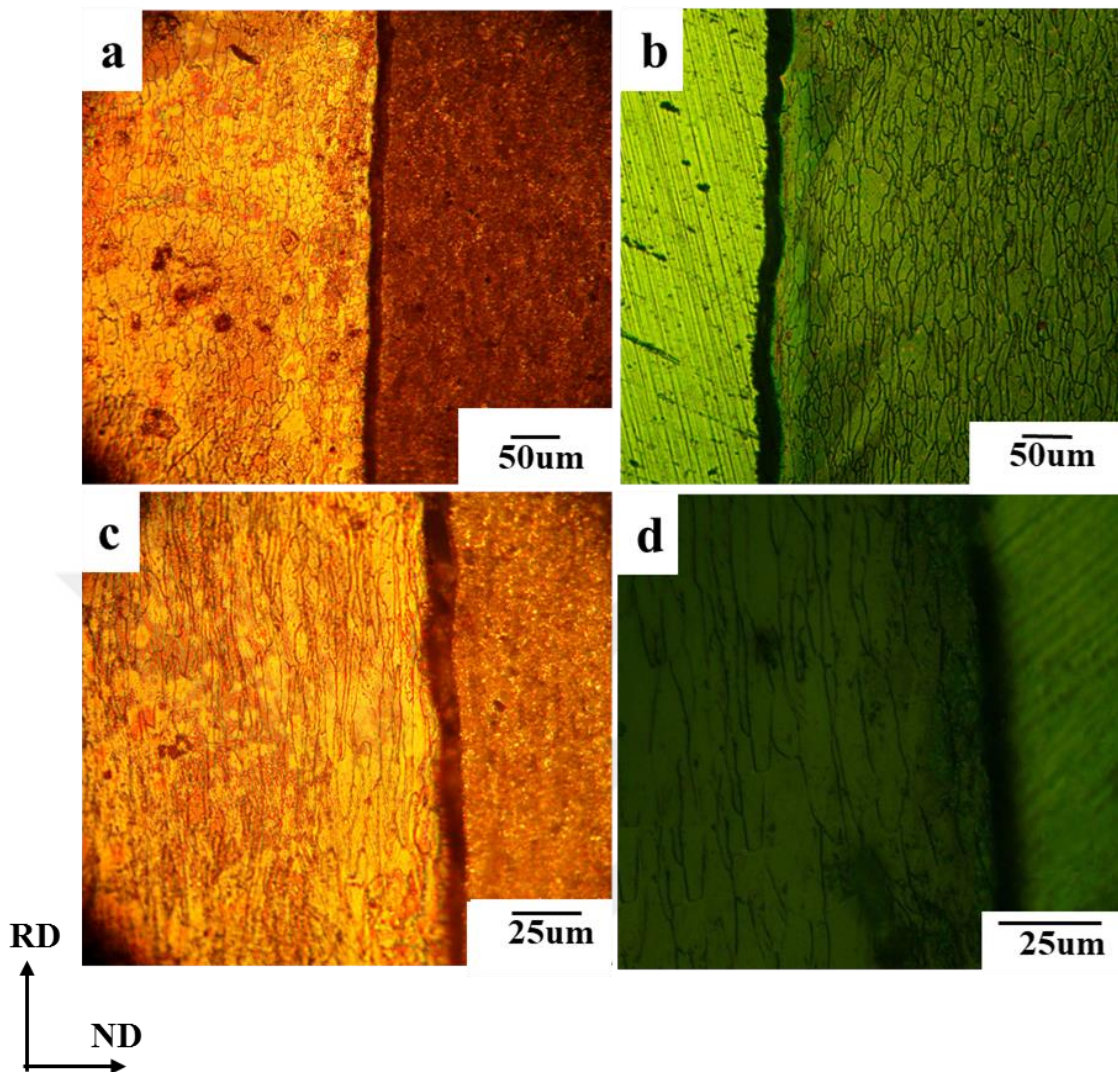


Figure 5.6: Optical micrographs of composite in the a) IF steel/Al2024 side after one cycle, b) IF steel/Al6061 side, after one cycle, c) IF steel/Al2024 side after the second cycle, d) IF steel/Al6061 side after the second cycle.

5.3 Mechanical properties of Al6061/IF and Al2024/IF

5.3.1 Microhardness

The Vickers microhardness of Al6061/IF composites ARBed sheet are presented in Fig. 5.7 with respect to the number of cycles. In all groups, a harsh enhancement was observed in the hardness after the initial stage (first cycle) due to the strain hardening and increasing the

density of dislocations and interaction between them during the rolling process. Afterward, the slope of hardness improvement decreased in relation to changing the hardening mechanism from the strain hardening of dislocations to the grain refinement in the next cycles of ARB [161]. The saturation state was achieved at high strains, which was previously observed in the other UFG materials fabricated by SPD methods [79,162,163]. This phenomenon is related to the fact that after a few ARB cycles, the density of dislocations reaches a steady state. Moreover, Fig. 5.7 illustrates that the hardness enhancements of the outer layers for each group of A and B occurs faster than the inner layers for either IF steel or Al6061 in the composite. This hardness improvement is related to the strain hardening due to high redundant shear strain induced by the friction between the metal sheets and roll surface in the ARB process.

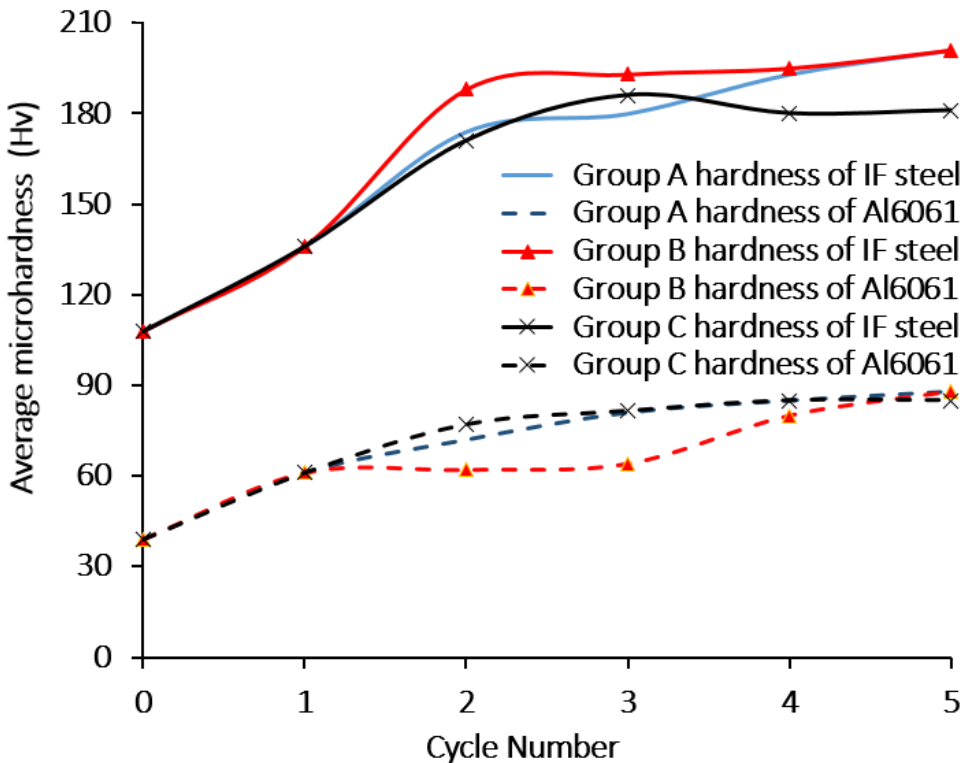


Figure 5.7: Variation of microhardness with the number of ARB cycles for group A (Al6061/IF/IF/Al6061), group B (IF/Al6061/Al6061/IF) and group C (IF/Al6061/IF/Al6061).

Also, Fig. 5.8 shows the microhardness of the Al2024/IF steel composites after different cycles of the ARB process. The same behavior was observed for the Al2024/IF steel which the hardness was sharply increased after the first cycle, and then the slope of enhancement was decreased till the steady-state region after the fourth pass.

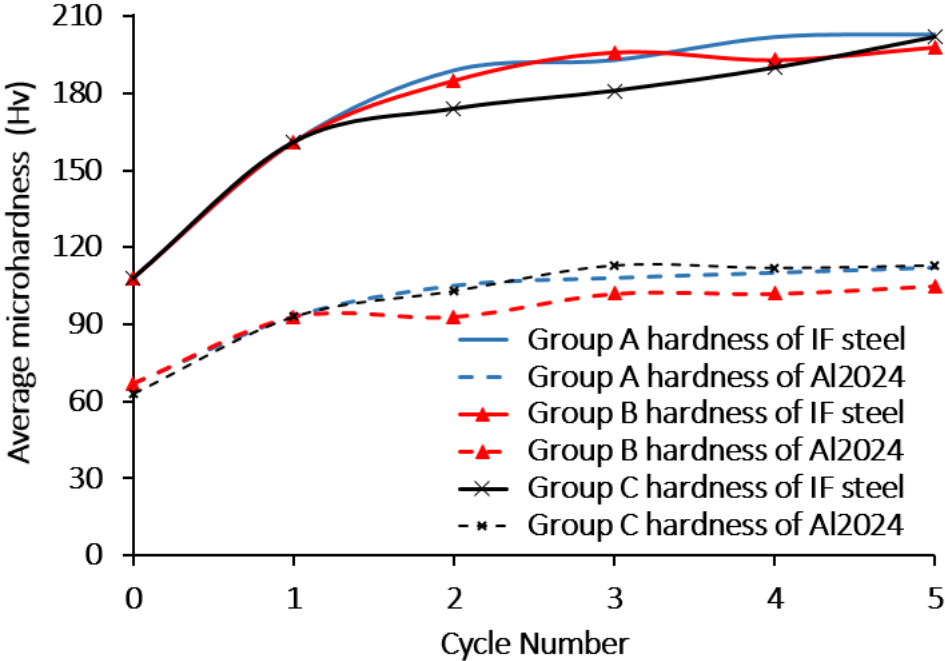


Figure 5.8: Variation of microhardness with the number of ARB cycle group A, Al2024/IF/IF/Al2024, group B IF/Al2024/Al2024/IF and group C Al2024/IF/Al2024/IF.

5.3.2 Tensile behavior

The monotonic mechanical properties of the Al/IF steel composites were investigated using the tensile test at ambient temperature under the quasi-static strain rate of 10^{-3} s^{-1} . Fig. 5.9 illustrates the effect of ARB cycles on the tensile behavior of each group of processed materials. It was found that both yield and ultimate tensile strength (UTS) of the IF/Al composites increased noticeably, with the expense of decreasing ductility for all groups. The enhancement of strength is attributed to the high density of dislocations after the first and

second cycle of ARB due to the strain hardening, contributed to the grain refinement with the formation of micro subgrains during the later cycles.

The resultant UTS values after N3 were ~ 440MPa and 380MPa for group B and C respectively, which was greater than that of group A ~345MPa. The reason for this improvement in strength is due to the work-hardening for both aluminum and IF steel which is associated with the ARBed, the presence of the continued IF steel layers and load transfer effect. Furthermore, the production of ultrafine-grained microstructure due to the accumulation of SPD [120,162,187]. In group B, the IF layers are located on the outside of the composite and they are acting as the transfer medium role for the load. It was observed that the ultimate strength of group B was about 100MPa higher than that of group A due to the positive effect of the transfer medium of a hard layer on the strengthening of the composite during the plastic deformation.

The IF steel (hard) layers started to wave after the third cycle of ARB process for all groups A, B, and C; afterward the necking and local fracture of the steel layer occurred after the fourth cycle. Therefore, the strength of the composites declined significantly for cycle N4 and N5 [44,187]. Moreover, the ductility of these composites dropped to lower than one percent after three cycles due to the plastic instability and rupture of steel layers [187].

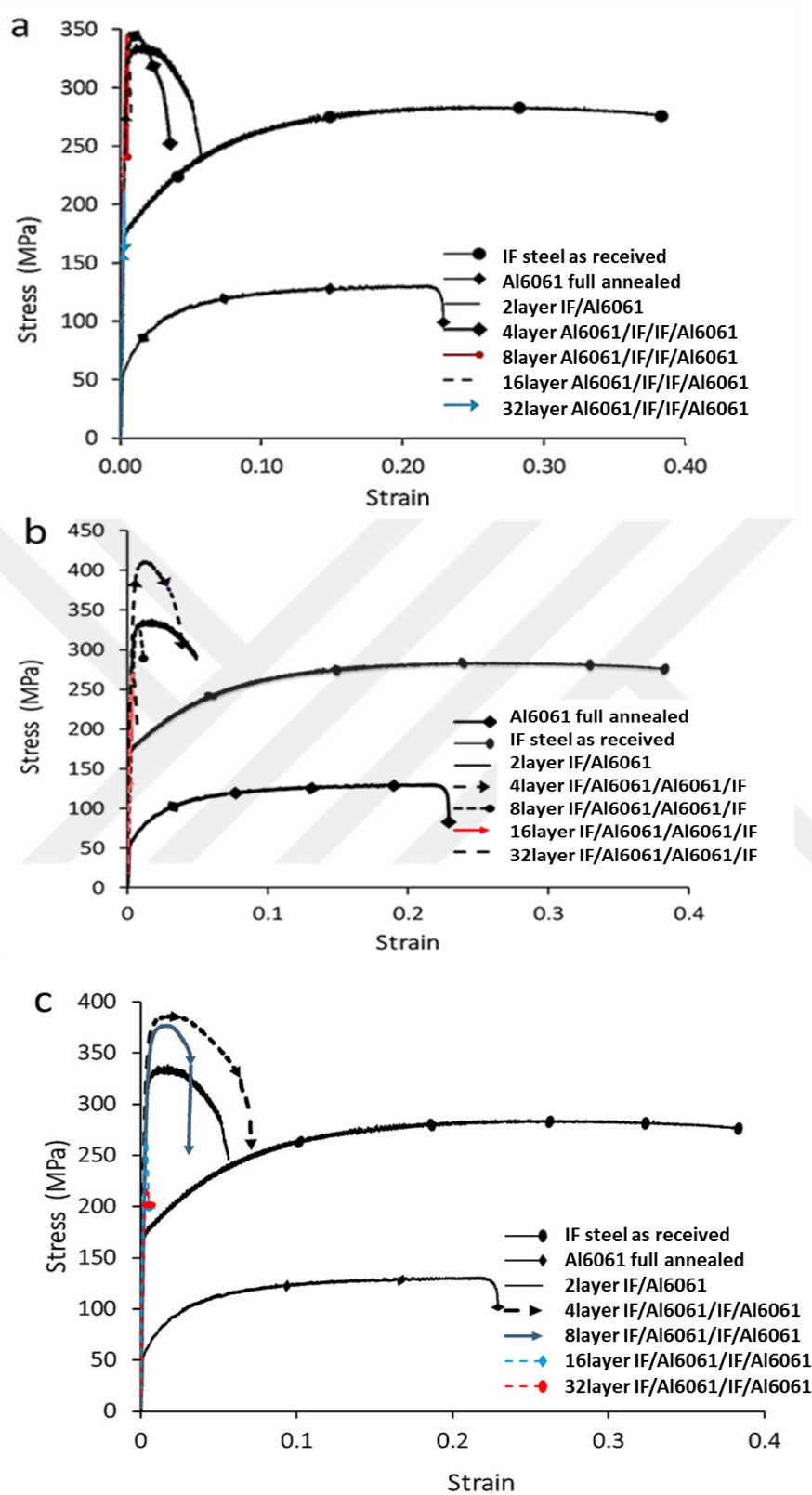


Figure 5.9: Stress-strain response of the fabricated composites of a) Al6061/IF/IF/Al6061 b) IF/Al6061/Al6061/IF c) Al6061/IF/Al6061/IF.

Tensile strength was significantly increased after the first pass, reaching 410MPa, but afterward, a slight increase has occurred with the forward ARB cycles in all groups. The maximum value of UTS was achieved after N3 which was ~ 455MPa, 495MPa and 485MPa for group A, B, and C respectively, which is 1.7 and 2.5 times larger than the initial condition of IF steel and Al2024 respectively.

The enhancement of the strength after three ARB cycles in all cases is due to the increasing the number of IF steel layers that lead to additional grain subdivision and accelerate the grain refinement, as well as the work-hardening for both aluminum and IF steel.

On the other hand, the total elongation decreased to 8% after one ARB cycle and reduced to 6%. The reason for the reduction of ductility is often due to strain hardening, which causes decreased mobility of dislocations, and thus, the elongation decreases [48]. In addition, the debonding in the interfaces regime plays an important role in reducing ductility [192]. Comparing the results of tensile tests for the composites made from Al2024 and Al6061 with IF steel, it can be observed that the combination of Al2024 with IF steel was remarkably stronger than the Al6061/IF composites (Fig.5.9 and 5.10). Later ARB passes decreased the strength of the composites due to the necking and local fracture, which was explained previously [187].

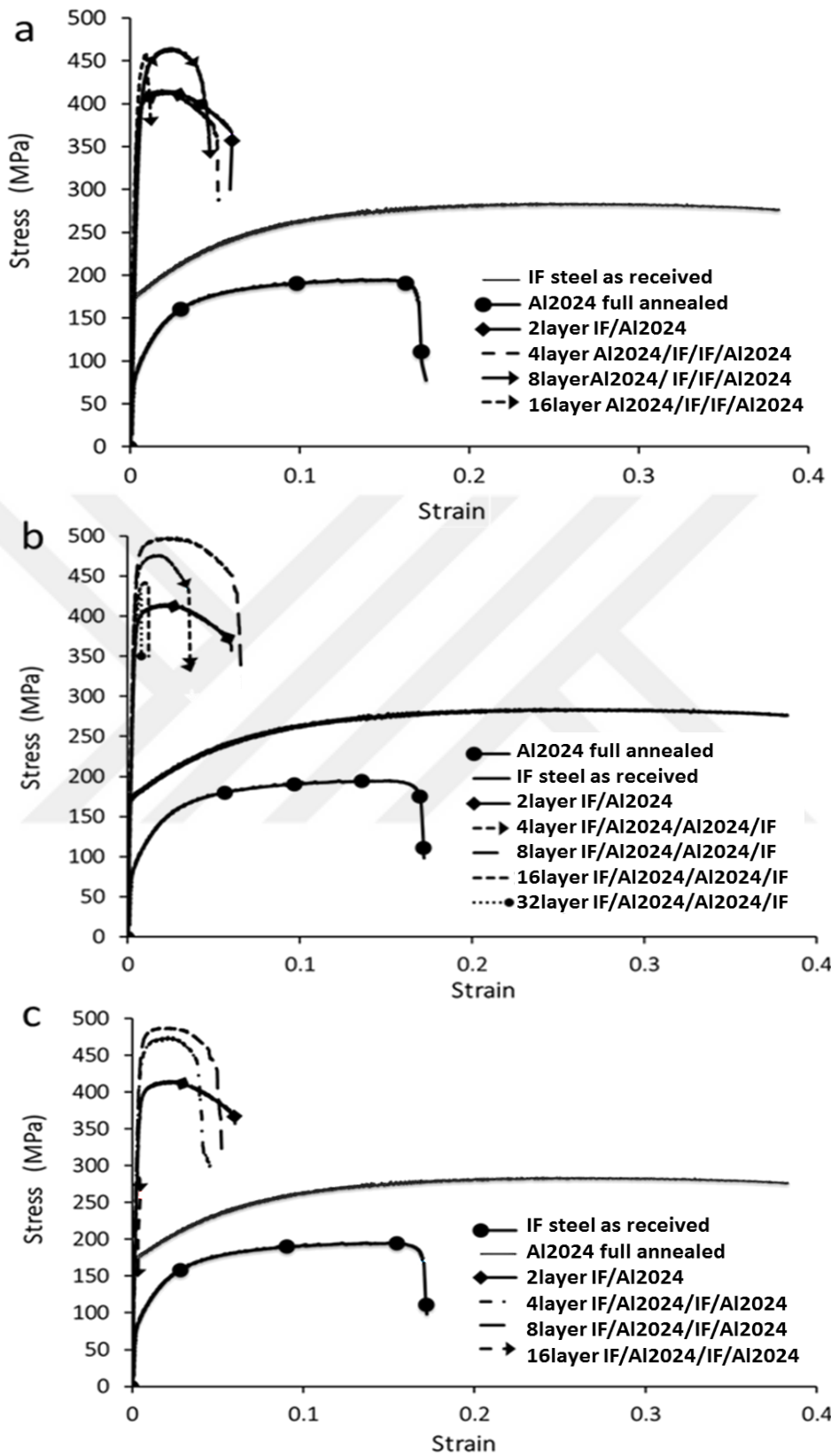


Figure 5.10: Stress-strain response of the fabricated composites of a) Al2024/IF/IF/Al2024 b) IF/Al2024/Al2024/IF c) Al2024/IF/Al2024/IF.

5.3.3 Al2024/Al6061/IF steel composite fabricated by ARB process

The stress-strain curves of the Al6061, Al2024 and IF steel in different layer architecture (after the two cycles) are shown in Fig. 5.11. The strength of IF/Al6061/Al2024/IF composite with four layers was significantly higher (450MPa), as well as the elongation which was 7%. On the other hand, after changing the stacking sequence of the IF layers from the outer sides of the inner section, Al6061/IF/IF/Al2024 composite exhibits low strength (390MPa) with a limited elongation of ~ 4.3%. The reason for this reduction is the fact that when the soft metals are on the outsides of the composite, the redundant shear strain will be higher for the soft parts and it cannot effectively impact on the IF steel.

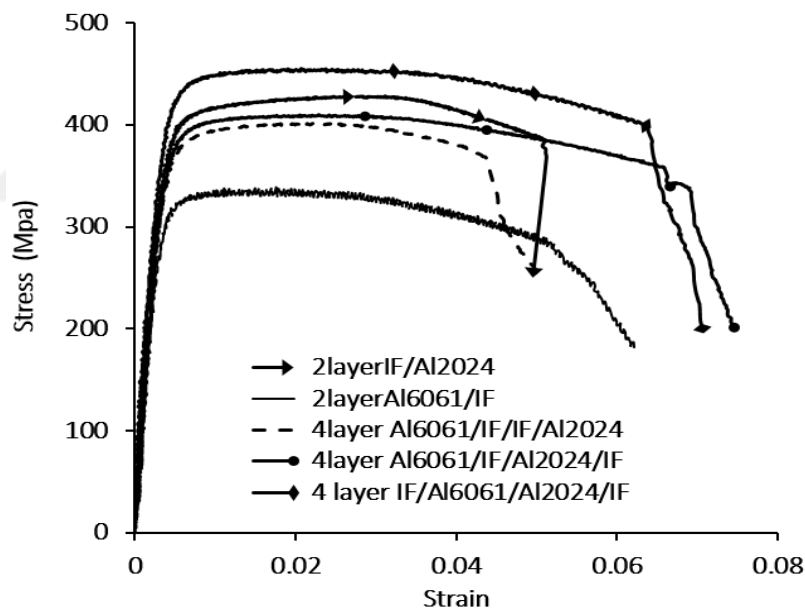


Figure 5.11: Stress-strain response of the fabricated composites of Al6061, Al2024 and IF.

Various mechanisms of strengthening such as strain hardening, grain refinement, precipitation hardening, and solid solution strengthening can affect on the mechanical properties of the materials and composites depends on the process which is applied on them. ARB process is a severe plastic deformation method and the main strengthening mechanisms in this process are strain hardening or work hardening and grain refinement. For the first cycle,

work hardening or dislocation strengthening performs the primary role in improving the strength. For further passes of the ARB process, the effect of strain hardening is decreasing, while enhancement of strength is gained by grain refinement. Comparing the tensile behavior of Al6061/IF/IF/Al2024 with Al6061/IF/Al2024/IF and IF/AL6061/Al2024/IF composites, it can be deduced that the layer architecture has a vital impact on the mechanical properties of the processed composite. The σ_y , σ_{UTS} and ε of Al/IF composite after ARB are listed in Table 4.2

Table 4.2 the results of σ_y , σ_{UTS} and ε of Al/IF steel composite after ARB process .

Alloy	Al6061/IF												
	Group A					Group B				Group C			
Cycle number	1	2	3	4	5	2	3	4	5	2	3	4	5
σ_y (MPa)	324	337	307	248	123	390	400	248	123	356	351	247	214
σ_{UTS} (MPa)	338	346	345	250	211	411	440	250	211	386	377	270	218
ε (%)	6.3	4.5	0.7	0.3	0.3	5.5	3.5	0.2	0.21	7.5	3.3	0.5	0.5
Alloy	Al2024/IF												
	Group A				Group B				Group C				
Cycle number	1	2	3	4	2	3	4	5	2	3	4		
σ_y (MPa)	393	400	440	435	444	465	430	405	445	460	301		
σ_{UTS} (MPa)	414	416	465	458	476	498	435	410	474	487.5	295		
ε (%)	6.5	5.6	5.5	1.1	4.2	6.4	0.9	0.8	5.0	6	0.5		
Alloy	Al2024/Al6061/IF												
	Group A				Group B				Group C				
	4layer Al2024/IF/IF/Al6061				4layer IF/Al2024/Al6061/IF				4layer IF/Al2024/Al6061/IF				
σ_y (MPa)	380				430				386				
σ_{UTS} (MPa)	396				455				410				
ε (%)	5.1				8				8.5				
Alloy	Materials as received												
	Al2024				Al6061				IF steel				
σ_y (MP)	99				62				183				
σ_{UTS} (MPa)	185				124				293				
ε (%)	17.5				21.3				41				

5.4 Cyclic Response under Stress Control

The cyclic strength of the processed materials, related damage, and fracture mechanisms were investigated by performing the fatigue tests. The Wöhler S–N curves of the ARBed Al /IF steel composites (group A and B), Al/Al sheet (group D) and IF/Al2024/Al6061/IF for the four-layer condition are demonstrated in Fig. 5.12. As mentioned, in the previous section, group A contains Al6061/IF/IF/Al6061 and Al2024/IF/IF/Al2024 composites, group B include IF/Al6061/Al6061/IF and IF/Al2024/Al2024/IF composites, and group D contains Al6061/Al6061 and Al2024/Al2024 similar layered composites. It is obvious that fatigue life increased by reducing the applied stress amplitude for all cases. In the high cycle fatigue (HCF) test, the fatigue life of the metal strongly depends on the initiation and propagation of cracks in the samples [193]. Usually, fatigue strength increases with increased static tensile strength [155]. Thus, material strength, hardness, and ductility are essential factors to be considered. The fatigue strength of the composite groups of A and B was about two times higher than that of group D due to the positive contribution of IF steel layer on the strength of the composites. Moreover, an effective load transfer, as well as a noticeable crack deviation interfaces between two different materials, improved the fatigue life of the composites when compared to the single material type.

The fatigue life of the ARBed composites is shorter than the other composites with a similar grain size attributed to the remaining cracks and defects on the surface of the outer layers and interfaces of the layers in the ARBed materials [194]. These surface defects act as favored sites for crack initiation and propagation. The hardness of outer layers is higher than the inner strips due to the high redundant shear strain induced by friction between the surface of these layers and rolls during the first and second pass of the ARB process [162,195]. The effect of the crack initiation and the direction of crack propagation will discuss in the next section.

Comparing the fatigue lives of Al2024/IF steel and Al6061/IF steel, under the higher stress amplitudes the cyclic performance of the composites contains Al2024 was significantly better than the Al6061/IF steel composites due to the high strength of the individual layers of Al2024 [193]. On the other hand, for lower stress amplitudes, the fatigue behavior of both is the same which means that the effect of the high strength of the layers under the lower stress amplitudes is not the main parameters of the fatigue life. Also, the high ductility of the Al6061 as an individual layer of the composites improves the cyclic behavior of composites under the lowest level of stress amplitudes.

As is shown in the S-N curve, the fatigue life of group A is higher than that of group B, for the same stress amplitude. The main reason of this difference is reducing the maximum stress in the outside aluminium layer attributed to the effective load transfer from the aluminum layers to the IF layer in the composite of group A. This reduction of stress on the Al surface can delay the crack initiation and improve the fatigue life of the composite with softer outside layers.

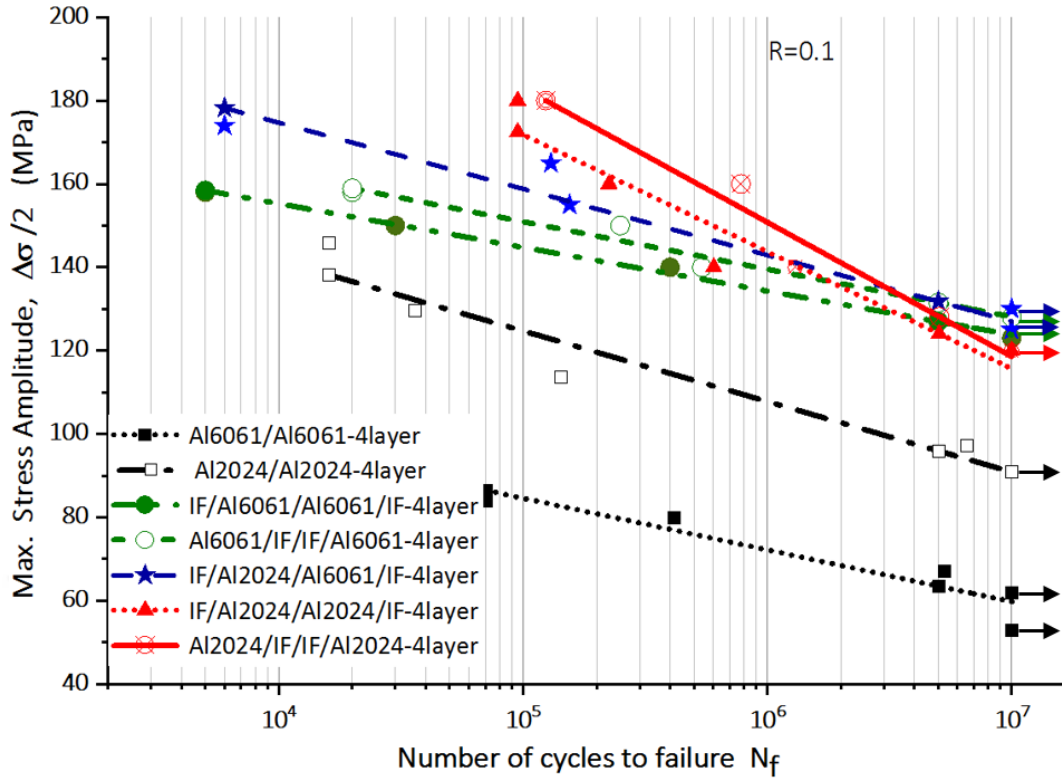


Figure 5.12: Variations between stress amplitude and fatigue life (S–N curve) for composites Al6061/IF/IF/Al6061, IF/Al6061/Al6061/IF, Al6061/IF/Al6061/IF, IF/Al2024/Al2024/IF, Al2024/IF/IF/Al2024, Al2024/IF/Al2024/IF and IF/Al2024/Al6061/IF four-layer composites and for single material type the Al6061 and Al2024.

5.5 Characterization of Microstructure

Fracture mechanisms of the composites are related to the fabrication method and also the loading conditions. Also, different materials and stacking sequence of the layers in the layered composites affect the fracture behavior during the loading. Therefore, observation of the fracture surface and fracture mechanisms of layered composites is very critical to characterize the mechanical properties. In this section, fracture morphologies of composites in different conditions were analyzed after tensile and fatigue tests separately. For all composites, SEM images were taken from the fracture surfaces of the ARBed samples after one, two, and three cycles.

5.5.1 Fracture morphology analysis of Al6061/IF and Al2024/IF steel composites after the tensile test

Fig. 5.13 displays the scanning electron microscopy (SEM) of fracture surface for IF steel in as-received condition after the tensile test with the strain rate of 0.001s^{-1} . Generally, ductile fracture behavior in the materials is characterizing with the deep and hemispheroidal dimples and coalescence of microvoids distributed on the fracture surface [181,196]. As shown in Fig. 5.13, the primary material performed a typical ductile fracture, represented by deep dimples. Additionally, Fig. 5.13a revealed the necking of the sample in a low magnification fracture surface, which proves the ductile fracture of IF steel after the room temperature tensile test.

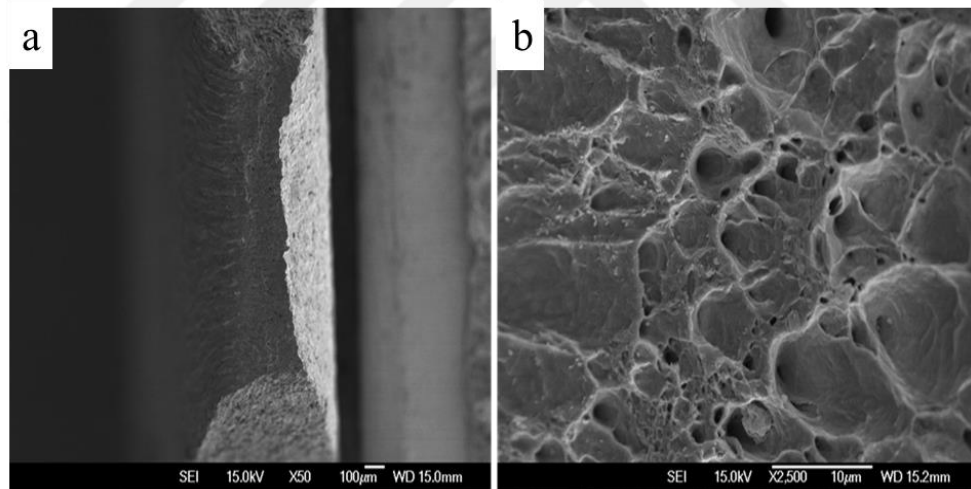


Figure 5.13: The fracture surface of the as-received IF steel tested under the strain rate of 0.001s^{-1} a) low magnification and b) in high magnification.

Fig.5.14 demonstrates the SEM image of the fracture surface of the specimen after the tensile test under the strain rate of 0.001s^{-1} at low and high magnification for Al6061/IF composite, after one cycle of ARB process. It shows that Al6061/IF composite has a ductile fracture contains dimples and parabolic cavities of shear zones. However, only a little deformation and a small amount of necking happened [196]. The stretched channels show that ruptures are shear dimples and IF layers show a ductile fracture in Al/IF multi-layered composite. The fracture surfaces of the sample after the first pass of the ARB process at low magnification is shown in Fig. 5.14a. Debonding can be observed in the interface between the Al6061 and IF steel. So, the weak interfaces are suitable locations for initiation of debonding and fracture. Figs. 5.14b and c at high magnification demonstrate that the specimen presented a typical ductile fracture with hemispherical or deep equiaxed dimples. This type of rupture occurs by microvoid generation and coalescence.

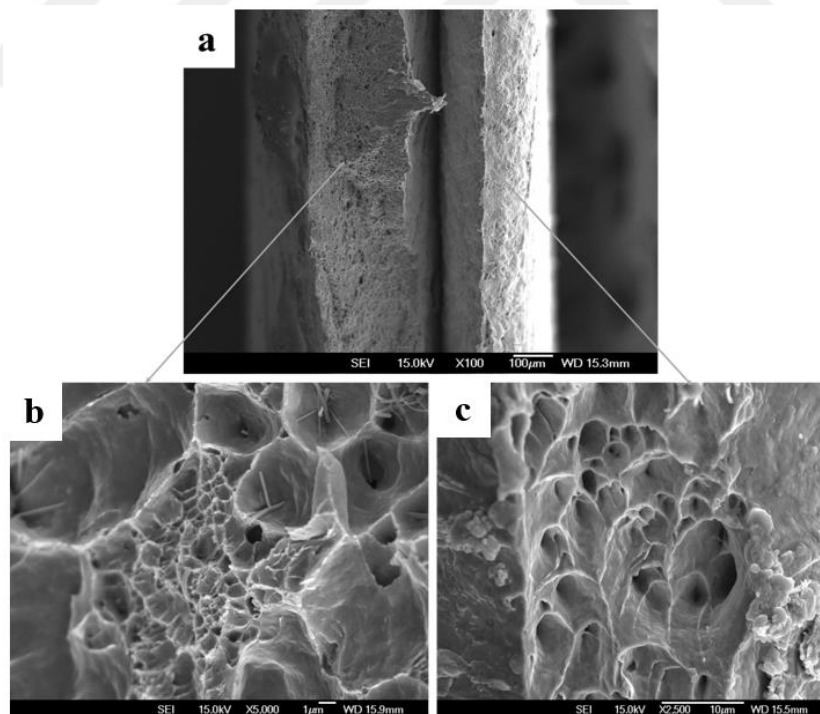


Figure 5.14: The fracture surface of 2 layers IF/Al6061 composite after one cycle ARB tested under the strain rate of 0.001s^{-1} in a) low magnification and in high magnification, b) the Al6061, and c) IF steel.

Fig. 5.15 illustrates the fracture surface of the Al6061/IF/Al6061/IF composite in low and high magnification. Ductile fracture mechanism represented by necked regions is obvious for the IF steel parts of the composite, while the relatively brittle fracture surface was observed for the Al6061. Figs. 5.15b and c demonstrate the deep dimples and microvoids for the IF steel sheet and cleavage fracture surface with a brittle manner for Al6061 in high magnification, respectively. As expected, observation of SEM images revealed that the interface between the layers which rolled for two cycles was stronger than the interface at the center which rolled for one pass. Thus, the interface between the second and third layers is the main potential region for debonding, crack nucleation and propagation, and finally, the failure of the composite (Fig. 5.15a) [78,182]. This is associated with augmentation in interlayer atomic diffusion because of the more significant normal pressure at higher cycles of the ARB process.

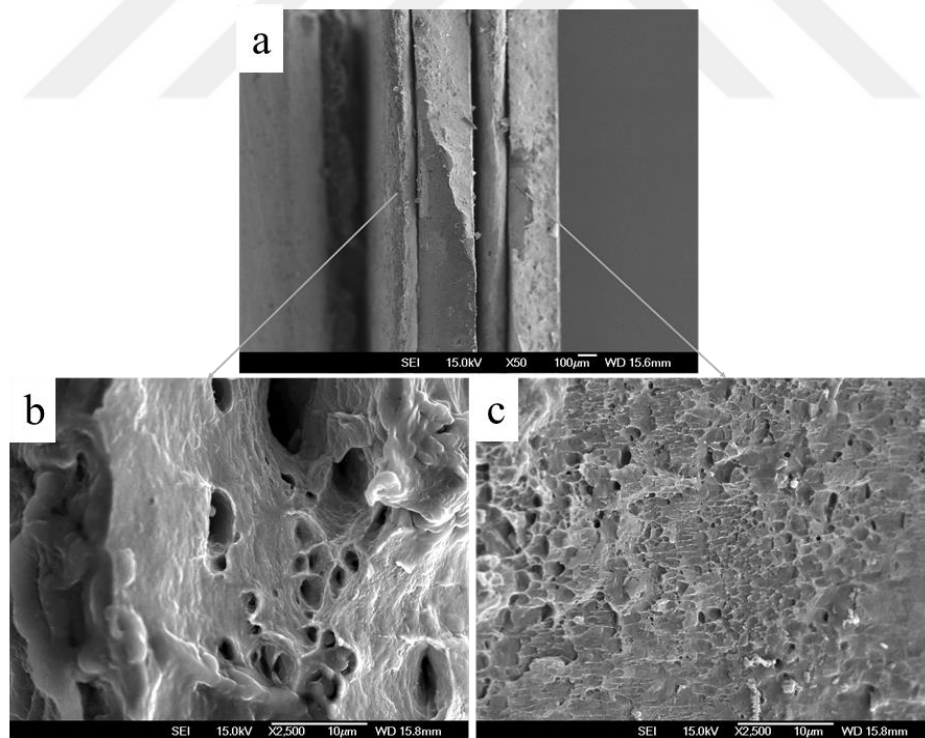


Figure 5.15: The fracture surface of 4 layers IF/Al6061/IF/Al6061 composite after two cycles ARB tested under the strain rate of 0.001s^{-1} in a) low magnification and in high magnification, b) IF steel, and c) Al6061.

Fig. 5.16 demonstrates the fracture surface of IF/Al2024/IF/Al2024 composite after the tensile test. The necked surface detected on the low magnification SEM (Fig. 5.16a) represents the ductile fracture of IF steel layer, while the flat shape fracture surface of Al2024 reveals the brittle fracture mode of these parts during the loading. Also, comparing the SEM micrographs of the Al6061 in four layers Al6061/IF steel and Al2024 in four layers Al2024/IF steel composites, higher magnification images revealed the fact that Al2024 layers fractured with an abrupt failure fracture manner, while the fracture behavior of the Al6061 was cleavage surface with a brittle fracture characteristic.

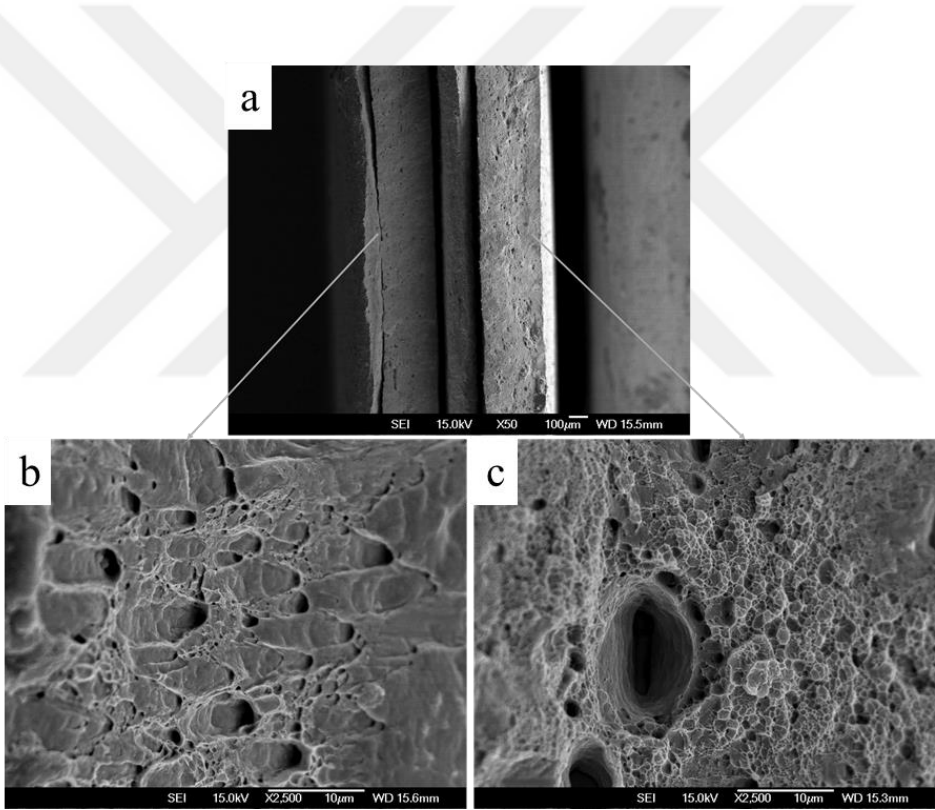


Figure 5.16: The fracture surface of 4 layers IF/Al2024/IF/Al2024 composite after two cycles ARB tested under the strain rate of $0.001s^{-1}$ in a) low magnification and in high magnification, b) IF steel, and c) Al2024.

After the second cycle, the interfaces formed between similar alloys are not visible and two sheets of metals act as one part (Figs. 5.17 and 5.18). These figures clarify that the difference between the fracture mechanisms of two dissimilar neighbor layers can be the origin of the cracks and debonding in the composites. Moreover, the stacking sequence of the layers is another important parameter. As shown in Fig. 5.17b, when the IF layers are in the outsides of the composite, the bonding between the IF parts and aluminum parts are better due to the redundant shear strain.

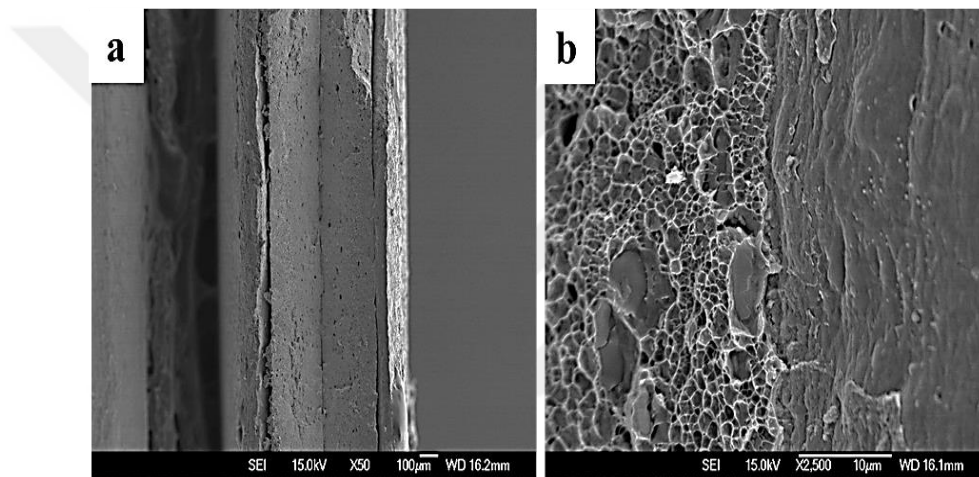


Figure 5.17: The fracture surface of 4 layers IF/Al2024/Al2024/IF composite after two cycles ARB tested under the strain rate of 0.001s⁻¹ in a) low magnification and in high magnification, b) the interface of Al2024/IF steel.

Fig. 5.18 depicts the fracture surface of 8 layers IF/Al2024 /Al2024/IF composite. The level of ductile fracture decreased after three cycles of ARB, and necked regions were limited due to the high level of strain hardening during the ARB passes. Also, high magnification images revealed that debonding between the similar layers of Al2024 occurs during the abrupt failure of the brittle fracture when the relatively brittle fracture observed at the interface of the Al2024 and IF steel (Figs. 5.18 b and c).

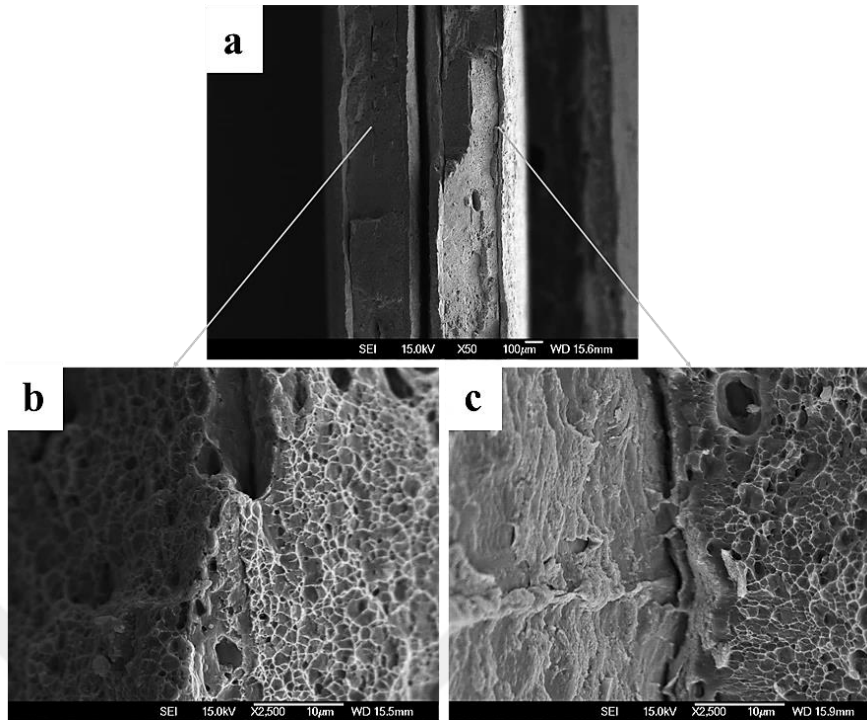


Figure 5.18: The fracture surface of 8 layers IF/Al2024/Al2024/IF composite after three cycles ARB tested under the strain rate of 0.001s^{-1} in a) low magnification and in high magnification for b) the interface of Al2024/Al2024, and c) the interface of Al2024/IF steel.

5.5.2 Fracture morphology analysis of Al6061/IF/Al2024/IF composite

Scanning electron microscopy micrograph of the fracture surfaces in low magnification (Fig. 5.19a) and in high magnification (Fig. 5.19b, c, d, e, and f) were observed after the tensile test to study the fracture behavior of composite after two cycles ARB. As mentioned previously, the interface between the layers, which performed in, two cycles have stronger bonds compared with the interface at the center of the composite. In high magnification, the fracture surface of IF steel shows shear zones and dimples, which are the characteristics of ductile fracture manner (Fig. 5.19b). On the other hand, intergranular brittle fracture surfaces on the fracture surface of the aluminum parts were observed with different levels (Figs. 5.19d and f). The cleavage fracture surface on the Al2024 represents a typical brittle fracture for this part and this

difference between the fracture mechanisms of the IF steel and Al2024 increased the potential of crack initiation of the interface between them (Fig. 5.18c).

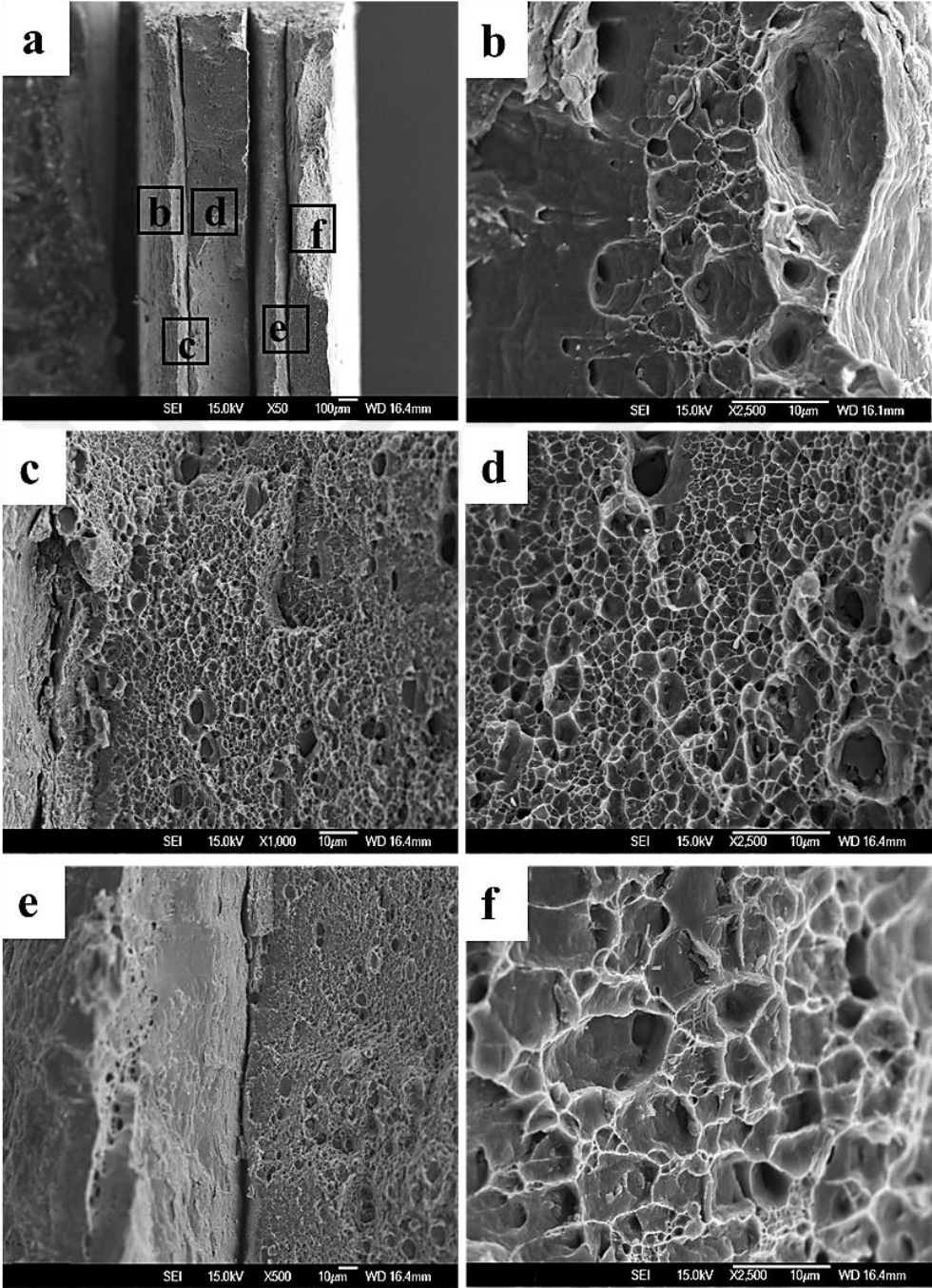


Figure 5.19: The fracture surface of 4 layers IF/Al2024/IF/Al6061 composite after two cycles ARB tested under the strain rate of $0.001s^{-1}$ in a) low magnification and in high magnification for, b) of IF steel, c) the interface between IF steel/ Al2024, d) Al2024, e) interface between Al6061/IF and c) Al6061.

5.5.3 Fracture morphology analysis of Al/IF steel composites after fatigue test

Fatigue cracks always initiate at free surfaces normally external surfaces and sometimes internal surfaces if the element contains voids, cracked second-phase particles, and other defects. Regular external surface defects involve surface roughness and geometric notches [154]. SEM observations of the fracture surfaces of the samples after fatigue tests are shown in Fig.5.20 and Fig. 5.21. For both (Al6061/IF and Al2024/IF), the cracks were initiated from the surface of the outside layers and also the interfaces between the sheets. This similarity reveals that the fracture mechanism of these composites is relatively independent of the layer architectures of them, which are also proved from the results of the fatigue tests (Fig. 5.12).

Additionally, it was observed in Fig. 5.22a, and Fig. 5.23a that after the crack nucleation on the surface, with approaching the crack from the plastically weaker Al layer to hard layer of the IF steel, the cracks are starting to divide and branch, then propagate perpendicular to the initial path due to the interaction between the damage zone of the crack tip and interface layer [44,152,153,197,198]. On the other hand, delamination at the interlaminar boundaries and crack arrest are the other effective reasons for fatigue life enhancement for multilayer composites.

Also, the bonded layer of IF steel at the interface regime provides a higher thickness of the hard layer in group A. Consequently, increasing the thickness of the hard layer, the fatigue life of group A improved compared with the group B due to the character of the stress field at the crack tip [153,197].

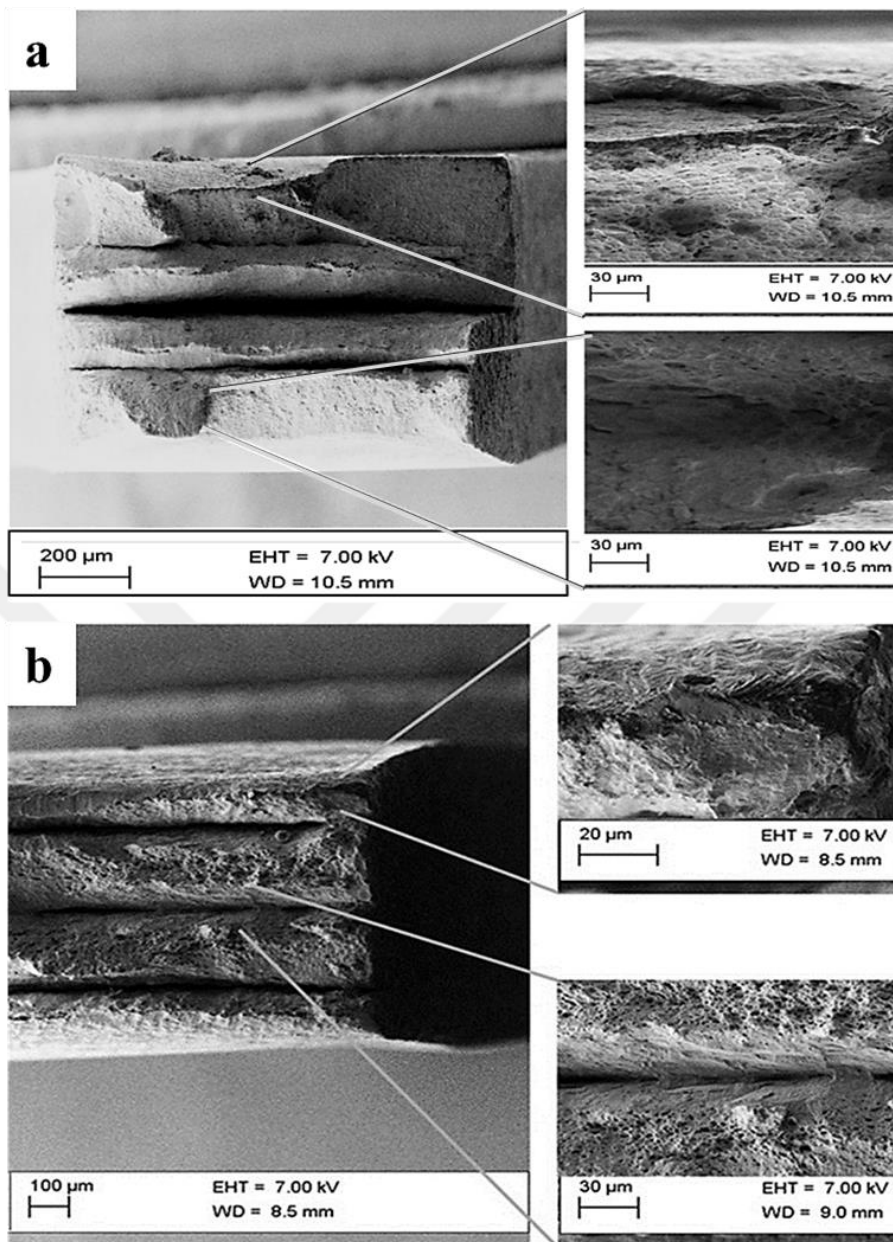


Figure 5.20: SEM observations of fatigue damage at the surface close to the fracture zone of a) Al6061/IF/IF/Al6061 layered composite. b) IF/Al6061/Al6061/IF layered composite and, observation of different fatigue fracture morphologies.

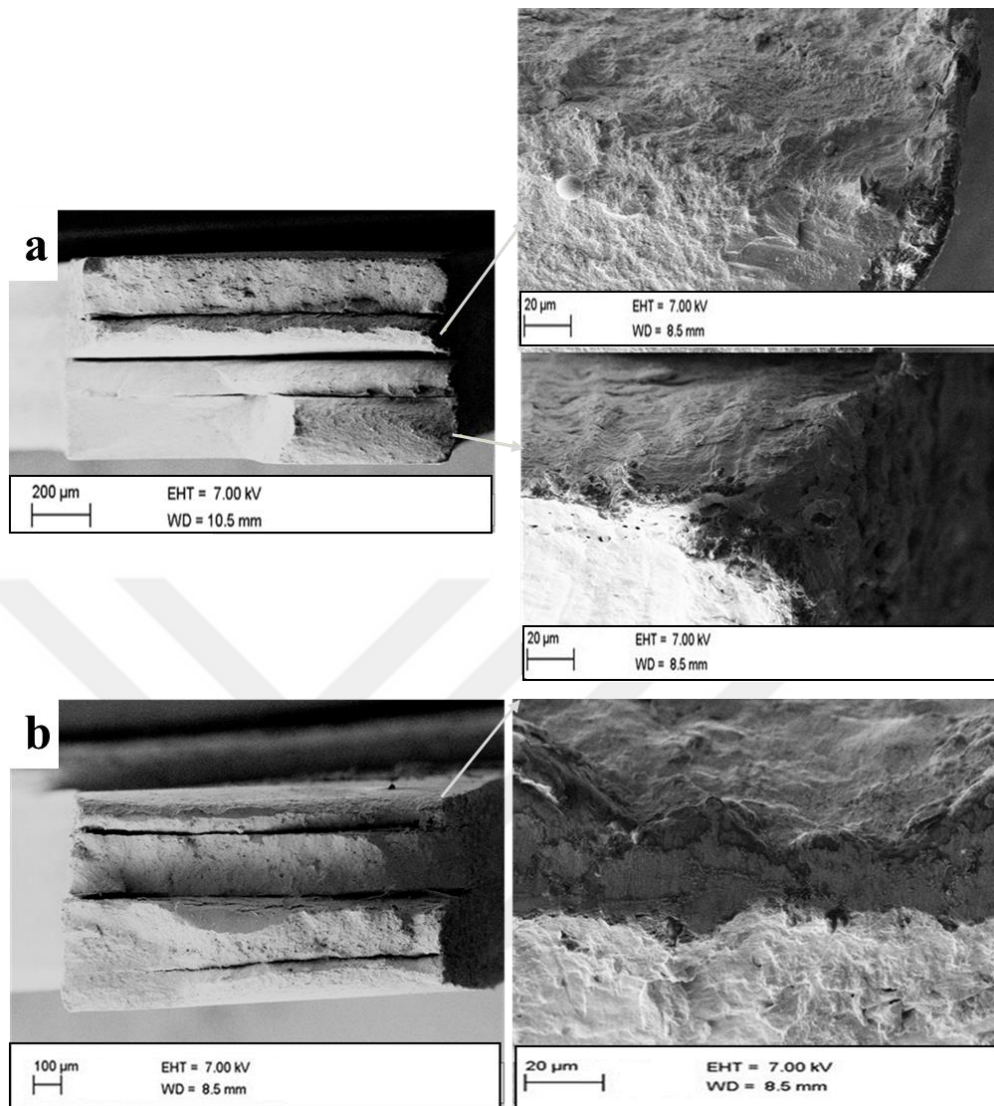


Figure 5.21: SEM observations of fatigue damage at the surface close to the fracture zone of a) Al2024/IF/IF/Al2024 layered composite. b) IF/Al2024 /Al2024/ IF layered composite and, observation of different fatigue fracture morphologies.

Otherwise, the crack routes for the group B were controlled by the IF steel at the outside layers and crack propagation rate accelerated after approaching to the interfaces, from the plastically stronger material to the weaker Al layers [153,197]. As shown in Fig. 5.22b, Fig. 5.23b and the crack initiation at the outer layers, which is a hard part of composite and the direction of the crack growth in the aluminum interface soft layer is similar to the case of the compound in group D of Al/Al composite which mentioned in the previous section.

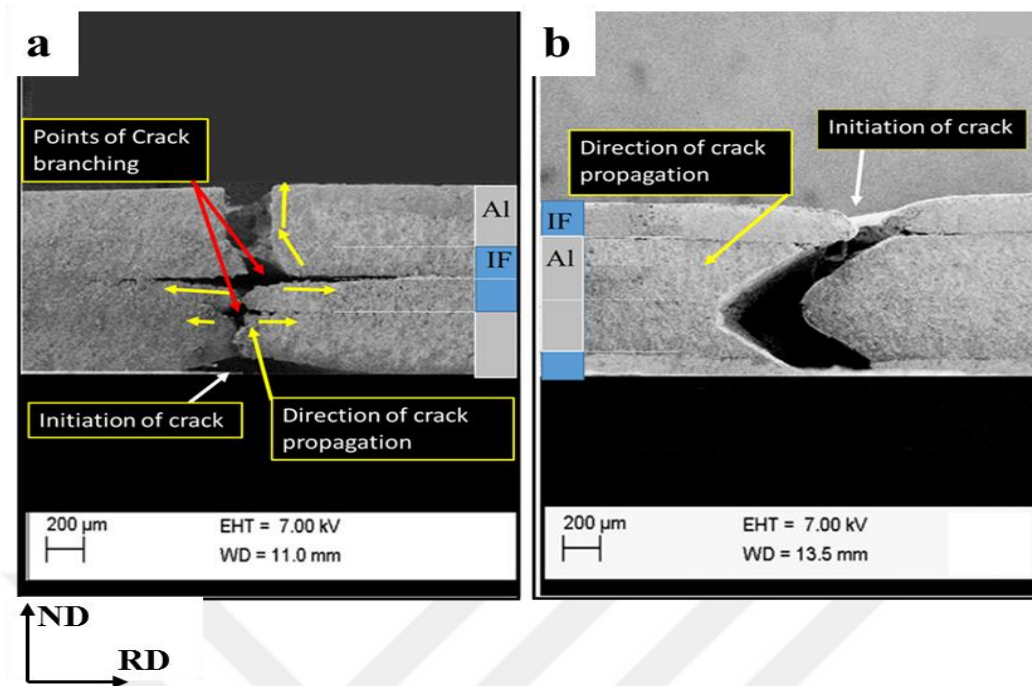


Figure 5.22: SEM of crack growth paths of the four layers a) Al6061/IF/IF/Al6061 composite b) IF/Al6061/Al6061/IF.

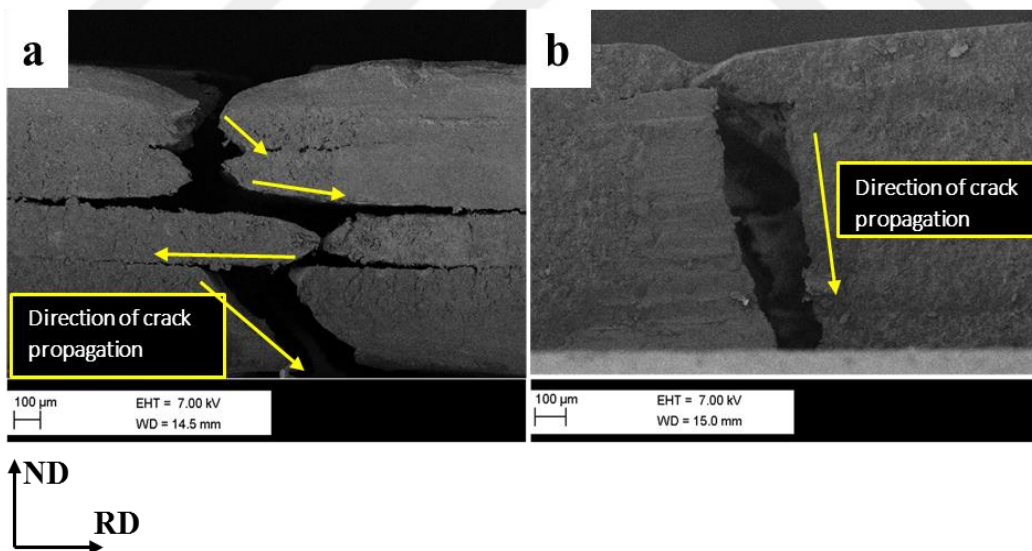


Figure 5.23: SEM of crack growth paths of the four layers a) Al2024/IF/IF/Al2024 composite b) IF/Al2024/Al2024/IF.

CHAPTER VI

NUMERICAL ANALYSIS

6.1 Introduction

In the last twenty-five years, numerical simulation techniques and the proper use of computer codes have become essential for modern engineering. Industries are increasingly investing in technologies such as CAE and FEM because they are fundamental tools in research, optimization, simulation, and prototyping. The finite element procedures were used professionally to simulate dynamic processes, including severe nonlinearity such as forging, plate forming, and rolling [199].

Several studies were performed using finite element analysis (FEA) for the other SPD processes, such as high-pressure torsion [200] equal-channel angular pressing (ECAP) [201], and warm calibrated rolling [169,199]. Also, there are few reports on ARB [68,202]. Tadanobu et al. [68] studied the influence of friction and roll diameter on the equivalent strain after the ARB process. The ARB for thin plates were simulated with a different friction model using FE-code ABAQUS, and the total strains were examined in the compound and the equivalent strain during rotation [202].

The main aim of this numerical analysis for the current work is to obtain the deformation on the sheets (the equivalent strain in ARB-processed) and compare them with experimental results, which performed by embedded pin method, to have a design data for the optimal estimation for later experiments. Equivalent strain, produced by rolling cycles in ND (Y-axis), was used to compare the simulation results of the ARB process with the experimental results. All the numerical analysis were achieved on the case study of the aluminum laminate composite.

6.2 Modeling of ARB process

The ARB process was simulated by the ANSYS software. Fig. 6.1 shows the model of the ARB process applied on Al2024/Al6061 bimetallic sheets. The X-axis is parallel to the rolling direction (RD), and the Y-axis along with the strip thickness (ND). Two slips were set to analyze three ARB cycles. Moreover, the properties obtained by the tensile test on the sheets after ARB were applied for the materials of the model. In this study, Al6061/Al2024 composite rolled at room temperature. The general process includes specifying the geometry and material of the samples, followed by simulating each practical step.

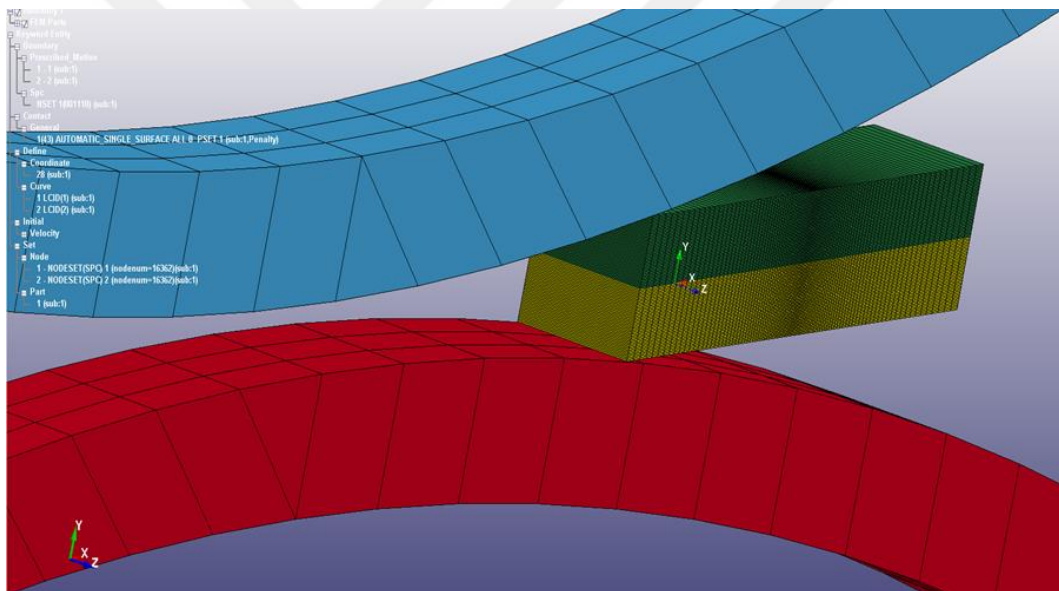


Figure 6.1: The model applied to the simulation of ARB of the dissimilar metal composite.

6.2.1 Assumptions

1. The rolls were modelled as rigid bodies.
2. The plates were modelled as isotropic elastic materials.
3. Al6061/Al2024 composites rolled at room temperature.
4. Young's modulus of 73GPa for Al2024 and 68.9GPa for Al6061, Poisson's ratio of 0.33 were used at room temperature.

5. The stress-strain relationships utilized in the analysis were described by ($\sigma = K \epsilon^n$), where K is 342MPa, and 220MPa also n is 0.25 and 0.23 for Al2024 and Al6061 respectively.
6. The frictional coefficient between roll and sheet was set as $\mu=0.35$ (unlubricated condition).

6.2.2 Initial conditions

1. The ϵ_{eq} increases with reducing the mesh size in ND (t_{el}) and tends to be relatively constant when the t_{el} is less than 0.03mm. Furthermore, the ϵ_{eq} at the center of the thickness is about 0.80 regardless of the t_{el} for values less than 0.26mm [190,203]. Therefore, the mesh size in RD (L_{el}) and ND, (t_{el}) was 0.025mm and 0.05mm, respectively. The finite element mesh in the sheet included 20167 nodes and 8412 elements.
2. The initial thickness of both sheets was 2mm, and the reduction ratio per pass was 50%. The sample was made from two layers with the dimensions of $t=1$ mm, $w=3$ mm and $L=12$ mm.
3. The roll diameter, $d\phi$ and the velocity (U_0) of the sheet was 110mm and 100mm/s, respectively.

6.2.3 Boundary conditions

1. Deformation of the plates is restricted in the Z-direction.
2. The initial velocity is given to thin plates in the X-direction and the roller is free to rotate only around the Z-direction.

In the ARB simulation presented in Figure 2a, b, the 2mm thickness plate was rolled to 1mm with $r = 50\%$ (first cycle ARB). Then the samples were stacked with a thickness of 1mm to a thickness of 2 mm and then rolled back to 1mm thick (2nd ARB cycle). The same procedure was repeated for the third cycles.

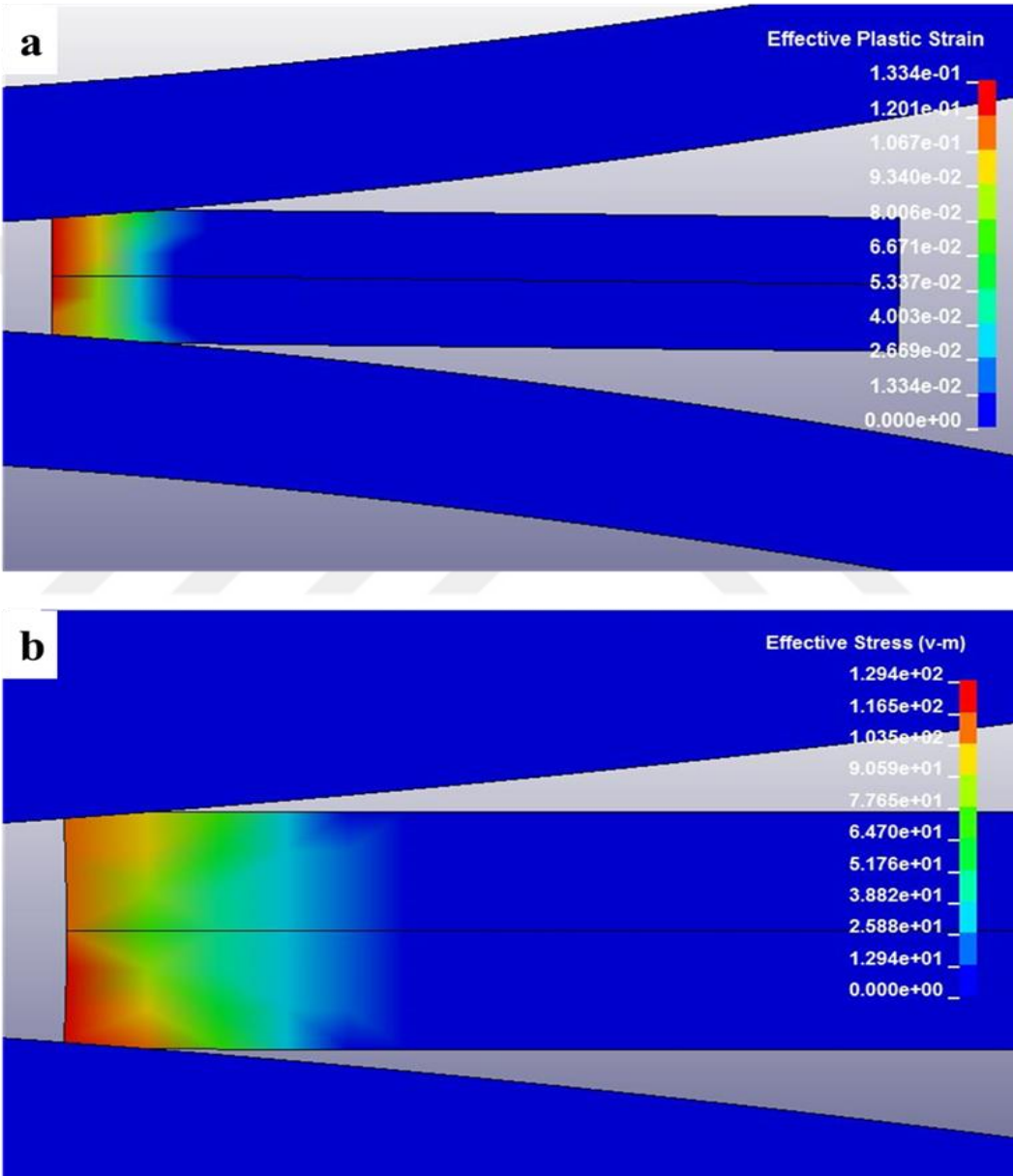


Figure 6.2: a) The effective plastic strain, b) the effective stress (v-m) (MPa) during the first cycle for 4layer Al6061/Al2024composite.

The results of the previous cycle were translated into the next cycle. The effective stress (v-m) and plastic strain are the main results transferred to the second stage. Fig. 6.3. shows the presence of effective stress in the sheets before the rolling process. These stresses and effective plastic strain were transferred from the second cycle, meaning that the sheets have the same characteristics of the plate produced from the second cycle. This procedure makes simulation results closer to those of experimental work.

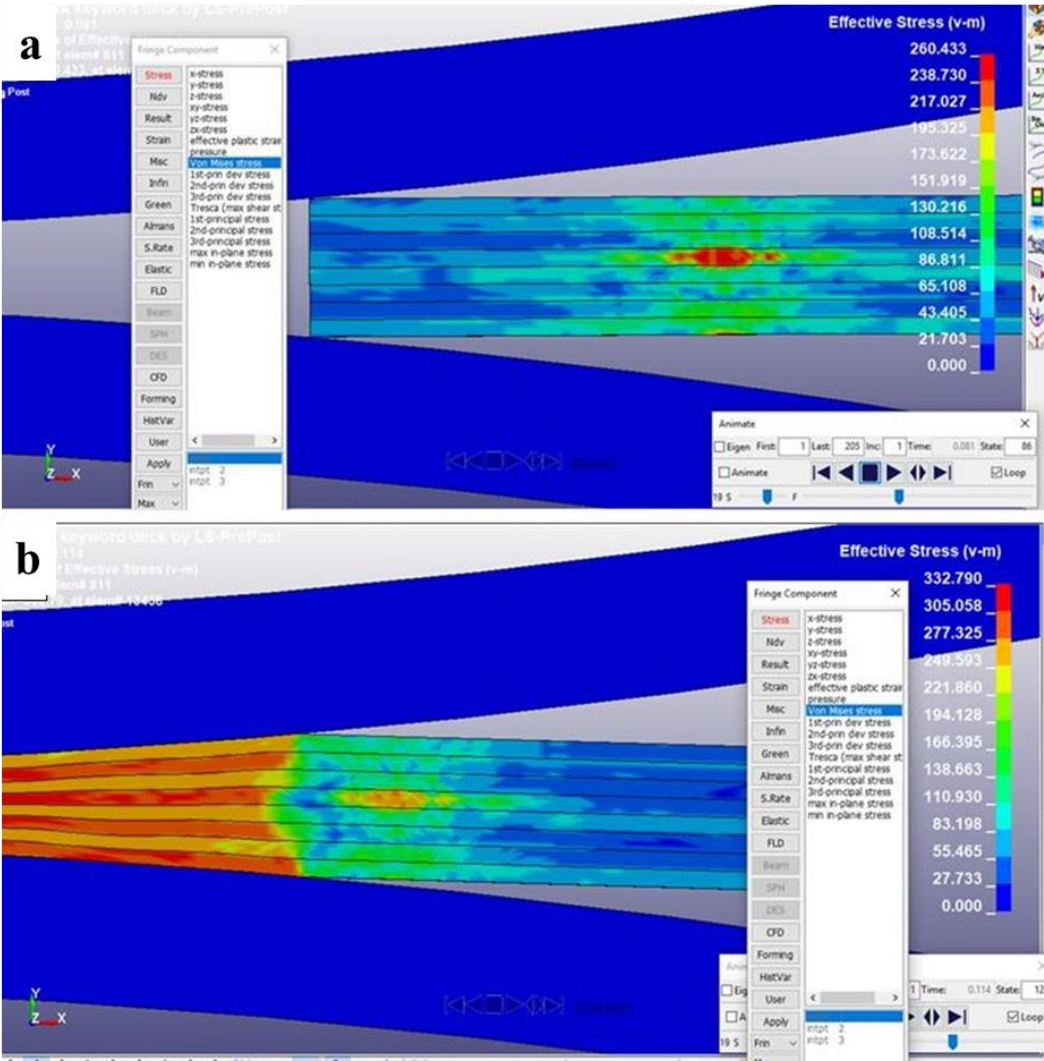


Figure 6.3: Illustration of the effective stress (v-m) of third cycles a) before rolling, b) during the rolling process for Al6061/Al2024 composite.

6.3 Results and discussion

Fig.6.4 shows the distributions of the equivalent strain (ϵ_{eq}) under unlubricated conditions ($\mu = 0.35$), along the plate thickness. The ϵ_{eq} has a distribution whose magnitude around 0.8 at the center of the thickness, which corresponds to a value of $0.8n$ due to no shear strain is presented at the center. After the 1st cycle, the ϵ_{eq} at the surface reaches 1.5. The ϵ_{eq} at the surface equals to 2.3 after the 2nd cycle, while it has a magnitude of 2.0 in the center of the samples. The greatest ϵ_{eq} at the surface shows the value of 3.3 after the 3rd pass, and the three peaks represent within the 1 mm thickness. The section with shown peaks at $x=0.25$ and 0.75 compared to the surface in the first pass. The maximum position at the center ($x=0.5$) compares to the surface in the second pass. The ϵ_{eq} increases almost linearly with respect to n [203]. This proportionality indicates that the effective strain on the outside of the sheet (surface) after the number of pass ARB-processed specimens can be determined by the conventional one-cycle rolling analysis. Hence, it is observed that a larger ϵ_{eq} can be presented to the plate surface by a complicated deformation through the shear strain influence.

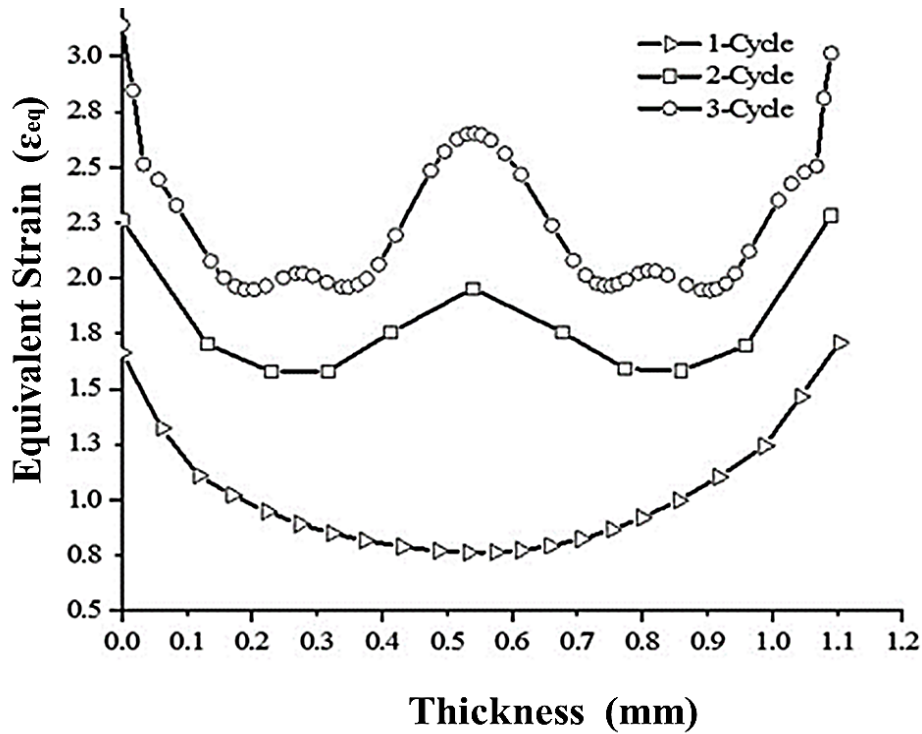


Figure 6.4: Distribution of the equivalent strain along the sheet thickness for Al6061/Al2024 composite after one, two, and three cycles.

Fig. 6.5 represents the histories of ϵ_{eq} in three positions: 1st at the center, 2nd near the center and 3rd at the surface respectively, during the rolling process. The ϵ_{eq} increase monotonously at the center, with increasing time and it is calculated depends on the reduction in thickness. This indicates that the strain rate (ϵ_{eq}/dt) in the center is approximately constant over the rolling process. These results are in good agreement with other studies [202] which is showing that the ϵ_{eq} at the center of the thickness is constant regardless of μ , and its magnitude indicates 0.80 because no shear strain is imposed at the center. Furthermore, ϵ_{eq}/dt near the surface increases higher and faster than that at the center, and the value of ϵ_{eq} at the surface is higher compared with the center. A large ϵ_{eq} of 1.5 at the surface after one cycle is attributed to large shear deformation. It means that the ϵ_{eq} at the surface is controlled by shear deformation and the value of shear deformation depends on the coefficient of friction [190,202].

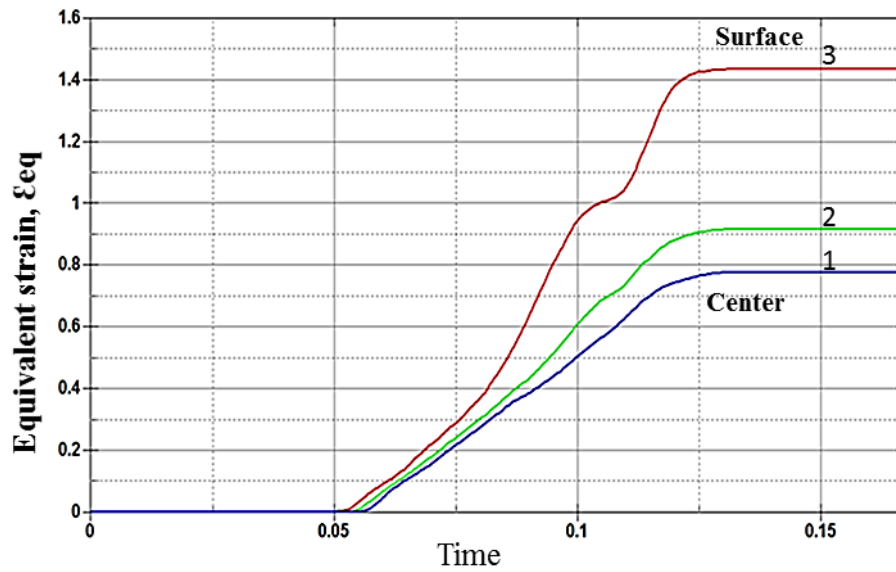


Figure 6.5: Histories of equivalent strain, ϵ_{eq} , at (1) center, (2) near the center and (3) surface during rolling, for Al6061/Al2024 composite after one cycle.

Fig. 6.6 shows the distribution of the effective stress (von Mises stress) through the thickness of the Al2024/Al6061 composite after one, two and three cycles. It is clear that effective stress increase with increasing value of plastic strain (number of ARB cycles) and it is found that maximum effective stress (240MPa, 263MPa, and 309MPa) in the layer for Al2024. However, the highest value of (v-m) can be observed close to the sheet surface due to high deformation by the effect of the frictional shear strain [202].

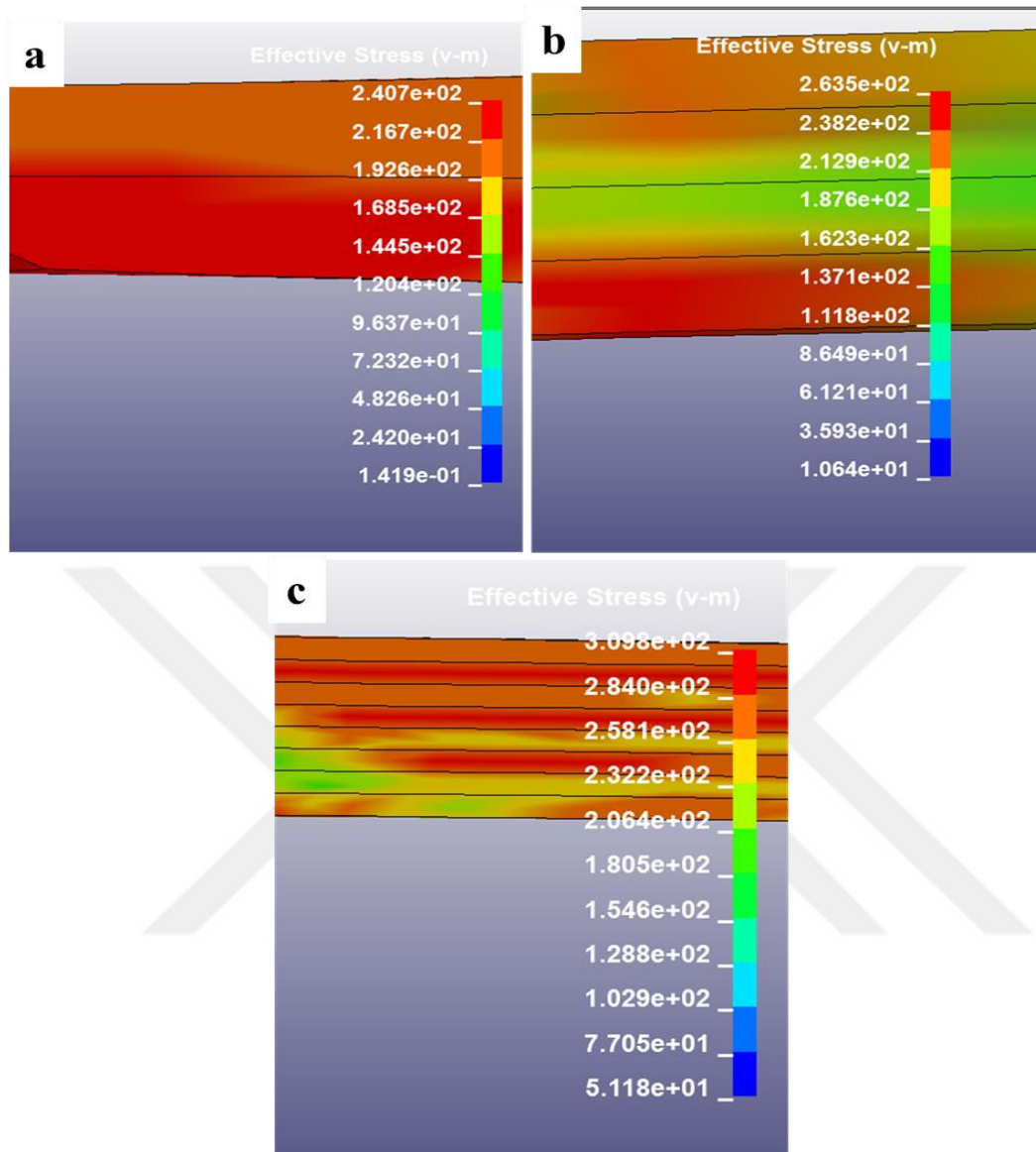


Figure 6.6: Von Mises stress distribution for Al6061/Al2024 composite after one, two, and three passes.

Eq. (6.1) below illustrates the mathematical relationship (von Mises criterion) between the effective stress ($\sigma_{(v-m)}$) and the tensile yield strength $\sigma_{(yld)}$ [204]. It is clear that, for a simple case of tension, the yield occurs when $\sigma_{(v-m)} = \sigma_{(yld)}$. Therefore, the left of Eq. (6.1) is the equivalent, or effective stress for the perfect general condition of stress given by σ_1 , σ_2 , and σ_3 . This effective stress is commonly called the von Mises stress. Thus, the value of the $\sigma_{(v-m)}$ is equal to the $\sigma_{(yld)}$ and the von Mises criterion can be written as:

$$\sigma_{(v-m)} = \sqrt{\frac{(\sigma_1 - \sigma_2)^2 + (\sigma_1 - \sigma_3)^2 + (\sigma_2 - \sigma_3)^2}{2}} = \sigma_{(yld)} \quad (6.1)$$

Therefore, the $\sigma_{(v-m)}$ calculated by numerical simulations can be compared with uniaxial tensile stress $\sigma_{(yld)}$ which obtained by tensile testing in the experimental part.

Table 6.1 shows the experimental results of $\sigma_{(yld)}$ and the numerical results of $\sigma_{(v-m)}$ for Al2024/Al6061 composite after one, two, and three ARB cycles. According to this table, there is an acceptable agreement between the effective stress (numerical results) and yield strength (experimental results) of the composite after the ARB process.

Table 6.1 Tensile yield strength and effective stress of Al2024/Al6061 composite after one, two, and three ARB cycles.

Cycle number	Tensile yield strength $\sigma_{(yld)}$ (MPa)	Effective stress ($\sigma_{(v-m)}$) (MPa)
1	248	240
2	290	260
3	275	309

6.4 Estimate the shear strain distribution over the thickness of sheets

Generally, the distribution of the equivalent strain along the thickness in a rolled samples depends on the attendance of shear deformation due to friction between the sheet and rolls and produces a change of microstructure (grain size, texture) through the thickness of the sample. In other words, a large amount of redundant shear strain is introduced on the surface of the rolled sheets due to the high friction between the surface of the plates and rolls.

In the ARB of Al1100, the redundant shear strain was assessed by Lee et al. [51]. Fig. 2.7, which was mentioned earlier, displays the flection of the embedded pin after the one cycle of the ARB. The authors write that the distribution of shear strain along the thickness of the samples was correlated well with the distribution of grain size.

Equivalent strain distributions through the Al2024/Al6061 sheet thickness are processed by one and two ARB cycles without lubrication. All of the previous studies were performed to measure the strain distribution after one ARB cycle, but to date, no one has studied the strain distribution after two ARB cycles. Therefore, in this study, the total distribution of the equivalent strain was evaluated experimentally after one and two cycles, and compared with the numerical results.

6.4.1 Total equivalent strain distribution

To investigate the distribution of the strain through the thickness of the ARB processed plates, shear strain measurement was performed by an embedded pin technique. This method can be summarized as follows: a cylindrical pin of 2mm diameter and a length of 2mm was embedded at the mid-width in the ND direction, vertical to the RD&TD plane. The material of the pin should be the same material of workpiece (sheet). The process is schematically described in Fig. 6.7. After installing the pin, the first ARB cycle was applied in the same method mentioned in the experimental section (3.2). Then, the sheet was cut at the center of the pin and perpendicular to the transverse direction (TD). The flections of the embedded pin were observed by optical microscopy Fig. 6.8.

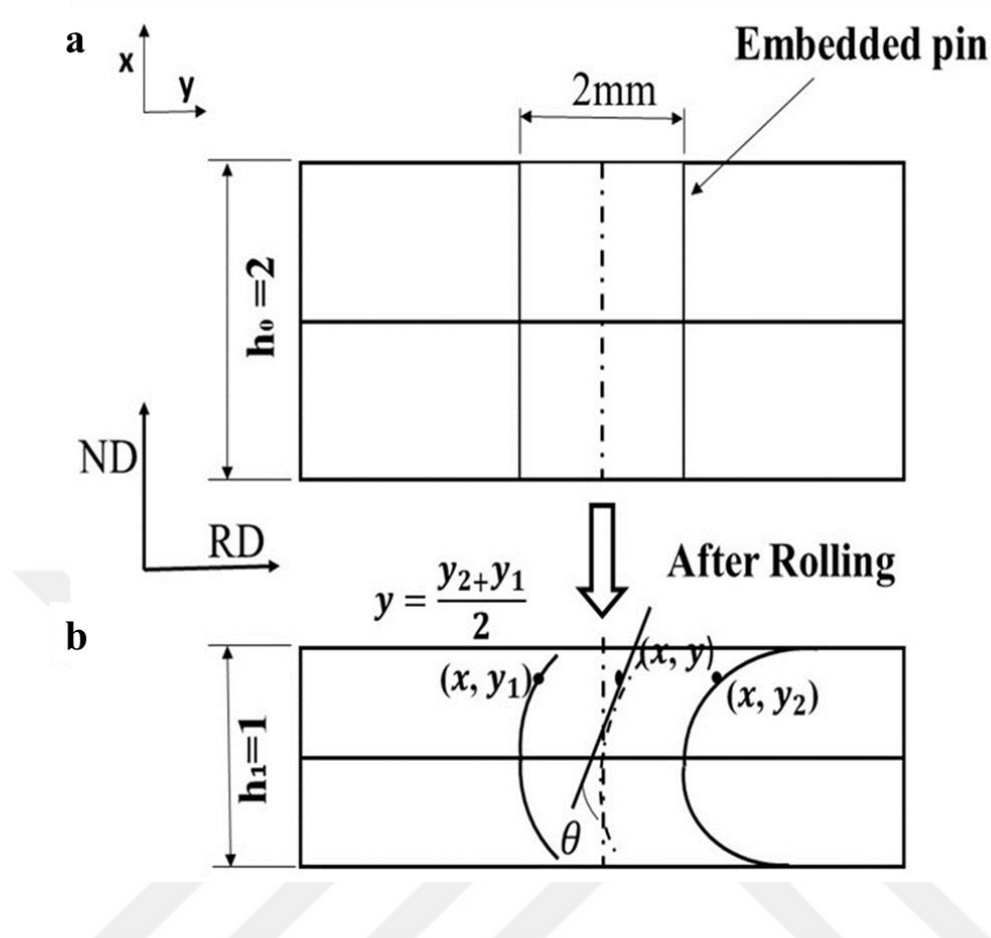


Figure 6.7: Schematic diagram showing the shear strain calculated by the embedded-pin method [51]: a) sketch before rolling, b) after rolling.

Redundant shear strain γ and equivalent strain ϵ_{eq} can be determined by the following equations. The rolling strain $\dot{\epsilon}$, which is the equivalent strain corresponding to the reduction in thickness $r = \left(1 - \frac{h_1}{h_0}\right)$, is equal to:

$$\dot{\epsilon} = \frac{2}{\sqrt{3}} \ln \frac{1}{1-r} \quad (6.2)$$

$$\gamma = \frac{2(1-r)^2}{r(2-r)} \tan\theta \cdot \ln \frac{1}{1-r} \quad (6.3)$$

$$\epsilon_{eq} = \sqrt{\frac{4}{3} \left(\ln \frac{1}{1-r}\right)^2 + \frac{\gamma^2}{3}} \quad (6.4)$$

From Eqs. (6.2) and (6.4), the equivalent strain can be rewritten as follows:

$$\varepsilon_{eq} = \sqrt{\dot{\varepsilon}^2 + \frac{\gamma^2}{3}} \quad (6.5)$$

where θ is the angle of pin inclination at each thickness.

Fig. 6.8 represents the form of the embedded pin after the first and second ARB cycle without lubrication. Two slabs were roll bonded strongly in both cases. After the rolling process, the pin is sheared in rolling direction in each case. The pin was highly deformed at the surface due to the high level of friction between the sheets and rolls, while the line of the pin is approximately vertically at the center of the slab which means no shear strain. Consequently, the redundant shear deformation in the specimen surface (Fig. 6.8a and b) is much larger than that in the center of the sheet for all cases. However, the redundant shear deformation in the second specimen (after second passes) (Fig. 6.8b) is larger than that in the first sheet (after the first pass) (Fig. 6.8a). From Eqs. (6.2)–(6.4), the distribution of the equivalent strain of the two cases was calculated and presented in Fig. 6.9. After two passes, the equivalent strain proves a maximum value of 2.5 at the surface and has another peak at the center where the surface was in the first cycle. It is clear that increasing the number of ARB passes, the number of equivalent strain peaks and the value of the equivalent strain increase. Fig. 6.9 shows that there was a considerable agreement between the results obtained from the numerical model and those obtained from experimental work.

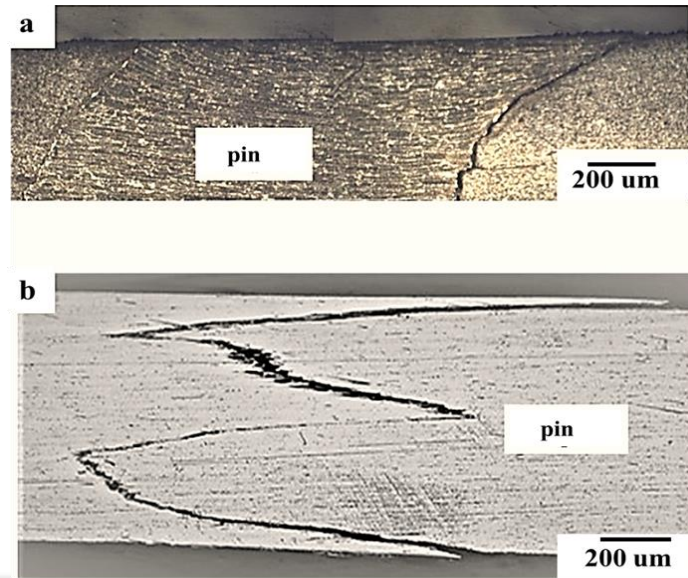


Figure 6.8: Shape of the embedded pin in the Al sheet processed by a) one ARB cycle and b) two ARB cycles.

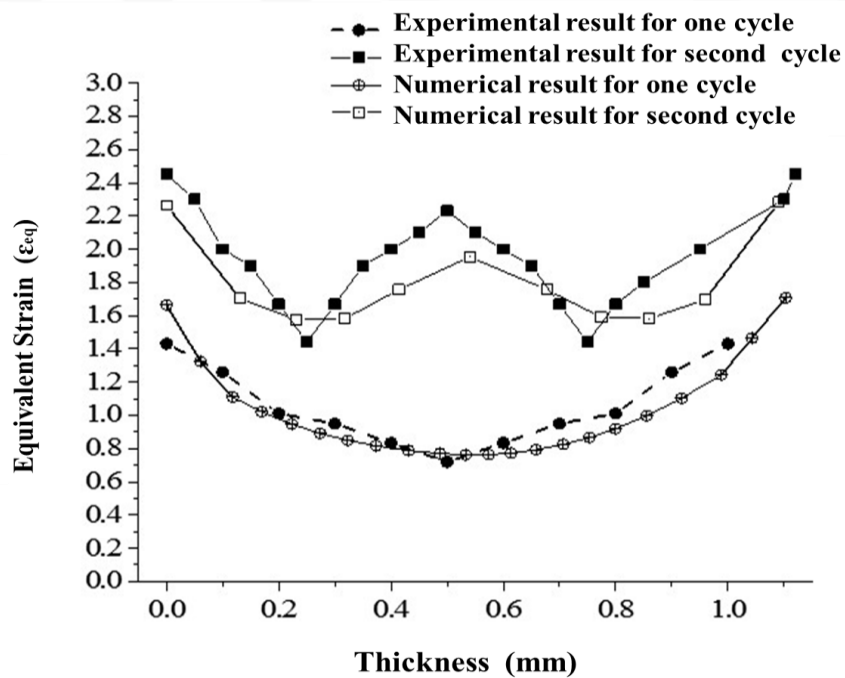


Figure 6.9: Equivalent strain distributions through the thickness of the Al composite sheet processed by one and two ARB cycle.

6.5 High cycle fatigue (HCF) models

The main aim of finite element simulation is the optimization of engineering design using the database of material properties achieved from the experiments. Therefore, the models are typically subject to various service conditions and operating requirements throughout their lives. So, it is necessary to consider the type of material and all possible scenarios like external loads and limitations as boundary conditions. The loads and possible constraints in the simulation rely on the conditions of the study.

The current study is designed by employing the boundary conditions as a fixture, and external loading precisely equal to the loading of experimental tests which are performed in the laboratory by fixing one head of the flat specimen without displacements in all directions and using the maximum force of the cyclic tension load on the other side, at room temperature. The forces are zero at the support part and maximum load applied at the opposite side.

The computational modeling using the finite element method (FEM) includes the following basic steps for the pre-processing: forming the model geometry, specification of boundary conditions (initial and loading), specification of material property, and mesh generation.

6.5.1 Creating the model geometry

According to the ANSYS software, there are three methods to form the finite element geometric models: direct generation, solid modeling, and importing a model. In this study, the high cyclic fatigue sample was developed and imported into the ANSYS WORKBENCH software (Fig. 6.10).

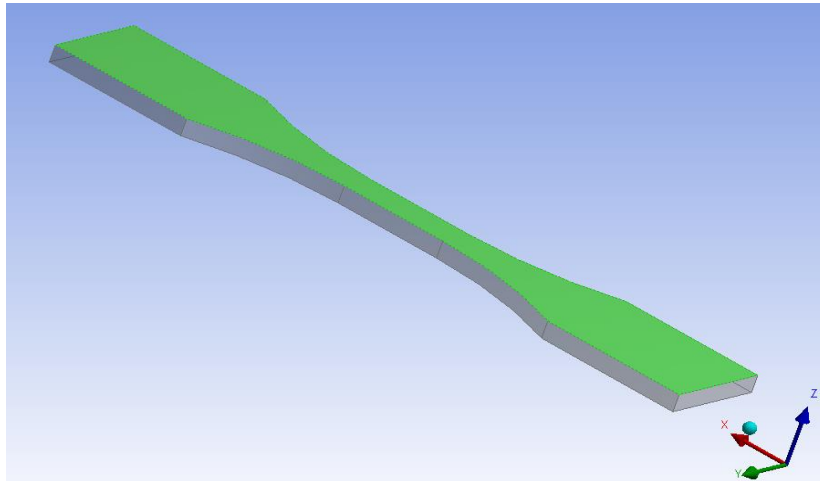


Figure 6.10: The geometrical model imported in the ANSYS Workbench software.

6.5.2 Mesh Generation

Creating a mesh is an essential part of the pre-processing. It may be a very time-consuming task for the analysis. The finite element mesh is shown in Fig. 6.11 using the fine element size, with the total element number of 9252 and the total node number of 1562.

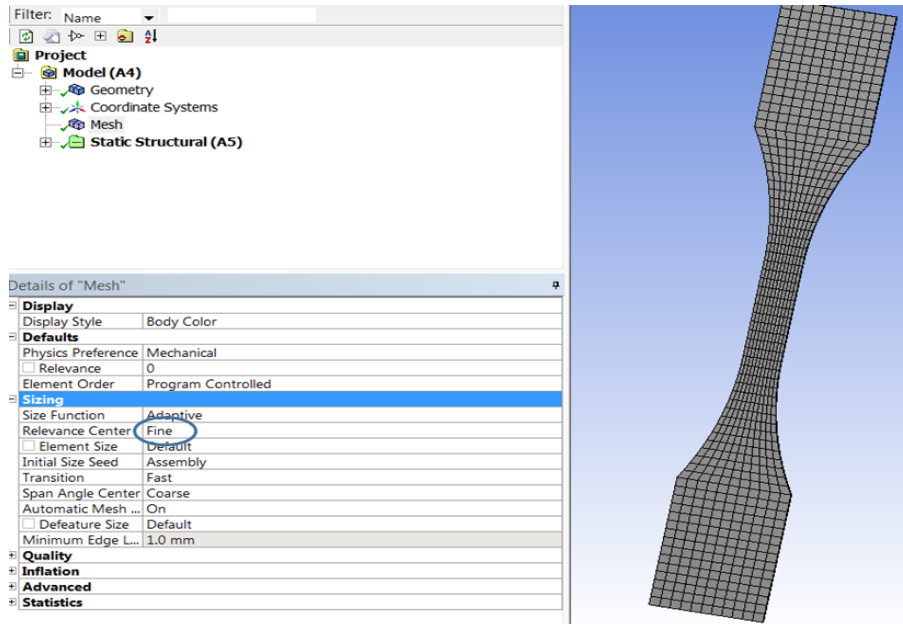


Figure 6.11: The meshing geometrical model of high cycle fatigue (HCF).

Also, solutions are presented by selecting the suitable project model in the analysis method choosing the static structural. Consequently, the initial material characteristics modified to the solution are as follows:

1. The density is the physical properties of materials.
2. Poisson's ratio and Young's modulus of elasticity are the Linear Elastic properties.
3. Tensile yield strength and ultimate tensile strength are the strength properties.

6.5.3 Simulation parameters

The details of the fatigue tool are utilized to define the different aspects of a fatigue analysis like handling of mean stress effects, loading type, etc. The simulation parameters of the high cycle fatigue for the 4layer Al6061/Al2024 composite are listed as follows.

1. Using fixed support at one end of the flat plate specimen.
2. Fatigue strength factor $K_f = 1$,
3. Stress ratio $R = \frac{\sigma_{min}}{\sigma_{max}} = 0.1$
4. Scale factor = 1.
5. Analysis type is for stress - life.
6. The employed stress component is the equivalent stress.

The simulation parameters of the high cycle fatigue are shown in Fig 6.12.

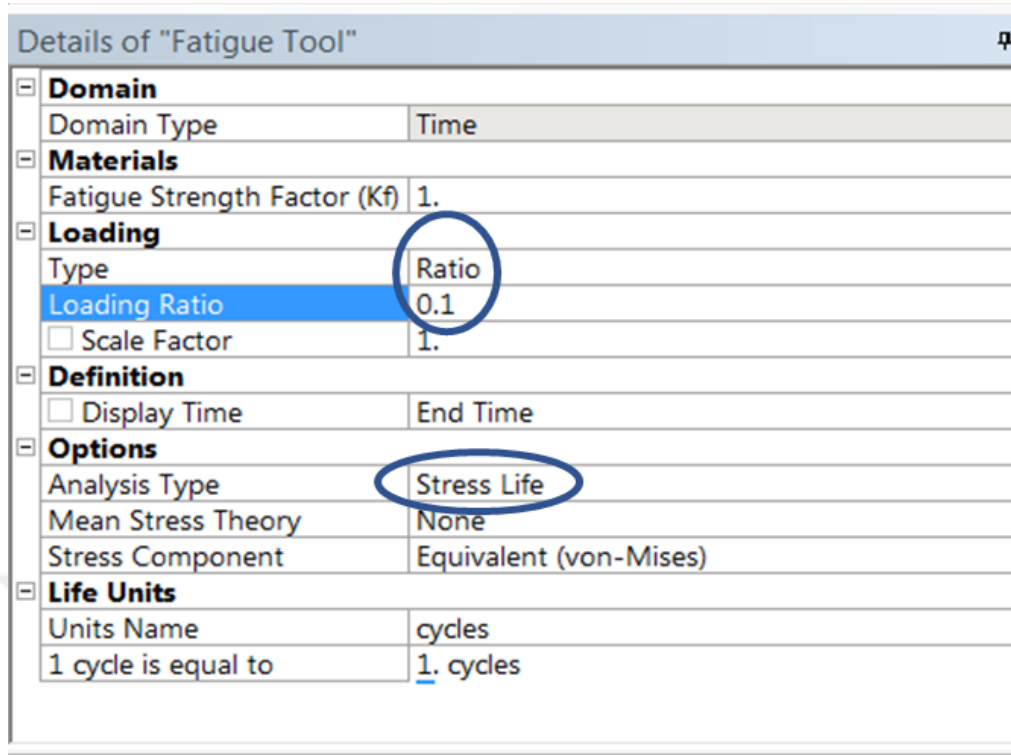


Figure 6.12: The simulation parameters of the high cycle fatigue.

6.6 Result and Discussion

The expected life patterns of the specimen under high cycle fatigue at various applied loading are displayed in Figs. 6.13-15. At the load level of 90% from the yield stress, the specimen failed at the minimum life. According to the results of the simulation, with decreasing the applied load to 80%, the fatigue life of the samples was increased significantly. It is the same behavior of the experimental data at the same load. Furthermore, the simulation results for all three cases represent a similar trend which decreasing the applied load enhanced the fatigue life of the samples. Also, as expected, the critical region with the minimum fatigue life was at the gauge length.

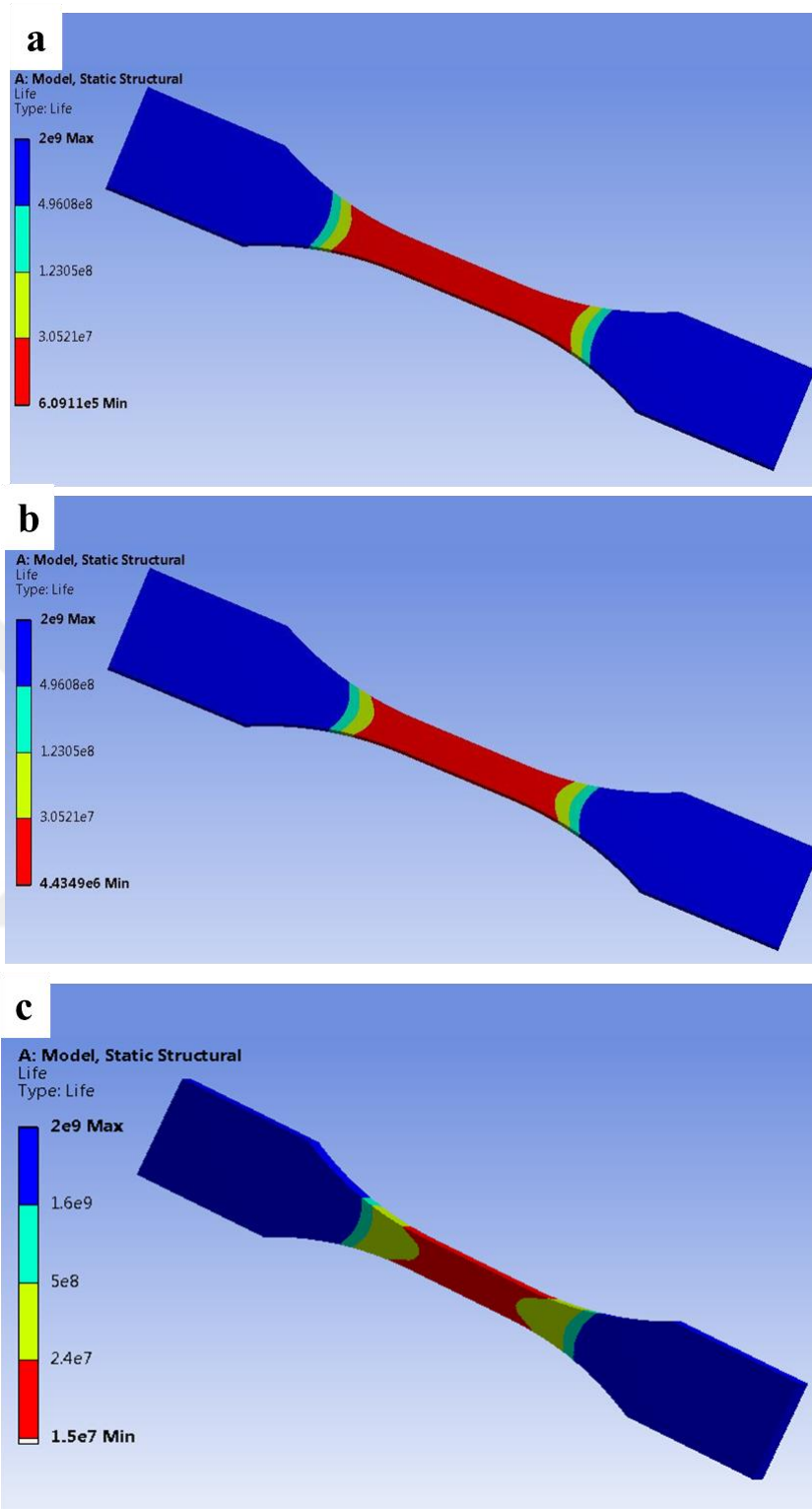


Figure 6.13: The fatigue life of Al6061/Al6061 under a) 90%, b) 80%, and c) 60% of yield strength.

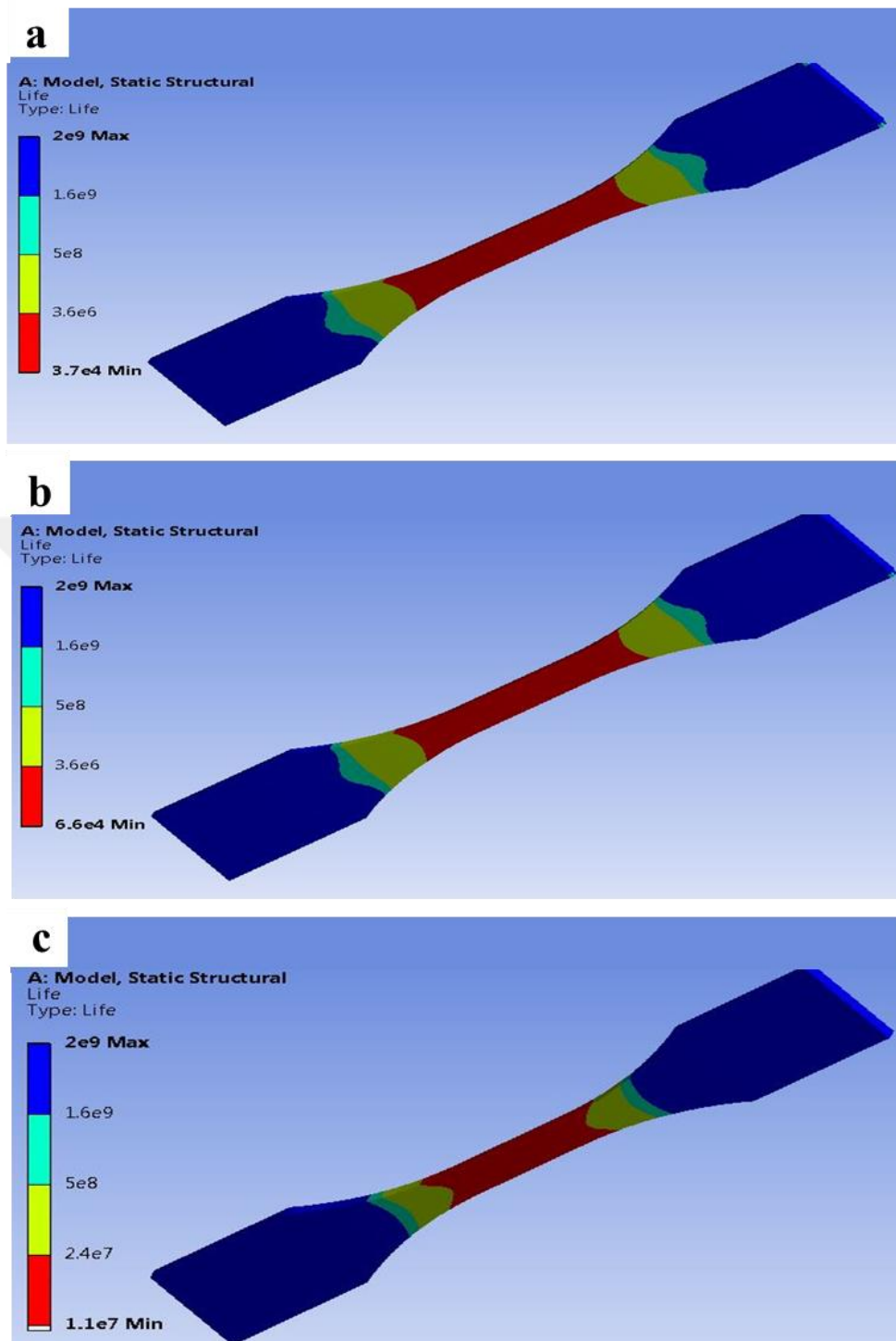


Figure 6.14: The fatigue life of Al2024/Al2024 under a) 90%, b) 80%, and c) 60% of yield strength.

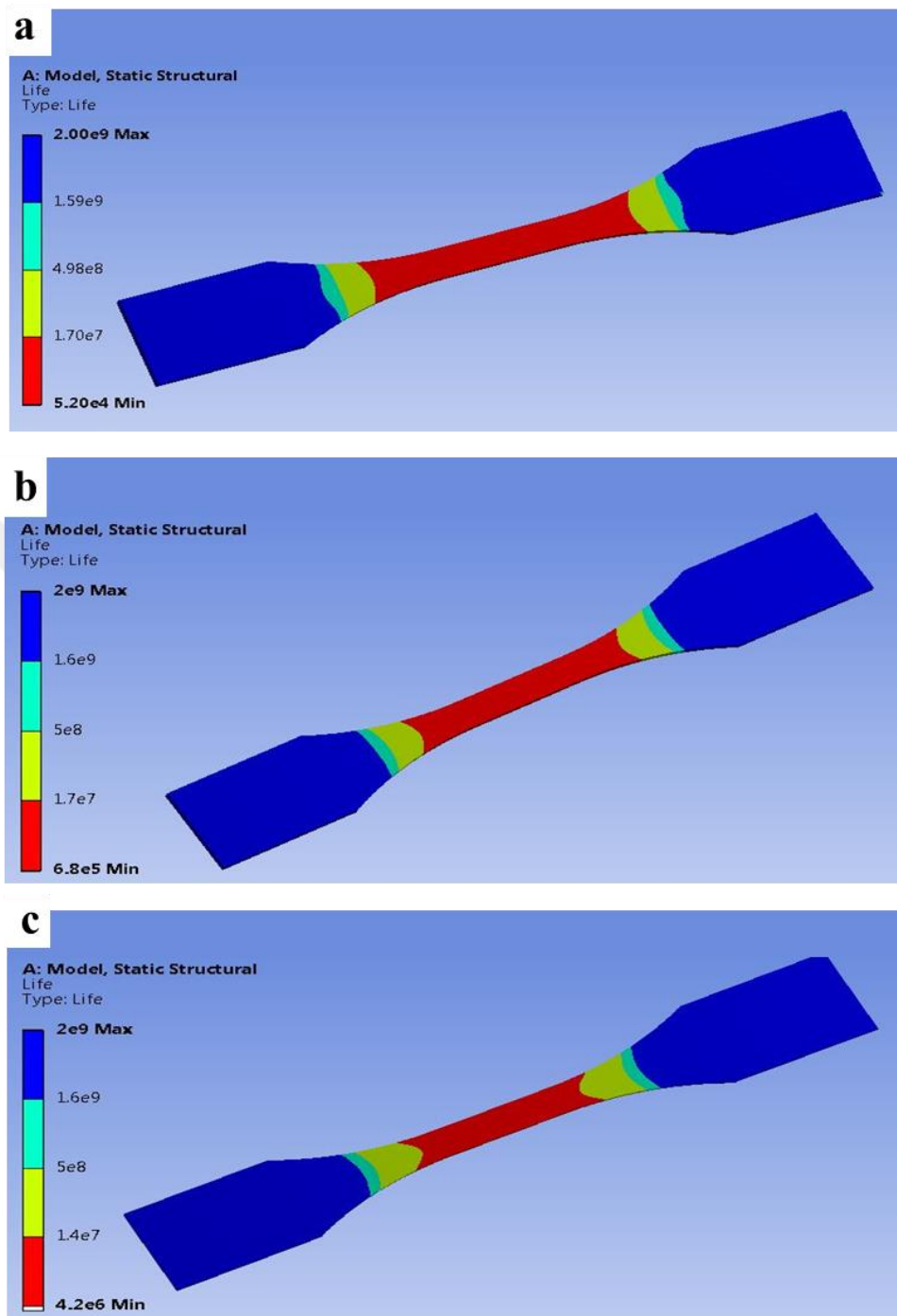


Figure 6.15: The fatigue life of Al6061/Al2024 under a) 90%, b) 80%, and c) 60% of yield strength.

The S-N curves for all conditions of Al6061/Al6061, Al2024/Al2024, and Al6061/Al2024 obtained from numerical analysis and experimental tests were shown in Fig. 6.17. Inspection of the results of the simulations and experimental works revealed that the

fatigue lives of the samples for all conditions are in good agreement and follow the same trend. The slopes of numerical results are nearly the same as experimental results for all cases. Additionally, for all conditions, the fatigue life obtained from the experimental results was lower than that of numerical analysis. This may be attributed to the microcracks and scratches on the surface of the samples which can affect the fatigue results while this parameter was not considered in the numerical analysis. Moreover, The fatigue simulation results show the estimated life in high fatigue strength is close to the experimental results, while in the low fatigue strength (long fatigue life) the difference between results were increased. This is due to the attendance of the effect of debonding between the layers in the experimental test, while the samples in the simulation part assumed to be solid and one layer.

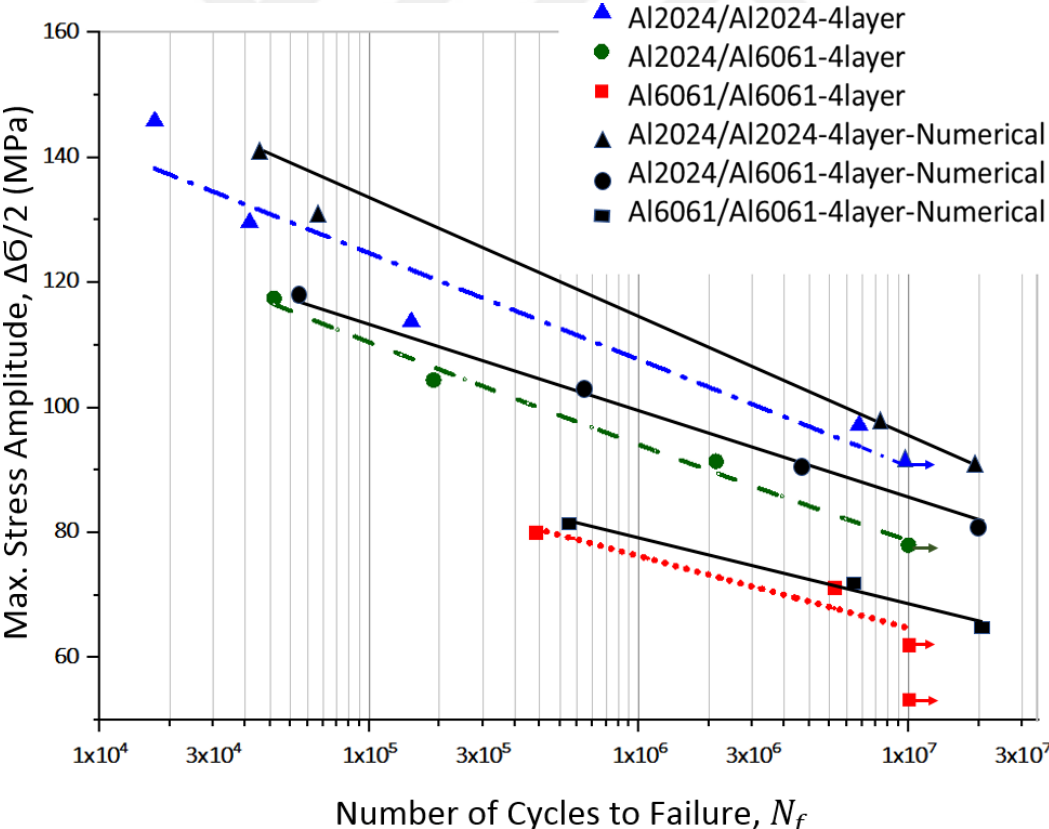


Figure 6.16: Comparison between experimental and simulation results of fatigue life.

6.7 Conclusions

The (ARB) process was simulated utilizing finite element analysis to evaluate the effective stress and the equivalent strain distribution through the thickness of the sheet after the ARB process. The experimental results of $\sigma_{(yld)}$ and the numerical results of $\sigma_{(v-m)}$ for Al2024/Al6061 composite after one, two, and three ARB cycles was calculated. The results show that there is an acceptable agreement between the effective stress and yield strength of the composite after the ARB process.

Also, the results of the finite element (FE) simulations of one and two-passes rolling process were utilized to achieve the material strain histories; the FE simulations were compared to embedded pin experiments to evaluate the shear deformation detected in ARB processed metals. The equivalent strain in a rolled slab gradually grows to the surface from the center and exhibits a distribution with the peak at the surface due to the influence of the frictional shear strain. There was a considerable agreement between the numerical and experimental results. Also, the results of the effective stress and equivalent strain were in good agreement with the results of the cold-rolled ARB. These equivalent strain analyses would provide useful guidelines for understanding the quantitative correlation between the microstructures and strain in the ARB process.

Finally, the high cycle fatigue simulation displays very close results. These are in good agreement with the empirical data in terms of fatigue life. Also, as expected, the experimental fatigue life values for all conditions were lower than the simulations in relation with the existence of microcracks and scratches on the sample surface.

CHAPTER VII

CONCLUSIONS

Accumulative roll bonding (ARB) has been shown to be a viable technique for producing different composites. In this work, multi-layered composites with IF steel and two aluminum alloys of 6061 and 2024 were successfully fabricated by ARB process. The highlighted results of the microstructure evolution and mechanical properties after ARB are listed below:

A general observation of all ARBed conditions revealed that the strength increases with increasing the number of ARB passes for all cases attributed to the work hardening and grain refinement. However, other factors such as the purity of sheet metal, the initial thickness of the layers, and the preheat temperature before the rolling process can affect the tensile strength.

Al6061/Al6061, Al2024/Al2024 and Al2024/Al6061 composites:

The effects of ARB on microstructure and mechanical properties response were investigated.

1. Bimetallic composite structures with up to 16 layers were successfully fabricated. Layer interfaces became obscure with increasing the number of cycles. Refinement down to the sub-micron regimes were achieved for Al2024 layers.
2. Improvement in hardness levels was observed up to 1.5 and 2 times for Al2024 and Al6061 layers, respectively. These values were attained rather quickly following the second pass in Al2024 layers, while the progress was moderate in Al6061 layers.

3. SPD induced work hardening and structural refinement led to a resultant strength exceeding 320MPa after two ARB cycles. On the contrary, the ductility decreased significantly to below 5% for the same composites.
4. The influence of the SPD on the mechanical properties was investigated in uniaxial and shear loading. The results show that shear strength follows a similar trend with tensile properties demonstrating improvement with increasing cycles.
5. The correlation between shear and ultimate tensile strength levels was obtained. This points to a rational way to assess the tensile properties using SPT results.
6. The bi-metallic composite demonstrates a significant enhancement in fatigue strength, especially at the low cycle regime.
7. The fatigue life of Al6061/Al2024/Al2024/Al6061 composite is higher than that of Al2024/Al6061/Al2024/Al6061 composite, for the same stress amplitude. The main reason for this difference is the reduction of the maximum stress of the outside aluminum layer attributed to the effective load transfer from the Al6061 softer layer to the Al2024 harder layer in the composite.
8. The direction of cracks starting from the soft layer of Al6061 was changed after propagating to the hard layer of Al2024 while on the opposite side when it originates from the hard layer to the soft layer, the direction of crack propagation was not affected.

Al6061/IF steel, Al2024/IF steel, and Al2024/Al6061/IF steel composite:

In this study, work was done to fabricate a multi-layered composite of the Al6061, Al2024, and IF steel in different layer architectures by utilizing the ARB process. The results are summarized as follows:

1. The development of surface and bulk mechanical properties of Al/IF steel composites were significantly higher than that of the Al/Al single material composite after the ARB process.
2. The tensile strength of the composites increased considerably in the first and second ARB cycles and the maximum strength was obtained at the second cycle; however, increasing the subsequent ARB cycles did not enhance the strength. Nevertheless, the strengths of the Al6061/IF steel layered composite were declined dramatically after the third ARB cycle due to necking and the rupture of IF steel layers.
3. Necking of IF steel layers took place after three cycles and rupture at the fourth and fifth cycles for Al6061/IF steel composite while necking and fracture started after four cycles ARB for Al2024/IF steel in relation to the difference of the flow stress between the Al and IF steel layers.
4. The strength of the composites in the case of the hard layers on the outside of the composite is higher than the other case where the hard layers are inside, due to the effect of load transfer from the Al to the IF layers.

5. The fatigue life of Al/IF/IF/Al composite is higher than that of the IF/Al/Al/IF, for the same stress amplitude as attributed to the branching of the cracks at the interface region that grew from the softer to harder metal.

The numerical modelling solution using Ansys software shows a good agreement with the experimental work results.

1. The results of the effective stress and equivalent strain were in good agreement with the results of the ARB processed composites.
2. The fatigue simulation results show that the life estimations in all conditions are close to the experimental results.

CHAPTER VIII

OUTLOOK

8.1 Further improvement of the ARB process

Although some efforts have been made to study the mechanical properties of multi-layered metal composites of aluminum and IF steel in the current work, these processes are not limited to the concluded experiments and the results achieved. As such, there are some suggestions for future projects.

Multi-layered metal composites fabricated by ARB method was studied by the use of monotonic and cyclic experiments at room temperature. HCF tests were used to observe the cyclic behavior of this composite. However, high cycle fatigue (HCF) with various temperature experiments was not premeditated in this study. Lack of discussion of the HCF response of multi-layered metal composites at elevated temperature may motivate investigators to consider this issue of interest. This holds true for LCF response as well.

The search for the creep-fatigue of the layered metallic composites is a very important indication for the design limitation of designing engineering. Therefore, this behavior can be one of the subjects of research in the future.

Investigations on the corrosion behavior of layered metallic composites fabricated by ARB process can be another subject of attention to complete this field of study.

The product of the ARB process can be used with other SPD processes for the purpose of further improvement in mechanical properties.

BIBLIOGRAPHY

- [1] E.A. Starke, J.T. Staley, Application of modern aluminum alloy to aircraft, *Prog. Aersp. Sci.* 32 (1996) 131–172. doi:10.1016/0376-0421(95)00004-6.
- [2] A. Hosseinzadeh, G.G. Yapici, High temperature characteristics of Al2024/SiC metal matrix composite fabricated by friction stir processing, *Mater. Sci. Eng. A.* 731 (2018) 487–494. doi:10.1016/j.msea.2018.06.077.
- [3] F. Kümmel, B. Diepold, K.F. Sauer, C. Schunk, A. Prakash, H.W. Höppel, M. Göken, High Lightweight Potential of Ultrafine-Grained Aluminum / Steel Laminated Metal Composites Produced by Accumulative Roll Bonding, 1800286 (2018) 1–8. doi:10.1002/adem.201800286.
- [4] F. Kümmel, H.W. Höppel, Layer architecture and fatigue life of ultrafine-grained laminated metal composites consisting of different aluminum alloys Author 's Accepted Manuscript, *Mater. Sci. Eng. A.* (2017). doi:10.1016/j.msea.2017.06.105.
- [5] F. Kümmel, T. Hausöl, H.W. Höppel, M. Göken, Enhanced fatigue lives in AA1050A/AA5005 laminated metal composites produced by accumulative roll bonding, *Acta Mater.* 120 (2016) 150–158. doi:10.1016/j.actamat.2016.08.039.
- [6] Y. Estrin, Y.T. Zhu, R.Z. Valiev, Y. Estrin, Z. Horita, T.G. Langdon, M.J. Zehetbauer, Producing bulk ultrafine-grained materials by severe plastic deformation [J] Producing Bulk Ultrafine-Grained Materials by Severe Plastic Deformation, (2006) 33–39. doi:10.1007/s11837-006-0213-7.
- [7] M. Kawasaki, Processing of ultrafine-grained materials through the application of severe plastic deformation, *Metall. Mater. Trans. A Phys. Metall. Mater. Sci.* 42 (2011) 3035–3045. doi:10.1007/s11661-010-0501-2.
- [8] M. Ahmadkhanbeigi, O. Shapourgan, G. Faraji, Microstructure and Mechanical Properties of Al Tube Processed by Friction Stir Tube Back Extrusion (FSTBE), *Trans. Indian Inst. Met.* 70 (2017) 1849–1856. doi:10.1007/s12666-016-0987-4.
- [9] A. Azushima, R. Kopp, A. Korhonen, D.Y. Yang, F. Micari, G.D. Lahoti, P. Groche, J. Yanagimoto, N. Tsuji, A. Rosochowski, A. Yanagida, Severe plastic deformation (SPD) processes for metals, *CIRP Ann. - Manuf. Technol.* 57 (2008) 716–735. doi:10.1016/j.cirp.2008.09.005.
- [10] G.G. Yapici, I. Karaman, Z.P. Luo, Mechanical twinning and texture evolution in severely deformed Ti-6Al-4V at high temperatures, *Acta Mater.* 54 (2006) 3755–3771. doi:10.1016/j.actamat.2006.04.007.
- [11] B.H. Kear, L.E. McCandlish, Nanostructured W-base materials. Synthesis, processing

- and properties, *J. Adv. Mater.* 25 (1993) 11–19.
- [12] R. Birringer, H. Gleiter, H.P. Klein, P. Marquardt, Nanocrystalline materials an approach to a novel solid structure with gas-like disorder: *Phys. Lett. A.* 102 (1984) 365–369. doi:10.1016/0375-9601(84)90300-1.
- [13] C.C. Koch, Top-down synthesis of nanostructured materials: Mechanical and thermal processing methods, *Rev. Adv. Mater. Sci.* 5 (2003) 91–99.
- [14] H. Chang, C.J. Altstetter, R.S. Averback, Characteristics of nanophase TiAl produced by inert gas condensation, *J. Mater. Res.* 7 (1992) 2962–2970. doi:10.1557/JMR.1992.2962.
- [15] U. Erb, Electrodeposited nanocrystals: Synthesis, properties and industrial applications, *Nanostructured Mater.* 6 (1995) 533–538. doi:10.1016/0965-9773(95)00114-X.
- [16] W. Chang, G. Skandan, S.C. Danforth, M. Rose, A.G. Balogh, H. Hahn, B. Kear, Nanostructured ceramics synthesized by chemical vapor condensation, *Nanostructured Mater.* 6 (1995) 321–324. doi:10.1016/0965-9773(95)00062-3.
- [17] R. Birringer, Nanocrystalline materials, *Mater. Sci. Eng. A.* 117 (1989) 33–43. doi:10.1016/0921-5093(89)90083-X.
- [18] A.P. Zhilyaev, T.G. Langdon, Using high-pressure torsion for metal processing: Fundamentals and applications, *Prog. Mater. Sci.* 53 (2008) 893–979. doi:10.1016/j.pmatsci.2008.03.002.
- [19] T.G. Langdon, Twenty-five years of ultrafine-grained materials: Achieving exceptional properties through grain refinement, *Acta Mater.* 61 (2013) 7035–7059. doi:10.1016/j.actamat.2013.08.018.
- [20] A. Korbel, F. Dobrzanski, M. Richert, Strain hardening of aluminium at high strains, *Acta Metall.* 31 (1983) 293–298. doi:10.1016/0001-6160(83)90106-2.
- [21] J.Y. Huang, Y.T. Zhu, H. Jiang, T.C. Lowe, Microstructures and dislocation configurations in nanostructured Cu processed by repetitive corrugation and straightening, *Acta Mater.* 49 (2001) 1497–1505. doi:10.1016/S1359-6454(01)00069-6.
- [22] K. Neishi, K. Kaneko, K. Nakamura, M. Nakagaki, Z. Horita, Development of Severe Torsion Straining Process for Rapid Continuous Grain Refinement, *Mater. Trans.* 45 (2005) 3338–3342. doi:10.2320/matertrans.45.3338.
- [23] M. Etou, S. Fukushima, T. Sasaki, Y. Haraguchi, K. Miyata, M. Wakita, T. Tomida, N. Imai, M. Yoshida, Y. Okada, Super Short Interval Multi-pass Rolling Process for Ultrafine-grained Hot Strip, *ISIJ Int.* 48 (25984) 1142–1147.
- [24] M.J. Zehetbauer, R.Z. Valiev, *Nanomaterials by Severe Plastic Deformation*, 2004.

doi:10.1002/3527602461.

- [25] R.. S. Mishra, M.. W. Mahoney, S.. X. McFadden, N.. a. Mara, A.. K. Mukherjee, High strain rate superplasticity in a friction stir processed 7075 Al alloy, *Scr. Mater.* 42 (1999) 163–168. doi:10.1016/S1359-6462(99)00329-2.
- [26] S. Mizunuma, Large Straining Behavior and Microstructure Refinement of Several Metals by Torsion Extrusion Process, *Mater. Sci. Forum.* 503–504 (2009) 185–192. doi:10.4028/www.scientific.net/msf.503-504.185.
- [27] Y. Saito, N. Tsuji, H. Utsunomiya, T. Sakai, R. Hong, Ultra-fine grained bulk aluminum produced by accumulative roll-bonding proces, *Scr. Mater.* 40 (1999) 795–800.
- [28] B. Beausir, J. Scharnweber, J. Jaschinski, H.G. Brokmeier, C.G. Oertel, W. Skrotzki, Plastic anisotropy of ultrafine grained aluminium alloys produced by accumulative roll bonding, *Mater. Sci. Eng. A.* 527 (2010) 3271–3278. doi:10.1016/j.msea.2010.02.006.
- [29] I. Topic, H.W. Höppel, M. Göken, Influence of rolling direction on strength and ductility of aluminium and aluminium alloys produced by accumulative roll bonding, *J. Mater. Sci.* 43 (2008) 7320–7325. doi:10.1007/s10853-008-2754-3.
- [30] N. Tsuji, Y. Saito, S.H. Lee, Y. Minamino, ARB (accumulative roll-bonding) and other new techniques to produce bulk ultrafine grained materials, *Adv. Eng. Mater.* 5 (2003) 338–344. doi:10.1002/adem.200310077.
- [31] Y. Saito, N. Tsuji, H. Utsunomiya, T. Sakai, R.G. Hong, Ultra-Fine Grained Bulk Aluminum Produced By Accumulative Roll-Bonding (Arb) Process, 39 (1998) 1221–1227.
- [32] D. Campanella, COMPUTER AIDED ENGINEERING PhD Thesis, (2014).
- [33] Y. Saito, H. Utsunomiya, N. Tsuji, T. Sakai, Novel ultra-high straining process for bulk materials development of the accumulative roll-bonding (ARB) process, *Acta Mater.* 47 (1999) 579–583. doi:10.1016/S1359-6454(98)00365-6.
- [34] R.M.C. William F. Hosford, *Metal Forming: Mechanics and Metallurgy*, 4th Edition, 2011.
- [35] I. Topi, Ultrafine-grained Metal Sheets produced using the Accumulative Roll Bonding Process for Light-Weight Structures, (2008).
- [36] Y. Saito, H. Utsunomiya, N. Tsuji, T. Sakai, Novel ultra-high straining process for bulk materials—development of the accumulative roll-bonding (ARB) process, *Acta Mater.* 47 (1998) 579–583. doi:10.1016/S1359-6454(98)00365-6.
- [37] T. Hausöl, H.W. Höppel, M. Göken, Microstructure and mechanical properties of

- accumulative roll bonded aluminium alloy AA5754, *J. Phys. Conf. Ser.* 240 (2010) 012128. doi:10.1088/1742-6596/240/1/012128.
- [38] L. Su, C. Lu, Microstructure and mechanical properties of AA5005 / AA6061 laminated composite processed by accumulative roll bonding, 45 (2014) 515–522.
- [39] N. Tsuji, Y. Saito, H. Utsunomiya, S. Tanigawa, Ultra-fine grained bulk steel produced by accumulative roll-bonding (ARB) process, *Scr. Mater.* 40 (1999) 795–800. doi:10.1016/S1359-6462(99)00015-9.
- [40] L. Jiang, M.T. Pérez-Prado, P.A. Gruber, E. Arzt, O.A. Ruano, M.E. Kassner, Texture, microstructure and mechanical properties of equiaxed ultrafine-grained Zr fabricated by accumulative roll bonding, *Acta Mater.* 56 (2008) 1228–1242. doi:10.1016/j.actamat.2007.11.017.
- [41] Y.B. Zhang, O. V. Mishin, N. Kamikawa, A. Godfrey, W. Liu, Q. Liu, Microstructure and mechanical properties of nickel processed by accumulative roll bonding, *Mater. Sci. Eng. A.* 576 (2013) 160–166. doi:10.1016/j.msea.2013.04.002.
- [42] V. Yousefi Mehr, M.R. Toroghinejad, A. Rezaeian, Mechanical properties and microstructure evolutions of multilayered Al-Cu composites produced by accumulative roll bonding process and subsequent annealing, *Mater. Sci. Eng. A.* 601 (2014) 40–47. doi:10.1016/j.msea.2014.02.023.
- [43] Y.F. Sun, N. Tsuji, H. Fujii, F.S. Li, Cu/Zr nanoscaled multi-stacks fabricated by accumulative roll bonding, *J. Alloys Compd.* 504 (2010) 443–447. doi:10.1016/j.jallcom.2010.02.201.
- [44] M. Talebian, M. Alizadeh, Manufacturing Al/steel multilayered composite by accumulative roll bonding and the effects of subsequent annealing on the microstructural and mechanical characteristics, *Mater. Sci. Eng. A.* 590 (2014) 186–193. doi:10.1016/j.msea.2013.10.026.
- [45] M. Hosseini, N. Pardis, H. Danesh Manesh, M. Abbasi, D.I. Kim, Structural characteristics of Cu/Ti bimetal composite produced by accumulative roll-bonding (ARB), *Mater. Des.* 113 (2017) 128–136. doi:10.1016/j.matdes.2016.09.094.
- [46] D. Yang, P. Cizek, P. Hodgson, C. Wen, Ultrafine equiaxed-grain Ti/Al composite produced by accumulative roll bonding, *Scr. Mater.* 62 (2010) 321–324. doi:10.1016/j.scriptamat.2009.11.036.
- [47] H. Solouki, E. Borhani, M.T. Nezhad, The effect of temperature and strain rate on elongation to failure in nanostructured Al-0.2wt % Zr alloy fabricated by ARB process, 48 (2016) 125–132. doi:10.7508/jufgnsm.2015.02.007.

- [48] N. Tsuji, Y. Ito, Y. Saito, Y. Minamino, Strength and ductility of ultrafine grained aluminum and iron produced by ARB and annealing, *Scr. Mater.* 47 (2002) 893–899. doi:10.1016/S1359-6462(02)00282-8.
- [49] Y.S. N. Tsuji, K. Shiotsuki, *Mater. Trans.*_Superplasticity of Ultra-Fine Grained Al-Mg Alloy Produced by Accumulative Roll-Bonding.*Mater. Trans. JIM* 1999, 40, 765, (1999) 765.
- [50] N. Tsuji, K. Shiotsuki, H. Utsunomiya, Y. Saito, Low Temperature Superplasticity of Ultra-Fine Grained 5083 Aluminium Alloy Produced by Accumulative Roll-Bonding, *Mater. Sci. Forum.* 304–306 (2009) 73–78. doi:10.4028/www.scientific.net/msf.304-306.73.
- [51] S.H. Lee, Y. Saito, N. Tsuji, H. Utsunomiya, T. Sakai, Role of shear strain in ultragrain refinement by accumulative roll-bonding (ARB) process, *Scr. Mater.* 46 (2002) 281–285. doi:10.1016/S1359-6462(01)01239-8.
- [52] T.R. Society, P. Transactions, E. Sciences, Development of Microstructure in FCC Metals during Cold Work Author (s): Niels Hansen and Dorte Juul Jensen Source : Philosophical Transactions : Mathematical , Physical and Engineering Sciences , Vol . 357 , No . 1756 , Deformation Processing of Metals, 357 (2013) 1447–1469.
- [53] X. Huang, N. Tsuji, N. Hansen, Y. Minamino, Microstructural evolution during accumulative roll-bonding of commercial purity aluminum, *Mater. Sci. Eng. A.* 340 (2003) 265–271. doi:10.1016/S0921-5093(02)00182-X.
- [54] S.H. Lee, T. Sakai, D.H. Shin, Fabrication of ultrafine grained aluminum by differential speed accumulative roll-bonding (ARB) process, *Mater. Trans.* 44 (2003) 1382–1385. doi:10.2320/matertrans.44.1382.
- [55] W. Yang, An Investigation of Bonding Mechanism in Metal Cladding By Warm Rolling, (2011).
- [56] N. Bay, Mechanisms Producing Metallic Bonds in Cold Welding, *Am. Weld. Soc.* 62 (1983) 137–142.
- [57] L. Li, K. Nagai, F. Yin, Progress in cold roll bonding of metals, *Sci. Technol. Adv. Mater.* 9 (2008) 023001. doi:10.1088/1468-6996/9/2/023001.
- [58] P. Groche, S. Wohletz, A. Erbe, A. Altin, Effect of the primary heat treatment on the bond formation in cold welding of aluminum and steel by cold forging, *J. Mater. Process. Technol.* 214 (2014) 2040–2048. doi:10.1016/j.jmatprotec.2013.12.021.
- [59] J.G. Lenard, Primer on Flat Rolling, 2007. doi:10.1016/B978-0-08-045319-4.X5000-1.
- [60] H.W. Wagener, J. Haats, Pressure welding of corrosion resistant metals by cold

- extrusion, *J. Mater. Process. Techn.* 45 (1994) 275–280. doi:10.1016/0924-0136(94)90352-2.
- [61] A. Anghelus, M.N. Avettand-Fönoöl, C. Cordier, R. Taillard, Microstructural evolution of aluminium/Al-Ni-Sm glass forming alloy laminates obtained by controlled accumulative roll bonding, *J. Alloys Compd.* 631 (2015) 209–218. doi:10.1016/j.jallcom.2014.12.231.
- [62] M. Slámová, P. Homola, M. Karlík, Thermal stability of twin-roll cast Al-Fe-Mn-Si sheets accumulative roll bonded at different temperatures, *Mater. Sci. Eng. A.* 462 (2007) 106–110. doi:10.1016/j.msea.2006.03.148.
- [63] P. Homola, M. Slámová, M. Karlík, J. Čížek, I. Procházka, Effect of the Temperature of Accumulative Roll Bonding on the Microstructure and Properties of Twin-Roll Cast AA8006 Alloy, *Mater. Sci. Forum.* 503–504 (2006) 281–286. doi:10.4028/www.scientific.net/MSF.503-504.281.
- [64] H. Yan, J.G. Lenard, A study of warm and cold roll-bonding of an aluminium alloy, *Mater. Sci. Eng. A.* 385 (2004) 419–428. doi:10.1016/j.msea.2004.07.018.
- [65] Y. Chen, H. Liu, J. Feng, Friction stir welding characteristics of different heat-treated-state 2219 aluminum alloy plates, *Mater. Sci. Eng. A.* 420 (2006) 21–25. doi:10.1016/j.msea.2006.01.029.
- [66] A.L.M. Costa, A.C.C. Reis, L. Kestens, M.S. Andrade, Ultra grain refinement and hardening of IF-steel during accumulative roll-bonding, *Mater. Sci. Eng. A.* 406 (2005) 279–285. doi:10.1016/j.msea.2005.06.058.
- [67] D. Terada; S. Inoue; N. Tsuji, Microstructure and mechanical properties of commercial purity titanium severely deformed by ARB process, (2007) 1673–1681. doi:10.1007/s10853-006-0909-7.
- [68] T. Inoue, A. Yanagida, J. Yanagimoto, Finite element simulation of accumulative roll-bonding process, *Mater. Lett.* 106 (2013) 37–40. doi:10.1016/j.matlet.2013.04.093.
- [69] S. Haribabu, W.S. Che, B. Srinivas, D. Venkateswarulu, S. Alapati, T. Ramachandraiah, M. Cheepu, S. Karna, Fabrication and Analysis of Accumulative Roll Bonding Process between Magnesium and Aluminum Multi-Layers, *Appl. Mech. Mater.* 877 (2018) 183–189. doi:10.4028/www.scientific.net/amm.877.183.
- [70] G. Krallics, J.G. Lenard, An examination of the accumulative roll-bonding process, *J. Mater. Process. Technol.* 152 (2004) 154–161. doi:10.1016/j.jmatprotec.2004.03.015.
- [71] N.V. Govindaraj, Nagaraj Vinayagam Govindaraj Light-weight materials produced by accumulative roll bonding, 2013.

- [72] J.E. Hatch, Aluminum Properties and Physical Metallurgy, ASM Int. (1984) 424. doi:10.1361/appm1984p001.
- [73] A.H. Ghobadlou, high temperature mechanical characteristics of friction stir processed high temperature mechanical characteristics of friction stir processed, (2018).
- [74] D. Terada, S. Inoue, N. Tsuji, Microstructure and mechanical properties of commercial purity titanium severely deformed by ARB process, *J. Mater. Sci.* 42 (2007) 1673–1681. doi:10.1007/s10853-006-0909-7.
- [75] H. Kitahara, T. Horike, M. Tsushida, S. Ando, N. Tsuji, Fatigue Fracture Behavior of ARB Processed Aluminum, *Mater. Sci. Forum.* 654–656 (2010) 2479–2482. doi:10.4028/www.scientific.net/MSF.654-656.2479.
- [76] R.S. V. G. Arigela , L. Lienshoeft¹, P.Chekhonin, Comparative study of texture evolution in ARB processed AA2014, AA6063 and AA2014/6063 aluminium laminates, *Kov. Mater.* 53 2015 245–249 DOI 10.4149/Km 2015 4 245. 53 (2015) 1–5. doi:10.4149/km-2015-4-245.
- [77] R. Zheng, T. Bhattacharjee, A. Shibata, N. Tsuji, C. Ma, Effect of Accumulative Roll Bonding (ARB) and Subsequent Aging on Microstructure and Mechanical Properties of 2024 Al Alloy, *Mater. Trans.* 57 (2016) 1462–1470. doi:10.2320/matertrans.MH201512.
- [78] M. Alvand, M. Naseri, E. Borhani, H. Abdollah-Pour, Nano/ultrafine grained AA2024 alloy processed by accumulative roll bonding: A study of microstructure, deformation texture and mechanical properties, *J. Alloys Compd.* 712 (2017) 517–525. doi:10.1016/j.jallcom.2017.04.117.
- [79] Z.P. Xing, S.B. Kang, H.W. Kim, Structure and properties of AA3003 alloy produced by accumulative roll bonding process, *J. Mater. Sci.* 37 (2002) 717–722. doi:10.1023/A:1013879528697.
- [80] M. Sato, N. Tsuji, Y. Minamino, Y. Koizumi, Formation of nanocrystalline surface layers in various metallic materials by near surface severe plastic deformation, *Sci. Technol. Adv. Mater.* 5 (2004) 145–152. doi:10.1016/j.stam.2003.10.015.
- [81] K.T. Park, H.J. Kwon, W.J. Kim, Y.S. Kim, Microstructural characteristics and thermal stability of ultrafine grained 6061 Al alloy fabricated by accumulative roll bonding process, *Mater. Sci. Eng. A.* 316 (2001) 145–152. doi:10.1016/S0921-5093(01)01261-8.
- [82] S.H. Lee, Y. Saito, T. Sakai, H. Utsunomiya, Microstructures and mechanical properties of 6061 aluminum alloy processed by accumulative roll-bonding, *Mater. Sci. Eng. A.* 325 (2002) 228–235. doi:10.1016/S0921-5093(01)01416-2.

- [83] H. Yu, L. Su, C. Lu, K. Tieu, H. Li, J. Li, A. Godbole, C. Kong, Enhanced mechanical properties of ARB-processed aluminum alloy 6061 sheets by subsequent asymmetric cryorolling and ageing, *Mater. Sci. Eng. A.* 674 (2016) 256–261. doi:10.1016/j.msea.2016.08.003.
- [84] L. Su, C. Lu, A.A. Gazder, A.A. Saleh, G. Deng, K. Tieu, H. Li, Shear texture gradient in AA6061 aluminum alloy processed by accumulative roll bonding with high roll roughness, *J. Alloys Compd.* 594 (2014) 12–22. doi:10.1016/j.jallcom.2014.01.125.
- [85] L. Hollang, J. Scharnweber, K. Reuther, W. Skrotzki, Deformation mechanisms in ARB processed aluminium alloy AA6016 at low temperatures, *J. Phys. Conf. Ser.* 240 (2010) 012148. doi:10.1088/1742-6596/240/1/012148.
- [86] H. Alvandi, K. Farmanesh, Microstructural and Mechanical Properties of Nano/Ultra-fine Structured 7075 Aluminum Alloy by Accumulative Roll-Bonding Process, *Procedia Mater. Sci.* 11 (2015) 17–23. doi:10.1016/j.mspro.2015.11.020.
- [87] P. Hidalgo-Manrique, C.M. Cepeda-Jiménez, A. Orozco-Caballero, O.A. Ruano, F. Carreño, Evolution of the microstructure, texture and creep properties of the 7075 aluminium alloy during hot accumulative roll bonding, *Mater. Sci. Eng. A.* 606 (2014) 434–442. doi:10.1016/j.msea.2014.03.105.
- [88] Z.P. Xing, S.B. Kang, H.W. Kim, Microstructural evolution and mechanical properties of the AA8011 alloy during the accumulative roll-bonding process, *Metall. Mater. Trans. A Phys. Metall. Mater. Sci.* 33 (2002) 1521–1530. doi:10.1007/s11661-002-0074-9.
- [89] M. Karlík, I. Procházka, M. Slámová, P. Homola, J. Čížek, Effect of the Temperature of Accumulative Roll Bonding on the Microstructure and Properties of Twin-Roll Cast AA8006 Alloy, *Mater. Sci. Forum.* 503–504 (2009) 281–286. doi:10.4028/www.scientific.net/msf.503-504.281.
- [90] M. Cieslar, M. Pokovö, Annealing effects in twin-roll cast AA8006 aluminium sheets processed by accumulative roll-bonding, *Materials (Basel).* 7 (2014) 8058–8069. doi:10.3390/ma7128058.
- [91] N. Kamikawa, T. Sakai, N. Tsuji, Effect of redundant shear strain on microstructure and texture evolution during accumulative roll-bonding in ultralow carbon IF steel, *Acta Mater.* 55 (2007) 5873–5888. doi:10.1016/j.actamat.2007.07.002.
- [92] H. Yu, C. Lu, A.K. Tieu, A. Godbole, L. Su, Y. Sun, M. Liu, D. Tang, C. Kong, Fabrication of ultra-thin nanostructured bimetallic foils by Accumulative Roll Bonding and Asymmetric Rolling, *Sci. Rep.* 3 (2013) 1–9. doi:10.1038/srep02373.
- [93] S.H. Lee, Y. Saito, T. Sakai, H. Utsunomiya, Microstructures and mechanical properties of 6061 aluminum alloy processed by accumulative roll-bonding, 325 (2002) 228–235.

- [94] M.R. Rezaei, M.R. Toroghinejad, F. Ashrafizadeh, Effects of ARB and ageing processes on mechanical properties and microstructure of 6061 aluminum alloy, *J. Mater. Process. Technol.* 211 (2011) 1184–1190. doi:10.1016/j.jmatprotec.2011.01.023.
- [95] M. Mahendra Boopathi, K.P. Arulshri, N. Iyandurai, Evaluation of mechanical properties of Aluminium alloy 2024 reinforced with silicon carbide and fly ash hybrid metal matrix composites, *Am. J. Appl. Sci.* 10 (2013) 219–229. doi:10.3844/ajassp.2013.219.229.
- [96] A. Shahsavari, F. Karimzadeh, A. Rezaeian, H. Heydari, Significant Increase in Tensile Strength and Hardness in 2024 Aluminum Alloy by Cryogenic Rolling, *Procedia Mater. Sci.* 11 (2015) 84–88. doi:10.1016/j.mspro.2015.11.111.
- [97] M. Naseri, M. Reihanian, E. Borhani, A new strategy to simultaneous increase in the strength and ductility of AA2024 alloy via accumulative roll bonding (ARB), *Mater. Sci. Eng. A.* 656 (2016) 12–20. doi:10.1016/j.msea.2016.01.020.
- [98] N. Tsuji, R. Ueji, Y. Minamino, Nanoscale crystallographic analysis of ultrafine grained IF steel fabricated by ARB process, *Scr. Mater.* 47 (2002) 69–76. doi:10.1016/S1359-6462(02)00088-X.
- [99] B. a. Movchan, F.D. Lemkey, Mechanical properties of fine-crystalline two-phase materials, *Mater. Sci. Eng. A.* 224 (1997) 136–145. doi:10.1016/S0921-5093(96)10455-X.
- [100] H. Sieber, G. Wilde, J.H. Perepezko, Thermally activated amorphous phase formation in cold-rolled multilayers of $\text{Al} \pm \text{Ni}$, $\text{Al} \pm \text{Ta}$, $\text{Al} \pm \text{Fe}$ and $\text{Zr} \pm \text{Cu}$, 252 (1999) 611–615.
- [101] J.M. Lee, B.R. Lee, S.B. Kang, Control of layer continuity in metallic multilayers produced by deformation synthesis method, *Mater. Sci. Eng. A.* 406 (2005) 95–101. doi:10.1016/j.msea.2005.06.030.
- [102] G. Min, J.M. Lee, S.B. Kang, H.W. Kim, Evolution of microstructure for multilayered Al/Ni composites by accumulative roll bonding process, *Mater. Lett.* 60 (2006) 3255–3259. doi:10.1016/j.matlet.2006.03.001.
- [103] L. Chen, Z. Yang, B. Jha, G. Xia, J.W. Stevenson, Clad metals, roll bonding and their applications for SOFC interconnects, *J. Power Sources.* 152 (2005) 40–45. doi:10.1016/j.jpowsour.2005.01.055.
- [104] T.H.E. Perfect, P. For, Bumpers made of clad metals, 2011, <http://www.cladit.com/examples/bumpers.html>. the Perfect Partner for Active, (n.d.).
- [105] X. Huang, Hardening by Annealing and Softening by Deformation in Nanostructured Metals, *Science* (80-.). 312 (2006) 249–251. doi:10.1126/science.1124268.
- [106] O. Yazar, T. Ediz, T. Öztürk, Control of macrostructure in deformation processing of

- metal/metal laminates, *Acta Mater.* 53 (2005) 375–381. doi:10.1016/j.actamat.2004.09.033.
- [107] M. Eizadjou, A. Kazemi Talachi, H. Danesh Manesh, H. Shakur Shahabi, K. Janghorban, Investigation of structure and mechanical properties of multi-layered Al/Cu composite produced by accumulative roll bonding (ARB) process, *Compos. Sci. Technol.* 68 (2008) 2003–2009. doi:10.1016/j.compscitech.2008.02.029.
- [108] M. Tayyebi, B. Eghbali, Study on the microstructure and mechanical properties of multilayer Cu/Ni composite processed by accumulative roll bonding, *Mater. Sci. Eng. A.* 559 (2013) 759–764. doi:10.1016/j.msea.2012.09.021.
- [109] H. Chang, M.Y. Zheng, C. Xu, G.D. Fan, H.G. Brokmeier, K. Wu, Microstructure and mechanical properties of the Mg/Al multilayer fabricated by accumulative roll bonding (ARB) at ambient temperature, *Mater. Sci. Eng. A.* 543 (2012) 249–256. doi:10.1016/j.msea.2012.02.083.
- [110] M. Reihanian, M. Naseri, An analytical approach for necking and fracture of hard layer during accumulative roll bonding (ARB) of metallic multilayer, *Mater. Des.* 89 (2016) 1213–1222. doi:10.1016/j.matdes.2015.10.088.
- [111] M. Slámová, P. Sláma, P. Homola, J. Uhlíř, M. Cieslar, Multilayer composite Al99.99/AlMg3 sheets prepared by accumulative roll bonding, *Int. J. Mater. Res.* 100 (2009) 858–862. doi:10.3139/146.110106.
- [112] N. Tsuji, T. Iwata, M. Sato, S. Fujimoto, Y. Minamino, Aging behavior of ultrafine grained Al-2 wt%Cu alloy severely deformed by accumulative roll bonding, *Sci. Technol. Adv. Mater.* 5 (2004) 173–180. doi:10.1016/j.stam.2003.10.019.
- [113] X. Li, G. Zu, M. Ding, Y. Mu, P. Wang, Interfacial microstructure and mechanical properties of Cu/Al clad sheet fabricated by asymmetrical roll bonding and annealing, *Mater. Sci. Eng. A.* 529 (2011) 485–491. doi:10.1016/j.msea.2011.09.087.
- [114] S. Roy, B.R. Nataraj, S. Suwas, S. Kumar, K. Chattopadhyay, Microstructure and texture evolution during accumulative roll bonding of aluminium alloys AA2219/AA5086 composite laminates, *J. Mater. Sci.* 47 (2012) 6402–6419. doi:10.1007/s10853-012-6567-z.
- [115] K. Nyirenda, L. Qing, C. Zejun, Processing a Multilayer laminate sheet by accumulative roll bonding, *2* (2013) 160–169.
- [116] F. Kümmel, M. Kreuz, T. Hausöl, H. Höppel, M. Göken, Microstructure and Mechanical Properties of Accumulative Roll-Bonded AA1050A/AA5005 Laminated Metal Composites, *Metals (Basel)*. 6 (2016) 56. doi:10.3390/met6030056.

- [117] F. Kümmel, T.S. Tegtmeier, H.W. Höppel, M. Göken, Optimized layer architecture for an extended fatigue life of ultrafine-grained AA1050/AA5005 laminated metal composites, *IOP Conf. Ser. Mater. Sci. Eng.* 194 (2017). doi:10.1088/1757-899X/194/1/012036.
- [118] A. Mozaffari, M. Hosseini, H.D. Manesh, Al/Ni metal intermetallic composite produced by accumulative roll bonding and reaction annealing, *J. Alloys Compd.* 509 (2011) 9938–9945. doi:10.1016/j.jallcom.2011.07.103.
- [119] T. Hausöl, H.W. Höppel, M. Göken, Microstructure and Mechanical Properties of Accumulative Roll Bonded AA6014 / AA5754 Aluminium Laminates, 669 (2011) 217–222. doi:10.4028/www.scientific.net/MSF.667-669.217.
- [120] Tailoring materials properties of UFG aluminium alloys by accumulative roll bonded sandwich-like sheets, (n.d.).
- [121] M. Cieslar, J. Uhlíř, P. Sláma, M. Slámovář, P. Homola, Multilayer composite al99.99/almg3 sheets prepared by accumulative roll bonding, *Int. J. Mater. Res.* 100 (2009) 858–862. doi:10.3139/146.110106.
- [122] S. Roy, B.R. Nataraj, S. Suwas, S. Kumar, K. Chattopadhyay, Accumulative roll bonding of aluminum alloys 2219/5086 laminates: Microstructural evolution and tensile properties, *Mater. Des.* 36 (2012) 529–539. doi:10.1016/j.matdes.2011.11.015.
- [123] H. Yu, C. Lu, A.K. Tieu, A. Godbole, L. Su, Y. Sun, M. Liu, D. Tang, C. Kong, Fabrication of ultra-thin nanostructured bimetallic foils by Accumulative Roll Bonding and Asymmetric Rolling, *Sci. Rep.* 3 (2013). doi:10.1038/srep02373.
- [124] C.-C. Hsieh, M.-C. Chen, W. Wu, Mechanical Property and Fracture Behavior of Al/Mg Composite Produced by Accumulative Roll Bonding Technique, *J. Compos.* 2013 (2013) 1–8. doi:10.1155/2013/748273.
- [125] M. Soltan Ali Nezhad, A. Haerian Ardakani, A study of joint quality of aluminum and low carbon steel strips by warm rolling, *Mater. Des.* 30 (2009) 1103–1109. doi:10.1016/j.matdes.2008.06.042.
- [126] S.L. Semiatin, H.R. Piehler, Deformation of sandwich sheet materials in uniaxial tension, *Metall. Trans. A.* 10 (1979) 85–96. doi:10.1007/BF02686411.
- [127] A.A. Roostaei, A. Zarei-Hanzaki, H.R. Abedi, M.R. Rokni, An investigation into the mechanical behavior and microstructural evolution of the accumulative roll bonded AZ31 Mg alloy upon annealing, *Mater. Des.* 32 (2011) 2963–2968. doi:10.1016/j.matdes.2011.01.038.
- [128] V. Karthik, P. Visweswaran, A. Vijayraghavan, K. V. Kasiviswanathan, B. Raj, Tensile-

- shear correlations obtained from shear punch test technique using a modified experimental approach, *J. Nucl. Mater.* 393 (2009) 425–432. doi:10.1016/j.jnucmat.2009.06.027.
- [129] A.R. Geranmayeh, R. Mahmudi, M. Kangooie, High-temperature shear strength of lead-free Sn-Sb-Ag/Al₂O₃ composite solder, *Mater. Sci. Eng. A.* 528 (2011) 3967–3972. doi:10.1016/j.msea.2011.02.034.
- [130] P. Hein, F. Vollertsen, Hydroforming of sheet metal pairs, *J. Mater. Process. Technol.* 87 (1999) 154–164. doi:10.1016/S0924-0136(98)00347-1.
- [131] S. Novotny, M. Geiger, Process design for hydroforming of lightweight metal sheets at elevated temperatures, *J. Mater. Process. Technol.* 138 (2003) 594–599. doi:10.1016/S0924-0136(03)00042-6.
- [132] S.M. Kurtz, C.W. Jewett, J.S. Bergström, J.R. Foulds, A.A. Edidin, Miniature specimen shear punch test for UHMWPE used in total joint replacements, *Biomaterials.* 23 (2002) 1907–1919. doi:10.1016/S0142-9612(01)00316-7.
- [133] M. Kuna, M. Abendroth, Identification and validation of ductile damage parameters by the small punch test, 15th Eur. Conf. Fract. ‘Advanced Fract. Mech. Life Saf. Assessments.’ 1(2004)710–725. <http://www.gruppofrattura.it/ocs/index.php/esis/ECF15/paper/view/8719/4785>.
- [134] S. Acharya, K.K. Ray, Assessment of tensile properties of spot welds using shear punch test, *Mater. Sci. Eng. A.* 565 (2013) 405–413. doi:10.1016/j.msea.2012.12.068.
- [135] P. Bahrami, A. Azizi, Investigation of Mechanical Properties for Commercial Purity Titanium Severely Plastic Deformed by Accumulative Roll-bonding Process, *J. Mod. Process. Manuf. Prod.* 6 (2017) 37–49.
- [136] G.E. Lucas, J.W. Sheckherd, G.R. Odette, S. Panchanadeeswaran, Shear punch tests for mechanical property measurements in TEM disc-sized specimens, *J. Nucl. Mater.* 122 (1984) 429–434. doi:10.1016/0022-3115(84)90635-4.
- [137] R.K. Guduru, K.A. Darling, R. Kishore, R.O. Scattergood, C.C. Koch, K.L. Murty, Evaluation of mechanical properties using shear-punch testing, *Mater. Sci. Eng. A.* 395 (2005) 307–314. doi:10.1016/j.msea.2004.12.048.
- [138] M.L. Hamilton, F.A. Garner, M.B. Toloczko, S.A. Maloy, W.F. Sommer, M.R. James, P.D. Ferguson, M.R. Louthan, Shear punch and tensile measurements of mechanical property changes induced in various austenitic alloys by high-energy mixed proton and neutron irradiation at low temperatures, *J. Nucl. Mater.* 283–287 (2000) 418–422. doi:10.1016/S0022-3115(00)00363-9.

- [139] G.R. Stewart, A.M. Elwazri, R. Varano, N. Pokutyłowicz, S. Yue, J.J. Jonas, Shear punch testing of welded pipeline steel, *Mater. Sci. Eng. A.* 420 (2006) 115–121. doi:10.1016/j.msea.2006.01.081.
- [140] M. Zabihi, M.R. Toroghinejad, A. Shafyei, Evaluating the mechanical behavior of hot rolled Al/alumina composite strips using shear punch test, *Mater. Sci. Eng. A.* 618 (2014) 490–495. doi:10.1016/j.msea.2014.09.037.
- [141] M. Karbasi, E. Keshavarz Alamdari, Improving the Mechanical Properties and the Microstructure of Pb Electrowinning Anodes Using Accumulative Roll Bonding, *Trans. Indian Inst. Met.* 69 (2016) 1097–1105. doi:10.1007/s12666-015-0627-4.
- [142] C. Schneider, S. Maddox, Best practice guide on statistical analysis of fatigue data, *Weld. Inst. Rep.* (2003) 1–30. <http://www.math.ntnu.no/~bo/stat2/welding.pdf>.
- [143] T. Street, *The Cyclic Properties of Engineering Materials*, 42 (1994) 365–381.
- [144] P.H. Wirsching, *Statistical Summaries of Fatigue Data for Design Purposes*, Nasa Cr 3697. (1983).
- [145] J. Carvill, *Mechanical engineer's data handbook*, (n.d.).
- [146] P. Cavaliere, Fatigue properties and crack behavior of ultra-fine and nanocrystalline pure metals, *Int. J. Fatigue.* 31 (2009) 1476–1489. doi:10.1016/j.ijfatigue.2009.05.004.
- [147] S.R. Agnew, J.R. Weertman, Cyclic softening of ultrafine grain copper, *Mater. Sci. Eng. A.* 244 (1998) 145–153. doi:10.1016/S0921-5093(97)00689-8.
- [148] C.C.F. Kwan, Z. Wang, Cyclic deformation of ultra-fine grained commercial purity aluminum processed by accumulative roll-bonding, *Materials (Basel)*. 6 (2013) 3469–3481. doi:10.3390/ma6083469.
- [149] H.W. Höppel, M. Kautz, C. Xu, M. Murashkin, T.G. Langdon, R.Z. Valiev, H. Mughrabi, An overview: Fatigue behaviour of ultrafine-grained metals and alloys, *Int. J. Fatigue.* 28 (2006) 1001–1010. doi:10.1016/j.ijfatigue.2005.08.014.
- [150] H.S. Liu, B. Zhang, G.P. Zhang, Enhanced toughness and fatigue strength of cold roll bonded Cu/Cu laminated composites with mechanical contrast, *Scr. Mater.* 65 (2011) 891–894. doi:10.1016/j.scriptamat.2011.08.001.
- [151] M. Reihanian, M. Naseri, M.J. Shahmansouri, Effect of the particle size on the deformation and fracture behavior of Al / 4vol .% Al₂O₃ composite produced by accumulative roll bonding (ARB), 2 (2015) 14–26.
- [152] C. Hsieh, M. Chen, W. Wu, Mechanical Property and Fracture Behavior of Al / Mg Composite Produced by Accumulative Roll Bonding Technique, 2013 (2013).

- [153] Y. Sugimura, P.G. Lim, C.F. Shih, S. Suresh, Fracture normal to a bimaterial interface: Effects of plasticity on crack-tip shielding and amplification, *Acta Metall. Mater.* 43 (1995) 1157–1169. doi:10.1016/0956-7151(94)00295-S.
- [154] R. Pippan, K. Flechsig, F.O. Riemelmoser, Fatigue crack propagation behavior in the vicinity of an interface between materials with different yield stresses, *Mater. Sci. Eng. A.* 283 (2000) 225–233. doi:10.1016/S0921-5093(00)00703-6.
- [155] S.T. Method, T.S. Exponents, M.S. Materials, *Astm e 646 – 98*, Annu. B. ASTM Stand. 2000. 03.01 (2009) (E 646 – 98), Section 3,.
- [156] A. International, *Fatigue, Elem. Metall. Eng. Alloy.* (2008) 243–265.
- [157] Standard Practice for Conducting Force Controlled Constant Amplitude Axial Fatigue Tests of Metallic Materials, (ASTM E 466-96, 1997), pp. 466–470., n.d.
- [158] L.E. Murr, Y. Li, R.D. Flores, E.A. Trillo, J.C. McClure, Intercalation vortices and related microstructural features in the friction-stir welding of dissimilar metals, *Mater. Res. Innov.* 2 (1998) 150–163. doi:10.1007/s100190050078.
- [159] G. Purcek, O. Saray, I. Karaman, H.J. Maier, High strength and high ductility of ultrafine-grained, interstitial-free steel produced by ECAE and annealing, *Metall. Mater. Trans. A Phys. Metall. Mater. Sci.* 43 (2012) 1884–1894. doi:10.1007/s11661-011-1063-7.
- [160] J. May, M. Dinkel, D. Amberger, H.W. Höppel, M. Göken, Mechanical properties, dislocation density and grain structure of ultrafine-grained aluminum and aluminum-magnesium alloys, *Metall. Mater. Trans. A Phys. Metall. Mater. Sci.* 38 A (2007) 1941–1945. doi:10.1007/s11661-007-9110-0.
- [161] M. Naseri, A. Hassani, M. Tajally, An alternative method for manufacturing Al/B₄C/SiC hybrid composite strips by cross accumulative roll bonding (CARB) process, *Ceram. Int.* 41 (2015) 13461–13469. doi:10.1016/j.ceramint.2015.07.137.
- [162] B.L. Li, N. Tsuji, N. Kamikawa, Microstructure homogeneity in various metallic materials heavily deformed by accumulative roll-bonding, *Mater. Sci. Eng. A.* 423 (2006) 331–342. doi:10.1016/j.msea.2006.02.028.
- [163] S. Tamimi, M. Ketabchi, N. Parvin, Microstructural evolution and mechanical properties of accumulative roll bonded interstitial free steel, *Mater. Des.* 30 (2009) 2556–2562. doi:10.1016/j.matdes.2008.09.039.
- [164] M. Eizadjou, H.D. Manesh, K. Janghorban, Microstructure and mechanical properties of ultra-fine grains (UFGs) aluminum strips produced by ARB process, 474 (2009) 406–415. doi:10.1016/j.jallcom.2008.06.161.

- [165] M. Shaarbafe, M.R. Toroghinejad, Nano-grained copper strip produced by accumulative roll bonding process, *Mater. Sci. Eng. A.* 473 (2008) 28–33. doi:10.1016/j.msea.2007.03.065.
- [166] M.R. Rezaei, M.R. Toroghinejad, F. Ashrafizadeh, Production of nano-grained structure in 6061 aluminum alloy strip by accumulative roll bonding, *Mater. Sci. Eng. A.* 529 (2011) 442–446. doi:10.1016/j.msea.2011.09.057.
- [167] H.W. Höppel, J. May, M. Göken, Enhanced strength and ductility in ultrafine-grained aluminium produced by accumulative roll bonding, *Adv. Eng. Mater.* 6 (2004) 781–784. doi:10.1002/adem.200306582.
- [168] M. Ruppert, M. Strebl, H.W. Höppel, M. Göken, Mechanical properties of ultrafine-grained AlZnMg(Cu)-alloys AA7020 and AA7075 processed by accumulative roll bonding, *J. Mater. Sci.* 50 (2015) 4422–4429. doi:10.1007/s10853-015-9008-y.
- [169] N. Kamikawa, N. Tsuji, X. Huang, N. Hansen, Quantification of annealed microstructures in ARB processed aluminum, *Acta Mater.* 54 (2006) 3055–3066. doi:10.1016/j.actamat.2006.02.046.
- [170] H.O. Asbeck, H. Mecking, Influence of friction and geometry of deformation on texture inhomogeneities during rolling of Cu single crystals as an example, *Mater. Sci. Eng.* 34 (1978) 111–119. doi:10.1016/0025-5416(78)90041-1.
- [171] T. Inoue, F. Yin, Y. Kimura, Strain distribution and microstructural evolution in multi-pass warm caliber rolling, *Mater. Sci. Eng. A.* 466 (2007) 114–122. doi:10.1016/j.msea.2007.02.098.
- [172] L. Ghalandari, M.M. Mahdavian, M. Reihanian, M. Mahmoudiniya, Production of Al/Sn multilayer composite by accumulative roll bonding (ARB): A study of microstructure and mechanical properties, *Mater. Sci. Eng. A.* 661 (2016) 179–186. doi:10.1016/j.msea.2016.02.070.
- [173] H. Alvandi, K. Farmanesh, Microstructural and Mechanical Properties of Nano/Ultra-fine Structured 7075 Aluminum Alloy by Accumulative Roll-Bonding Process, *Procedia Mater. Sci.* 11 (2015) 17–23. doi:10.1016/j.mspro.2015.11.020.
- [174] C. Lu, K. Tieu, D. Wexler, Significant enhancement of bond strength in the accumulative roll bonding process using nano-sized SiO₂ particles, *J. Mater. Process. Technol.* 209 (2009) 4830–4834. doi:10.1016/j.jmatprotec.2009.01.003.
- [175] P. Hidalgo-manrique, O.A. Ruano, F. Carreño, Materials Science & Engineering A Evolution of the microstructure, texture and creep properties of the 7075 aluminium alloy during hot accumulative roll bonding, *Mater. Sci. Eng. A.* 606 (2014) 434–442. doi:10.1016/j.msea.2014.03.105.

- [176] N. El Mahallawy, A. Fathy, M. Hassan, Evaluation of mechanical properties and microstructure of Al/Al–12%Si multilayer via warm accumulative roll bonding process, *J. Compos. Mater.* (2017) 002199831769214. doi:10.1177/0021998317692141.
- [177] L. Su, C. Lu, A.K. Tieu, G. Deng, X. Sun, Ultrafine grained AA1050/AA6061 composite produced by accumulative roll bonding, *Mater. Sci. Eng. A.* 559 (2013) 345–351. doi:10.1016/j.msea.2012.08.109.
- [178] G.L. Hankin, M.B. Toloczko, M.L. Hamilton, R.G. Faulkner, Validation of the shear punch-tensile correlation technique using irradiated materials, *J. Nucl. Mater.* 258–263 (1998) 1651–1656. doi:10.1016/S0022-3115(98)00203-7.
- [179] H.R. Abedi, A. Zarei-Hanzaki, M. Bagherzadeh Biucki, M. Emamy, Evaluating the room temperature mechanical properties of age hardened AZ80 magnesium alloy using shear punch testing method, *Mater. Sci. Eng. A.* 606 (2014) 360–369. doi:10.1016/j.msea.2014.03.106.
- [180] F. Kümmel, H.W. Höppel, M. Göken, Layer architecture and fatigue life of ultrafine-grained laminated metal composites consisting of different aluminum alloys, *Mater. Sci. Eng. A.* 702 (2017) 406–413. doi:10.1016/j.msea.2017.06.105.
- [181] A. Pineau, A. Amine Benzerga, T. Pardoen, Failure of metals III: Fracture and fatigue of nanostructured metallic materials, *Acta Mater.* 107 (2016) 508–544. doi:10.1016/j.actamat.2015.07.049.
- [182] L. Su, C. Lu, Microstructure and mechanical properties of AA5005 / AA6061 laminated composite processed by accumulative roll bonding, *Metall. Mater. Trans. B.* 45 (2014) 515–522.
- [183] M. Naseri, A. Hassani, M. Tajally, Fabrication and characterization of hybrid composite strips with homogeneously dispersed ceramic particles by severe plastic deformation, *Ceram. Int.* 41 (2015) 3952–3960. doi:10.1016/j.ceramint.2014.11.079.
- [184] L. Su, C. Lu, H. Li, G. Deng, K. Tieu, Investigation of ultrafine grained AA1050 fabricated by accumulative roll bonding, *Mater. Sci. Eng. A.* 614 (2014) 148–155. doi:10.1016/j.msea.2014.07.032.
- [185] C. Przybyla, R. Prasannavenkatesan, N. Salajegheh, D.L. McDowell, Microstructure-sensitive modeling of high cycle fatigue, *Int. J. Fatigue.* 32 (2010) 512–525. doi:10.1016/j.ijfatigue.2009.03.021.
- [186] P. Lukáš, Fatigue Crack Initiation Mechanisms, *Encycl. Mater. Sci. Technol.* (2004) 2882–2891. doi:10.1016/b0-08-043152-6/00514-3.
- [187] J. Nie, M. Liu, F. Wang, Y. Zhao, Y. Li, Y. Cao, Y. Zhu, Fabrication of Al/Mg/Al

- composites via accumulative roll bonding and their mechanical properties, *Materials* (Basel). 9 (2016). doi:10.3390/ma9110951.
- [188] S.E. Ion, F.J. Humphreys, S.H. White, Dynamic recrystallisation and the development of microstructure during the high temperature deformation of magnesium, *Acta Metall.* 30 (1982) 1909–1919. doi:10.1016/0001-6160(82)90031-1.
- [189] N. Mohammad Nejad Fard, H. Mirzadeh, R. Mohammad, J.-M. Cabrera, Accumulative Roll Bonding of Aluminum/Stainless Steel Sheets, *J. Ultrafine Grained Nanostructured Mater.* 50 (2017) 1–5. doi:10.7508/JUFGNSM.2017.01.01.
- [190] H.D. Manesh, H.S. Shahabi, Effective parameters on bonding strength of roll bonded Al/St/Al multilayer strips, *J. Alloys Compd.* 476 (2009) 292–299. doi:10.1016/j.jallcom.2008.08.081.
- [191] H.Q. Sun, Y.N. Shi, M.X. Zhang, K. Lu, Plastic strain-induced grain refinement in the nanometer scale in a Mg alloy, *Acta Mater.* 55 (2007) 975–982. doi:10.1016/j.actamat.2006.09.018.
- [192] M. Science, x Strain variations on rolling condition in accumulative roll-bonding by finite element analysis, (2010) 589–611.
- [193] T. Inoue, S. Torizuka, K. Nagai, Effect of shear deformation on refinement of crystal grains, *Mater. Sci. Technol.* 18 (2003) 1007–1015. doi:10.1179/026708302225005855.
- [194] M. Naseri, M. Reihanian, E. Borhani, A new strategy to simultaneous increase in the strength and ductility of AA2024 alloy via accumulative roll bonding (ARB), *Mater. Sci. Eng. A.* 656 (2016) 12–20. doi:10.1016/j.msea.2016.01.020.
- [195] L. Kunz, P. Lukáš, M. Svoboda, Fatigue strength, microstructural stability and strain localization in ultrafine-grained copper, *Mater. Sci. Eng. A.* 424 (2006) 97–104. doi:10.1016/j.msea.2006.02.029.
- [196] T. Leitner, A. Hohenwarter, R. Pippan, Fatigue Crack Growth Behavior of Ultrafine-grained Nickel Produced by High Pressure Torsion, *Procedia Mater. Sci.* 3 (2014) 1044–1049. doi:10.1016/j.mspro.2014.06.170.
- [197] S. Tamimi, M. Ketabchi, N. Parvin, Microstructural evolution and mechanical properties of accumulative roll bonded interstitial free steel, *Mater. Des.* 30 (2009) 2556–2562. doi:10.1016/j.matdes.2008.09.039.
- [198] F. Hahnenberger, M. Smaga, D. Eifler, Microstructural investigation of the fatigue behavior and phase transformation in metastable austenitic steels at ambient and lower temperatures, *Int. J. Fatigue.* 69 (2014) 36–48. doi:10.1016/j.ijfatigue.2012.07.004.
- [199] F. Kümmel, B. Diepold, K.F. Sauer, C. Schunk, A. Prakash, H.W. Höppel, M. Göken,

- High Lightweight Potential of Ultrafine-Grained Aluminum/Steel Laminated Metal Composites Produced by Accumulative Roll Bonding, *Adv. Eng. Mater.* 1800286 (2018) 1–8. doi:10.1002/adem.201800286.
- [200] D. Rahmatabadi, M. Tayyebi, A. Sheikhi, R. Hashemi, Fracture toughness investigation of Al1050/Cu/MgAZ31ZB multi-layered composite produced by accumulative roll bonding process, *Mater. Sci. Eng. A.* 734 (2018) 427–436. doi:10.1016/j.msea.2018.08.017.
- [201] L. Fratini, M. Merklein, W. Boehm, D. Campanella, Modelling Aspects in Accumulative Roll Bonding Process by Explicit Finite Element Analysis, *Key Eng. Mater.* 549 (2013) 452–459. doi:10.4028/www.scientific.net/KEM.549.452.
- [202] S.C. Yoon, Z. Horita, H.S. Kim, Finite element analysis of plastic deformation behavior during high pressure torsion processing, *J. Mater. Process. Technol.* 201 (2008) 32–36. doi:10.1016/j.jmatprotec.2007.11.204.
- [203] H.S. Kim, P. Quang, M.H. Seo, S.I. Hong, K.H. Baik, H.R. Lee, D.M. Nghiep, Process Modelling of Equal Channel Angular Pressing for Ultrafine Grained Materials, *Mater. Trans.* 45 (2004) 2172–2176. doi:10.2320/matertrans.45.2172.
- [204] T. Inoue, N. Tsuji, Quantification of strain in accumulative roll-bonding under unlubricated condition by finite element analysis, *Comput. Mater. Sci.* 46 (2009) 261–266. doi:10.1016/j.commatsci.2009.03.005.
- [205] T. Inoue, A. Yanagida, J. Yanagimoto, Finite element simulation of accumulative roll-bonding process, *Mater. Lett.* 106 (2013) 37–40. doi:10.1016/j.matlet.2013.04.093.
- [206] Richard G. Budynas, J. Keith Nisbett, *Design Engineering Mechanical*, 2006

PUBLICATIONS BASED ON THE WORK OF THIS THESIS

The results and discussions in this dissertation conclude the work completed in the duration of the author's Ph.D. program. Some of the discussions presented in this work have been published and listed as follows:

Refereed Journal Publications

1. On the mechanical behavior of accumulative roll bonded lightweight composite.

Manuscripts in Preparation for Refereed Journal Publications

1. Effect of Layer Architecture Process on the Monotonic and Cyclic Properties of Severely Deformed IF steel/Aluminum Composite.

Refereed Conference Publications

1. Evaluating the Mechanical Behavior of ARB Processed Aluminum Composites Using Shear Punch Testing.

VITA

Dhyai Hassan Jawad Aljashaami was born in 1970 in Babylon, Iraq. He graduated from Al Musayib High School and starting his education at the University of Technology-Baghdad, Iraq. In 1996 he received his B.Sc. degree in Mechanical Engineering. In January 2005, he completed his M.S. studies at the same university in Mechanical Engineering/Design. Then, he worked at the University of Babylon as a lecturer in the Mechanical Engineering Department for eight years. In 2013, he received a scholarship from the Iraqi Government to complete his doctoral studies in the Republic of Turkey. In September 2014, he started working towards his Ph.D. degree in Mechanical Engineering at Ozyegin University. His research interests at MEMFIS group of Ozyegin University mainly concentrate on the mechanical properties of light alloys and layered metallic composites processed by severe plastic deformation.